Lifetime and Coherence of the Coupled Electron and Nuclear Spin Systems in Semiconductor Quantum Dots

George Gillard

A thesis submitted in partial fulfilment of the requirements for the degree of Doctor of Philosophy

Supervisor: Dr. Evgeny Chekhovich

April, 2022

Low Dimensional Structures and Devices Group
Department of Physics and Astronomy
Faculty of Science

Abstract

This thesis presents experimental investigations into the underlying mechanisms limiting the spin state longevity of III-V InGaAs/GaAs self-assembled quantum dots (QDs), a key step towards realising QDs as a viable quantum computing resource. We investigate the coupled electron and nuclear spin system within the QD using a range of optical and nuclear magnetic resonance techniques to provide an in-depth understanding of the sources causing spin relaxation and decoherence.

Several InGaAs charge-tuneable structures were investigated with varying Fermi reservoir tunnel coupling. We present a comprehensive study of the spin lifetimes, T_1, for the electron and nuclear spin systems for a range of magnetic fields, charge states and tunnel couplings. We combine previously observed mechanisms affecting T_1 to estimate the fundamental limits of the spin lifetimes, in addition to demonstrating measurement of the longest observed InGaAs QD electron spin lifetime of ≈ 1 s.

Existing work suggested nuclear spin ensemble coherence time $T_{2,\mathrm{N}}$ is strongly affected by the presence of an electron, limiting the prospects of QD qubits. We reveal a $T_{2,\mathrm{N}}$ on the scale of milliseconds in a charged QD, in addition to developing a spectral diffusion model to explain nuclear spin decoherence in the presence of a fluctuating electron spin. We show that the nuclear spin bath can be used as an electron spin state sensor with a readout fidelity of $F > 99.8\%$, improving on state of the art spin sensing techniques.

In addition to the studies on QDs, we present results from the testing of recently developed keyhole resonators to be used for fast coherent control of electron spins using magnetic resonance techniques. We demonstrate the ability of keyhole resonator to coherently control electron spins in diamond with high power microwave pulses and pulse lengths on the scale of tens of nanoseconds.

Acknowledgements

I would like to thank those who have assisted me throughout the writing of this thesis and the duration of the PhD, as it would not have been possible without an immense amount of support from my colleagues, friends and family.

I would first like to thank the **Royal Society** for making my PhD possible by funding my studentship. I would like to thank my supervisor **Evgeny Chekhovich** for both the opportunity to participate in such engaging research and the support he has provided throughout the duration of my PhD. His supervision has allowed me to learn many skills and to develop as a researcher.

Thank you to my colleagues from within the C11 lab, with whom I have had many fruitful discussions over the last four years. First of all, **Gau Ragunathan**, who assisted in teaching me how to operate a wide variety of equipment in the lab during the first months of my PhD. I would also like to thank **Ian Griffiths** for fabricating the Schottky diodes that were required for the results within this thesis. Thanks are also deserved for **Peter Millington-Hotze**, who has provided a great deal of assistance in the lab over the final year of my PhD.

I also owe plenty of thanks to many colleagues outside of our C11 lab. Thanks to **Ed Clarke**, who grew the InGaAs quantum dot samples I have studied over the duration of my PhD. I would like to thank **Chris Vickers**, **Phil Taylor** and **Thomas Ball** who work hard to ensure we have the liquid helium needed for our cryostat.

A broader thank you goes out to all of the members of the Low Dimensional Structures and Devices (LDSD) research group with whom I have had many useful discussions over the years, in addition to providing me with valuable feedback about my work. A particular

mention goes to **Maurice Skolnick**, and more recently **Mark Fox**, for their leadership of LDSD throughout my PhD, creating a productive and pleasant research group of which I am grateful to have been involved.

An enormous amount of thanks and gratitude goes to my partner, **Jessica Forsyth**, who has provided unwavering support throughout the duration of the PhD.

I would like to thank my parents **Andrew Gillard** and **Suzanne Gillard** who have always been there to support me in whatever I chose to do. I would also like to thank my brother, **Elliot Gillard**, who has put up with many of my quantum dot ramblings over the years. Thank you to my granddad, **Robert Gillard**, whose tales of scientific mischief are in part responsible for my choice of career. Thank you to my grandma, **Margaret Speed**, who has always shown great interest in what I do.

A final thank you to all the rest of my friends and family whose names and contributions are too numerous to list individually. I would not have been able to complete this PhD without the great times we have had over the last four years.

"There is one more thing... it's been emotional"

– Big Chris, *Lock, Stock and Two Smoking Barrels*

Declaration

I, the author, confirm that the Thesis is my own work. I am aware of the University's Guidance on the Use of Unfair Means (www.sheffield.ac.uk/ssid/unfair-means). This work has not previously been presented for an award at this, or any other, university.

Publications and Conferences

Papers

Presented within thesis

G. Gillard, I. M. Griffiths, G. Ragunathan, A. Ulhaq, C. McEwan, E. Clarke, E. A. Chekhovich. "Fundamental limits of electron and nuclear spin qubit lifetimes in an isolated self-assembled quantum dot". *npj Quantum Information*, **7**, 43 (2021), doi:10.1038/s41534-021-00378-2.

Additional Papers

A. M. Waeber, **G. Gillard**, G. Ragunathan, M. Hopkinson, P. Spencer, D. A. Ritchie, M. S. Skolnick, E. A. Chekhovich. "Pulse control protocols for preserving coherence in dipolar-coupled nuclear spin baths". *Nature Communications*, **10**, 3157 (2019), doi:10.1038/s41467-019-11160-6.

G. Ragunathan, J. Kobak, **G. Gillard**, W. Pacuski, K. Sobczak, J. Borysiuk, M. S. Skolnick, E. A. Chekhovich. "Direct Measurement of Hyperfine Shifts and Radio Frequency Manipulation of Nuclear Spins in Individual CdTe/ZnTe Quantum Dots". *Physical Review Letters*, **122**, 096801 (2019), doi:10.1103/PhysRevLett.122.096801

Conference Presentations

G. Gillard, I. M. Griffiths G. Ragunathan, C. McEwan, A. Ulhaq, E. Clarke, P. Patil, I. Farrer, M. S. Skolnick, E. A. Chekhovich "Optimisation of Electron and Nuclear Spin Lifetimes in InGaAs/GaAs Quantum Dots", *UK Semiconductors 2019*, Sheffield, UK: July 2019

G. Gillard, I. M. Griffiths G. Ragunathan, C. McEwan, A. Ulhaq, E. Clarke, P. Patil, I. Farrer, M. S. Skolnick, E. A. Chekhovich "Optimisation of Electron and Nuclear Spin Lifetimes in InGaAs/GaAs Quantum Dots", *International Conference on Optics of Excitons in Confined Systems (OECS 2019)*, St. Petersburg, Russia: September 2019

G. Gillard, E. Clarke, E. A. Chekhovich "Achieving Long Collective Coherence of Nuclear Spins Coupled to Quantum Dot Electron Spin", *International Conference on Optics of Excitons in Confined Systems (OECS17)*, (Virtual) Dortmund, Germany: September 2021

Posters

G. Gillard, T. J. Broomhall, I. M, Griffiths, G. Ragunathan, A. Ulhaq, C. McEwan, E. Clarke, M. S. Skolnick, E. A. Chekhovich, "Optimisation of electron spin lifetime in InGaAs/GaAs quantum dots", *Quantum Dot Day 2019*, Lancaster, UK: January 2019

G. Gillard, I. M. Griffiths, G. Ragunathan, A. Ulhaq, C. McEwan, E. Clarke, E. A. Chekhovich "Optimisation of Electron and Nuclear Spin Lifetimes in InGaAs/GaAs Quantum Dot Qubits", *International Conference on Nonlinear Optics and Excitation Kinetics in Semiconductors, NOEKS 15*, (Virtual) Munster, Germany: September 2020

G. Gillard, I. M. Griffiths, G. Ragunathan, A. Ulhaq, C. McEwan, E. Clarke, E. A. Chekhovich "Optimisation of Electron and Nuclear Spin Lifetimes in InGaAs/GaAs Quantum Dots", *11th International Conference on Quantum Dots*, (Virtual) Munich, Germany: December 2020

G. Gillard, E. Clarke, E. A. Chekhovich "Long Coherence of a Nuclear Spin Bath Coupled to Electron Spin Qubit in an InGaAs Quantum Dot", *Quantum Dot Day 2021*, Virtual Conference: March 2021

List of Acronyms

AlAs	Aluminium Arsenide
BNC	Bayonet Neill-Concelman radio frequency connector/cable
BS	Beamsplitter
CB	Conduction Band
CHASE	Combined Hahn and solid echo
CPW	Coplanar waveguide
CT	Central transition
CW	Continuous wave
DBR	Diffracted Bragg reflector
ESR	Electron spin resonance
FvdM	Frank-van der Merve
HWP	Half-waveplate
InAs	Indium Arsenide
InGaAs	Indium Gallium Arsenide
KHR	Keyhole resonator
MBE	Molecular beam epitaxy
ML	Monolayer
MW	Microwave
NMR	Nuclear magnetic resonance
NV	Nitrogen vacancy
ODNMR	Optically detected nuclear magnetic resonance

PCB Printed circuit board

QWP Quarter-waveplate

ResFl Resonance fluorescence

RF Radio frequency

RWA Rotating wave approximation

SiC Silicon carbide

SK Stranski-Krastanow

ST Satellite transition

Ti Titanium

VB Valence Band

VW Volmer-Weber

WL Wetting layer

Contents

List of Figures

1

Introduction

Quantum mechanics has been at the heart of developing our fundamental understanding of the universe since its inception a century ago, in addition to being the driving force behind many technological innovations. Its counter-intuitive properties have challenged some of the greatest scientists of the 20th century, and further deepened our understanding of the world around us. Despite complex theoretical and computational techniques available to us, fundamental quantum mechanical systems are both challenging and resource-intensive to simulate.

Several separate publications by Feynmann, Deutsch and Benioff in the early 1980's came to the conclusion that simulating quantum mechanical systems would ultimately require a computer that relied on quantum mechanical properties instead of classical techniques [1–5]. Phenomena such as entanglement and superposition are extremely computationally intense to simulate in a typical computer using binary states (0 or 1). A system built to exploit quantum mechanics would require a fundamental change to the states used. The new states are known as qubits - states that themselves exhibit the quantum mechanical phenomena. The qubits are not pure binary, 0 or 1, instead possessing a wavefunction that can be an arbitrary superposition of the two-level system basis states 0 and 1. The two-level system wavefunction can be more accurately described by a simple equation,

$$|\Psi\rangle = \alpha|0\rangle + \beta|1\rangle \tag{1.1}$$

where $|\Psi\rangle$ is the wavefunction of the qubit state, α and β are probability amplitudes describing the likelihood of the system collapsing to that state and $|0\rangle$, $|1\rangle$ represent the two basis states of the qubit. Here we can see that the state can be in either the $|0\rangle$ or $|1\rangle$ states, or occupy a superposition state defined by the probability amplitudes. Multiple qubit states can be entangled, allowing shared information transfer across a quantum network which can form the basis of a quantum computer.

Quantum algorithms were developed proving the significant impact quantum computing could have on non-trivial computational problems, such as the Deustch-Jozsa's algorithm [6], Grover's list search [7], and Shor's prime factorization [8]. They all theoretically demonstrated faster computation times when compared to classical computers solving the problem, a milestone that came to be referred to as quantum supremacy. Physical realisation of the quantum computer involves overcoming a plethora of physics and engineering challenges, with quantum supremacy only being demonstrated for the first time as recently as 2019 by Google's 53-qubit superconducting quantum processor called Sycamore [9].

The criteria for implementation of quantum computing were laid out in a paper by David P. DiVincenzo [10], describing the properties required for creation of a useful qubit system. The criteria are as follows:

- A **scalable** physical system. The physical system possessing the potential qubits must be able to be scaled up, allowing for N qubits to be used during computation. In addition to the physical system, the supporting hardware such as lasers, cryostats and other control hardware must also be scalable.

- Qubit state **initialisation**. All computational operations require the states involved to start in a known configuration (e.g Initial state: $|0\rangle$)

- Ability to **manipulate** qubit state through application of quantum gates. The state

must be able to be changed arbitrarily by an externally controlled source (e.g Change state: $|0\rangle \rightarrow |1\rangle$).

- Reliable **readout** of the qubit state. It must be possible to read the information stored within the system at a given time.

- **Long-lasting states**. The qubit state will irretrievably lose information over time due to interactions with the environment, and as such, it is critical to ensure this time is much longer than the time over which computations are performed.

In addition to the requirements highlighted above, we must also be able to transmit and store quantum information through the interchanging of information between a "stationary" qubit at a fixed location and a "flying" qubit allowing transfer of the information to another location.

A photon is generally used as a "flying" qubit, as useful information can be stored in the polarisation of light. Travelling at the speed of light has a clear advantage for information transfer, however, there is no way to store a photon at a single location. Properties such as charge and spin can be found in particles, which can be spatially trapped to allow information storage. There are a large number of candidates for "stationary" qubits that fulfill the stated requirements, such as superconducting qubits [9, 11–13], trapped ions [14–16], donors in silicon [17] and defects in crystals [18–20]. Particular interest was placed on solid state based platforms as this could operate in parallel with classical computing platforms running on silicon computing chips. One suggestion for a solid state computer was made by DiVincenzo and Loss [21], where they provide theoretical schematics for a two qubit quantum gate based upon the spin properties of electrons trapped within semiconductor quantum dots.

The quantum dot is an ideal candidate to fulfil the criteria laid out thus far. The majority of self-assembled quantum work in the literature is carried out on InGaAs quantum dots due to their excellent optical properties, displaying strong optical signals due to the large optical dipole moment [22]. Optical emission has narrow linewidths with high photon indistinguisha-

bility, making them ideal candidates for solid state single photon sources and fulfulling the requirement to produce "flying" qubits [23–25]. Quantum dots are formed within a semiconductor matrix, making them not only scalable through having multiple QD qubits on the same chip, but allow integration with additional fabricated devices such as optical cavities or diodes for charge tuning [26]. Charge-tuneable devices allow on-demand occupation of the quantum dot with an electron, stably confining the electron at the quantum dot site and allowing use as a "stationary" spin qubit.

One major challenge of the quantum dot qubit proposals is that the growth process results in randomly positioned quantum dots, limiting the ability to create a regular array of quantum dots on the same substrate. Additional challenges arise when considering the electron spin qubit in a quantum dot, as the rich nuclear spin environment provides an intrinsic and irremovable source of environmental interaction. Initial work into optimising the spin qubit system framed the nuclear spin bath as a limiting property of the self assembled quantum dot spin qubit [27, 28]. More recently, the nuclear spin bath has come to be studied as a quantum resource itself owing to the large number of long lasting spin states [29, 30]. A hybrid electron-nuclear spin qubit system has been demonstrated by which the electron is used as a fast qubit that can transfer information to longer lasting nuclear spin memory [31].

Study of spin qubits within the self assembled InGaAs/GaAs semiconductor quantum dot system is the focus of the work presented within this thesis. We set out to demonstrate the initialisation, manipulation and readout of spin qubits in quantum dots through the use of optical and magnetic resonance techniques, with major focus on investigating the dynamic interactions that drive the loss of coherence of both electron and nuclear spins. Complete understanding of the various environmental interactions present in the quantum dot will allow us to determine ideal operating conditions for a long lasting coherent spin qubit.

Long lasting states form one part of the two technical challenges for coherent control of the electron spin through electron spin resonance (ESR) techniques, something that has been only achieved once in the literature [32]. The second technical hurdle is the requirement to

produce magnetic resonance pulses at GHz frequencies while minimising parasitic electric fields that will negatively affect the electron spin state. Consequently, we also investigate new experimental resonators capable of generating the required microwave pulses for the coherent control the InGaAs QD electron spin state.

Contents of this thesis

Chapter 2 introduces the quantum dot system, discussing the hetereoepitaxial techniques used in quantum dot growth. We review the band structure of the quantum dot under three dimensional confinement and the implications this has on the optical properties. Exciton structure is discussed, in addition to the exchange interaction and external field effects upon the excitons. Additionally, we provide a summary of the quantum dot spin system, covering both carrier and nuclear spins within the quantum dot and their hyperfine interaction. Finally, we discuss the theory behind initialising, manipulating and readout the quantum dot spin qubit.

Chapter 3 provides an overview of the experimental apparatus used for investigations in this thesis, primarily focusing on the liquid helium bath cryostat, optical excitation and detection configuration. A detailed description of the techniques for both pulsed and broadband nuclear magnetic resonance methods is included, in addition to an explanation about the process of measuring resonance fluorescence.

Chapter 4 presents a published paper on results from a study of electron and nuclear lifetimes within multiple InGaAs/GaAs quantum dot structures. The structures were designed to have a varying tunnel coupling from the doped layer to quantum dots and allowed systematic measurement of spin lifetimes for a range of tunnel couplings, magnetic field and charge states. We present fundamental limitations placed on the lifetimes within quantum dots, in addition to never seen before electron spin lifetimes of ≈ 1 s.

Chapter 5 is presented in the form of a preprint manuscript, which has been submitted

to a journal for peer review. Here, we investigate the coherence times of the nuclear spin ensemble within a charged quantum dot, providing insight into the effects of hyperfine interaction on coherence. We present results providing a complete understanding of the effect of the electron on nuclear spin coherence, in addition to a series of single shot nuclear spin coherence measurements, which ultimately lead to development of a high fidelity ($F > 99.7$ %) electron spin readout technique exploiting the electron-nuclear interaction.

Chapter 6 discusses the testing of keyhole resonator designs under short 8 GHz microwave bursts, a key requirement for performing fast coherent control of the electron in charged quantum dots. We present basic characterisation of improved designs of the recently developed keyhole resonator [33], in addition to testing of the resonators on NV^- centres in diamond. We demonstrate pulsed electron spin resonance of the NV^- centres in diamond and compare the efficiency of the resonators to alternative designs in the literature.

Chapter 7 summarises the findings of the thesis and comments on the direction of future research.

2

Background

2.1 Quantum dots

Quantum dots are nanostructures exploiting the confinement properties of semiconductor materials. Early work into semiconductor epitaxial growth focused on attempting to create new structures of heteroepitaxial materials. Heteroepitaxy is the process of layering materials to integrate different types of crystalline structures into a single substrate. It was found that by layering materials with differing bandgaps, a potential well could be formed, confining carriers within a certain region of the sample. In the case of alternating layers of material, single-dimensional confinement is found, preventing movement of charge carriers between the layers but allowing movement in a two-dimensional plane, forming a structure known as a Quantum Well [34]. Such a structure allowed the first study of confined charged carriers, revealing effects such as the quantum Hall effect [35], and providing useful structures which have been used for many applications such as quantum cascade lasers [36].

Further theoretical development endeavoured the search for higher-order confinement effects up to 3 dimensions, which would allow a particle to be confined in all spatial directions. Such a system would act as an artificial atom, with discrete energy levels and a delta function density of states. Early work into quantum information processing realised the potential

for such well-defined states, and confined atoms were being studied for qubit purposes [21]. With the semiconductor fabrication industry in full swing in the early 90s, it was recognised that being able to fabricate artificial atoms on a crystal substrate would provide the robustness of the atoms with the scalability of standard computing hardware [37]. Discovery of structures with delta function density states occurred in the late 1980s by Goldstein et al. [38], where imperfections in quantum well growth provided sharp lines in photoluminescent studies. Further work into this demonstrated the imperfections could be reliably reproduced through changing the rate of material deposition, opening up the possibility to deterministically create these artificial atoms which later became known as quantum dots [39–41].

2.1.1 Quantum dot growth

Several types of quantum dots exist, each with varying growth techniques and useful properties. The two primary growth methods are heteroepitaxy and wet chemical synthesis [39]. While the wet chemical synthesis provides interesting results, the work in this thesis focuses on heteroepitaxial quantum dots, specifically InGaAs/GaAs self assembled quantum dots.

As mentioned previously, heteroepitaxy is the deposition of a material on to a substrate, where the subtrate and deposition material are different. The structural and chemical differences between the materials and other parameters such as temperature and deposition rate determine how the deposited material "grows" on the substrate. During heteroeptiaxial growth, there are three types of growth mode that can occur due to thermodynamics and kinetics of the surfaces interacting. Control of these processes is determined by the interplay of bond strength between a deposited atom and its surrounding deposited atoms, and the bond strength of the deposited atom and the atoms forming the substrate [39].

The first case is known as the Frank-van der Merve (FvdM) growth mode and is where deposited-substrate bonds are stronger than the bonds between deposited atoms, resulting in perfect two dimensional layer growth [42]. The second case is known as Volmer-Weber growth [43], and is the opposite extreme of the FvdM growth mode. Deposited-substrate

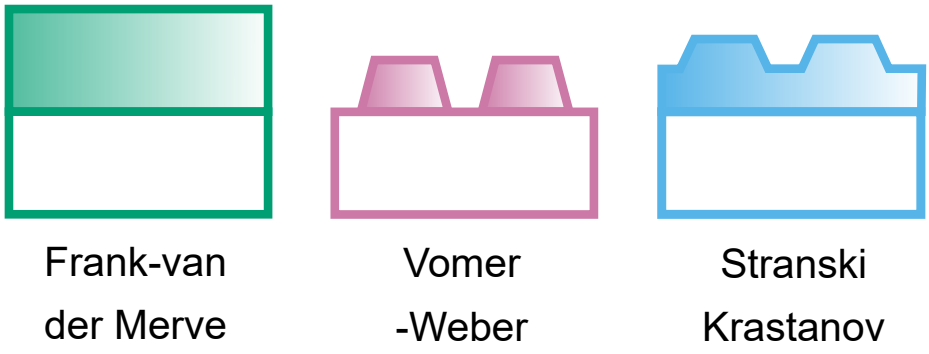

Figure 2.1: Different growth modes in heteroepitaxial growth. Adapted from [39]

atomic bonding is weaker than inter-deposited material bonding in this scenario, resulting in islands forming on the surface of the substrate. The third and final case is a compromise between the two previous scenarios, and is called Stranski-Krastanow (SK) growth [44]. Here, a two dimensional layer forms followed by the nucleation of islands on this new surface. Visualisation of these three growth modes can be seen in Fig 2.1.

Self-assembled quantum dots are grown through the SK growth mode. Deposition of the QD material first forms a two dimension layer referred to as the wetting layer (WL), followed by nucleation of islands which form the quantum dots. The islands form as a relaxation of the strain built up due to the difference in lattice constants between the substrate and deposited material. The presence of a lattice mismatch is an underlying requirement for both the VW and SK growth modes. Careful selection of the lattice mismatch allows a range of energies and sizes of quantum dot to be formed [45].

For the InGaAs quantum dots discussed in this thesis, InAs is deposited upon a GaAs substrate until a wetting layer of sufficient thickness is created, at which point the relaxation of the 7% strain mismatch between InAs and GaAs causes formation of the islands that become quantum dots [46]. The critical thickness of the wetting layer for InGaAs dots formation is approximately $\sim$ 1.7 monolayers (ML) [47–49]. Ideally, there would be no wetting layer in order to minimise the interaction of wetting layer states with the QD states, which causes broadening of PL linewidths and increasing sources of decoherence [50, 51].

There has been some successful work into growing quantum dots without a wetting layer through overgrowth of the InAs QD layer with AlAs [52].

Once the dot layer has formed on the wetting layer, it is necessary to apply another layer of material in order to improve confinement effects [45]. QDs with this additional layer are referred to as capped QDs. Capping of the QD changes the morphology of the quantum dot as material from the cap can alloy with the QD, creating imperfections in the shape due to strain decrease [53–55]. The change in morphology in the case of In(Ga)As dots introduces Ga atoms to the QD, hence the dots being referred to as In(Ga)As QDs instead of just the deposited dot layer InAs [45].

Formation of SK quantum dots occurs in a random manner, resulting in a layer of quantum dots on top of the wetting layer with a range of positions and sizes. As we will see when studying the confinement effects within the SK QDs, size has a strong effect on the emission energy of the quantum dot. Variation in dot size across the substrate results in a broad distribution of dot energies across the sample [39].

Density of quantum dots is an important quantity to control as a high density will not allow optical interaction with a single quantum dot. This can be controlled by using a low deposition rate of InAs and monitoring the surface patterns with reflection high energy electron diffraction (RHEED), allowing the deposition of material to be halted at the desired time during dot formation. Deposition can be halted as soon as the change starts to occur providing a low density of self-assembled quantum dots [49].

Random formation of the dots in self-assembled growth is undesirable as the positions of the dots cannot be reliably predicted. The majority of current research on self-assembled dots involves searching the surface of a sample in order to find dots with desirable properties. For a solid-state matrix of quantum dots to be used together as the basis for a quantum computer, reliable site control of dot formation is required for precise device fabrication and targeted control. Some success has been found in using pre-patterned substrates [56, 57], with the drawback of poor optical linewidths of the quantum dots. Improvements have been

made over the years, from $\sim$ 100s μeV [58] down to more recent linewidths of $\sim 30\mu$eV [59]. While hopeful, site controlled dots still do not match the optical quality of self assembled quantum dots with transform-limited linewidths (FWHM $\approx 1\mu$eV) [60, 61].

2.1.2 Band structure of quantum dots

Materials used for III-V semiconductor quantum dots, such as InAs or GaAs, have a zincblende crystal structure. Bulk semiconductor crystals with a zincblende structure have parabolic band structures for the conduction (CB) and valence (VB) band near the centre of the Brillouin zone, as seen in Fig 2.2a [39]. Parabolic band structure of the CB and VB allows expression of the energy dispersion relation $E(\boldsymbol{k})$ as a second-order Taylor expansion. As the bands are centred at $\boldsymbol{k} = 0$, the energy of both the CB and VB be described by the following equation [62],

$$E_c(\boldsymbol{k}) \approx E_G + \frac{\hbar^2 \boldsymbol{k}^2}{2m^*_\alpha} \qquad\qquad E_v(\boldsymbol{k}) \approx -\frac{\hbar^2 \boldsymbol{k}^2}{2m^*_\alpha} \tag{2.1}$$

where $E_c(\boldsymbol{k})$ and $E_v(\boldsymbol{k})$ are the energy dispersion relations of the CB and VB respectively, m^*_α is the relevant charge carrier effective mass and $\boldsymbol{k}$ is the crystal momentum. As seen in Eqn 2.1 and Fig 2.2a, the conduction and valence bands are separated by the bandgap E_G, which is determined by the material forming the semiconductor. Minimum (maximum) energy points for the conduction (valence) band occur at Γ for GaAs and InAs, allowing interband transfer of carriers via optical excitation with no additional momentum $\boldsymbol{k}$ from phonons required. Promotion of electrons from the valence band to the conduction band allows the electrons to move freely within the crystal [62]. While useful for many applications such as diodes and detectors, a freely moving electron is both difficult to control and experiences rapid spin relaxation due to spin-orbit effects, preventing use in quantum information protocols.

To understand the band structure of a confined system, a picture of the bulk semiconductor band structure should first be considered. First, the conduction band states have s-like atomic shell orbitals, and as a result, it can be inferred that they have an orbital angular

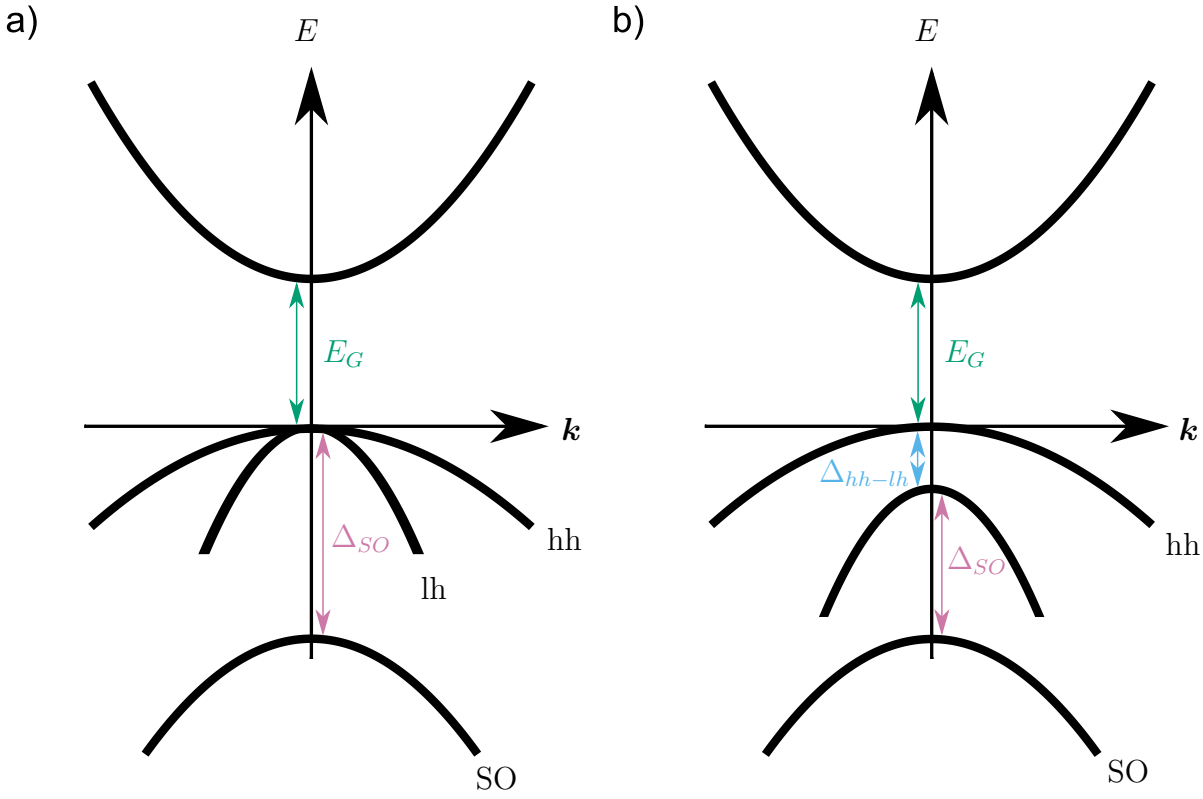

Figure 2.2: Band structure diagrams of a) zincblende crystal semiconductor in the absence of strain b) zincblende crystal semiconductor in the presence of uniaxial strain. Similar to bulk zincblende crystals in the presence of uniaxial strain shown in b), QDs also experience a heavy-hole light-hole splitting quantified by Δ_{hh-lh}. The splitting is induced by large confinement resulting in heavy holes becoming the lowest-lying v-band states. Both bulk materials and QD structures experience large splitting between hole states and the split-off (SO) band with an approximate strength of $\Delta_{SO} \sim 300$ meV [63]. Figure adapted from [39]

momentum of $L = 0$, thus only spin angular momentum states $\hat{\boldsymbol{S}}$ need to be considered. If the system is quantized along the $+z$ axis, the CB electron state can be defined by the spin projection in the $+z$ axis, $S_e = \pm\frac{1}{2}$ [39].

The valence band states have p-like symmetry, meaning that angular momentum is $L = 1$. Due to the presence of both spin angular moment $\hat{\boldsymbol{S}}$ and orbital angular momentum $\hat{\boldsymbol{L}}$, consideration of the spin-orbit interaction is required for a full description of the states within the VB. The spin orbit interaction couples the $\hat{\boldsymbol{S}}$ and $\hat{\boldsymbol{L}}$ momentum together, resulting in total angular momentum $\hat{\boldsymbol{J}} = \hat{\boldsymbol{L}} + \hat{\boldsymbol{S}}$ as the only possible description of momentum within the VB. As a consequence, a more complex set of states are available to the carriers within

the VB.

While under ideal conditions the VB will be completely filled with electrons, interesting physics generally occurs once an electron has been excited to the conduction band, leaving behind a positively charged absence of charge referred to as a hole. Due to this, the VB states are usually described using holes with spin J_h, and are formed of three distinct bands. For $J_h = \frac{1}{2}$ there are two possible states $J_z = \pm\frac{1}{2}$, which forms the split-off (SO) band. $J_h = \frac{3}{2}$ has four states, $J_z = -\frac{3}{2}, -\frac{1}{2}, +\frac{1}{2}, +\frac{3}{2}$, which can be split into two more sub-bands. The $J_z = \pm\frac{3}{2}$ forms the heavy hole (hh) and the $J_z = \pm\frac{1}{2}$ forms the light hole (lh) band, named for the different effective masses of holes within each band. Typical direct bandgap III-V semiconductors have degenerate hh and lh states at $\boldsymbol{k} = 0$, while the SO band is offset by some energy Δ_{SO} [39, 62]. Bulk semiconductor band structure is visualised in Fig 2.2a.

One of the defining characteristic of a quantum dot is the strong confinement in all three spatial dimensions [45]. Confinement creates quantized energy states, providing atom-like energy structures and delta-function density of states. The strong confinement provides a potential well in which freely moving carriers generated in the bulk crystal due to thermal or optical excitation can become trapped. There are two key features of the quantum dot band structure when discussing spins. Firstly, degeneracy of the hh and lh states is removed through a combination of confinement effects and uniaxial strain [39], with hh becoming the lowest lying VB state [64]. A second point to consider is the large energy difference between the lh, hh bands and the SO band (Bulk InAs: $\Delta_{SO} \sim 370$ - 410 meV, Bulk GaAs: $\Delta_{SO} \sim 340$ meV [63]), such that effects from the SO band are generally not considered. A visual representation of a bulk semiconductor under uniaxial strain is shown in Fig 2.2b and demonstrates the effect of splitting between the hh, lh and SO states. Calculation of the states found in a quantum dot can be modelled using potential well solutions to a high level of accuracy.

2.1.3 Quantum dot confinement energy states

The simplest model of a quantum dot is the spherical quantum dot. Complete confinement in all three dimensions provides clear and discrete energy levels which can be modelled with a 3D finite potential well. While this model is relevant for spherical dots such as collidial quantum dots [65], the quantum dots studied in this thesis are self assembled InGaAs/GaAs QDs. The dots grown in the SK growth mode are not spherical in nature, but instead are anisotropic, with a small height in the $+z$ direction and a wider base in the x-y plane [38, 44, 47]. As a result, confinement cannot be simply described by a spherical model. Approximations can be made for the $+z$ direction, treating the system as a 1D finite potential well. This is effective in providing a fully quantized system defined in the $+z$ direction. Similar confinement lengths in the $+x$ and $+y$ direction means the confinement in these dimensions can described by a 2D parabolic potential. In reality, the relatively weak confinement of the $+x$ and y dimensions means the confinement is not perfectly parabolic, which can be further exacerbated by growth anisotropy resulting in an elliptical potential. The $+z$ 1D finite potential well and x-y parabolic potential approximations can be considered separately [39].

Strong confinement in the $+z$ direction results in large energy gaps between $+z$ states in both the conduction and valence band. The gaps are large enough that any states higher than the ground state are not seen in experiments, as they lie above the wetting layer band, resulting in any carriers absorbing the required energy to reach these states being removed from the potential well rather than occupy the higher $+z$ state. Instead, the $+z$ confinement can be approximated as an offset $E_{z,0}$ to the bandgap of the bulk crystal E_G.

Bulk InGaAs has a bandgap which depends strongly on the ratio of In to Ga [68]. Measurement of In content within self assembled quantum dots via NMR techniques has given an estimate of $\sim 20\%$ In composition [69], which for bulk $In_{0.2}Ga_{0.8}As$ gives a bandgap of approximately ~ 1 eV at cryogenic temperatures $T = 4$ K [63, 70, 71]. Self assembled InGaAs quantum dots emit in the range ~ 1.3 eV [41, 64], giving an approximate value for $E_{z,0} \sim 300$ meV [72]. The offset $E_{z,0}$ is equal to the sum of the energy offset of the $+z$ ground state of

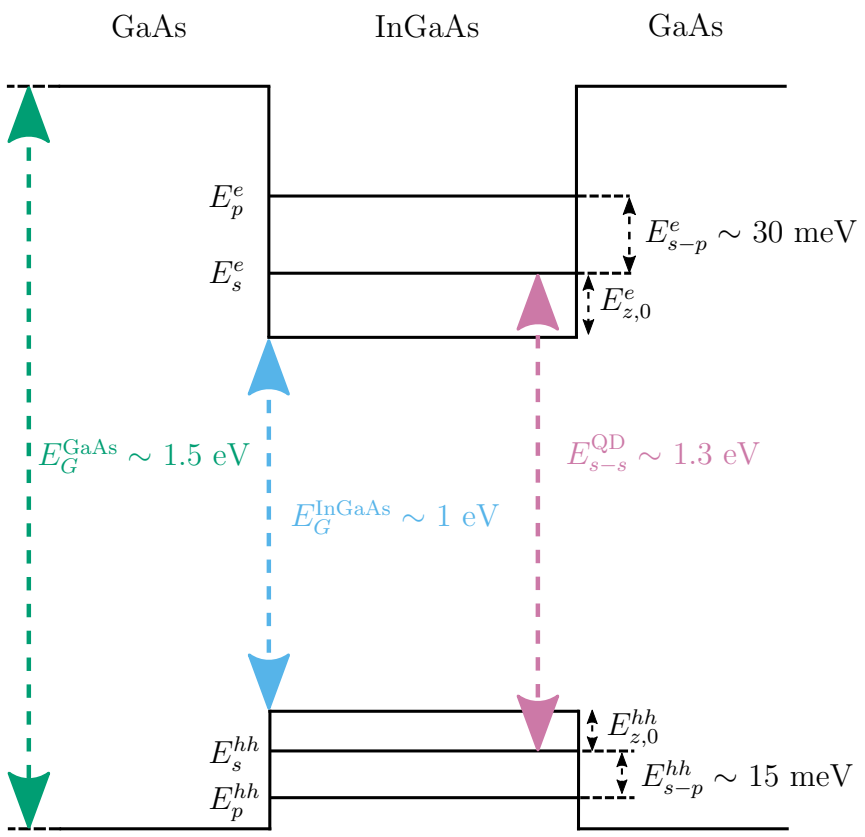

Figure 2.3: Energy level diagram of an InGaAs quantum dot. The QD acts as a potential well due to the lower bandgap compared to the surrounding bulk material ($E_G^{\text{GaAs}} \sim 1$ eV) from the wetting and capping layers of GaAs. Confinement effects result in an energy increase to the lowest energy transition of magnitude $E_{z,0} = E_{z,0}^e + E_{z,0}^{\text{hh}} \approx 300$ meV, increasing transition energy from the bulk InGaAs $E_G^{\text{InGaAs}} \sim 1$ eV to $E_{s-s}^{\text{QD}} \sim 1.3$ eV. Higher level states form similar to atomic orbitals *s*-, *p*-, *d*-, with equal energy spacings within the *c* and *v* band. Experimental measurement of the shell spacings are $E_{i,j}^e \sim 30$ meV and $E_{i,j}^{\text{hh}} \sim 15$ meV [66, 67]

both the electron $E_{z,0}^e$ and hole $E_{z,0}^{hh}$ from the conduction and valence band respectively, see Fig 2.3.

Now considering the in-plane x-y confinement, we can safely assume that higher level states in $+z$ do not need to be considered. The two dimensional confinement can be modelled accurately using the parabolic potential described by,

$$V(x,y) = \frac{1}{2} m_\alpha^* \omega_\alpha (x^2 + y^2) \tag{2.2}$$

where α represents either an electron (e) or hole (hh), m^*_α is the carrier effective mass, ω_α is the separation frequency. This potential then provides the energy eigenvalue solutions,

$$E^\alpha_{m,n} = \hbar\omega_\alpha(m + n + 1) \tag{2.3}$$

Under the assumption of a perfectly cylindric confining potential $x = y$ and taking the $+z$ confining potenial as an energy offset $E^\alpha_{z,0}$, we can consider the quantum dot energy states as atom like shell states s-, p-, d- shells for $l = 0, 1, 2$, where $l = m + n$. Each shell has an increasing number of degenerate state pairs, for example, the s-shell has 1 pair, the p-shell has 2 pairs and so on. Spacing between the shells is described by energy $E^\alpha_{i-j} = \hbar\omega^\alpha_{i-j}$, where i, j is the shell state s-, p-, d-. The spacing between states is different for the CB and VB due to differing charge carriers, but remain constant within the band. Typical values for these are $E^e_{i-j} \sim 30$ meV and $E^{hh}_{i-j} \sim 15$meV [66, 67]. The current model only considers pure hh states due to the Δ_{hh-lh} splitting, but mixing of these states can occur due to anisotropy of the quantum dot, which results in a more complex system [73–75].

2.2 Optical properties

Discrete energy levels within the quantum dot system mean that energetic transitions between the states are also discrete. As mentioned previously, InGaAs/GaAs quantum dots are formed of direct band gap semiconductors, meaning that interband transitions can occur purely through optical (photon) energy input/output. This is in contrast to indirect bandgap materials that may require input of crystal momentum $\boldsymbol{k}$ via phonon processes. The purely optical addressing of states in quantum dots is one of their primary advantages.

For applications requiring low noise such as quantum information protocols, minimising background interactions is key. Thermal energy within crystal lattice is represented by the presence of phonons, and at room temperature the population of phonon modes is significant, broadening and preventing potential optical transitions. Room temperature thermal energy

($E = k_B T \approx 26$ meV) is greater than the spacing between electron energy states, allowing thermal excitation to promote electrons to higher energy states within the CB. This can remove electrons from the QD before optical recombination, limiting optical transitions in the low lying CB states. At low cryogenic temperatures, the population of phonon modes is small enough such that the CB states experience minimal thermal excitation, allowing reliable and regular promotion of carriers to the lowest lying CB state. The temperature at which quantized energy levels can be accessed occurs when the energy spacing between states is larger than $k_B T$ [39]. As a consequence, all the work in this thesis is carried out at cryogenic temperatures of $T \approx 4.5$ K unless stated otherwise.

The quantum dot system can absorb photons with energy equal to the quantum dot interband transition energies, which is determined by the bandgap of the quantum dot E_G^{QD} and the energy states of the hole E_{hh} and electron E_e for the conduction and valence band respectively,

$$\hbar\omega = E_G^{\mathrm{QD}} + E_e + E_{\mathrm{hh}} \tag{2.4}$$

Absorption of a photon allows promotion of an electron from the valence band to the conduction band, leaving a hole in the valence band. The hole can be considered to be a positively charged particle within the quantum dot valence band. The electron and hole confined within the dot form a bound state referred to as an exciton. Excitons are formed through the Coulomb interaction of opposing charges in bulk semiconductor, with a binding energy equal to the strength of Coulomb interaction. Within a confined structure, confinement effects also increases the binding energy between charges. The quantum dots we study are generally in the strong confinement regime, where confinement energy is greater than Coulomb energy [39]. As seen in Section 2.1.2, $E_{z,0}^{e}$ and $E_{z,0}^{hh}$ have energies of $\sim$ 100 meV and $\sim$ 25 meV, which is large compared to the measured Coulomb interaction energy for two carriers of $\sim$ 20 meV [76]. As a consequence of the confinement being the dominant energy, it is clear that the optical spectrum will be primarily determined by confinement length, and

thus dependant on dot size. However, the Coulomb effect is still necessary to consider as the attractive energy will weaken the overall binding energy created by confinement [77].

Optical selection rules determine the allowed transitions that can occur through the absorption/emission of energy. Quantum dots typically interact with photons via electron-dipole transitions. Photons possess an angular momentum of $l = \pm 1$ and parity of -1. From this we consider the states that are present from our previous discussion of states in both the conduction and valence bands. Parity alternates between states (s-, p-, d-...) within a band, and the CB and VB have opposite parities. In order to conserve parity, only interband transitions between same sub-levels can occur, for example $s_v \rightarrow s_c$ [45]. Angular momentum conservation requires a change in momentum for an interband transition. Momentum change is determined by the polarisation of the absorbed photon ($\sigma\pm$), resulting in different states being occupied under perpendicular polarisation states. Spin is conserved through optical transitions [39].

There are two distinct categories of optical excitation. The first, resonant excitation, is the simplest to consider from a theoretical standpoint. Photons of $\hbar\omega = E_G^{\mathrm{QD}} + E_e + E_{hh}$ can promote electrons via an interband transition to the low lying s-shell CB state, leaving a heavy hole and creating the bound state of a neutral exciton, X^0. After a short time, characterised by the radiative lifetime τ_R of the exciton, the state recombines and emits a photon of the exact same energy $\hbar\omega$, and results in the electron returning to the VB (Fig 2.4a). Direct transitions preserve the coherence of the system, and reduce broadening effects, allowing the true spectrum of the two level system to be revealed [39]. While resonant transitions provide a coherent state, they are not experimentally trivial to measure due to the emitted photons having the same energy as the excitation, resulting in any luminescence signal being lost in scattered excitation signal. This can be circumvented through cross-polarisation techinques [78], which will be discussed further in Chapter 3. The direct absorptions are not limited to the low lying s-shell states, it is possible to excite the p- or d- shell transitions with a higher energy photon. This process is known as quasi-resonant excitation, and follows the

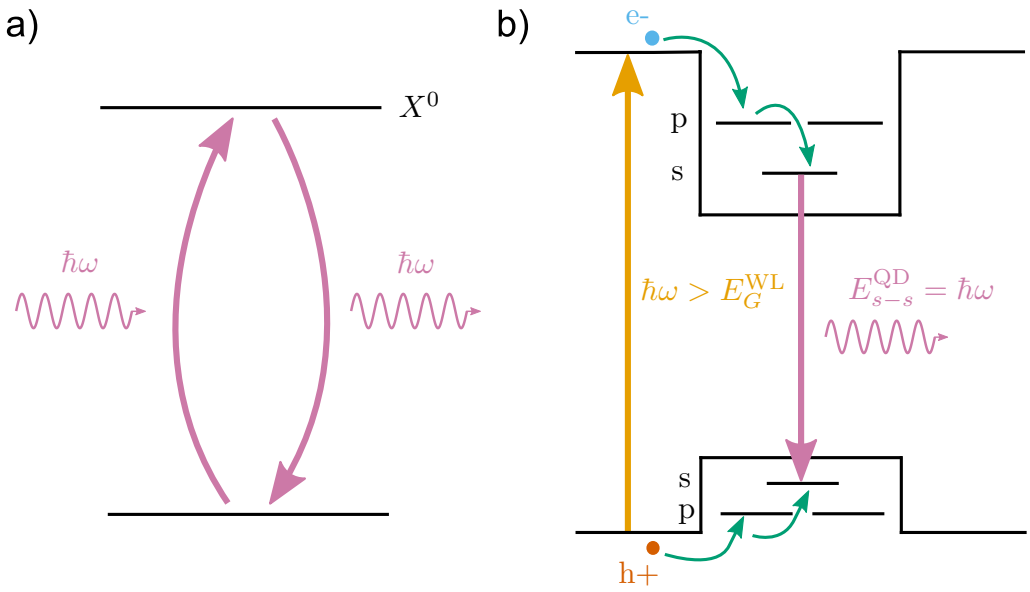

Figure 2.4: A schematic of off-resonant and resonant excitation. a) Optical excitation resonant with the X^0 transition will coherently create an X^0 exciton that will shortly recombine, the time-scale of which is defined by the radiative lifetime which for InGaAs QDs is $\tau_R \sim 1$ ns. b) Off-resonant excitation is an incoherent process that promotes an electron to the wetting layer, creating a bound exciton that will become confined by the nearby QD potential well. The exciton relaxes through intraband non-radiative processes to the low lying s-state, allowing radiative recombination at E_{s-s}^{QD}

previously mentioned requirement for interband transitions preserving angular momentum $l = \pm 1$ and parity.

The second type of excitation is nonresonant excitation, where photons with energy higher than the bandgap of the wetting layer, $\hbar\omega > E_G^{WL}$, excite carriers into the wetting layer conduction band as seen in Fig 2.4a. The formed exciton is quickly confined by the nearby quantum dot, where the energy relaxes to the s-shell state via intraband non-radiative processes. The exciton can then optically recombine, releasing a photon of energy E_{s-s}^{QD}. Non-resonant excitation is not a coherent process, and so is not ideal for precise optical control of the states within the dot. Effects such as time jitter or the trapping of charges from the wetting layer can affect the indistinguishably of emitted photons [79, 80]. However, it is experimentally trivial, as scattered excitation will be at a different wavelength to the excitonic recombinations observed from the quantum dot, in contrast to resonant excitation.

2.2.1 Charged excitons

The bound electron-hole pair previously introduced is not the only form of exciton that can be created. Additional carriers can also become bound, forming a charged exciton. An extra electron will result in a negatively charged exciton X^-, whereas a hole results in a positively charged exciton X^+. Charged excitons are not limited to singly charged states, as additional charges can also become bound in the states such as, $X^{2\pm}, X^{3\pm}, ...$[26, 81–84]. One other configuration is the biexciton, where two electrons and two holes form a bound state, and is generally labelled $2X^0$ [67]. The four most common charge configurations studied are shown in Fig 2.5.

For the quantum dot system, there are two methods for generating additional charges. High power optical excitation with energy greater than the wetting layer band gap can generate many conduction band electrons, which can in turn become trapped within a quantum dot. Optical excitation can populate the QD with valence band holes, which are generated by promotion of electrons through photon absorption. Differing tunnelling rates for electrons and holes can create a preferential charging of the system as one carrier is removed faster than the other. Probability of charged states occuring is reduced compared to the simplest system of the neutral exciton, which can be seen when studying photolumiscence measurements of the quantum dot. The brightest peaks will indicate the neutral exciton, and charged excitons will appear offset in wavelength due to change in bandgap as a result of Coulomb effects of the additional charges [39].

Coulomb interaction adjusts the total binding energy of the exciton. For the neutral complex there is an attraction due to the opposing charge states of the electron and hole, reducing overall energy released in a radiative recombination. Addition of more charges further modifies the total Coulomb interaction, providing different energy transitions for different charged excitons.

It is also possible to create devices that will allow selective charge control over the quantum dot. Diode structures allow tunnelling of charges from a doped layer through application of

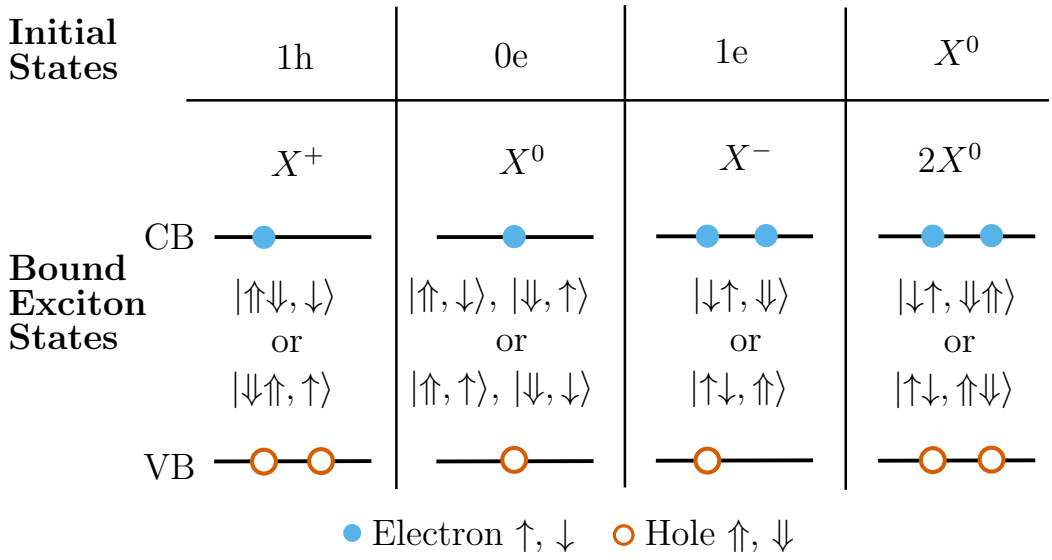

Figure 2.5: Charged excitonic carrier configurations for the most common excitons: positively charged, neutral, negatively charged and the biexciton (from left to right). Two excitonic states are available for each exciton depending on spin orientation of carriers. Specific configurations can be accessed with circularly polarised excitation.

an electric field. Either holes or electrons can be used to fill the quantum dot, depending on the type of doped layer (*p*- or *n*-). In the case of a charge controlled structure the probability of observing charged excitons can be increased. For example, in the case of a singly charged quantum dot, any exciton formed in the dot will likely include the resident electron forming a negative trion. As a result, photoluminescence will reveal a much larger intensity at the trion energy in contrast to an uncontrolled sample [26]. The bias to generate a stable resident charge in the quantum dot (e.g V_{1e}) and the bias which the equivalently charged exciton is stable and observed in PL (V_{X^-}) are not always the same. The difference in charging conditions for the two states is a non-trivial relationship [85].

2.2.2 Exciton fine structure

We have discussed the neutral exciton and the potential other types of charged exciton that can exist within the quantum dot. We can now focus on the smaller effects present within the exciton, which add further depth to the spectral profile of the quantum dot under optical

excitation.

Considering the neutral exciton X^0, we can determine how the fine structure due to spin arises. Combination of the heavy hole spin $J_h = \frac{3}{2}$, $J_{h,z} = \pm\frac{3}{2}$ and electron spin $S_e = \frac{1}{2}$, $S_{e,z} = \pm\frac{1}{2}$ allows us to define the total spin of the exciton as $M = J_{h,z} + S_{e,z}$, which gives possible spin projections of the neutral exciton as $M = \pm 1, \pm 2$. Spin projection magnitude determines the coupling between the exciton and a photon. The $|M| = 1$ states allow photonic coupling and $|M| = 2$ has no coupling to incoming photons due to the optical selection rule $\Delta M = 1$, leading to the names bright and dark excitons for the respective states [39, 72].

The fine structure of the exciton arises from the interaction of the electron and hole spins, and is commonly referred to as the exchange interaction. Without the exchange interaction, all four spin states of the neutral exciton X^0 are degenerate. The exchange interaction can be split into two components, isotropic and anisotropic exchange interaction. Isotropic exchange interaction is always present, while anisotropic interaction relies on asymmetry within the quantum dot. The general spin Hamiltonian for electron-hole spin-spin interaction is given by,

$$H_{Exchange} = -\sum_{i=x,y,z} (a_i J_{h,i} S_{e,i} + b_i J_{h,i}^3 S_{e,i}) \tag{2.5}$$

where $J_{h,i}$ is the spin projection in the i direction for the hole, and $S_{e,i}$ is the same for the electron and a_i and b_i are spin-spin coupling constants [39, 86, 88]. We only consider the heavy hole here as a result of the previously mentioned large lh-hh splitting. Expressing the exchange interaction in the basis of the four exciton states introduced previously, $M = \pm 1, \pm 2$, the following matrix representation is generated,

$$H_{Exchange} = \frac{1}{2}\begin{pmatrix} +\delta_0 & +\delta_1 & 0 & 0 \\ +\delta_1 & +\delta_0 & 0 & 0 \\ 0 & 0 & -\delta_0 & +\delta_2 \\ 0 & 0 & +\delta_2 & -\delta_0 \end{pmatrix} \tag{2.6}$$

Here δ_N terms are simplifications of matrix elements that correspond to physical splitting

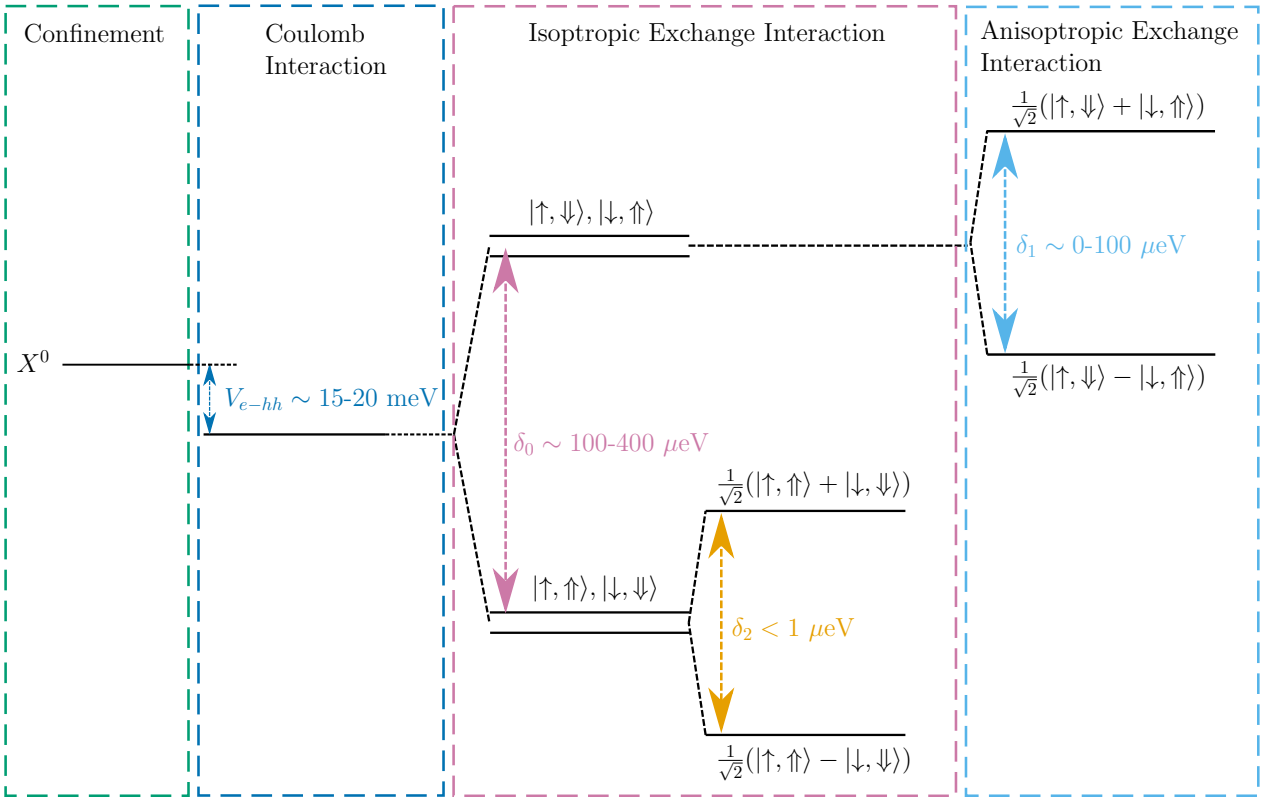

Figure 2.6: Energy levels for neutral exciton X^0 in a asymmetric quantum dot. Coulomb interaction between the hole and electron reduces energy of exciton recombination by V_{e-hh}. Isotropic exchange introduces splitting between dark and bright excitons δ_0. Splitting of dark states δ_2 also occurs due to isotropic exchange interaction. Anisotropic exchange arises from dot asymmetry and splits the bright exciton states by δ_1. Values from [86, 87]

parameters, and are dependent on the spin-spin coupling constants a_i, b_i. Splitting between the bright and dark exciton is represented by $\delta_0 = 1.5(a_z + 2.25b_z)$. Experimental values of δ_0 have been shown to be $\delta_0 \sim$ 100 - 400 μeV in InGaAs QDs, with an inverse relation between dot size and δ_0 [86]. For the scenario with only isotropic exchange interaction (i.e no asymmetry in the dot, $b_x = b_y$), the two bright exciton states are degenerate. The dark excitons always hybridise and are no longer degenerate, the splitting of which is described by $\delta_2 = 0.75(b_x + b_y)$ [86]. The splitting terms δ_0 and δ_2 are symmetry independant, and as a consequence will be present in any shape quantum dot. Splitting δ_2 is too small to resolve in photoluminscent spectra [86, 89], but recent theoretical estimates give a rough value of $\delta_2 < 1$ μeV [87].

State	Energy
$M = \pm 1$	$\frac{1}{2}\delta_0 \pm \frac{1}{2}\delta_1$
$M = \pm 2$	$\frac{1}{2}\delta_0 \pm \frac{1}{2}\delta_1$

Table 2.1: Energy levels of bright and dark excitons for $B_z = 0$ T in an asymmetric quantum dot ($b_x \neq b_y$). Derivations from [86]

The anisotropic exchange interaction further modifies the exciton states, splitting the bright exciton states by $\delta_1 = 0.75(b_x - b_y)$. It is clear from the definition of δ_1 that asymmetry ($b_x \neq b_y$) is required for a non-zero δ_1. In the presence of asymmetry, the bright exciton states are no longer pure spin states of $M = \pm 1$, but a linear combination of both states which prevents circularly polarised transitions. Instead, the bright exciton states can only be accessed by linearly polarised transitions [86]. Typical values for δ_1 are found to be $\sim 0 - 100$ μeV. A summary of the different splittings arising from the exchange interactions is shown in Table 2.1 with an energy level diagram in Fig 2.6.

Charged exciton states such as the negatively charged trion X^- do not experience exchange interaction fine structure as a consequence of Kramer's degeneracy theorem [90]. Using X^- as an example, there are two electrons and a hole present within the state, which can be viewed as a hole spin interacting with a single electron spin doublet. As a result, the energy levels of the charged exciton take the form of a degenerate Zeeman doublet, which will break with the addition of magnetic field. There is only one unpaired spin, and therefore no exchange interaction to create fine structure. This has the additional effect of the charged excition X^- states coupling to circularly polarised transitions, in contrast to the linear polarisation transitions found in the neutral exciton X^0. Presence (absence) of fine structure splitting in the neutral (charged) excitons is particularly useful when identifying components of quantum dot photoluminescent spectra [86, 90].

2.2.3 External fields

Now that we have considered quantum dots and the excitons that can be created, we can discuss the effect of external influences on the quantum dot and any excitons created within. Both magnetic and electric fields provide unique effects that need to be considered when working with the quantum dot system. In addition to allowing selective tunnelling of charge carriers at particular electric field strengths, the strength of the magnetic and electric fields also affect the energy levels of the excitons formed within the quantum dot. This is true for all charge states of the exciton, and so is important to consider.

Electric field

The effect of electric field on quantum dots can be used to control the charge state of the quantum dot via semiconductor diode structures, as briefly introduced in Section 2.2.1, in addition to allowing selective tuning of the transition energy of excitons via the Quantum Confined Stark Effect (QCSE).

Diode structures allow tunnelling of charges from a doped layer in a structure through application of an electric field [26]. The strength of the coupling between the doped layer and the quantum dots is determined by the thickness of the barrier, t_B, separating the two layers, and is referred to as the tunnelling barrier. By applying an electric field, the lowest lying energy state of the quantum dot can be brought into resonance with the Fermi Level ϵ_F of the Fermi resevoir, allowing a charge carrier to tunnel into the quantum dot. The voltage required to generate this electric field we label V_{1e}. Further charges that tunnel into the dot are highly likely to remain under low temperature conditions due to the Coulomb interaction between the charge within the dot and the Fermi reservoir charge carriers. Under the low temperature conditions, the energy difference between a single charge and two charges occupying the quantum dot results in a plateauing effect by which a range of biases allow a singly charged quantum dot to be held in stable operating conditions. This effect is referred to as the Coulomb blockade and allows us to create a spin qubit on demand [26, 91, 92]. This

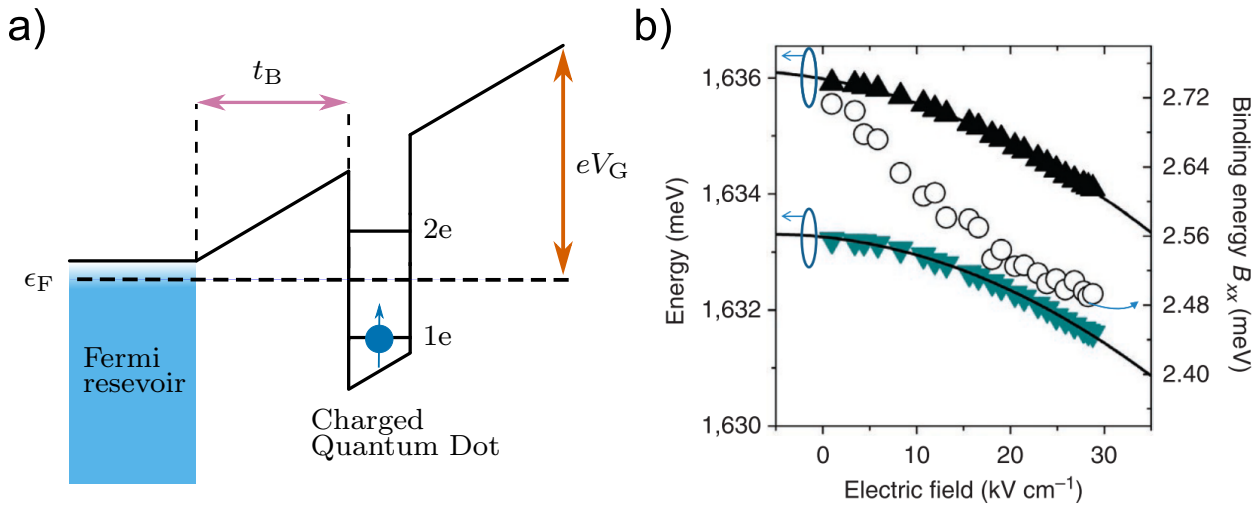

Figure 2.7: a) Energy level diagram of Schottky diode charge control strucutre. Variation of the gate voltage applied to the diode V_{Gate} can bring occupation levels in resonance with the Fermi energy of the n-doped layer, overcoming the Coulomb blockade and allowing additional charges to occupy the QD. b) Energy of neutral exciton X^0 (upward triangles) and biexciton $2X^0$ (downward triangles) PL signal with varying electric field $\boldsymbol{F}$ from GaAs island QDs at $T = 4$ K. Solid lines are fitted with equation $E = E_G + \Delta E_{\text{QCSE}}$ to give a value for $\boldsymbol{p}_0 \approx 4.5 \times 10^{-29}$ C m. Figure from Ghali et al. [93] licensed under CC BY-NC-SA 3.0

effect can apply to both electrons (n-doped reservoir) and holes (p-doped reservoir) to allow either to be used as a spin qubit. A diagram of a Schottky diode is shown in Fig 2.7a.

The Quantum Confined Stark Effect describes the response of a quantum state to a linear electric field $\boldsymbol{F}$ [39, 94]. Here we focus on the DC Stark effect that occurs from electric field applied via charge controlled structures. The AC Stark effect also exists, and is an optical phenemona by which the oscillating electric field from many photons at high power can induce the Stark shift [95].

As introduced previously, an exciton is formed of an electron and hole with opposing charges. The bound charges can form an electric dipole through a small displacement. The shift of exciton energy due to this interaction with the dipole depends on the strength of the dipole and the external field,

$$\Delta E_{\text{QCSE}} = -\boldsymbol{p} \cdot \boldsymbol{F} \tag{2.7}$$

where $\boldsymbol{F}$ is the static electric field, and $\boldsymbol{p}$ is the exciton dipole moment. It is clear from this

equation that external electric field will change the energy of transitions within the QD. It is important to consider that within a QD the electron and hole already undergo a small degree of separation without the influence of external electric field due to confinement effects. As a result, there is zero-field dipole moment characterised by the displacement of the electron and hole $\boldsymbol{s}_0$. This splits the exciton dipole moment into two parts, one intrinsic dipole $\boldsymbol{p}_0$ and one externally controlled moment $\boldsymbol{p}_{ext}$. The externally controlled moment depends on the external field, $\boldsymbol{F}$, and the polarisability, β, which is a measure of how easily the electron and hole can be separated. This gives us a new expression for the dipole moment $\boldsymbol{p}$,

$$\boldsymbol{p} = \boldsymbol{p}_{ext} + \boldsymbol{p}_0 = \beta \boldsymbol{F} + \boldsymbol{p}_0 \tag{2.8}$$

which when substituted into our Stark shift equation (Eqn. 2.7) gives us,

$$\Delta E_{\text{QCSE}} = -\boldsymbol{p} \cdot \boldsymbol{F} = -(\boldsymbol{p}_0 \boldsymbol{F} + \beta F^2) \tag{2.9}$$

Using this equation it is possible to fit the PL spectra of self-assembled quantum dots within diode structures for varying electric field, as shown for GaAs island QDs in Fig 2.7b. Fitting allows estimation of the strength of $\boldsymbol{p}_0$, which for InGaAs/InAs quantum dots used within this thesis is $\sim 7 \times 10^{-29}$ C m [96]. From the simple relation of distance between charges and dipole strength $p = er$, electron-hole seperation can be estimated to be ~ 4 Å [96, 97]. Altering the direction of the applied $\boldsymbol{F}$ electric field revealed that the electron wavefunction is localised to the base of the dot, and the hole wavefunction localized at the top [96]. This is a result of the increased indium content at the peak of the dot, which increases biaxial strain and strongly localises the hole wavefunction due to the higher effective mass of holes [39].

Understanding the shift caused by the Stark effect also provides another useful application, the tuning of the energy of emitted photons from the QD. The random nature of self-assembled growth adds limitations to the ability to grow dots emitting at a desired wavelength. The QCSE allows fine tuning of the QD optical resonances to bring two dots of

similar wavelength into resonance with each other [98] or an optical cavity [99].

Magnetic field

Introduction of an external magnetic field $\boldsymbol{B}$ causes additional effects due to interaction between the field and the electron, S_e, and hole, J_h, spins. Magnetic field is generally applied either parallel to the optical excitation axis z, or perpendicular to the optical excitation axis in the xy-plane. We refer to fields in these geometries as either Faraday configuration, B_z, or Voigt configuration, B_x, B_y for parallel and perpendicular geometries respectively. Magnetic field parallel to the optical axis results in spin degeneracy being lifted to provide distinct spin states, while field perpendicular to the optical axis results in mixing of heavy hole and light hole spin states. Optical excitation is applied parallel to the growth direction of the quantum dot $+z$ for all experiments within this thesis. In addition to this, all experiments are carried out with magnetic field applied parallel to the growth and optical axis, which shall be the focus of our discussion in this section.

Considering a general Hamiltonian for spin interaction with an external magnetic field, we can derive an expression for the specific scenario of field applied in the z-direction [72, 88, 100],

$$H_{\text{Zeeman}}(B) = -\mu_B \sum_i (+g_{e,i} S_{e,i} - g_{h,i} J_{h,i}) B_i \tag{2.10}$$

Applying field in the z-direction results in simplification of Eqn. 2.10 due to $\boldsymbol{B} = (0, 0, B_z)$, giving us an expression for magnetic field interaction strength for magnetic field parallel to the growth axis,

$$H_{\text{Zeeman}}(B) = -\mu_B (+g_{e,z} S_{e,z} - g_{h,z} J_{h,z}) B_z \tag{2.11}$$

where $g_{e,z}$, $g_{e,h}$ are the g-factors for the electron and hole respectively. The Zeeman Hamiltonian in Faraday geometry is a diagonal matrix comprised of two terms which we call $\beta_1 = \mu_B(g_e + g_h)B_z$ and $\beta_2 = -\mu_B(g_e - g_h)B_z$ [86]. As expected for Zeeman splitting, we see a linear dependence of interaction strength with magnetic field. We can combine $H_{\text{Zeeman}}(B)$

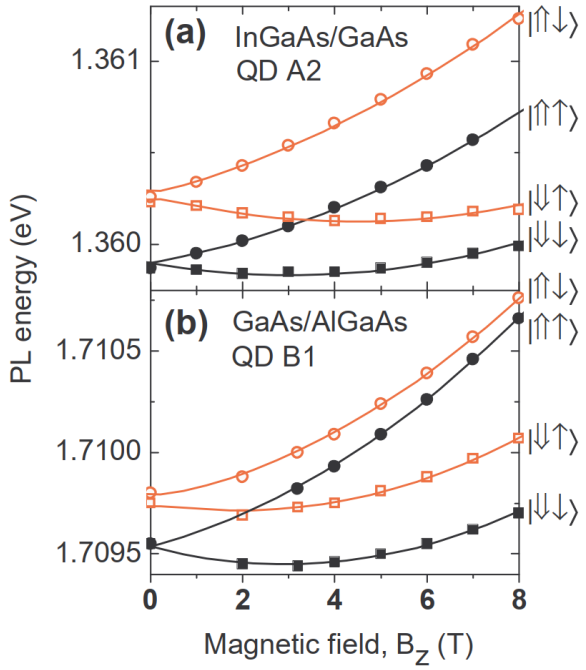

Figure 2.8: Energy of bright and dark excitons from a) InGaAs/GaAs and b) GaAs/AlGaAs QDs in Faraday magnetic field B_z, demonstrating the effect of the Zeeman splitting and diamagnetic shift experienced by the excitons. Solid lines are fits from the energy equations described in Table 2.3, providing estimates of γ_2 and g_e for a) InGaAs QDs: $\gamma_2 = 7$ μeV T^{-2}, $g_e = -0.35$ and $g_h = 1.9$ b) GaAs QDs: $\gamma_2 = 10$ μeV T^{-2}, $g_e = 0.3$ and $g_h = 1.8$. Reprinted figure with permission from [89]. Copyright (2021) by the American Physical Society. doi:10.1103/PhysRevB.88.045306

and H_{Exchange} (Eqn 2.6) and diagonalise the total Hamiltonian $H = H_{\text{Zeeman}} + H_{\text{Exchange}}$ to calculate the effect of exchange and Zeeman interaction on the energy levels of the exciton states, as shown in Table 2.2.

The $\sqrt{\delta_N + \beta_N}$ term results in a quadratic splitting of exciton states for low B_z, which transitions to a linear dependence for $\beta_N \gg \delta_N$. Strong magnetic field also results in coupling of bright exciton states to circularly polarised light, breaking the linear polarisation basis created by exchange interaction [39, 86].

Considering experimental measurement of photoluminescence over a range of magnetic fields, such as the results from Puebla et al. [89] shown in Fig 2.8, we can observe that there is a shift in the centre of mass of the Zeeman split bright exciton states. This is caused by a diamagnetic shift characterised by γ_2, which is quadratically dependant on the field, leading

State	Energy
$M = \pm 1$	$+\frac{1}{2}\delta_0 \pm \frac{1}{2}\sqrt{\delta_1^2 + \beta_1^2}$
$M = \pm 2$	$-\frac{1}{2}\delta_0 \pm \frac{1}{2}\sqrt{\delta_2^2 + \beta_2^2}$

Table 2.2: Energy shift of bright ($M = \pm 1$) and dark ($M = \pm 2$) excitons calculated from $H = H_{\text{Zeeman}} + H_{\text{Exchange}}$, to quantify shifts of exciton energy as a result of exchange and Zeeman interaction for magnetic fields $B_z > 0$ T in Faraday geometry [86, 89].

to the average energy of the Zeeman doublet increasing with magnetic field. The diamagnetic shift γ_2 arises from the strong confinement squeezing the exciton wavefunction.

Fitting the trend line for exciton energies over magnetic field allows measurement of both the electron and hole g-factors, as well as the diamagnetic parameter γ_2. For the InGaAs quantum dots shown in Fig 2.8, values for these parameters are $g_e = -0.35$, $g_h = 1.9$ and $\gamma_2 = 7$ μeV T^{-2} [89]. Energy levels for an anisotropic quantum dot in a Faraday-geometry magnetic field are displayed in Table 2.3 using a combination of parameters discussed here and the exchange interaction parameters introduced in Section 2.2.2.

State	Energy
$M = \pm 1$	$E_0 + \gamma_2 B_z^2 + \frac{1}{2}\delta_0 \pm \frac{1}{2}\sqrt{\delta_1^2 + \beta_1^2}$
$M = \pm 2$	$E_0 + \gamma_2 B_z^2 - \frac{1}{2}\delta_0 \pm \frac{1}{2}\sqrt{\delta_2^2 + \beta_2^2}$

Table 2.3: Total energy levels of bright ($M = \pm 1$) and dark ($M = \pm 2$) excitons in Faraday configuration external magnetic field $B_z > 0$ T, combining the QD band-gap energy E_0, diamagnetic shift, exchange interaction H_{Exchange} and Zeeman interaction H_{Zeeman} [86, 89].

2.3 Spin system of a quantum dot

We have so far considered the growth of quantum dots, in addition to the band structure and exciton properties of quantum dots. Quantum dot applications in quantum computing requires use of the available spin states within the dot as a basis for a spin qubit. For use in any quantum information protocol, we need to be able to achieve reliable spin state preparation, coherent control and fast readout in order to store, process and read information

as described in Chapter 1. A further underlying requirement is long lasting spin states to prevent loss of information to the environment.

Spins within the quantum dot come in two forms, carrier spin (electron S_e or hole J_h) and the nuclear spin system formed of 10^3 - 10^5 nuclear spins, $\boldsymbol{I}$. The two systems are inherently coupled together, and as such can be studied under the framework of the central spin model, where a single carrier spin interacts with a fluctuating bath of spins. It is critical to understand the mechanisms affecting both spin systems in order to optimize the quantum dot for long lasting qubit states. In this section we will discuss the complete spin system found within a quantum dot, followed by a discussion on the ways to interact with the spin states.

2.3.1 Carrier spins

We can first consider the spin system that describes the carrier spin within a quantum dot. As mentioned previously (Section 2.2.3), stable charge states can be created through the use of diodes. In this section we will consider a quantum dot charged with a single carrier, as even-numbered carriers cannot change spin state within the s-shell due to Pauli's exclusion principle, and higher energy states in other shells such as the p-shell add unnecessary complexity to the system.

Considering an electron charge first, we have a quantum dot charged with a carrier $S_e = \frac{1}{2}$. We call the two spin states $m_s = \pm\frac{1}{2}$ the spin-up state ($m_s = +\frac{1}{2} = |\uparrow\rangle$) and the spin-down state ($m_s = -\frac{1}{2} = |\downarrow\rangle$), where spin-up and spin-down refers to the direction of the spin component in the $+z$-axis. In the absence of magnetic field $\boldsymbol{B} = 0$ T, the spin-up and spin-down states are degenerate, causing rapid loss of quantum information due to energy conserving spin-flips with the nuclear environment allowed via Fermi contact hyperfine interaction [39]. This results in flucations of the electron spin occurs on a timescale of ~ 1 ns for the electron at $B = 0$ T [101]. Addition of a magnetic field, $\boldsymbol{B} > 0$ T, breaks the degeneracy, providing energetically distinct spin levels and adding a energy requirement to

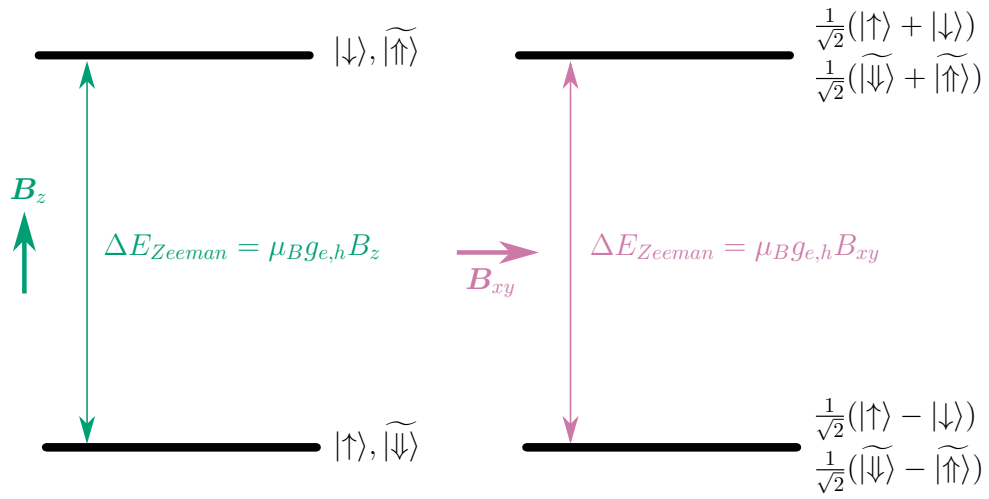

Figure 2.9: Energy level diagram of the carrier spins S_e or J_{hh} in Faraday (left) or Voigt (right) geometry along the growth/optical axis basis $+z$.

electron-nuclear spin flips [28, 101, 102].

For the electron, the spin states now form a two level system that can be used as a qubit basis. As for excitons, direction of the magnetic field is important to consider relative to the optical axis. Considering the states in the growth axis basis $+z$, Faraday geometry, $\boldsymbol{B} = (0, 0, B_z)$, results in pure splitting of the states $|\uparrow\rangle$, $|\downarrow\rangle$. If carrier states are initialised orthogonal to the magnetic field, as described by the Voigt geometry, $\boldsymbol{B} = (B_x, B_y, 0)$ the states will create of superpositions between the two states, described by $\frac{1}{\sqrt{2}}(|\uparrow\rangle \pm |\downarrow\rangle)$, which causes a precession of spins of frequency $\Omega = g_e \mu_B \boldsymbol{B}$ [45].

Carrier holes can also be used to charge the quantum dot and provide a spin basis. As previously mentioned (Section 2.1.2), the heavy-hole light-hole splitting is non-zero due to the in-built strain of the quantum dot. Consequently, the lowest-lying hole states are heavy hole in nature ($J_h = \pm\frac{3}{2}$) but due to asymmetry in the quantum dot, the heavy hole state undergoes mixing with the light hole state ($J_h = \pm\frac{3}{2}$) and can be treated as a pseudo spin-$\frac{1}{2}$

with states,

$$\begin{aligned} \widetilde{|\Uparrow\rangle} &= |3/2\rangle + \beta|-1/2\rangle \\ \widetilde{|\Downarrow\rangle} &= |-3/2\rangle - \beta|+1/2\rangle \end{aligned} \tag{2.12}$$

where β is the valence band mixing parameter [103, 104]. In applied magnetic field $\boldsymbol{B} > 0$ T, the holes pseudo-state can then form two stable spin states for Faraday geometry $\widetilde{|\Downarrow\rangle}, \widetilde{|\Uparrow\rangle}$, while for Voigt geometry, the two level system is defined by superposition states similar to that found for the electron $\frac{1}{\sqrt{2}}(\widetilde{|\Downarrow\rangle} \pm \widetilde{|\Uparrow\rangle})$ [46, 105, 106].

The most interesting difference between the electron and hole is that the hole state is primarily p-like, which has no overlap with the nuclear spin sites, resulting in minimal coupling to the nuclear spin bath via Fermi-contact hyperfine interaction (see Section 2.3.3). Initial research into hole spins suggested that there would be no coupling to the nuclear sites at all, making the hole spin an ideal spin qubit candidate. However, further investigation revealed the hole spin couples to the nuclear spin sites through the dipolar interaction, with the hole hyperfine coupling being a factor of 10 lower than the electron hyperfine coupling [103, 107]. Further hole decoherence mechanisms also arise from an admixture of p-shell and d-shell orbit states, with a $\sim$ 20% contribution from the d-shell, allowing hole spin flips without exchange of spins with nuclei [108]. Despite these interaction mechanisms, optical hole spin state preparation schemes have been created at $B = 0$ T using the fluctuation of the electron spin in a positively charged exciton X^+ to preferentially shelve hole spins into a desired state [103, 109].

2.3.2 Nuclear spins

While the carrier spin may be the best way to have a controllable spin qubit, it is important to consider the second type of spin within the system, the bath of nuclear spins $\boldsymbol{I}_i$ that form the quantum dot. All of the nuclei present within the dot possess magnetic moments $\boldsymbol{\mu}$ in InGaAs systems, with nuclear spins of $I \geq 3/2$, illustrated in Fig 2.10. A list of nuclear spin

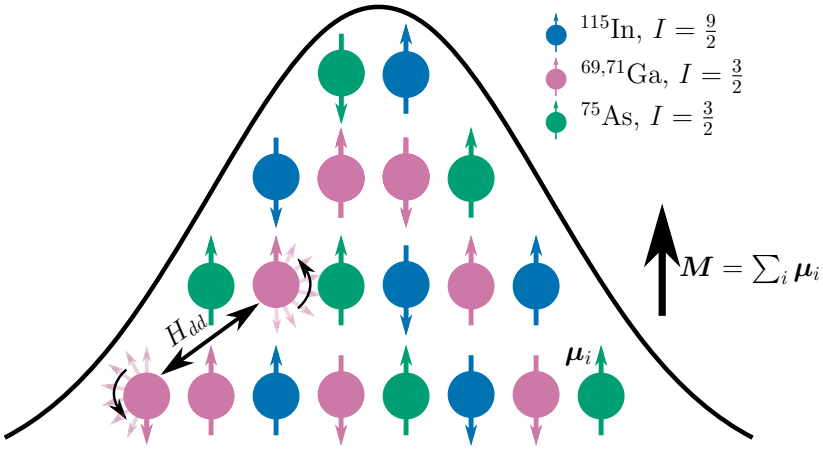

Figure 2.10: Nuclear spin bath in an InGaAs quantum dot structure. Nuclear spins $\boldsymbol{I}$ with magnetic moment $\boldsymbol{\mu}_i = \gamma\hbar\boldsymbol{I}$ form an overall magnetization $\boldsymbol{M}$. In the case of a fully polarised spin bath, maximum magnetization is achieved in the direction of the spin projection $\boldsymbol{M} = \pm M$. Nuclear dipole-dipole interaction can induce transfer of spin across the dot through spin flips flops illustrated by the H_{dd} interaction.

properties of different isotopes in InGaAs QDs is found in Table 2.4.

The effect of a large quantity of spins is an overall magnetization $\boldsymbol{M}$ generated by the nuclear spin bath, which is defined by,

$$\boldsymbol{M} = \sum_i \boldsymbol{\mu}_i \tag{2.13}$$

where μ_i is the magnetic moment generated by the i-th nuclear spin. In thermal equilibrium, $\boldsymbol{\mu}$ is randomly distributed among the spin states of the nuclei $I_{z,i}$, which for infinite nuclear spins would cause the effect of the nuclear spin bath to average out and $\boldsymbol{M} = 0$. However, the finite number of spins $\sim 10^4$ results in statistical fluctuations becoming an important consideration. Input of energy via optical pulses can alter this state to provide a non-zero magnetization. Nuclear spins can interact with other nuclear spins and also interact with the carrier spins in the QD via the hyperfine interaction, which we discuss in Section 2.3.3. In this section, we consider the internal dynamics of a rich nuclear spin bath found within the InGaAs QD system.

Nuclear dipolar interaction

The nuclear spin bath is a complex system of spins which can interact among the constituent nuclei within the nuclear spin bath and nearby nuclei in the wetting layer. For GaAs and InAs, this manifests primarily in the form of nuclei dipole-dipole interaction, H_{dd}. In the simple case of two nuclear spins $\boldsymbol{I}_i$, $\boldsymbol{I}_j$ separated by a distance $\boldsymbol{r}_{ij}$ can be considered for the whole system as such,

$$H_{dd} = \frac{\mu_N^2}{2} \sum_{i \neq j} \frac{g_i g_j}{r_{ij}^3} (\boldsymbol{I}_i \boldsymbol{I}_j - 3 \frac{(\boldsymbol{I}_i \boldsymbol{r}_{ij})(\boldsymbol{I}_j \boldsymbol{r}_{ij})}{r_{ij}^2}) \tag{2.14}$$

where μ_N is the nuclear magneton, and $g_{i,j}$ is the g-factor of the nuclear isotope at site i, j. The dipole-dipole interaction allows spin-flips with other nuclei of the same isotope within the quantum dot, allowing spin polarisation to be transferred (shown in Fig 2.10). Spreading of the spin polarisation is called spin diffusion, and can result in loss of spin polarisation to the material surrounding the quantum dot [110]. Overall spin is lost to the crystal due to the nonsecular part of the equation at magnetic fields lower or similar to the dipolar field ~ 0.1 T [104, 111]. Each nuclei interacts with an effective field generated by the summation of the dipole-dipole interaction with every other nuclei. Dipole-dipole nuclear interaction can cause significant loss of spin polarisation through diffusion in bulk crystal semiconductors, however, quantum dots experience strong Knight fields and quadrupole effects which overcome the effects of the dipole-dipole interaction induced spin diffusion. While these effects limit dipole-dipole interaction, nuclear spin-flip flops within the quantum dot still occur and can become a limitation in maintaining coherence of a nuclear spin bath [112].

Nuclear electric quadrupolar effects

Atomic nuclei do not possess an electric dipole moment, resulting in no interaction with static electric fields. However, any nuclei with $I > 1/2$ do posses an electric quadrupolar moment, arising from a non-spherical distribution of charges within the nucleus. Quadrupolar moments

do not interact with static electric fields but instead interact with electric field gradients arising from local stain variations at each crystal lattice site [111]. Cubic structures such as bulk InAs or GaAs possess no electric field gradient, but the presence of strain and defects created by QD formation can break local symmetry and result in quadrupolar coupling of the nuclei near the electric field gradient. To quantify the effect of strain on electric field gradients, a gradient field tensor is introduced S_{ijkl}, such that the electric field gradient is described by,

$$V_{ij} = \sum_{k,l} S_{ijkl}\epsilon_{kl} \tag{2.15}$$

where ϵ_{kl} is the symmetric strain tensor. In the principle axis reference frame $+z$, nuclear quadrupole coupling to the electric field gradient V_{ij} can be described by the Hamiltonian H_Q [111],

$$H_Q = \frac{eQ}{4I(2I-1)}(V_{zz}(3I_z^2 - I^2) + (V_{xx} - V_{yy})(I_x^2 - I_y^2)) \tag{2.16}$$

where Q is the quadrupolar moment for a particular nucleus. Quadrupolar moment for the relevant nuclei can be found in Table 2.4. We can simplify the electric field gradient terms into two expressions, an asymmetry parameter $\eta = (V_{xx} - V_{yy})/V_{zz}$ and the field gradient parameter q, where $eq = V_{zz}$. Often the axial symmetry assumption is made, resulting in $V_{xx} = V_{yy}$ and therefore $\eta = 0$. The overall Hamiltonian for the principal axis frame $+z$ can then simplified to,

$$H_Q = \frac{e^2qQ}{4I(2I-1)}(3I_z^2 - I^2) \tag{2.17}$$

The general Hamiltonian for nuclear spin states in a magnetic field considering the Zeeman effect and quadrupolar coupling can be written as such:

$$H = H_Z + H_Q \tag{2.18}$$

For the majority of experiments in this thesis, we operate at high magnetic field in the Faraday geometry. We can assume that the magnetic interaction is stronger than the quadrupolar

coupling ($H_Z \gg H_Q$), allowing a treatment of the quadrupolar effect with perturbation theory [113]. Considering a simple scenario where there are no quadrupolar effects $H_Q = 0$. We can see in Fig 2.11 that all nuclear spin states for a particular nuclei would have equal energy splitting due to the Zeeman effect $H_Z = \hbar\omega_L \boldsymbol{I}$, where ω_L is the Larmor precession frequency of the nuclei. Now considering the presence of the quadrupolar effects, we can define a new set of axes with the electric field gradient principal axis along z'. The angle between the electric field gradient axis z' and the static magnetic field axis z is defined as θ. The angular momentum projection on to the principle axis of the electric field gradient can be defined as $I_{z'}$. It is possible to use the assumption $I_{z'} = I_z \cos(\theta) + I_x \sin(\theta)$ without loss of generality to give an expression for H_Q in terms of the growth axis z [104, 111, 113]. The energy levels of the Hamiltonian can then be expressed as the Zeeman effect with first and second order perturbations due to the quadrupolar interaction.

$$E_m = E_m^{(0)} + E_m^{(1)} + E_m^{(2)} \tag{2.19}$$

Transition energies from some spin state m to $(m+1)$ can then be calculated to varying orders in terms of the Larmor precession frequency $\omega_L = -\gamma_N B_z$, quadrupolar frequency $\omega_Q = \dfrac{3e^2qQ}{h2I(2I-1)}$, and the angular displacement θ of the electric field gradient principal axis and static magnetic field [111].

$$\begin{aligned}
\Delta E^{(0)} =& \hbar\omega_L \\
\Delta E^{(1)} =& -\hbar\omega_Q(I_z + \tfrac{1}{2})\frac{3\cos^2\theta - 1}{2} \\
\Delta E^{(2)} =& -\hbar\frac{\omega_Q^2}{32\omega_L}\sin^2(\theta)(6I_z(I_z+1) \\
& (1 - 17\cos^2(\theta)) - 2I(I+1)(1 - 9\cos^2(\theta)) \\
& + 3(1 - 13\cos^2(\theta))
\end{aligned} \tag{2.20}$$

We now have a reasonable approximation to how the energy levels of the nuclear spin will be affected by the quadrupolar effect. We can consider the effect of the perturbative terms $\Delta E^{(\beta)}$ on the resulting dipole transition frequencies using $\omega^{(\beta)} = \Delta E^{(\beta)}/\hbar$ where β is the perturbation order. A visualisation of these effects for a nucleus of $I = \frac{3}{2}$ under compressive strain is shown in Fig 2.11.

The next simplest scenario beyond $H_Q = 0$ is the scenario with the electric field gradient axis z' being parallel to the growth axis z, such that $\theta = 0$. The second order term vanishes due to the $\sin^2(\theta)$ term, and the first order term becomes $-\omega_Q(I_z+\frac{1}{2})$. The resulting transition frequencies will be equally shifted by ω_Q. More generally, we can expect an offset between the z axis and the electric field gradient principal axis z', requiring consideration of the second term. For the central transition $-\frac{1}{2} \leftrightarrow \frac{1}{2}$, the $(I_z + \frac{1}{2})$ term becomes zero, indicating the first order quadrupolar interaction has no effect on this transition. As a consquence the $-\frac{1}{2} \leftrightarrow \frac{1}{2}$ transition energy becomes $\omega_L + \omega_Q^{(2)}$.

For the satellite transitions (STs) we do however observe a shift in energies causing an increase (decrease) in energy for the $\frac{1}{2} \leftrightarrow \frac{3}{2}$ $(-\frac{3}{2} \leftrightarrow -\frac{1}{2})$ transitions for compressive elastic strain. It is usually the case that $\Delta E^{(1)} \gg \Delta E^{(2)}$, and so the satellite transitions are unaffected by the second order term [113]. In the specific case of the self-assembled InGaAs QDs studied within this thesis, there is large inhomogeneous strain arising from the self-assembly process. Inhomogeneity of the strain causes local strain variations which results in each nuclei experiencing a different $\Delta E^{(1)}$, which causes significant broadening of the STs in nuclear magnetic resonance studies [104, 114].

The presence of the quadrupolar effect ultimately results in distinct energies for transitions between different spin states, lifting the single frequency transition found in the absence of quadrupolar interaction $H_Q = 0$, which provides two useful applications.

Firstly, the differing energy levels of nuclei spin states due to the presence of quadrupolar interaction can suppress the dipole-dipole flip-flops introduced in Section 2.3.2. Mismatch in energy levels between nuclear sites results in dipolar spin flip flops requiring energy input,

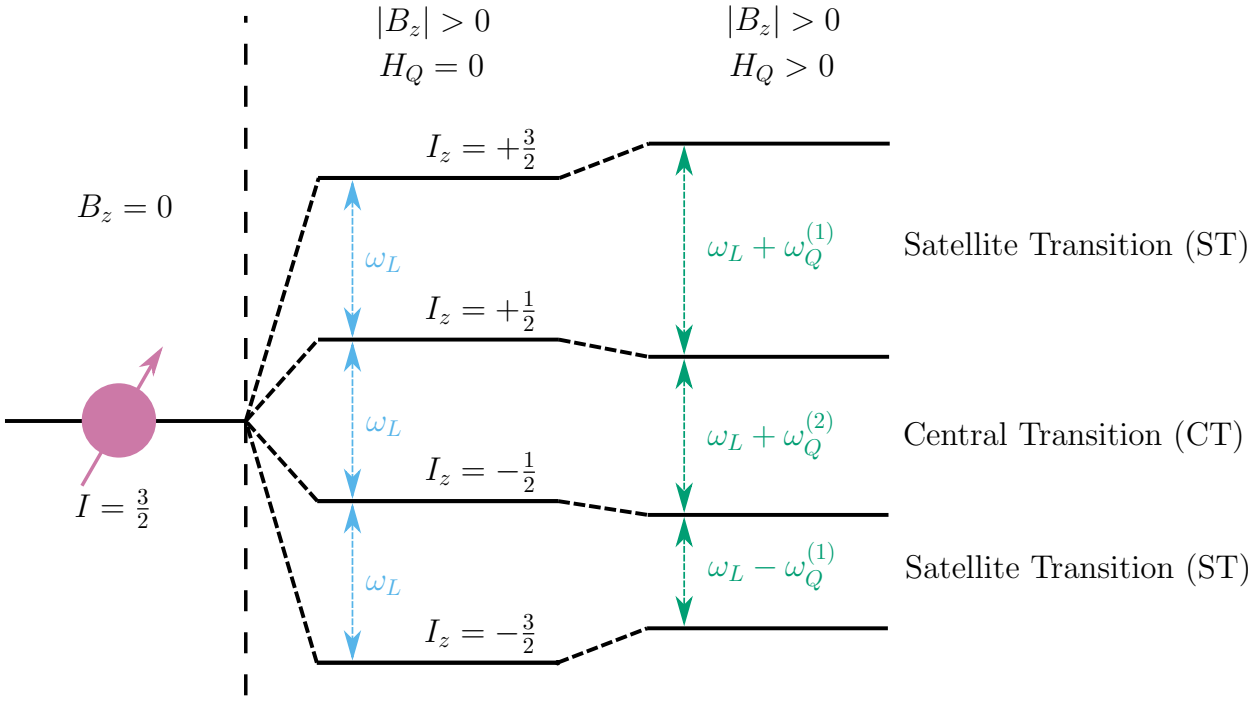

Figure 2.11: Splitting of nuclear spin state energies of a $I = 3/2$ nucleus in the presence of Zeeman and quadrupolar interaction. This schematic assumes compressive strain resulting in a positive quadrupolar contribution $+\omega_Q$. Absence of quadrupolar interaction, $H_Q = 0$, results in identical transition energies for all spin states. Presence of quadrupolar effects $H_Q > 0$ results in energetically distinct transitions. Central transition is unaffected as $\Delta E^{(1)} = 0$ for this transition, leaving only the second order term. The second order effect can also be ignored for satellite transitions as generally $\Delta E^{(1)} \gg \Delta E^{(2)}$ [113].

effectively suppressing the interaction. Furthermore, this mechanism suppresses nuclear spin diffusion with nuclei in the material surrounding the quantum dot. A highly strained dot causes large energy mismatch when compared to the nuclei in the material surrounding, preventing transfer of spin polarisation out of the QD [115]. Secondly, the unique transitions for each spin allow each nuclear spin transition to be addressed induvidually, allowing full control of the nuclear spin basis. This has been recently used to create a nuclear spin register within a strain-free GaAs quantum dot [29].

It is also necessary to consider the scenario at lower magnetic field where $H_Q \gg H_Z$, at which point the Zeeman effect is negligible. In this regime, the quadrupole splitting will dominate separation between nuclear spin states, resulting in degenerate $\pm m$ spin states,

but an energy difference between $(\pm m)$ and $\pm(m+1)$ allowing nuclear quadrupole resonance [113]. For InGaAs quantum dots, the quadrupolar shifts become comparable to the Zeeman splitting at approximately $B_z = 1$ T, indicating that fields below this threshold will observe deviation from the described model of $H_Z \gg H_Q$ [112].

Isotope	Nuclear Spin $\boldsymbol{I}$	Hyperfine Constant A (μeV)	Quadrupolar moment Q (b)
^{69}Ga	3/2	43	+0.171
^{71}Ga	3/2	54	+0.107
^{75}As	3/2	46	+0.314
^{115}In	9/2	56	+0.770

Table 2.4: List of nuclear spin properties for materials within InGaAs quantum dots. Hyperfine constants were taken from [104, 116]. Quadrupolar moments were taken from [117].

2.3.3 Hyperfine interaction

A perfect spin qubit would have no source of interaction to cause decoherence. An isolated spin-$\frac{1}{2}$ system is unfortunately not possible within the quantum dot system due to the nuclear spin bath discussed in the last section. Estimates for the quantity of nuclear spins within a typical InGaAs quantum dot suggests $N \sim 10^4$ - 10^5 [104]. Even with a factor of ~ 1000 difference between the carrier and nuclear magnetic moment, the large number of nuclear spins results in strong interaction with the charge carrier residing in the quantum dot via the hyperfine interaction, H_{HF}. Despite the adverse effect on carrier spin longevity, the presence of a large nuclear spin bath provides a platform for creating quantum memory storage due to the long lived nuclear spin states [115, 118]. Exploitation of the electron-nuclear interactions also can allow the carrier to transfer information to a long lived spin bath [31]. It is therefore important to understand the hyperfine interaction in order to minimise unwanted interactions.

The hyperfine interaction is the interaction between a nuclear spin and the magnetic field

produced by an electron, and is described by,

$$H_{HF} = 2\mu_B\gamma\hbar\boldsymbol{I}(\frac{\boldsymbol{l}}{r^3} - \frac{\boldsymbol{s}}{r^3} + 3\frac{\boldsymbol{r}(\boldsymbol{s}\cdot\boldsymbol{r})}{r^5} + \frac{8}{3}\pi\boldsymbol{s}\delta(\boldsymbol{r})) \tag{2.21}$$

$$\begin{aligned} H_{\mathrm{HF}} =& H_{\mathrm{HF}}^{Orb} + H_{\mathrm{HF}}^{Dip} + H_{\mathrm{HF}}^{FC} \\ H_{\mathrm{HF}}^{Orb} =& 2\mu_B\gamma\hbar\boldsymbol{I}(\frac{\boldsymbol{l}}{r^3}) \\ H_{\mathrm{HF}}^{Dip} =& 2\mu_B\gamma\hbar\boldsymbol{I}(3\frac{\boldsymbol{r}(\boldsymbol{s}\cdot\boldsymbol{r})}{r^5} - \frac{\boldsymbol{s}}{r^3}) \\ H_{\mathrm{HF}}^{FC} =& 2\mu_B\gamma\hbar\boldsymbol{I}(\frac{8}{3}\pi\boldsymbol{s}\delta(\boldsymbol{r})) \end{aligned}$$

where μ_B is the Bohr magneton, γ is the nuclear gyromagnetic ratio, $\boldsymbol{l}$ and $\boldsymbol{s}$ are the orbital and spin angular momentum operators respectively, $\boldsymbol{I}$ is the nuclear spin operator and $\boldsymbol{r}$ is the distance between the electron and nucleus. The first term, H_{HF}^{Orb} is the spin-orbit interaction. The second term, H_{HF}^{Dip}, describes the dipolar interaction between carrier and nuclei over a long distance. The final term, H_{HF}^{FC}, describes the Fermi-contact hyperfine interaction, arising from the overlap of nuclear and electron wavefunctions [111].

Fermi-Contact hyperfine interaction

The Fermi-contact hyperfine interaction is the dominant process affecting the electron, owing to its s-like state symmetry, enabling interaction through spatial overlap of the nuclear and electron wavefunction. The electron envelope wavefunction spreads over the whole quantum dot system, providing a channel to interact with the entire nuclear system of up to 10^5 spins [27, 119, 120]. Holes are unaffected by this interaction as their p-like state symmetry results in no spatial overlap with the nuclear lattice sites.

The Fermi-contact hyperfine interaction can also be expressed as:

$$H_{HF}^{FC} = \frac{\nu_0}{2}\sum_i A^i|\psi(\boldsymbol{R}_i)|^2(2\hat{S}_z^e\hat{I}_z^i + (\hat{I}_+^i\hat{S}_-^e + \hat{I}_-^i\hat{S}_+^e)) \tag{2.22}$$

where ν_0 is the volume of the unit cell, $\boldsymbol{S}$ is the electron spin, $|\psi(\boldsymbol{R}_i)|^2$ is the electron density

at the ith nuclear site, $\boldsymbol{I}^i$ and $\boldsymbol{R}^j$ are the spin and coordinate of the ith nucleus and A^i is the hyperfine interaction constant. As we have a single carrier interacting with a large nuclear spin bath, it is possible to approximate the nuclear interaction under the mean field approximation. Here we now observe an overall effective magnetic field B_N, which interacts with the electron as such:

$$H_{HF}^{FC} = \frac{1}{2}A\langle I_z\rangle \hat{S}_z^e = (\mu_B)g_e\hat{S}_z^e B_N \tag{2.23}$$

where $\langle I_z\rangle$ is the average nuclear spin, and $A = \sum_i A^i$. The value of A_i varies for different nuclear types, which directly determines the strength of interaction each isotope in the dot contributes to the overall hyperfine interaction [121]. A_i can be expressed as such:

$$A_i = -\frac{\mu_0}{4\pi}\cdot\frac{8\pi}{3}\gamma_S\gamma_{N,i}|\psi(0)|^2 \tag{2.24}$$

where μ_0 is the vacuum permeability, γ_S is the electron gyomagnetic ratio, $\gamma_{N,i}$ is the nuclear gyromagnetic ratio of a given isotope and $|\psi(0)|$ represents the electron wavefunction overlap with the nuclear site. A list of hyperfine constants for isotopes present in InGaAs QDs is found in Table 2.4.

The effective field created by the polarisation of nuclear spins is known as the Overhauser field, and its presence can induce further splitting of the spin states with the QD. Total Zeeman splitting of the electron can be expressed as $H_{Zeeman} = \mu_B g_e B_{Tot}$ where $B_{Tot} = B_z + B_{OH}$. As such, we can directly measure the average polarisation of the nuclear spin bath from measuring the change in Zeeman splitting in QD photoluminescence measurements due to variations in the Overhauser field. A more technical description of how this is implemented experimentally can be found in Chapter 3 .

As a consequence of the hyperfine interaction, the nuclei spins also experience an effective field from the electron's averaged spin projection known as the Knight field, B_K, which is quantified by the following expression:

$$B_{K,i} = f_e \frac{\nu_0 A_i}{g_N \mu_N} |\psi(\boldsymbol{R}_i)|^2 \langle \hat{S}_e \rangle \tag{2.25}$$

where f_e describes the occupation state of an electron within the quantum dot $f_e \in [0, 1]$, and $\langle \hat{S}_e \rangle$ is the electron spin polarisation. The instantaneous electron spin polarisation can be used for scenarios where electron spin correlation time τ_e is similar or greater than the nuclear precession period $2\pi/\omega_L$. For the scenario where the electron correlation time is much faster than nuclear precession period $\tau_e \ll 2\pi/\omega_L$, electron spin polarisation can be time-averaged.

The presence of an electron induces a Knight field on the nuclei, shifting the nuclear Zeeman splitting, resulting in $H_{Zeeman} = \mu_N g_N B_{Tot}$ for a single nuclei, where $B_{Tot} = B_z + B_K$. The effect is complicated by the non-uniform distribution of the envelope of the electron wavefunction density, resulting in nuclei in the centre of the dot being more strongly affected than the nuclei on the edges [104, 122]. Further implications of the effect of the Knight field are explored in Chapter 5.

Carrier-nuclei dipole interaction

After studying the Fermi-contact hyperfine interaction, there are two other terms in Eqn. 2.21. These two terms become key when considering the hole spin hyperfine interaction with nuclear spins. As mentioned in the previous section, p-like symmetry of the hole spin states result in vanishing wavefunction overlap at the nuclear spin sites, resulting in no coupling of the hole to the nuclei via Fermi-contact hyperfine interaction. Consequently, the most significant hyperfine interaction affecting the carrier hole is a combination of the electro-nuclear dipole interaction H_{HF}^{Dip} and the nuclear-orbital interaction H_{HF}^{Orb}.

Previous discussions of the carrier hole within a quantum dot has been limited to a simple model considering only heavy hole states $J_h = \pm\frac{3}{2}$. However, to consider the interactions of the hole with nuclei via dipole interaction, it is important to include valence band mixing for a full description. Dipole interaction results in a spin flip-flop between the carrier hole and a

nuclei, with a required transfer of angular momentum $\Delta J = \pm 1$. Finite heavy-hole light-hole splitting causes the heavy-hole $J_h = 3/2$ to be the lowest lying hole state separated from the light-hole state by Δ_{lh-hh}. Transfer of spin to a nuclei from the heavy hole via spin flip-flop would require energy input to overcome the splitting Δ_{lh-hh}. The energy requirement is circumvented through valence band mixing, where an admixture of the heavy and light hole states occurs due to the anisotropic strain and shape of the QD. Valence band mixing is quantified by the parameter β, and is related to a term known as the anisotropy factor $\alpha = 2|\beta|/\sqrt{3}$. Now that light hole states $J_h = 1/2$ may arise with no energy input, dipolar flip flops of the hole and the nuclei can occur. By accounting for small valence band mixing ($\beta \ll 1$), the following expression for hole-nuclei dipolar coupling is found [104]:

$$H_{Dip} = \nu_0 \sum_i \frac{A_i^h}{1+\beta^2} |\psi(\boldsymbol{r}_i)|^2 (I_z^i J_z^h + \frac{\alpha}{2}(I_+^i J_-^h + I_-^i J_+^h)) \tag{2.26}$$

where A_i^h is the dipole-dipole hyperfine constant. Due to the direct dependence on dot anisotropy, the dipolar interaction can also be referred to as the anisotropic hyperfine interaction.

Nuclei-orbital interaction

The final contribution to hyperfine interaction is the coupling of the momentum of the carrier to the field generated by the nuclear magnetic moments, and is known as the nuclei-orbital interaction H_{HF}^{Orb}. The effect is very relevant for holes as it has a large effect on bands of non-zero angular momentum, such as the p-like band the carrier holes occupy. It is described with the following expression

$$H_{HF}^{Orb} = g_e \mu_B \gamma_N \hbar \frac{\boldsymbol{I} \cdot \boldsymbol{L}}{\boldsymbol{r}_i^3} \tag{2.27}$$

where $\boldsymbol{L}$ is the angular momentum of the carrier hole. Occurances of hole-nuclei spin flips can arise from contribution of the d-shell orbitals which induce spin flip-flops. Inclusion of

d-shell orbitals also reduces the symmetry of the system from spherical to the real crystal symmetry, resulting in a hyperfine interaction that does not conserve angular momentum and allows spin flips between the two heavy hole states $|\Uparrow\rangle, |\Downarrow\rangle$ [108]. Combination of these effects results in a significant hole-nuclei hyperfine interaction A^h. Experimental measurement of A^h reveals that the hole spin states couple to the nuclei by a factor of 10 weaker than the electron $A^h/A \sim 0.1$ [107, 109, 123]. Considering both H_{HF}^{Orb} and H_{HF}^{Dip} completes the specific picture of hole-nuclear hyperfine interaction, and provides a full description of hyperfine interaction within a quantum dot [39, 104, 124].

2.4 Controlling spins within quantum dots

We now have a complete picture of the spins within the quantum dot system. It is now possible to discuss what implementation of quantum computing protocols would look like within a quantum dot spin qubit. This is achieved in three key steps as described in Chapter 1, state preparation, state manipulation and state readout. State preparation involves establishing an initial spin condition which is a known state. State manipulation then can arbitrarily rotate and control the spin to carry out computations using the spin qubit. Finally, a measurement of the state needs to be made in order to extract information. A fourth underlying key step is also required, long lasting quantum states such that information is not lost during computation. In this section, we will discuss how this is achieved for both the electron and nuclear spin system within an InGaAs quantum dot.

2.4.1 State preparation

Initialisation and readout of the both the electron and nuclear spin systems involve the input of energy to the quantum dot via optical excitation. Any precise spin state measurement will require some initialisation process first.

First, we can study the state preparation of carrier spins within a quantum dot. Generally

we are most interested in the electron spin as this is the focus of experiments in this thesis, but we shall also include brief discussion of hole spins for completeness. Consider the system discussed in Section 2.3.1. We have two spin states $|\uparrow\rangle$ and $|\downarrow\rangle$ ($\widetilde{|\Uparrow\rangle}$ and $\widetilde{|\Downarrow\rangle}$) for the electron (hole) spin. Both carriers experience state degeneracy at $B_z = 0$ T, with the electron coherence time being only ~ 1 ns due to Fermi-contact hyperfine interaction with the Overhauser field. The addition of a magnetic field breaks the degeneracy, suppresses this decoherence mechanism and provides two distinct electron spin states. The hole spin also experiences fast decoherence on a timescale of ~ 14 ns [125] as a result of hyperfine hole-nuclei dipole interaction, instead of the Fermi-contact hyperfine interaction as discussed in Section 2.3.3 [109, 125].

From these spin systems, we need to be able to quickly initialise the states into some known initial conditions, for example, the spin-up $|\uparrow\rangle$ ($\widetilde{|\Uparrow\rangle}$) state. The energy level diagram demonstrating the initialising of the electron spin state is illustrated in Fig 2.12a. To the first order, there is no interaction between the two spin states once degeneracy is broken. The spin will therefore be stable once initialised, and so we can use resonant excitation to spin pump the state. Two distinct optical transitions occur in the presence of B_z due to the selection rules that arise from Faraday geometry, one for each of the spin states. Application of a photon with frequency tuned to one of the transitions, for example $|\uparrow\rangle$, will result in resonance fluorescence at a rate of Γ, where by the two level system will emit photons at the same frequency as excitation in a scattering process [126].

Presence of a weakly allowed mechanism, γ, allows relaxation of the trion state into the opposing carrier spin state ($|\downarrow\rangle$). The γ transition is forbidden via optical selection rules but is weakly allowed due to misalignment of static magnetic field to confinement axis or heavy-hole light-hole mixing [126]. The spin in the opposing state cannot trivially relax into the original spin state through a spin-flip process $\epsilon_{\uparrow\downarrow}$, and it is now detuned from the resonant optical excitation as a consequence of the magnetic field [126, 127]. This results in the spin becoming "shelved" in the opposing spin state. The spin will eventually relax

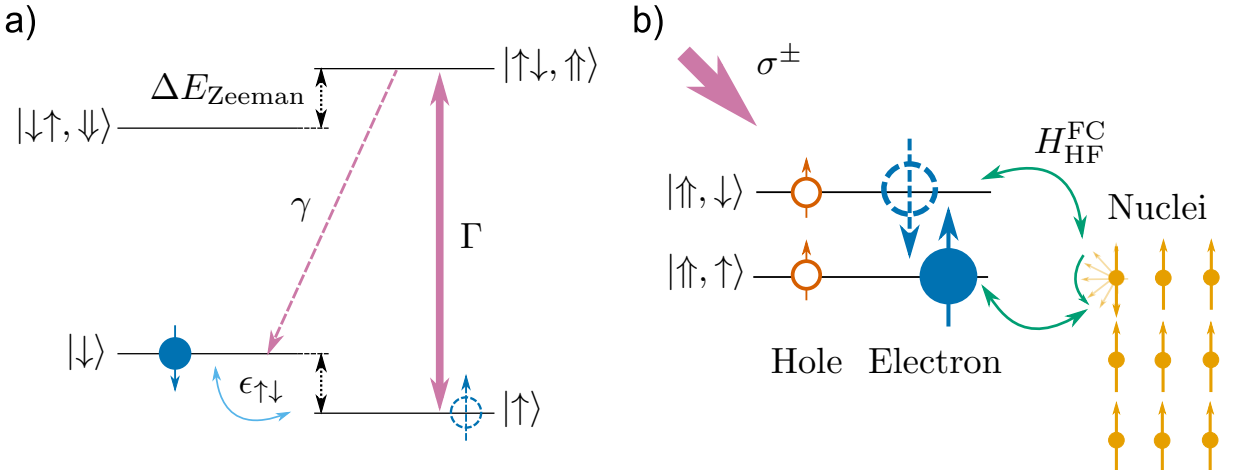

Figure 2.12: Optical spin initialisation techniques for both the carrier and nuclear spins. a) Resonant optical spin pumping allows initialisation of a spin state to the spin down state $|\downarrow\rangle$ by exciting the spin-up to trion transition Γ until the weakly allowed recombination γ occurs b) High power circularly polarised excitation of a QD allows spin to be quickly transferred to the nuclear spin bath (yellow) by hyperfine induced electro-nuclear spin flip-flops (green arrows) mediated by the Fermi-contact hyperfine interaction H_{HF}^{FC}.

on the timescale of $\epsilon_{\uparrow\downarrow} = 1/T_1$ due to spin-flip processes such as cotunnelling or phonon mediated transitions, further discussed in Section 2.4.4 and studied in detail in Chapter 4. Repeated resonant excitation of the Γ optical transition will eventually result in the weakly allowed transition γ occurring, successfully initialising the spin to a known state $|\downarrow\rangle$, allowing computational operations to be performed.

A similar scheme can be used to initialise the hole spin state, but instead of utilising the weakly allowed γ transitions it is possible to take advantage of electron-nuclear hyperfine interaction [103]. Generation of a trion via circularly polarised resonant optical excitation of a hole $|\Downarrow\rangle$ creates a trion of $|\Uparrow\Downarrow, \downarrow\rangle$. The most likely relaxation mechanism will release a photon at the same energy as the excitation, as seen for the electron initialisation scheme. However, a weakly allowed interaction between the electron in the trion and the in-plane field of the nuclear spin bath B_{xy}^{Nuc} can occur. This results in electron precession of ~ 1 ns and is the reason electron spin state are short-lived at $B_z = 0$. The rotation of the electron spin results in the recombination of the $|\Downarrow\rangle$ with the electron spin instead of the orignal $|\Uparrow\rangle$.

As a result, the hole now occupies the opposing spin state and is shelved here, shielded from optical excitation due to polarisation of the incoming excitation [103]. The scheme works at $B_z = 0$ T due to small hole-nuclear hyperfine interaction as discussed in 2.3.3 . Another scheme has been developed by preferentially tunnelling carrier electrons from the QD while forcing the hole to remain with a thick blocking barrier, allowing high fidelity ($F > 99\%$) and fast control (~ 30 ps) [105].

The nuclear spin system is somewhat different to the electron spin system owing to the presence of many spins as opposed to one. Polarisation of the nuclear spin bath can be achieved through both resonant and non-resonant excitation. Non-resonant excitation uses circularly polarised light $\sigma^{\pm}$ to pump the electron spin. Electron-nuclear spin flips can then occur via the hyperfine interaction, polarising a single nuclear spin in the bath [128]. High power nonresonant excitation results in repeated spin polarisation transfer to the spin bath, polarising the majority of the nuclear spins in short period of time. This is not completely efficient however, as the hyperfine interaction can cause spin flips and reduce the overall spin bath polarisation. Measurements of DNP via non-resonant excitation in III-V quantum dots have shown consistent results above 50% [128–130] with the highest nuclear polarisation of $\sim 80\%$ [131].

Resonant excitation of the exciton states can also successfully induce significant DNP. One techinque involves resonant excitation of the neutral exciton X^0 while operating a charge controlled structure at a bias corresponding to fast electron tunnelling [132]. During the radiative lifetime of the exciton X^0 exciton $\tau_{\mathrm{r}} \sim 1$ ns, an additional electron tunnels on a much shorter time scale of $\tau_{\mathrm{In}} \sim 35$ ps creating a trion. The trion recombines leaving an electron within the QD for a short period of time $\tau_{\mathrm{Out}} \sim 5$ ps, in which time the electron can undergo a spin flip-flop with a nuclei via the Fermi-contact hyperfine interaction. After a short time $\tau_{\mathrm{Out}} \sim 5$ ps the electron leaves the dot, allowing resonant excitation to repeat the cycle generating a build up of DNP to a maximum of $\sim 13\%$ [132].

Another resonant nuclear spin pumping technique is achieved through spin-forbidden

transitions [128]. Excitation of weakly allowed transitions γ described earlier in this section can induces a second order process that is allowed through the spin flip of an electron and a nuclei. The weakly allowed transition is difficult to saturate as a consequence of the weak coupling, allowing continuous excitation for transfer of spin to the nuclear spin bath. This techinque can achieve DNP levels of $\sim 65\%$ [128] . Both resonant and non-resonant excitation generate spin bath that are not fully polarised, which although not ideal, still provides a substantial number of spins available for coherent manipulation.

2.4.2 Spin manipulation

Once the spin states are prepared, it is possible to start attempting to control them. Combined with our previous discussions on spin interaction, we can now discuss the fundamentals of coherent spin control, to allow arbitrary rotation of spins within the Bloch sphere, providing a spin qubit basis for use in a quantum computer.

Consider a simple system of a single spin with $S = 1/2$. When placed in some static magnetic field B_0 along the z axis, the degenerate spin states split via the Zeeman effect as mentioned in previous sections. We then have a two-level system with states $m_s = \pm 1/2$ where the splitting of the states is quantified by $\Delta E = g\mu B_z$. In large enough B_0, the spins will precess around the field at the Larmor frequency ω_L [113]. Control over the spin state can be achieved through the application of an oscillating magnetic field generally referred to as B_1. The field oscillates at a frequency of ω_{rf}, and when $\omega_{rf} = \omega_L$ the system responds resonantly to the field. The technique of applying an alternating magnetic field to spins in some static field was originally developed to probe atomic nuclei, and is known as nuclear magnetic resonance (NMR). However, the technique can be extended to control electron spins through electron spin resonance (ESR) [32]. Both are powerful tools for manipulating spin systems within quantum dots, as we will discuss below.

The alternating field B_x applied perpendicular to the system is described by a simple

oscillating function,

$$B_x(t) = B_{x,0}\cos(\omega_{rf}t) \tag{2.28}$$

where $B_{x,0}$ is the perpendicular field amplitude. The easiest analysis of the effect of B_x comes from breaking it down into two opposite rotating components with amplitude B_1 [113],

$$\begin{aligned} B_R &= B_1(\hat{\boldsymbol{x}}\cos(\omega_{rf}t) + \hat{\boldsymbol{y}}\sin(\omega_{rf}t)) \\ B_L &= B_1(\hat{\boldsymbol{x}}\cos(\omega_{rf}t) - \hat{\boldsymbol{y}}\sin(\omega_{rf}t)) \end{aligned} \tag{2.29}$$

One term will rotate in the same direction as precession of the spin, the other will rotate in the opposite direction and are related to Eqn 2.28 through the expression $B_x = (B_R + B_L)/2$. It is possible to neglect the opposing rotation under the conditions of resonance when the static field is much stronger than the alternating field $B_0 \gg B_1$. This allows us to only consider a single rotating field represented by $\boldsymbol{B}_1 = B_1(\hat{\boldsymbol{x}}\cos(\omega_{rf}t) + \hat{\boldsymbol{y}}\sin(\omega_{rf}t))$. It is now possible to write an equation of motion describing the spin in the presence of both B_0 and B_1. We write this in terms of the classical magnetic moment of the spin $\boldsymbol{\mu}$,

$$\frac{d\boldsymbol{\mu}}{dt} = \boldsymbol{\mu} \times \gamma(\boldsymbol{B}_0 + \boldsymbol{B}_1(t)) \tag{2.30}$$

where $\boldsymbol{B}_0 = B_0\hat{\boldsymbol{z}}$ and γ is the gyromagnetic ratio of the spin. Oscillation of $\boldsymbol{B}_1$ creates a time dependence of the field, which can be removed if we consider the spin system within the rotating frame. The rotating frame coordinate system is defined such that the coordinates rotate at angular frequency ω_L of precession around $\hat{\boldsymbol{z}}$. This causes $\boldsymbol{B}_1$ to become static when strictly resonant with ω_L. The static field in the laboratory frame, $\boldsymbol{B}_0$, remains static as the coordinates are rotating about its axis. Converting the equation of motion to a frame of reference along the axis of $\boldsymbol{B}_1$ results in the following expression of the equation of motion in terms of static fields B_0 and B_1.

$$\frac{d\boldsymbol{\mu}}{dt} = \boldsymbol{\mu} \times \gamma((B_0 - \frac{\omega_L}{\gamma})\hat{\boldsymbol{z}} + B_1\hat{\boldsymbol{x}}) \tag{2.31}$$

This can also be expressed in terms of the effective magnetic field $\boldsymbol{B}_{eff}$ felt by the moment.

$$\begin{aligned} \frac{d\boldsymbol{\mu}}{dt} &= \boldsymbol{\mu} \times \gamma \boldsymbol{B}_{eff} \\ \boldsymbol{B}_{eff} &= (B_0 - \frac{\omega_L}{\gamma})\hat{\boldsymbol{z}} + B_1 \hat{\boldsymbol{x}} \end{aligned} \tag{2.32}$$

This equation demonstrates the effect of application of an oscillating field, as we would expect the moment to precess around $\boldsymbol{B}_{eff}$ by moving away from the static field $\hat{\boldsymbol{z}}$ and then return after some time defined by the frequency $\gamma \boldsymbol{B}_{eff}$. As we want to resonantly excite the transition between spin states, it is important to consider what happens under resonant conditions where $\omega_{rf} = \omega_L$. Here, $\omega_{rf} = \gamma B_0$ resulting in the equation of motion depending entirely upon the perpendicular field B_1. Under these conditions, the nuclear magnetic moment will precess perpendicular to the applied field in the yz plane, periodically becoming parallel and antiparallel to the static field [113].

Selective application of B_1 allows control of the spin state of the system. Applying B_1 for a length of time t will cause rotation of the spin by angle $\theta = \gamma B_1 t$. This allows arbitrary control of the spin projection by applying different length pulses. Common pulse lengths are rotations of π and $\pi/2$, referred to as 90 degree and 180 degree pulses, where $t_{90} = \frac{\pi}{2}/(\gamma B_1)$ and $t_{180} = \pi/(\gamma B_1)$.

In the scenario described so far, the spin will precess infinitely under application of B_1. However, this is not a realistic scenario, as we expect loss of energy to the lattice and interactions with other spins nearby. The longitudinal spin-lattice decay T_1, transverse decay due to spin-spin interaction T_2 and transverse decay due to field inhomogeneities T_2^* determine the time scales of relaxation parallel and perpendicular to the static field. In the presence of the static magnetic field B_0, any macroscopic magnetic moment will eventually become parallel to the static field. Considering some magnetization $\boldsymbol{M}(t) = M_x(t)\hat{\boldsymbol{x}} + M_y(t)\hat{\boldsymbol{y}} + M_z(t)\hat{\boldsymbol{z}}$ in the static field along $\hat{\boldsymbol{z}}$, eventually $\boldsymbol{M}(t) = M_z(t)$. To account for this relaxation towards

the static field, we can write the equation of motion for the M_z component.

$$\frac{dM_z}{dt} = \frac{M_0 - M_z}{T_1} \tag{2.33}$$

From this equation we can see that the system will reach equilibrium once M_z equals the magnitude of the equilibrium magnetisation vector M_0. If the magnetic moment is aligned along the $\hat{\boldsymbol{z}}$ axis in equilibrium, we require the $M_{x,y}$ components to tend to zero.

$$\begin{aligned} \frac{dM_x}{dt} &= \gamma(\boldsymbol{M} \times \boldsymbol{B})_x - \frac{M_x}{T_2} \\ \frac{dM_y}{dt} &= \gamma(\boldsymbol{M} \times \boldsymbol{B})_y - \frac{M_y}{T_2} \end{aligned} \tag{2.34}$$

The equations above (Eqn 2.34) are known as the Bloch equations and were first introduced by Bloch in 1946 [133]. It is now possible to calculate the expressions for the magnetization components and observe that we expect exponential decay of magnetisation on two separate time scales T_1 and T_2. Consider a system in the rotating frame with no oscillating field. The effective field in this scenario is therefore $\boldsymbol{B} = 0$, resulting in simple linear differential equations. Solving these provides the following solutions to the Bloch equations, which clearly indicate the loss of magnetization in the x-y plane over time scale T_2 and complete alignment to the thermal equilibrium magnetization M_0 over time scale T_1.

$$\begin{aligned} M_x &= M_x(0)e^{-t/T_2} \\ M_y &= M_y(0)e^{-t/T_2} \\ M_z &= M_0 - (M_0 - M_z(0))e^{-t/T_1} \end{aligned} \tag{2.35}$$

The nuclear spins within a quantum dot require slight adjustment to the above model, as the nuclear spin bath forms a total magnetization as a consequence of the sum of the magnetic moments of all i nuclei $\boldsymbol{M} = \sum_i \boldsymbol{\mu}_i$. An additional consideration also needs to be made for the larger total spin for nuclei within InGaAs/GaAs quantum dots, where all nuclei have

$I > 3/2$, which is accounted for by a generalisation of the above model.

Nuclear magnetic resonance within semiconductor quantum dots is a well researched field, with much success in investigating the relaxation mechanisms within the nuclear spin system, as well as the effect of the hyperfine interaction on the nuclear spin bath [114, 123, 134–136].

Electron spin resonance (ESR) in optically active quantum dots on the other hand has only been achieved once using standard oscillating field techniques [32]. A major difference between the nuclear and carrier spin system is the difference in splitting between spin states. For a nuclear spin within an InGaAs quantum dot experincing a static magnetic field of 8T, the NMR resonances are in the range $\omega_{rf} \sim 50 - 120$ MHz [123]. In contrast, an electron spin in a self assembled QD, with typical g-factors of -0.7 to -0.35 [89, 137, 138], would require an oscillating field of frequency $\omega_{rf} \approx 4$ to 9 GHz at a field of 1 T, which proves challenging to generate without significant technical difficulties. High frequency resonators generate high fluctuating electric field which will interact with the spin states within the QD. Recent work on keyhole resonators have given some hope to generating the required fields from resonators off chip [33], but the majority of work on coherent control of electrons in InGaAs QDs so far has been carried out under Voigt geometry using optical control of the spin [31]. We explore microwave resonator designs for ESR applications in more detail in Chapter 6.

2.4.3 State readout

Once we have prepared and applied the desired manipulation to the spin states, optical readout can be achieved for both the carrier and nuclear spin systems. Readout of the carrier spin system can be achieved using resonant optical pulses to detect the presence (or absence) of optical emission from a specific spin state, indicating which state the carrier was in the time of measurement [126]. Nuclear spin readout uses the Overhauser field generated by a polarised nuclear spin bath. The additional shift in Zeeman splitting can be measured through photoluminescence, giving a direct measurement of the ensemble polarisation [128, 139].

Further details on these techniques will be discussed Chapter 3.

2.4.4 Spin relaxation

Long spin lifetimes, T_1 and coherence times T_2 are desirable if quantum dots are to be used in spin qubit applications. The primary findings of this thesis investigate the various mechanisms affecting T_1 in both the electron and nuclei, in addition to coherence times of the nuclei $T_{2,N}$, and as such we will limit discussion here to a brief overview of the mechanisms affecting these parameters.

We shall quickly reconsider the physical meaning of T_1 and T_2. Consider a spin initialised into the spin-up state $|\uparrow\rangle$, parallel to some static magnetic field (B_0) along the quantization axis ($+z$). The relaxation of the spin magnetization can be described by two parameters. The first, longitudinal relaxation T_1, describes loss of energy from the spin to the surrounding environment. This manifests as a loss of the magnetization towards the thermal equilibrium state of magnetization as shown in Fig 2.13. Once the spin system has fully relaxed longitudinally, it has returned to its equilibrium state, and will require re-initialising before more operations can be carried out. As a result, longitudinal relaxation T_1 is often referred to as lifetime of the spin.

The second, transverse relaxation T_2, describes the loss of magnetization in the x-y plane, and is essentially a loss of phase information over time. Transversal relaxation can occur without energy transfer, resulting in T_2 being faster than T_1 in dipolar rigid solids where spins are located at a fixed point. Loss of phase can occur by random spin-spin interactions which over time will result in total loss of magnetization and the information stored within the phases of the spins. This can also be described as decoherence and as such T_2 is often referred to as coherence time.

Additional loss of transverse magnetization can occur through inhomogeneities in the magnetic field. Local fluctuations in field cause different spins to precess at marginally different rates, resulting in the spin precession becoming out of phase. This process is known

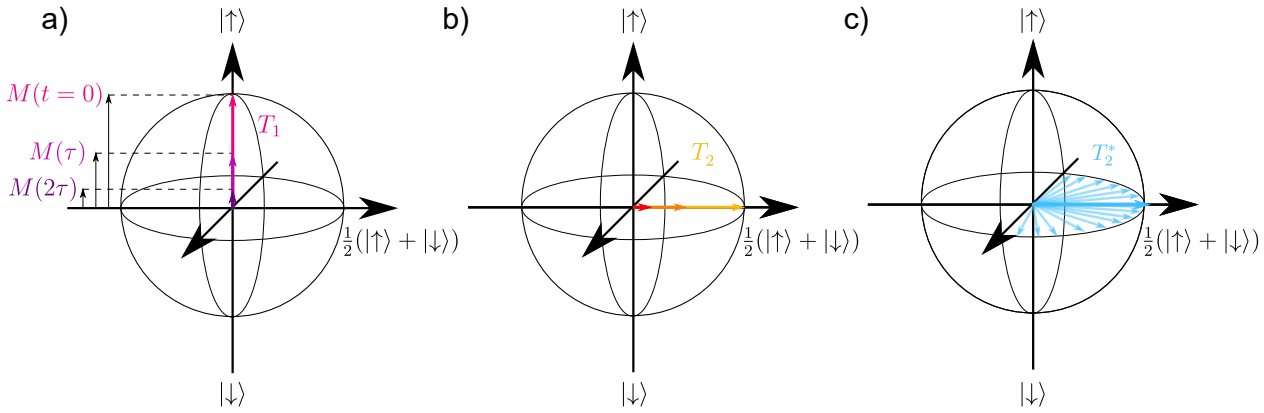

Figure 2.13: Relaxation times T_1, T_2 and dephasing time T_2^* of a spin in the rotating frame. Graphical projection of a pure two level spin state in the rotating frame as shown in the figures provides visualisation of the spin state space and is known as a Bloch sphere. a) Longitudinal relaxation (pink) returns the systems magnetization to the thermal equilibrium state over time T_1, represented by a loss of magnitude of magnetization vector over time $M(t)$ in Bloch sphere. b) Transversal relaxation (orange) of the magnetization vector occurs on time scale T_2 due to spin-spin interactions, resulting in irretrievable loss of phase information. c) Pure dephasing (blue) results in a loss of phase information due to inhomogeneities in the magnetic field which can be visualised as a spreading out of the magnetization vector of the spin, and as a consequence losing spin state information over time T_2^*. Dephasing can be refocused through the technique of spin echoes as discussed in Section 2.4.2.

as dephasing and is quantified by the dephasing time T_2^*. Loss of energy to the environment through longitudinal relaxation will eventually cause a loss in phase information. The magnitude of the effect of T_1 on T_2 is given as such:

$$\frac{1}{T_2} = \frac{1}{2T_1} + \frac{1}{T_2^*} \tag{2.36}$$

Measurement of T_1 and T_2 for both the electron and nuclear subsystems will provide a complete understanding of the timescales available for quantum computing algorithms. The mechanisms affecting the relaxation/coherence terms need to be understood in order to mitigate or remove their effect, prolonging spin states and allowing more computational operations to be performed in a single initialisation sequence.

Nuclear spin relaxation $T_{1,N}$ can be measured through the observation of loss of dynamic nuclear polarisation. Extremely long $T_{1,N} > 10000$ s observed for uncharged self assembled

InGaAs dots in the literature [139–141] indicate that nuclear spin diffusion is not a dominant source of relaxation. This is explained due to nuclear spin diffusion being suppressed by the quadrupolar freezing [128, 140, 142] of nuclear spin flip flops, as discussed in Section 2.3.2. The primary contributor to loss of nuclear polarisation in charged InGaAs QDs is the electron-nuclear spin flip-flops caused by the hyperfine interaction, allowing the electron to act as a mediator to transfer the spin polarisation to another system such as phonon modes or the Fermi sea. This has been clearly observed both in the literature and in our work shown in Chapter 4 as a reduction in $T_{1,N}$ for a singly charged quantum dot when compared to uncharged/doubly charged quantum dots.

Electron spin lifetime $T_{1,e}$ is affected by two key processes, phonon mediated spin flip interaction and cotunnelling effects. Spin orbit interaction creates an admixture between opposing spin states in the electron, allowing transitions to occur via phonon related effects. This dependance has a strong relationship with magnetic field, $T_{1,e} \propto B^{-5}$, which was predicted [143] and experimentally measured [144]. Cotunnelling is an exchange of electron spin with the Fermi resevoir and has no field dependence, instead depending on the strength of coupling between the dot and the Fermi resevoir [145]. A full description of spin relaxation of quantum dots is considered in Chapter 4.

Coherence time of the electron $T_{2,e}$ is usually approached using the Merkulov-Efros-Rosen (MER) model [28], considering an electron in the absence of magnetic field. Here we define three distinct time scales to describe interactions between the electron and the nuclei causing decoherence of the electron. The first describes electron precession around nuclear field fluctuations and causes dephasing of ~ 1 ns. The second is the nuclear precession around the Knight field, limiting coherence to ~ 1 μs. Dipole-dipole nuclear flip flops near the electron can also reduce coherence, placing a limit of ~ 100 μs on coherence time [28, 104]. Application of a magnetic field to split the spin states was predicted and proven experimentally to remove the first effect by stabilising the electron spin along the static field axis [28, 101]. The effects of the electron precession around nuclear field fluctuations are suppressed for fields as small

as $B \sim 10$ mT. As the majority of experiments in this thesis are carried out with a static magnetic field $B \sim 0.5$ - 8 T, only the second and third processes would need to be considered for investigations into $T_{2,e}$. Longest reported coherence times for the electron are $T_{2,e} \sim 4$ μs, utilising spin echo techniques to suppress nuclear field fluctuations and prolong electron coherence time [104, 146]

Nuclear coherence times in InGaAs dots are measured through pulsed NMR techniques such as Hahn echo. Pure dephasing T_2^* results in loss of phase over a short time for transverse magnetization in the x-y plane. It was shown by Hahn in 1950 that the application of resonant RF pulse of length t_{180} would rotate the in-plane magnetisation and cause the magnetization to refocus [147]. The technique of applying refocusing pulses was named spin-echoes and provides direct measurement of true T_2 through the elimination of the trivial inhomogeneous broadening caused by dephasing T_2^*. Further discussion of spin echo techniques is carried out in Chapter 5.

Measurement of $T_{2,\mathrm{N}}$ for the various isotopes within an uncharged InGaAs dots gives $T_{2,\mathrm{N}} \sim 0.5$ - 10 ms depending on the isotope [112]. Decoherence is attributed to nuclear dipole-dipole interaction, which can be suppressed through the use of dynamical decoupling sequences such as Carr-Purcell (CP), Carr-Purcell-Meibloom-Gills (CPMG) or the more recently developed CHASE sequence [114]. Dynamical decoupling techinques allow further prolonging of nuclear coherence times with up to a factor of 5 improvement [114]. Addition of an electron to charge the quantum dot was thought to provide a source of fast nuclear decoherence via the hyperfine interaction, with nuclear coherence times reduced by a factor of 100 [136]. In fact, we have shown millisecond length nuclear coherence times $T_{2,\mathrm{N}}$, which is discussed in further detail in Chapter 5.

3

Experimental techniques

3.1 Samples

The quantum dot structures studied in this thesis are a series of charge-tuneable InGaAs/GaAs samples grown using MBE. The SK growth mode allows the formation of InAs quantum dots as discussed in Section 2.1.1. All samples were grown at the National Epitaxy Facility in Sheffield by E. Clarke. In order to create charge tunable structures, an n-doped layer is grown and separated from the single InAs quantum dot layer by a GaAs tunnelling barrier of thickness t_{B}. The aim of this series of samples was to alter the thickness of the tunnelling barrier t_{B} in order to investigate the effect of QD coupling to the Fermi reservoir on the longevity of the spin states within the QD.

A total of four samples were grown with tunnelling barrier thickness's $t_{\mathrm{B}} = 37$, 42, 47, 52 nm. A full layer diagram of the charge-tuneable structures can be seen in Fig 3.1, which we shall now describe in detail. The tunnelling barrier separating the dot layer from the doped layer were grown in a two-step process, first a 15 nm layer of GaAs at 470 °C and then a $(t_{\mathrm{B}} - 15)$ nm layer at 580 °C. Starting with cold growth of the tunnelling barrier limits Si segregation and diffusion from the doped layer.

In addition to the layer required for charge controlled structures, an asymmetric DBR

cavity was grown. Fewer layers are used above the QD layer to enhance optical emission in the $+z$ axis for photoluminescent studies. The DBR is formed of alternating GaAs/AlAs layers, with 15 repeats below the dot layer and 2 repeats above. The cavity is centred at ~ 950 nm for cryogenic temperatures, enhancing the larger quantum dots emitting at a longer wavelength. Focusing on longer wavelength dots in the tail of the broad QD PL distribution allows for spectrally isolated quantum dots to be measured, limiting inter-QD interaction for experiments. The samples grown were also designed to have a low density of QDs to further limit inter-QD interaction, achieved through low InAs deposition rates during growth of the dot layer (Section 2.1.1).

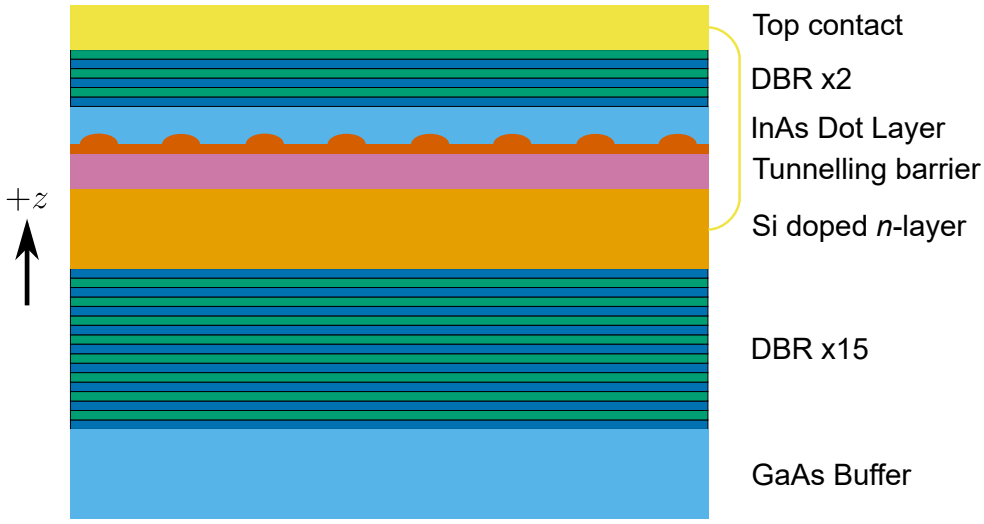

Figure 3.1: Layer diagram of the charge-tuneable InGaAs quantum dot structure with a DBR cavity centred at $\lambda = 950$ nm. Asymmetric DBR enhances optical emission in $+z$ direction. Bonded gold wiring connects the top and back contact to allow electric field $\boldsymbol{F}$ to be applied across the n-doped and QD layers for charge tuning. QD layer is separated from the Si doped n-layer by a tunnelling barrier of thickness t_{B}.

Charge control is achieved by fabricating a Schottky diode structure after MBE growth is completed. Fabrication of the diode structures on the samples used in this thesis was carried out by I. M. Griffiths. A gold back contact is deposited first, and can be seen in Fig 3.2 as a gold strip surrounding the dark area with 4 diodes. The sample is then annealed to allow

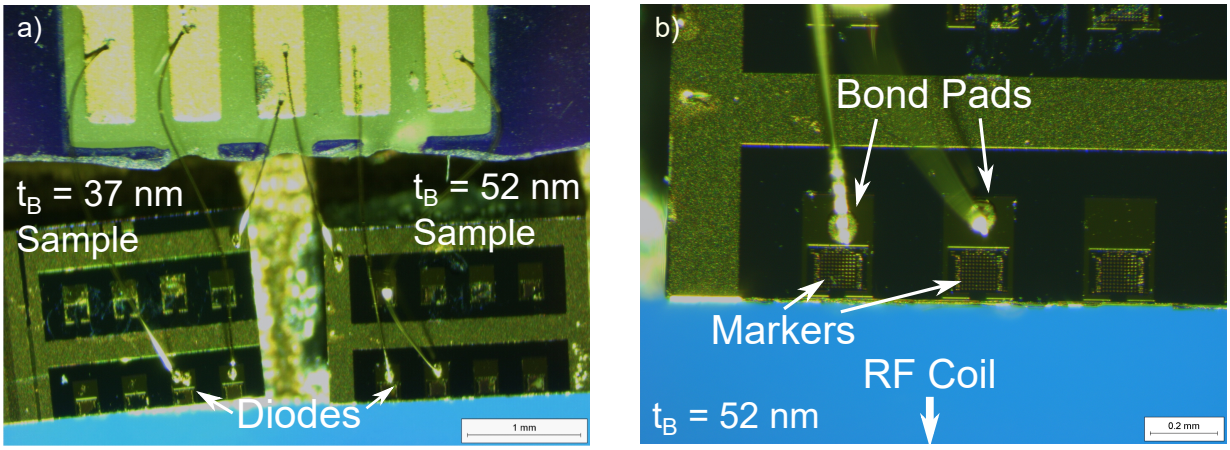

Figure 3.2: a) Microscope image of $t_B = 37$ and 52 nm processed samples. Rows of 4 diodes are cleaved near the edge of diode to allow close proximity of sample to RF coil. b) Closer zoom image of $t_B = 52$ nm sample. Bond pads have gold wire bonded to the surface allow application of bias. Below the bond pads is an unmasked region allowing optical access and to dots within the diode, with gold markers deposited on the unmasked region to use as positional reference when moving across the sample. An RF coil sits close to the sample below the view of the image, discussed further in Section 3.2.

gold diffusion down to the n-doped layer to create the back contact. A thin titanium (Ti) layer of thickness ≈ 5 nm is deposited in 4 locations as the base of the Schottky diode top contacts. Careful calibration of the Ti layer thickness is required as too much Ti severely limits optical transmission from the QDs, but a layer too thin does not allow for a high quality electrical contact. Gold bond pads and markers are then deposited on top of the Ti layer. A 10 x 10 square of markers with labels for each column and row allows more reliable location and relocation of desirable QDs for experimental study. Samples are cleaved close to the bottom of a row of diodes in order to maximise proximity to the RF coil. The sample is then mounted on to a copper block with indium epoxy. Ball bonding is used to bond a thin gold wire to the bond pad and connect the sample to a printed circuit board (PCB) (seen in top of Fig 3.2a), which can be connected to any desired circuit for external control of applied voltage to the diodes.

Photoluminescence spectra of the quantum dots present in both $t_B = 37$ and 52 nm samples were carried out for optical characterisation, as shown in Fig 3.3. PL was carried

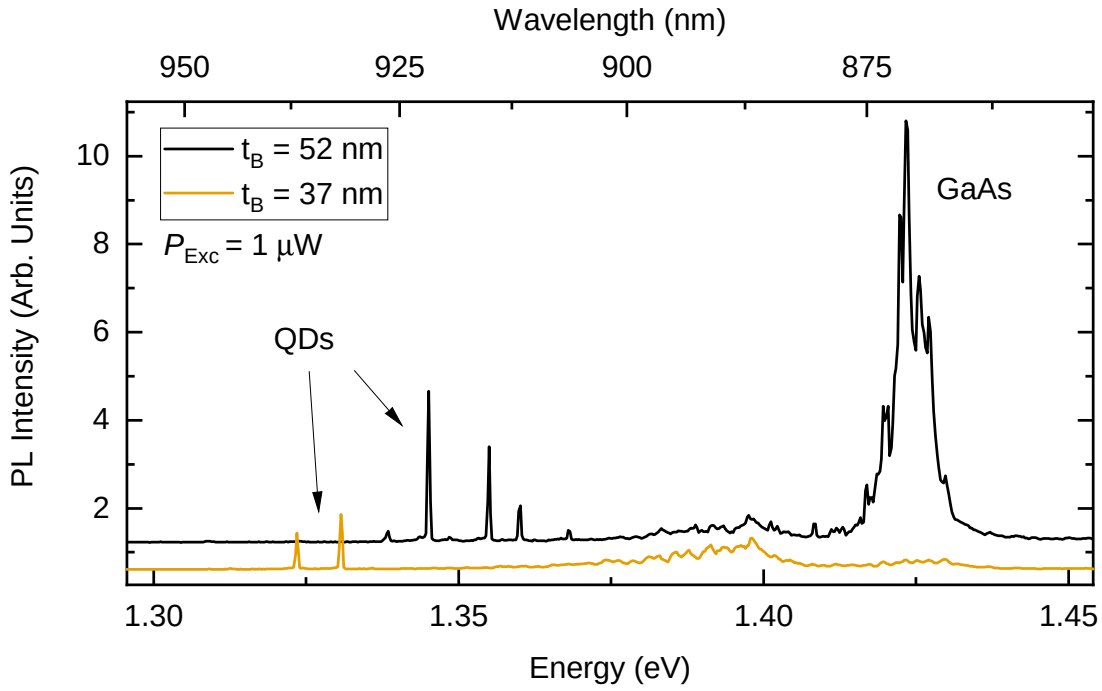

Figure 3.3: PL spectra at $T \approx 4.5$ K for the $t_{\mathrm{B}} = 52$ and 37 nm samples at an arbitrary position on each sample. Optical excitation was performed using a $\lambda = 850$ nm diode laser with an optical power of $P_{\mathrm{Exc}} = 1$ μW. A distribution of QDs are visible at 1.4 eV, but bright dots are found at longer wavelengths as emission is enhanced by DBR cavity.

out at ≈ 4.5 K in the bath cryostat described in Section 3.2, using optical excitation from an 850 nm diode laser with an excitation power of $P_{\mathrm{Exc}} = 1$ μW. Bulk GaAs can be observed at $\sim$ 870 nm, next to a broad spectrum of QD signals observed at 900 nm. The broad distribution of dots is optically active but not individually resolvable. The effect of the DBR cavity can be seen as longer wavelength dots are bright compared to the broad distribution, which is a direct consequence of the cavity being centred at 950 nm. The long tail of the QD distribution demonstrates the desired low density of long wavelength quantum dots was achieved.

3.2 Bath cryostat set-up

All experimental work in this thesis has been carried out at $T \approx 4.5$ K unless specified otherwise. To achieve stable cryogenic temperatures at all times for the quantum dot samples

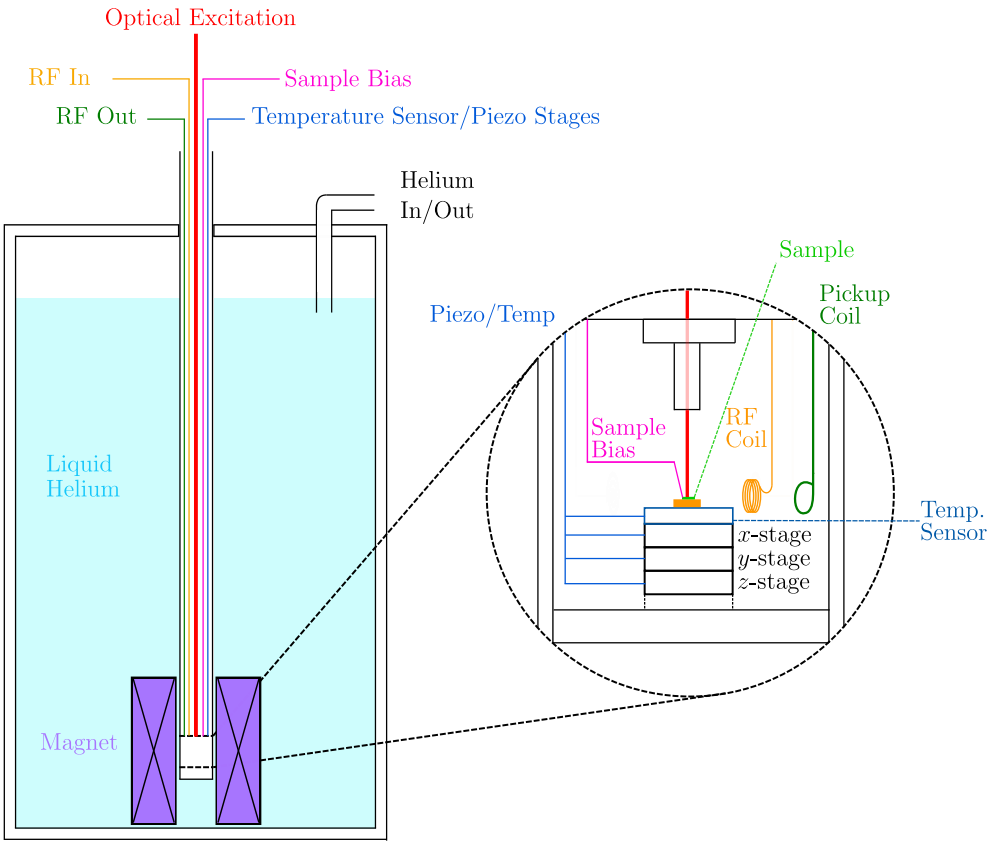

Figure 3.4: Schematic of Attocube bath cryostat set up. The cryostat is filled with liquid helium to keep samples at temperatures of $T \approx 4.5$ K. Optical excitation passes through a window into the sealed insert and through a lens to focus on the sample. RF pulses are transmitted and measured by copper coils connected to BNC cables at the top of the cryostat. 12-pin connectors allow control of the piezo stages and readout of the temperature sensor below the sample. A BNC connector at the top of the insert allows application of bias to the sample in order to provide charge control of diode samples.

studied, we use an Attocube bath cryostat set-up. Liquid helium is stored within the cryostat with a long metal insert submerged inside it. The quantum dot samples are stored inside the insert, which has a small amount of helium exchange gas added after vacuum pumping. A full schematic of the bath cryostat set-up is shown in Fig 3.4.

At the base of the cryostat there is a superconducting ring magnet surrounding the insert, allowing generation of static magnetic fields parallel to the insert axis. The magnet is controlled via a Mercury iPS control unit and allows largely homogeneous static magnetic fields of up to $B = 8$ T to be generated.

Within the metal insert, a cage system holds 3 nanopositioner stages to allow translation in x-, y- and z-directions, allowing accurate alignment of optical signal. A small window sits at the top of the insert to allow optical excitation to enter the insert and excite the sample. The optical excitation is focused by a lens near the sample and collimates any emission from the sample.

At the top of the insert, there are several BNC connections in addition to two 12-pin connectors. Two of the BNC connectors are for application and detection of radio-frequency (RF) pulses. A non-magnetic coaxial cable is routed from the "RF In" port at top of the insert (Fig 3.4) down to the sample, which allows attachment of a small copper coil used to generate oscillating magnetic fields for NMR experiments. The RF coil can be positioned an arbitrary distance from the sample in order to strengthen applied B_1 fields. Ideally, the sample needs to reside as close as possible to the coil for maximum B_1 for a given power (see Section 3.6.5 for more detail). Minimising proximity of the sample and coil needs to be balanced with ensuring there is no contact between the coil and sample due to the heating effects that arise from high power RF. Additionally, we require enough room for movement of the piezo stages, providing a usable area of the sample to allow search for QDs. On the opposite side of the RF coil there is a pickup coil that can detect emitted RF signal and transmits it back up the insert to the "RF Out" BNC connector. This can then be connected to a spectral analyzer to allow information about the applied fields to be monitored.

The remaining BNC connectors are connected to the diodes of charged-tuneable samples. Bias can be applied from a generator to allow arbitrary control of sample charge. This is critical when running measurements investigating charged quantum dots. Cables are connected to the sample by soldering wiring between the insert cabling and the PCB sample mount (Section 3.1.)

One of the 12-pin connectors links the Attocube ANC150 piezo control unit with the stages underneath the sample, allowing translation of the sample in the x-y plane. The movement of the sample in the x-y plane allows different parts of the sample to be excited

and therefore different quantum dots to be investigated. This is significantly easier than moving the optical beam. The ANC150 allows control of the step size and frequency of each piezo stage, providing the ability for broad movement around the sample and fine-tuning of single quantum dot excitation. An additional piezo stage allows movement of the sample in the z-plane, adjusting the distance between the sample and the lens focusing on the optical excitation. Most efficient optical excitation occurs when the beam focuses on the surface of the sample, which can be easily tuned with the z-direction piezo stage.

The other 12-pin connector links with a resistive temperature sensor underneath the sample in the cryostat, allowing a CryoCon 1200 cryogenic temperature monitor to provide readout of sample temperature. Application of high power optical or RF excitation can cause heating and as a result damage the diode structure or quantum dot and so monitoring temperature allows all experiments to be tuned to run at safe power levels without damage to the sample. In addition to the sensor, there is a heater placed underneath the sample allowing deliberate increase in sample temperature for temperature dependant investigations (see Chapter 4).

3.3 Optical spectroscopy

Optical excitation of quantum dot samples is the most common form of investigation into quantum dots. Microphotoluminesence (μ-PL) techniques are well reported in the literature as it provides insight into the states within the QD system, and is relatively simple to implement. Here we provide a full description of the optical set-up to accompany the schematic in Fig 3.5, allowing photoluminescence investigations of quantum dot samples within the bath cryostat.

Optical excitation is sent to the sample via a window in the top of the sample insert described in the previous section. For the InGaAs quantum dots studied within this thesis, optical excitation is generated by various lasers ranging from 600 - 950 nm in wavelength.

An optical breadboard resides on top of the insert with a central aperture allowing optical beams to be directed towards the sample through the insert window. The lens above the sample (Fig 3.4) is aspheric to allow focusing and collection of large aperture beams to areas of $\sim 1\ \mu m^2$, providing optical resolution which enables precise excitation of a single quantum dot. Optical emission from the QD is collimated by the same aspheric lens and transmitted back out of the insert window.

There are two primary configurations of the optical breadboard used in the work conducted throughout this thesis. The first is configured to allow transmission of pulses of both the high power pump laser and the below-saturation power probe, which allows us to pump and readout the state of nuclear spins within the quantum dot. Tuning of the laser powers allows either the pump or probe laser to be used for standard μ-PL or more complex pump-probe measurements. The second configuration is for resonance fluorescence investigations, where the excitation wavelength matches the signal wavelength, requiring polarisers and waveplates to create a cross-polarised signal arm to compensate for the large background. Both configurations are displayed in Fig 3.5.

3.3.1 Photoluminescence configuration

The majority of experiments within this thesis use an optical pump-probe scheme to study QDs. Optics involved in pump-probe measurements are displayed in Fig 3.5 in red, with each component labelled for ease of reference. In order to perform pump-probe measurement schemes, two arms of the set-up exist, the primary arm referred to as the "pump" arm, and the secondary "probe" arm. Two fibre couplers allow the two separate laser excitation sources to be input in to one of the two arms.

For pump-probe measurements, a high power pump laser and a low power probe laser are used. Both lasers are set up separately from the optical breadboard and coupled into a fibre leading to the pump (1) and probe (2) arm out couplers shown in Fig 3.5. For the work carried out in this thesis, a 850 nm Thorlabs diode laser (250 mW) was used for

optical pumping, and a 850 nm Roithner diode laser (30 mW) was used for optical probing, providing non-resonant excitation for efficient polarisation generation and optical emission. Laser excitation passes through half-wave plates (HWPs) (3) after the outcouplers to allow rotation of the laser polarisation for maximum laser power.

The pump arm excitation (1) enters a linear polariser (4) to ensure the excitation is polarised. A motorised HWP (5) follows the linear polariser providing control of polarisation during automated measurements. The beam is then routed through a 90:10 pellicle beamsplitter (6) and into the 50:50 broadband beamsplitter (BS) (8) situated above the input window of the sample insert. The 50:50 BS can also be replaced with a dichroic mirror that reflects wavelength excitation at $\sim$ 800 - 900 nm and transmits longer wavelength QD emission at $\sim$ 920 - 960 nm instead of splitting the beam in half, avoiding the 50% loss in signal present with the beamsplitter.

The probe arm (2) is routed into the 90:10 BS (6) to add the probe beam to the main optical pathway. The asymmetry in the BS allows high pump power to be transmitted while attenuating the probe beam. This is an acceptable attenuation as the probe pulse is only required to be low power ($P_{\text{Exc}} < 20$ μW) to acquire PL spectra of the QDs.

Once either beam has entered the 50:50 BS (8), the beams are directed down towards a quarter waveplate (QWP). Both beams pass through the QWP (9) which linearly polarises the probe beam and transforms the pump beam from linearly to circularly polarised light. The QWP is also motorised, allowing changing of circularly polarised basis for pump excitation to allow access to different spin states (see Section 2.1.2). After this, light is directed down to the sample (10) where it is is focused on to the sample by an aspheric lens and is either absorbed or reflected.

Returning light from the sample will pass through the 50:50 BS upwards towards a mirror which then couples the optical signal into a fibre to be sent to a detector (15). A second pellicle BS (11) on a flipper mount can be added/removed as needed before the fibre to divert some laser power towards a Thorlabs CCD detector (12). The camera can provide imaging

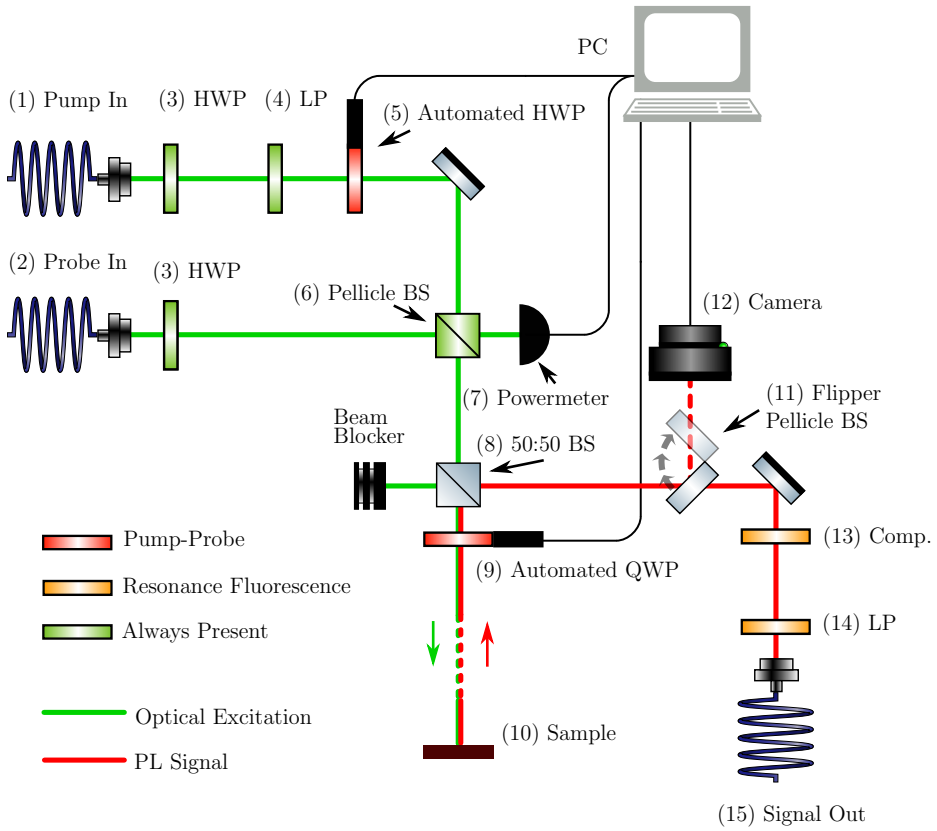

Figure 3.5: Schematic of the optical configuration above the cryostat to provide both pump-probe (red components) and resonance fluorescence (orange components). Pump/Probe signal enters the central 50:50 beamsplitter and is directed down towards the sample. For the nuclear Pump-Probe configuration, a combination of a half wave plate (HWP) (5) and a quarter wave plate (QWP) (6) allow control of pump laser circular polarisation ($\sigma^{\pm}$). Resonance fluorescence measurements rely on a linear polariser (13) and a variable waveplate (compensator) (14) to minimise reflected excitation laser through cross-polarisation (see Section 3.4). Optical excitation power of pump and probe is monitored using a powermeter (7) sampling the beam at the pellicle beamsplitter (6).

of the sample surface, aiding focusing of the lasers and identification of key features on the sample (e.g markers) during QD searches.

Optical excitation is coupled to the breadboard via optical fibre out couplers owing to a lack of space on the breadboard. Consequently, lasers are set up on a separate optical table which allows a variety of different laser types to be trivially coupled into the probe and pump arms and directed towards the set-up on top of the bath cryostat. A variety of static and tunable neutral density filters can be placed in the laser beam path for investigations into optical excitation power P_{Exc}. Both arms have shutters allowing fast modulation of laser

pulses with resolution of 1 ms and ensures essentially infinite on/off ratio. Shutters are the preferable method of optical modulation, as the alternative is switching the laser current on and off which results in reduced stability of the diodes.

Once signal has been emitted from the sample and coupled into the signal out fibre, the signal is outcoupled at a separate location where it is routed through a lens to focus the light onto a double grating spectrometer (U1000 Jobyn Yvon), which is then projected on to a CCD camera for measurement. The exposure time of the CCD can be arbitrarily set and the acquisition window triggered automatically. Short constant exposure times can be used for a live spectrum of the quantum dot sample allowing precise alignment of optical signal through changing the sample position. Long exposures can be used in conjunction with automated experiments and a shutter in front of the spectrometer to set one acquisition for several cycles of pump-probe measurements.

3.3.2 Resonance fluorescence configuration

In addition to high power optical pump-probe measurements, we also carry out resonance fluorescence (ResFl) studies through low power resonant excitation of QDs. ResFl measurements require a cross-polarised detection scheme in order to separate the spectrally similar laser reflection and optical ResFl signal. Implementation of a cross-polarisation scheme requires modification to the set-up described previously, using the second configuration of optics shown in yellow in Fig 3.5. The motorised waveplates (5, 9) used in pump-probe schemes are removed, leaving a half waveplate (3) and linear polariser (4) in the pump arm, to ensure excitation is a single polarisation. The excitation laser is a tunable single-mode diode laser with a spectral range of 920 - 960 nm, as precise matching of laser excitation to dot transition energy is required. The condition for resonance fluorescence is that the excitation linewidth should be much less than the optical transition rate ($\approx$ 2 GHz) of the InGaAs QDs, and therefore we use a laser with narrow optical linewidth (<100 MHz). Linear polarised resonant light is then sent down the bath cryostat to the sample where it is either absorbed

and re-emitted or scattered from the surface of the sample.

Both signal and scattered light is sent back up to the beamsplitter, where it is then passed through a compensator (13) which acts as a tunable waveplate. The compensator has two degrees of freedom; the compensator retardation and the orientation of the fast axis. Alteration of the fast axis orientation allows broad suppression for maximum signal to noise ratio of resonant signal. Signal and scatter then pass through a linear polariser (14), which allows further tuning of cross-polarisation through rotation of the polariser angle. Finally, the compensator retardation can be adjusted for fine tuning of laser suppression. Suppression is strong enough once ResFl signal is observable against the background of the scattered laser. Ratio of ResFl signal to laser background is easily measured by turning the relevant exciton transmission on and off with sample bias. The suppression of the described configuration provides an extinction ratio of laser scatter up to 10^8.

Signal from resonant excitation can be routed into the spectrometer, as seen for other experiments. However, signal from resonant excitation is relatively low, and as such we use an avalanche photo diode (APD) to provide single photon detection in addition to time-resolved detection. The APD will measure all incoming photons regardless of spectral properties, giving a measure of the total photons emitted in a certain time window. It is important to use differential measurements to remove any background from either scattered laser signal or background light.

The simplest method for a differential measurement would be to turn the laser on and off. This would provide a measurement of the background signal compared to the measured signal of the quantum dot. However, this would not account for the detected scattered laser. Changing the wavelength of the laser from resonant to off-resonant of the QD transition would remove the QD signal and somewhat account for laser scatter. This also has issues as the suppression of the scatter signal can be wavelength dependant. The most accurate method of measuring differential resonant measurements takes advantage of the charge controlled samples used in this thesis. The resonant laser can be kept at a specific wavelength while

the quantum dot charge state can be modulated to provide QD On/Off signal, accounting for all background and scattered laser signal and providing an accurate measurement of the QD system.

3.4 Resonance fluorescence

Resonant optical excitation measurements allow coherent excitation of the excitonic states within a quantum dot, and are a key step in controlling carrier charges within the QD. Subsequent readout of the states can be achieved through the measurement of resonance fluorescence signal. As introduced previously in Section 2.4.2, the identical energies of excitation and emission adds the challenge of seperating the fluorescence from the reflected laser. Some success has been found with collecting signal in an orthogonal orientation to the excitation [148]. However, due to the spatial limitations within the bath cryostat system, it is considerably easier to implement a cross-polarisation set-up [78]. As discussed in the previous section, we filter out the reflected excitation with polarisation orthogonal to the ResFl signal, leaving only the signal to pass through the detectors.

3.4.1 Resonance fluorescence excitation spectroscopy

In order to characterise the QD transitions under resonant excitation, we need to first find the transition energy of a desired exciton state. The experiments within this thesis are generally focused on the single electron regime, and as such we will focus discussion on the negatively charged trion state in this section.

The basic premise of measuring the resonant frequency f_{Res} of the trion involves taking exposures with an APD at different frequencies of excitation f_{Exc}. By scanning the laser frequency over the frequency of the trion transition estimated from PL, an excitation spectrum can be measured based on the number of counts measured for each laser excitation frequency f_{Exc}.

Despite the cross-polarisation set-up used to remove scatted laser excitation, there will still be a non-negligible quantity of scattered laser detected by the APD, which changes as the excitation frequency f_{Exc} is altered. This can be accounted for by carrying out a differential ResFl measurement. The measurement is made differential through switching the QD trion transition "On" and "Off" by modulating sample bias between V_{1e} and V_{0e}. In the "Off" state, we directly measure the laser scatter signal I_{Off} at a given f_{Exc}, while the "On" state measures both ResFl signal from the QD and laser scatter I_{On}. ResFl signal is calculated by taking the difference between I_{On} and I_{Off}, removing the scattered laser at the current f_{Res} and giving an direct measurement of ResFl signal $I_{\mathrm{ResFl}} = (I_{\mathrm{On}} - I_{\mathrm{Off}})$.

The resonant laser frequency is finely tuned via a piezo and allows automated tuning through a range of approximately 20 GHz. Coarse tuning through a micrometer screw is possible but does not reliably produce stable laser modes, and as such can not reliably be tuned through the narrow resonance of the QD ($\sim$ 2 GHz). As a consequence, we find a stable laser mode as close to the QD resonance as possible and then use fine piezo tuning to run the measurements. Due to the hysteresis present in tuning the piezo controls, the same voltage will not always correspond to the same laser frequency. To ensure reliable recording of counts for a given laser frequency f_{Exc}, we pass the resonant laser through a 90:10 beamsplitter and couple the low power arm into a wavelength meter. The high power arm continues to a single-mode fibre connected to the pump arm of the optical breadboard seen in Fig 3.5. Laser frequency is measured synchronously with the APD acquisition to give the most accurate spectrum, an example of which is shown in Fig 3.6.

Continuous wave resonance fluorescence measurements are the simplest to run, where resonant light excites the sample for a fixed exposure time-window, allowing collection of RF signal. There are no shutters required and acquisition time can be arbitrarily set for the APD. However, continuous resonant excitation of the quantum dot can induce dynamic nuclear polarisation build up in the nuclear spin bath through transfer of angular momentum of light to the nuclei (See Section 3.5). Presence of DNP will alter the transition energy of the

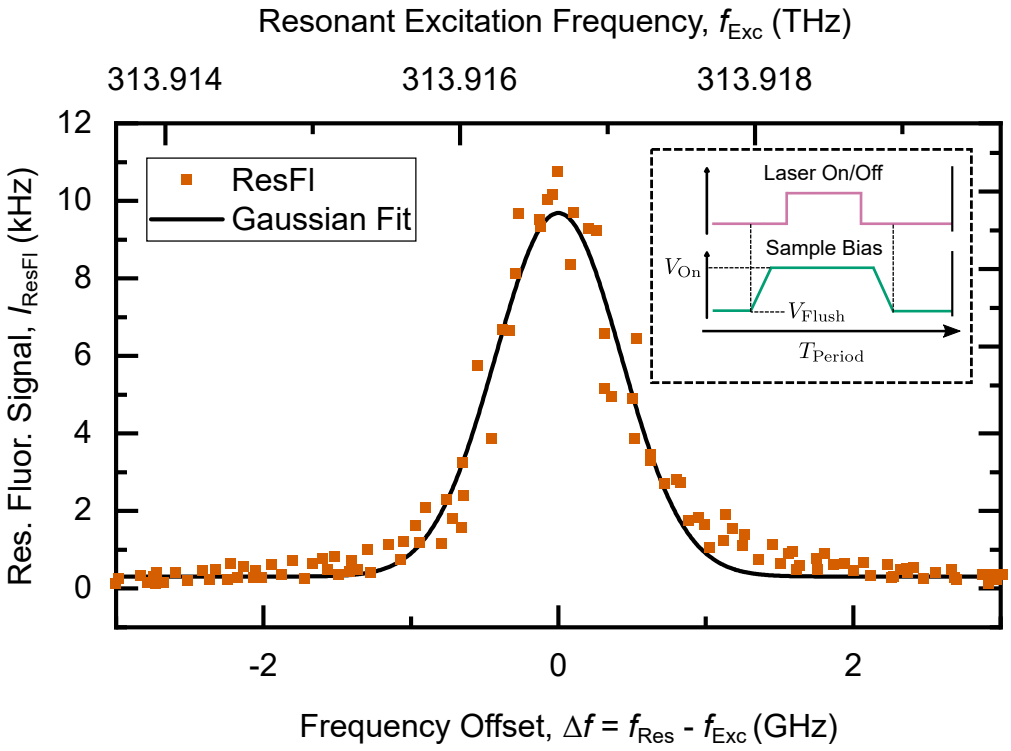

Figure 3.6: An example of typical resonance fluorescence excitation spectroscopy. A tuneable laser steps the excitation frequency f_{Exc} across one of the states in an X^- Zeeman doublet, emitting ResFl photons at the frequency of the transition f_{Res}. A pulsed excitation scheme is used to prevent DNP build up, as demonstrated in the inset. Short laser pulses limit spin transfer to the nuclei, and each pulse is followed by a flush of DNP by setting the bias to a resonant tunnelling bias V_{Flush} where fast electron tunnelling depolarises the nuclear spin bath. Additional accuracy is achieved by using a differential measurement that measures emission from the transmission with the dot turned "On" and "Off". Measurement of the "Off" signal for a given laser frequency accounts for any variation in laser power or suppression strength of reflected laser.

trion, changing the required excitation frequency. The dynamics of this effect are described by a dragging effect [149, 150], and effectively broadens the measured resonance fluorescence spectrum.

To counteract this effect, we use pulsed resonance fluorescence measurements where the quantum dot is exposed to laser light for a short period of time at the desired bias, followed by a period of bias in a region of fast electron tunnelling. Switching the quantum dot to the flush bias V_{Flush} allows fast transfer of spin from the nuclear spin bath to the Fermi reservoir via

the tunnelling electron, effectively resetting DNP and therefore the QD resonance frequency. Combination of short optical pulses ($T_{\mathrm{Opt}} \approx 1$ - 10μs) and flushing the QD ($T_{\mathrm{Flush}} \approx 50$ μs) after each cycle results in reliable excitation of the QD resonance. An example of a resonance fluorescence spectra is shown in Fig 3.6.

3.4.2 Time-resolved resonance fluorescence

We have previously introduced the use of resonant excitation as a means to prepare and readout the spin state of an electron residing within a quantum dot (see Section 2.4.1). To quickly summarise electron spin state preparation, we reintroduce the system of a negatively charged quantum dot placed in an external magnetic field, where we have two energetically distinct optical transitions for the spin-up and spin-down states. Resonant excitation of the spin-down state $|\downarrow\rangle$ creates a trion that can either recombine to the spin down state $|\downarrow\rangle$, or relax to the opposing spin up state $|\uparrow\rangle$ through a weakly coupled relaxation enabled via admixture of spin states caused by the spin-orbit interaction. Relaxation results in a shelved electron spin that on short time scales is stable.

To observe the dynamics of the spin state preparation we can use time-resolved resonance fluorescence (TRRF). Photon signals are time binned and stored while the system undergoes many cycles of resonant optical excitation. By monitoring the detected signal during an optical pulse, we will initially see a strong resonance fluorescence signal as the transition matching the laser frequency emits photons at the same frequency as resonant excitation. ResFl signal will drop as the electron is shelved to the opposing spin state through a weakly coupled transition, effectively blocking further resonant excitations. Individual decays of electron spin state will be abrupt, which when averaged over many repeats gives an exponential decay in signal (Fig 3.7) that can be used to estimate the typical time for the spin to be shelved, referred to as the spin build-up time. Typical values for spin build-up time are ~ 0.5 - 1 μs. A resonant optical pulse longer than the spin build-up time can act as the initialisation stage of any measurement involving the electron spin directly, such as electron

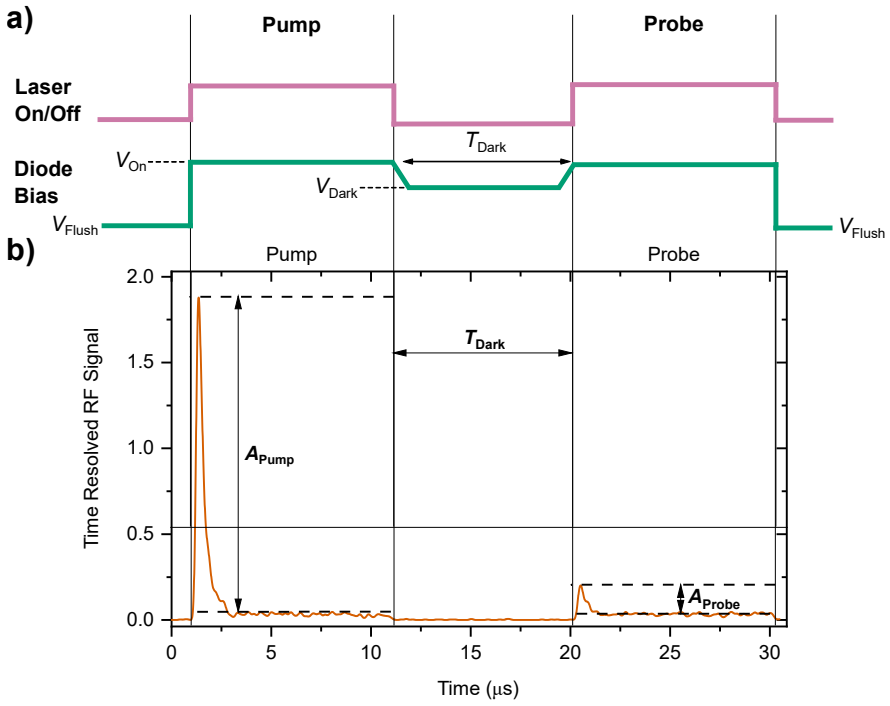

Figure 3.7: Illustration of time-resolved resonance fluorescence measurement scheme. a) The timing diagram demonstrates how the laser pulses are synchronised with activation of the single charged dot at V_{On} to allow optical access to the trion transitions. In between the pump and probe pulses the dot is left in the dark for some time under arbitrary charging conditions V_{Dark} to allow the electron spin state to evolve or undergo coherent control. After each cycle, the dot is flushed at V_{Flush}, where fast electron tunnelling occurs removing any DNP build up. b) Time trace of ResFl signal, acquisition of photo counts at the APD are time binned to give full dynamics of the QD spin state. Optical signal indicates the electron resides in the spin state resonant with excitation. Reduction in amplitude represents the shelving of the electron in the opposing spin state. Polarisation of the electron spin after the probe pulse can be calculated through the difference in pump and probe signals $\langle S_z \rangle / S_0 = (A_{Pump} - A_{Probe})/A_{Pump}$.

spin resonance or measurement of electron lifetimes.

For the time resolved measurements, we run a pump-probe scheme to initialise (pump) and readout (probe) the electron spin state. After initialising (shelving) the spin into a known state, the readout pulse provides a direct measurement of the electron spin state after a certain period of time T_{Dark}. If a peak in the time binned signal is observed, the electron has returned either through coherent control or has decayed back to the pre-initialisation state, and thus can be excited by resonant excitation. If there is no optical signal, the

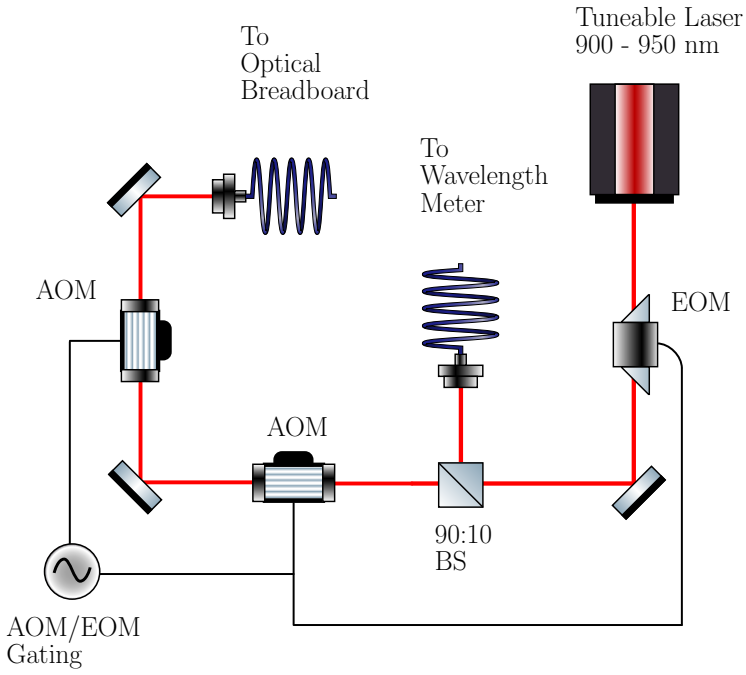

Figure 3.8: A simplified schematic of the pulsed resonant laser set-up. A tuneable laser is passed through an electro-optical modulator (EOM) and two acousto-optical modulators (AOMs) to provide high On/Off ratio for transmittion of photons to the sample. Gating of the EOM/AOMs is controlled by a signal generator and synchronised with the rest of the set-up as shown in the timing diagrams for Fig 3.6 and Fig 3.7. A 90:10 beamsplitter provides enough light for the laser wavelength to be recorded throughout the measurement and allows monitoring of shifts in wavelength due to ambient temperature or optical misalignment.

electron has remained shelved. An illustration of this can be seen in the TRRF traces seen in Fig 3.7. By measuring repeats of the pump-probe cycle, we can approximate the average electron spin projection $\langle S_z \rangle$ at the probe pulse. An unpolarised electron $\langle S_z \rangle = 0$ signal is demonstrated in the pump pulse with amplitude A_{Pump}. By calculating the difference in amplitudes of TRRF peaks in the pump and probe, we obtain the average spin projection $\langle S_z \rangle / S_0 = (A_{Pump} - A_{Probe})/A_{Pump}$, where S_0 is the initial state of the electron spin. This enables measurement of the electron spin after any desired manipulation steps have been performed.

Time binning of ResFl requires many repeats of the sample cycle to collect enough signal. Resonant optical pulses are generally 1 - 10 μs long, allowing the full pulse to be acquired within a single trace on the oscilloscope. Once spacing between the pump and probe pulse

becomes large, both pulses cannot be acquired at the same time, and so pump and probe pulses are acquired in separate trace acquisitions with different trigger times to account for the temporal offset, illustrated in Fig 3.7.

Control over the bias of the quantum dot is critical to effective repeat measurements of the electron spin. Pump and probe pulses are set to the same bias corresponding to the centre of the single-electron charging plateau, resulting in a charged quantum dot and allowing trion creation. Between the pump and probe pulses, a dark bias can be set to investigate changes in electron dynamics with different biases V_{Dark}, as demonstrated in Fig 3.7 (also see Chapter 4). After a pump-probe cycle, a flush bias is applied for $\sim$ 500 - 1000 μs, and set to a bias level corresponding to fast electron tunnelling between the $0e$ and $1e$ state, efficiently removing DNP as we also do for pulsed resonance fluorescence measurements.

The short optical pulse requirements of the time-resolved measurements require high-quality modulation of the input laser signal. Mechanical shutters can only modulate light on a time scale of $\sim$ 1 ms, which is far too long for the required optical pulses of $\sim$ 5 μs. We use a series of acousto-optical modulators (AOMs) and electro-optical modulators (EOMs) that allow fast modulation of the optical excitation as seen in Fig 3.8. All the modulators can provide optical pulses down to $\sim$ 500 ns, and are all controlled by a single trigger from a generator, allowing a short arbitrary length optical pulse to pass through to the sample. One disadvantage of the modulators is they do not perfectly prevent light transmission, with each AOM providing an optical power On/Off ratio of $\sim$ 1100, and the EOM providing $\sim$ 180. To completely remove any stray resonant photons being emitted during the dark parts of the measurement, we combined two AOMs and a single EOM to provide an overall On/Off Ratio of $\sim 2.25 \times 10^8$. As a result, long delays between pump and probe can be used with minimal parasitic optical excitation during dark time-windows. This becomes critical when performing experiments with long delays between the probe and pump pulse such as in Chapter 4.

3.5 Optimizing dynamic nuclear polarisation

Measurements of the nuclear spin bath are carried out through the study of the change in Zeeman splitting of an exciton to determine the effective magnetic field generated by the polarised nuclei. Introduced in Chapter 2, the effective magnetic field causes a shift in the Zeeman splitting referred to as the Overhauser shift, and is a direct measure of the net magnetization of the nuclear spins. An example of the effect of the Overhauser shift on a Zeeman split doublet is shown in Fig 3.9. Circularly polarised light direction $\sigma^{\pm}$ determines whether the Overhauser shift increases or decrease the Zeeman splitting $\Delta E_{\text{Zeeman}} \pm \Delta E_{\text{OHS}}$.

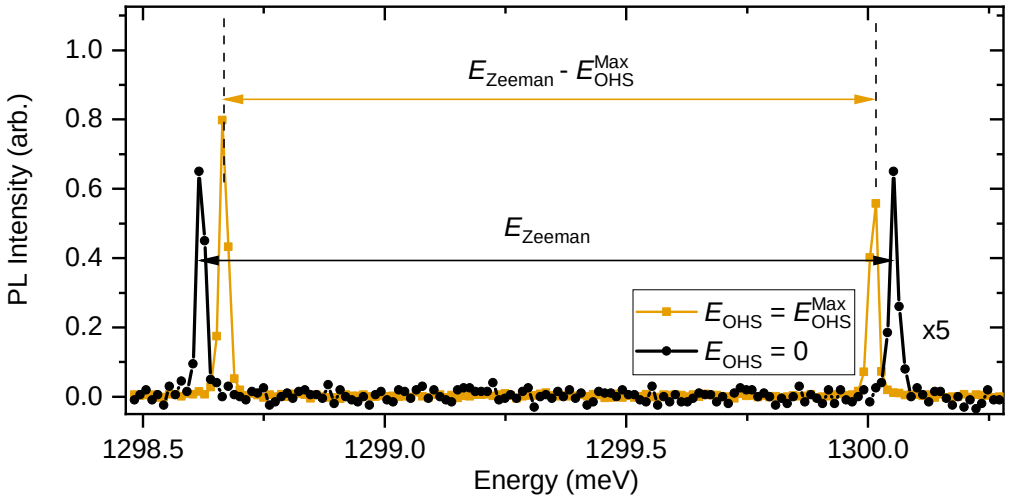

Figure 3.9: PL spectra of QD Zeeman doublet in the absence (circles) and presence (squares) of an Overhauser field. The Zeeman doublet is split by a static magnetic field B_z giving a splitting of E_{Zeeman}. Changes in Zeeman splitting due to the Overhauser field is referred to as Overhauser shift (OHS) ΔE_{OHS}. Measurement of Overhauser shift ΔE_{OHS} provides an insight to the overall polarisation of the nuclear spin bath and forms the basis for all measurements on the nuclear spin states within this thesis. PL Intensity for $E_{\text{OHS}} = 0$ is multiplied by 5 for convenient comparison.

To measure the dynamics of the nuclear spins, it is first important to generate large levels of nuclear polarisation. High power off-resonant optical excitation transfers momentum from the photons in the circularly polarised light to electron spins, which in turn is transferred to the nuclear spin bath via the hyperfine interaction. The polarisation generated during this excitation is known as dynamic nuclear polarisation (DNP), and represents the number of

nuclei polarised in the same direction. The highest values of DNP have been measured up to ~ 80 % [131]. It is critical to maximise generation of DNP possible in order to provide a larger observable change in Zeeman splitting and allow observation of smaller changes to the spin bath polarisation.

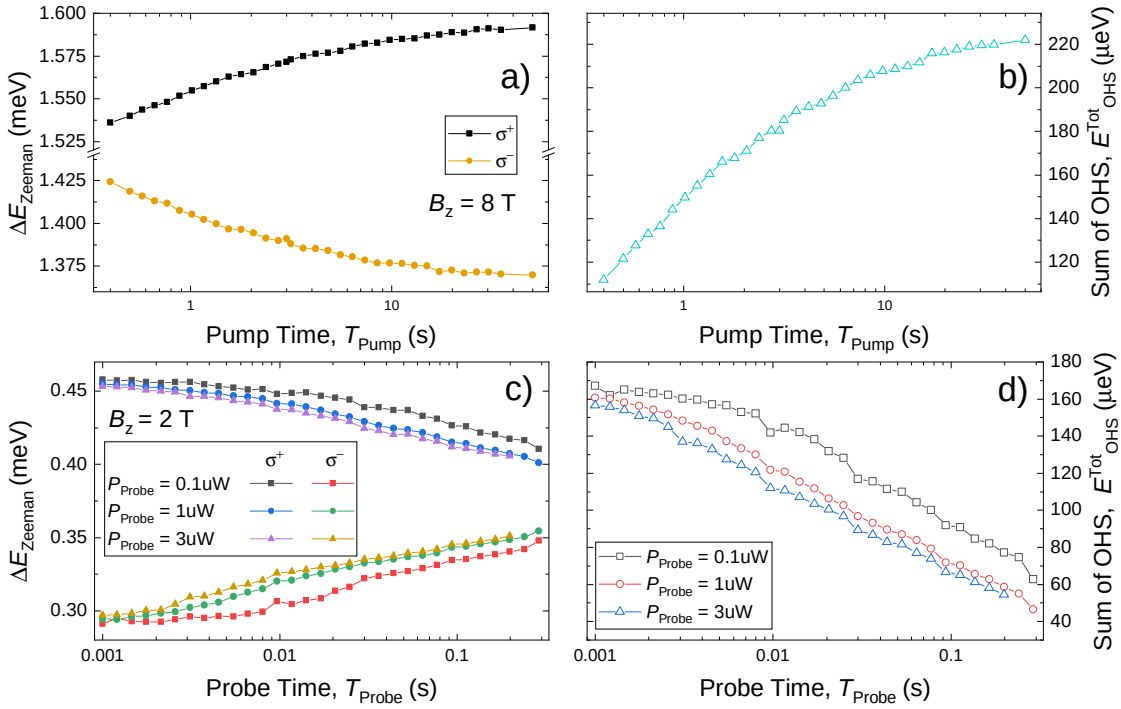

Figure 3.10: Pump and Probe Rise time calibration for opposing circular polarisations $\sigma^{\pm}$ of optical excitation for optimal DNP generation. Calibrations were carried out at a magnetic field B_z as indicated in each figure. a) Measurement of variation in splitting of Zeeman doublet energies due to changing Overhauser shift ΔE_{OHS} for pump-probe cycle with varying pump times T_{Pump} at $P_{\mathrm{Pump}} = 8$ mW. A clear increase in Zeeman splitting for increased T_{Pump} is observed. c) Same as a) for T_{Probe}, showing a decrease in DNP as nuclei are depolarised for longer probe pulses and high optical power. b, d) Differential version of a, c showing the sum of Overhauser shifts $E^{\mathrm{Tot}}_{\mathrm{OHS}} = \Delta E^{\sigma+}_{\mathrm{OHS}} - \Delta E^{\sigma-}_{\mathrm{OHS}}$ further demonstrating the trends observed in a and c. Symmetry of the $\sigma^{\pm}$ datasets allows $E^{\mathrm{Tot}}_{\mathrm{OHS}}$ to be used as a metric for efficiency DNP generation, but could be meaningless in asymmetric data.

We use a well-known pump-probe measurement scheme to measure DNP [128, 139]. A long high power pump laser polarises the nuclear spin bath, then after some time, a probe pulse arrives to allow measurement of a PL spectrum. The Zeeman splitting of the quantum dot can then be analysed to provide a value for DNP for the current measurement.

Careful calibration of the parameters is required for efficient generation of DNP and measurement of the Zeeman doublet in PL, which is signalled by the largest change in Zeeman splitting ΔE_{Zeeman} and strongest optical signal. Firstly, it is important to calibrate the length of time of both the pump, T_{Pump}, and probe, T_{Probe}. Signal generators control the length of time for which the pump and probe shutters are open. A series of measurements on the quantum dot with varying T_{Pump} allows selection of a pump time that provides maximum DNP while keeping experimental runtime relatively short. An example of pump time calibration is shown in Fig 3.10a and b, in which we choose $T_{\text{Pump}} = 8$ s.

Calibrating probe time has the inverse timing requirements to the pump pulse, valuing short pulses as optical excitation will quickly destroy built up DNP. It is important to balance the destruction of DNP against receiving enough optical signal for accurate measurements. A plot showing the results of a T_{Probe} calibration is shown in Fig 3.10c. Probe times are usually $T_{\text{Probe}} = 5$ - 40ms. A single spectral acquisition requires several cycles of pump-probe to give a good amount of signal. Shorter probe pulses requires a higher number of pump-probe cycles increasing experimental runtime.

In addition to investigating pulse lengths, we also need to optimise optical excitation power P_{Exc}. Probe power requirements are sensitive as high probe power will be above QD saturation and limit signal. We measure DNP vs T_{Probe} for different powers P_{Probe} in Fig 3.10c, and it is clear from this figure that more photons per unit time results in higher DNP loss. However, taking a ratio of measured DNP against the magnitude of the optical signal provides insight into the most efficient power for high signal and low DNP disruption. We find in the samples studied that a probe pulse of $T_{\text{Probe}} \sim 5$ - 30 ms with power near optical saturation of the QD, $P_{\text{Probe}} \sim 13$ μW, gives the highest signal with minimal disruption to DNP.

For charge-tuneable structures we also require calibrations that can be used to optimize DNP generation in bias dependant measurements. The pump-probe measurement scheme can be aligned with a cycle of diode bias states to optimize the necessary charging mechanisms within the QD. By changing the bias during the pump or probe, we can measure the change

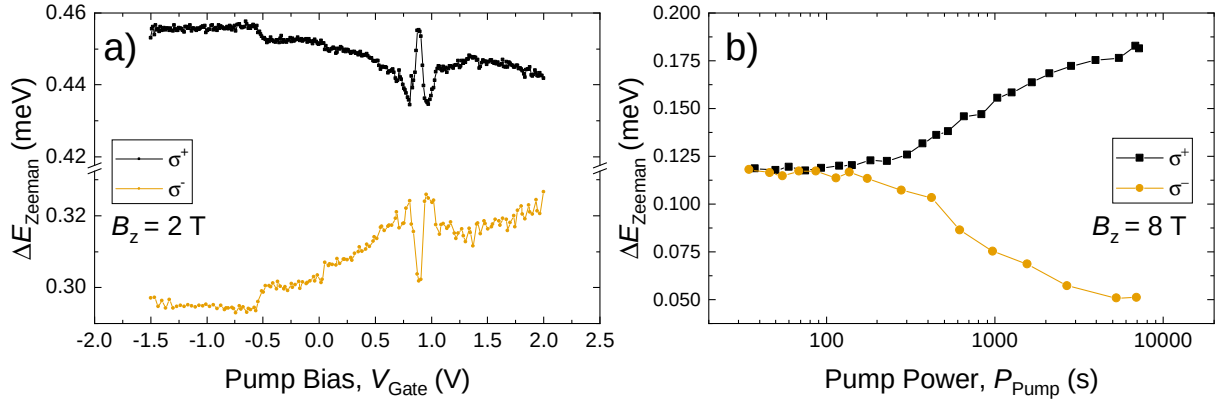

Figure 3.11: Optimisation of pump pulse parameters for optimal DNP generation. Calibrations were carried out at a magnetic field B_z as indicated in each figure. a) Change in Zeeman doublet splitting ΔE_{Zeeman} due to varying E_{OHS} as the sample bias during the pump pulse V_{Pump} is changed, with optimal DNP at $V_{\text{Pump}} = -0.6$ V b) Optical pump pulse power P_{Pump} dependence of Zeeman splitting ΔE_{Zeeman}, where a larger shift in splitting demonstrates efficient DNP generation at high power $P_{\text{Pump}} > 5$ mW.

in DNP to determine the most effective biases for each pulse.

Pump pulse biases V_{Pump} are calibrated for maximum DNP, with the results demonstrating strongest DNP at V_{Pump} above single electron QD charging plateau $V_{\text{Pump}} > +1.0$ V, or far below, $V_{\text{Pump}} < 0$ V, an example of which can be seen in Fig 3.11a. The change of bias alters the charging environment allowing faster/slower transfer of spin via optical pulses depending on the charges available.

Probe pulse bias V_{Probe} calibrations are primarily to ensure the maximum optical signal of the desired exciton. In most scenarios we use the PL of the charged exciton to monitor the state of the nuclear spin bath, where the optimal probe bias varies through the range $0.2 < V_{\text{Probe}} < 0.8$ V.

Finally, we must calibrate the optical powers of the optical excitation. Pump laser power, P_{Pump}, is calibrated for maximum DNP generation for which an example calibration is shown in Fig 3.11b. Similar results were found for all of the samples studied in this thesis. A high power laser provides strong DNP with no evidence of saturation, and so we use the maximum

power possible of $P_{\text{Pump}} \approx 8$ - 12 mW. Probe pulse power, P_{Probe}, is set for maximum optical signal, which is usually comparable to optical saturation of the QDs resulting in $P_{\text{Probe}} \approx 1$ - 10 μW

A combination of all the above calibration results allows an optimal pump-probe cycle to be generated, in which maximum DNP is generated and the fastest readout can be achieved. This provides a platform to reliably prepare the nuclear spin bath, perform studies upon the bath and then read out the nuclear state, forming the basis of all nuclear spin work in this thesis.

3.6 Nuclear magnetic resonance

Control over the nuclear spin bath within a quantum dot is possible through the use of nuclear magnetic resonance. Radio frequency (RF) pulses applied to QDs within a static magnetic field can induce rotations and allow control of the spin states. A detailed description of the theory behind NMR was discussed in Section 2.4.2. We can now lay out the experimental implementation of this technique.

3.6.1 Optically detected NMR

NMR experiments on quantum dot systems can be carried out by using optical signals to provide a measure of the effect of NMR on the nuclear spins within the system, a technique which is known as optically detected NMR (ODNMR). In Section 3.5 we briefly covered the techniques used for pump-probe measurements of the nuclear spin bath via high power optical pumping and fast optical probing of the system. Modifications to the pump-probe scheme can be used to study the effects of NMR by introducing NMR pulses between the pump and probe pulse.

To quickly recap, a high power circularly polarised ($\sigma^{\pm}$) optical excitation is applied to the quantum dot to generate dynamic nuclear polarisation. Angular momentum is transferred

from the light to the nuclear spins via electro-nuclear hyperfine interaction, creating DNP. The DNP builds up parallel (anti-parallel) to the static magnetic field for σ^- (σ^+) polarised light, increasing (decreasing) the Zeeman splitting by the strength of the Overhauser field E_{OHS} [131, 151]. Optimal generation of DNP is carried out by altering a variety of experimental parameters discussed in Section 3.5.

The application of radio frequency pulses can now be applied in order to coherently rotate or depolarise spins within the nuclear bath. The NMR resonant frequency is determined by the Zeeman splitting of the nuclear spin states, which varies depending on the nuclear isotope and magnetic field. Within the InGaAs system, inhomogeneous strain results in a strong broadening of satellite transitions. As a consequence, NMR experiments are usually only carried out on the central transition $-\frac{1}{2} \leftrightarrow \frac{1}{2}$.

Once the desired manipulation of nuclear spin states has been applied, the resulting state of the nuclear spin bath can be optically probed. A short linearly polarised optical pulse produces PL of the QD, where the splitting of the Zeeman doublet can be measured to observe the shift in Overhauser field ΔE_{OHS}. Additional accuracy can be introduced through the use of a differential measurement, by which two separate spectra are measured with RF On/RF Off. The difference between the two Zeeman splitting provides a direct measurement of NMR signal within the quantum dot system and is used in the majority of experiments within this thesis.

3.6.2 Inverse NMR

The population of the spin states within the nuclei is an important consideration when measuring NMR. Our previous discussion of optical spin pumping of the nuclear spin bath described the polarising of the nuclear spins with $\sigma^\pm$ polarised light, aligning nuclei parallel or anti-parallel to the static magnetic field. As all nuclei within InGaAs QDs have $I > 3/2$, there are multiple spin transitions and states to occupy. Pumping of the nuclear spins with σ^+ (σ^-) excitation shifts the overall spin bath population towards $I_z = -3/2$ ($I_z = +3/2$)

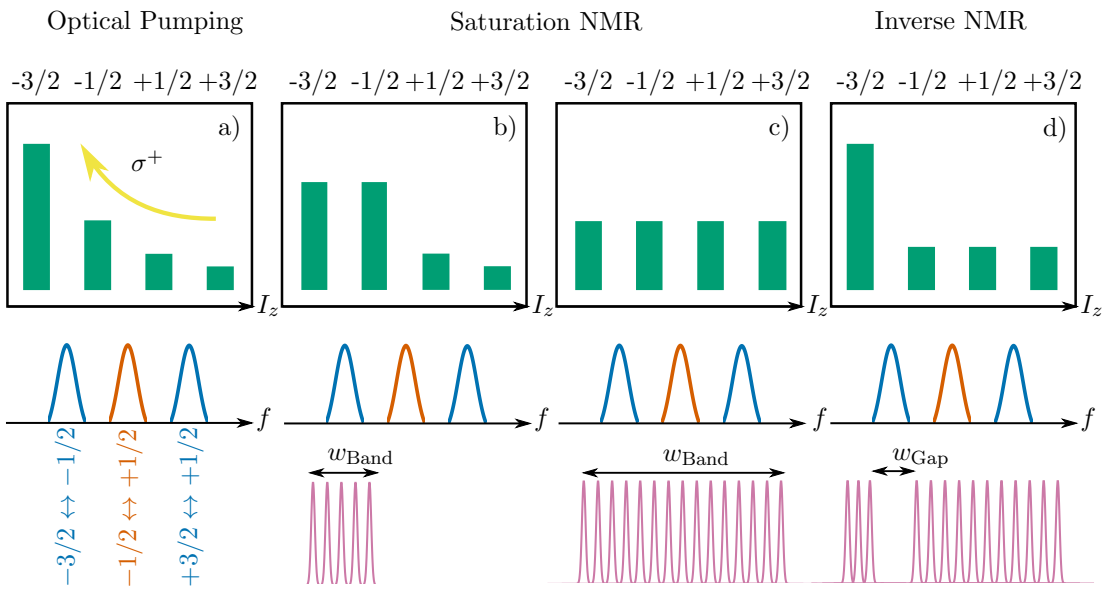

Figure 3.12: Illustration of the change in nuclear spin populations for a I = 3/2 spin in an InGaAs QD subject to an electric field gradient that lifts the degeneracy of dipolar transitions (see Section 2.3.2) a) Optical spin pumping with circularly polarised light σ^+ (σ^-) shifts the nuclei spin population towards the $-3/2$ ($+3/2$) spin state, leaving Boltzmann distribution of populations across the spin basis. Transitions between spin states are shown in red and blue. b) Saturation NMR applies a band of frequencies, w_{Band}, to full cover a specific transition, depolarising the spins and therefore equalising the populations of the relevant states. c) Demonstration of complete spin depolarisation through application of wide band RF frequency excitation, equalising populations across all states. d) Inverse NMR applies two wide bands of frequencies, w_{Band}, with a gap in between, w_{Gap}, in order to fully depolarise all nuclei except those with frequencies within the gap. This leaves the populations of the relevant transitions unchanged, while depolarising the rest of the transitions, resulting in a large reduction in ΔE_{OHS} and thus large ODNMR signal.

[131, 151], creating a Boltzmann distribution across all spin states, as shown in Fig 3.12a.

Probing of nuclear resonances can be achieved simply by measuring the ODNMR signal for a range of different continuous wave (CW) radio frequency excitations f_{RF}, providing an NMR spectrum of one of the isotopes within the QD. Application of a continuous transverse magnetic field with a band of frequencies of width w_{Band} centred at an arbitrary frequency f_{RF} will selectively depolarise nuclei with Larmor frequencies within the frequency range. Depolarisation of nuclei reduces the magnitude of the Overhauser shift ΔE_{OHS} compared to the fully polarised spin bath. It is this reduction that quantifies the ODNMR signal. The

nuclear spin state populations of the transitions excited (e.g CT $-1/2 \leftrightarrow +1/2$) will equalise through selective depolarisation as shown in Fig 3.12b. Full depolarisation of the nuclear spin bath can be achieved through applying CW RF with a bandwidth much greater than the frequency width of all nuclei spin states, driving all transitions and returning the system to thermal equilibrium, illustrated in Fig 3.12c.

In order to improve the ODNMR signal amplitude of the measurement, we use a technique known as Inverse NMR. Two broad RF bands of width, w_{Band}, are created with a small gap in between of width w_{Gap}. Both bands are shifted relative to the central frequency in the gap, f_{RF}, depolarising all nuclei within the quantum dot except those whose Larmor frequencies lie within the gap. The result is the equalisation of all spin populations for transitions outside of the gap, while preserving the populations of states in the transition lying within the gap. Consequently, the difference in populations is larger, resulting in a greater ODNMR signal. An illustration of the Inverse NMR technique is shown in Fig 3.12d. Selective depolarisation of all populations except the targeted transition gives a greater signal differential for more accurate measurements. The effect of broad and low power frequency bands provides additional utility in InGaAs dots as the strongly broadened satellite transitions require wide bands of RF to fully depolarise, which with conventional NMR would require RF pulses with $\sim$MHz bandwidths. In order to fully depolarise the broad nuclear frequency spectrum, the RF bands are set to widths of 12 MHz each. Alteration of the gap width w_{Gap} can change the balance of the measurement between the ODNMR signal amplitude and resolution, allowing detailed measurement of the narrow CT ($\sim$ 2 - 100 kHz).

3.6.3 Pulsed NMR

Continuous wave NMR provides useful insight into the resonance frequencies of the quantum dot, but does not allow coherent rotations of nuclear spins. To achieve coherent control of nuclear spins, we use short pulse bursts of single-frequency high power RF to induce rotations around a chosen equatorial axis on the Bloch sphere. Due to the broad STs in InGaAs dots,

all pulsed NMR experiments are performed on the narrow CT transition f_{CT}. As discussed in Section 3.6, the angle of rotation of the spin projection in the Bloch sphere is controlled by the length of the RF pulses, with $\pi/2$- and π-pulses corresponding to the times for rotation to the equatorial plane or opposing spin state respectively. A combination of different pulses can form complex spin-echo sequences used to dynamically decouple the system from decoherence effects thus lengthening T_2 times [114, 147]. A more detailed discussion of spin-echo schemes is carried out in Chapter 5.

Pulsed NMR sequences are created using an arbitrary waveform generator, allowing us to create sequences of RF pulse bursts with given burst lengths and amplitudes. Bursts are a carrier sine signal of frequency f_{RF} which is amplitude modulated by a pulse. Pulse burst length controls the angle of rotation in the Bloch sphere θ with respect to the $+z$ axis, while the phase of the carrier sine signal ϕ controls the projection in the x-y plane. Larger amplitudes increase the B_1 RF field and therefore the frequency of rotations, as described in Section 2.4.2. Higher amplitude pulse bursts can shorten the amount of time the burst needs to be applied for a given rotation angle θ.

An example pulse burst sequence (Hahn echo) is shown as an oscillogram in Fig 3.13. Design of pulse burst sequences are limited by a minimum pulse burst length in addition to a minimum delay between consecutive bursts due to hardware limitations. Slow rise and fall of waveform amplitude of the bursts generated is required to avoid generating frequency components that cannot be absorbed by the RF coil, resulting in potentially dangerous reflection amplitudes that may damage the amplifier. The length of time needed for the slow rising and falling of amplitude is carefully calibrated through monitoring reflections through a bidirectional coupler and is set to $T_{\mathrm{RiseFall}} = 0.6\ \mu$s. The requirement of a rise and fall section in the pulse limits the minimum pulse burst length to $2T_{\mathrm{RiseFall}} = 1.2\ \mu$s.

The minimum delay T_{MinDelay} between consecutive bursts is due to the strong reflections occurring at the end of the bursts that can constructively interfere with the forward voltages in the amplifier transistors. This effect becomes very significant for pulses with opposing

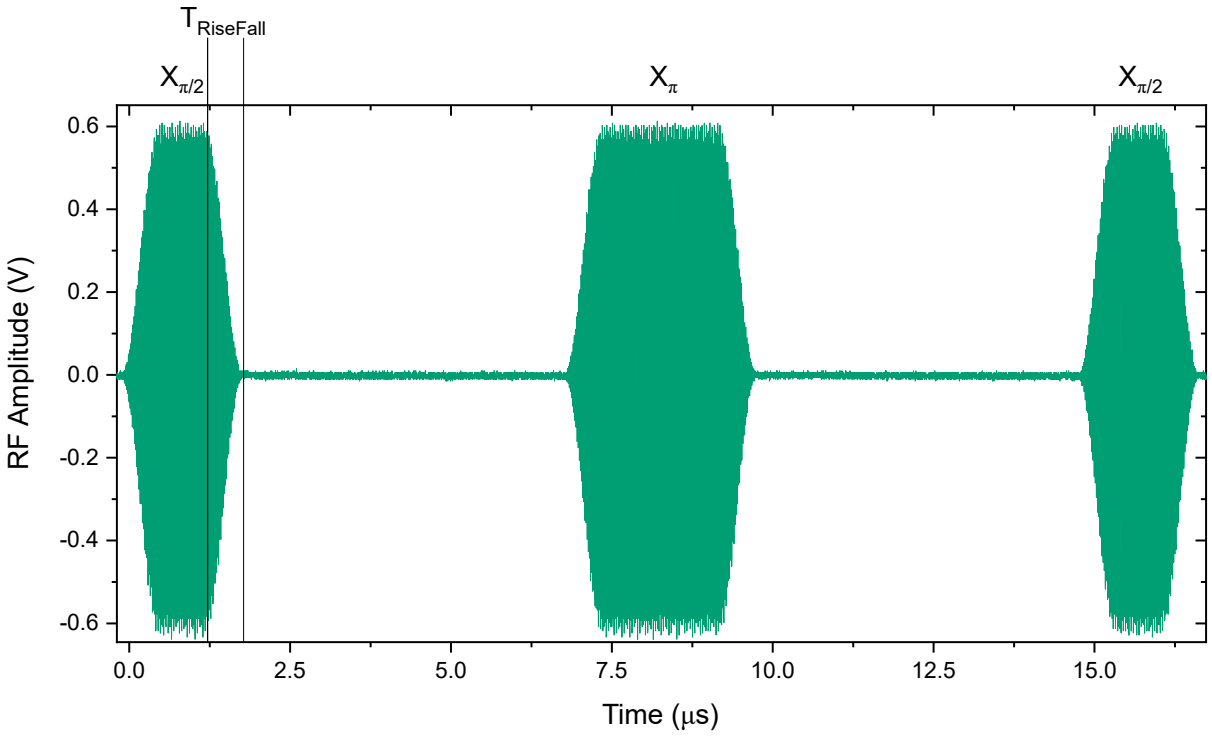

Figure 3.13: Oscilloscope measurement of a sample of the RF signal directed the RF coil in pulsed NMR measurements, with sample coupling -50 dB. This pulse sequence is known as Hahn Echo and is formed of a pulse train of $\pi/2$, π and $\pi/2$. The phase of the pulse bursts relative to each other is critical to the proper rotation of nuclear spin states around the Bloch sphere. We define pulses as X, -X, Y, -Y for pulse bursts with RF carrier phases of $\phi = 0$, π, $\pi/2$, $3\pi/2$. Each burst has a rising and falling part of length T_{RiseFall} to prevent sharp high amplitude reflections to the amplifier.

phase and can result in excessively high voltage on the output of the amplifier, which can damage the output stage transistors. In order to determine safe operating parameters, we generated two opposing phase pulses (to maximise constructive interference) and gradually decreased the delay T_{Delay} to observe when the amplifier mismatch fail-safe started to trigger. Consequently we determined the minimum delay between pulses to be $T_{\text{MinDelay}} = 0.45$ μs.

3.6.4 Adiabatic sweep NMR

An additional step is required for pulsed NMR measurements on InGaAs QDs. Optical pumping of a $I > 3/2$ nuclear spin bath creates a Boltzmann distribution of populations as described in Section 3.6.2. Single-frequency pulsed NMR can be used to excite a specific

transition, either of the STs or the CT, coherently rotating the spin state projection between the relevant spin states. Strong broadening of the STs makes coherent control of satellite transitions difficult as a broad range of frequencies would be required to rotate all nuclei. This is in contrast to the spectrally narrow CT transition allowing rotation of most spins in the $I_z = \pm 1/2$ states. As a result, we only apply single-frequency pulsed NMR to the CT and observe population change between the CT states $I_z = \pm 1/2$ in ODNMR. In order to improve the measurement signal, we use a technique known as adiabatic sweeps which are used to shift the population to the two central states, increasing the number of nuclei undergoing rotations and therefore increasing ODNMR signal [112].

Two single-frequency NMR signals are applied through the broadband cascade at frequencies starting far from the CT, $f_{\mathrm{CT}} \pm f^{\mathrm{Sw}}_{\mathrm{Start}}$. In order to transfer the population of all $I_z > \pm 1/2$ states, we require the starting frequency to be larger than the largest nuclear spin quadrupolar splitting $|f^{\mathrm{Sw}}_{\mathrm{Start}}| > f_{\mathrm{CT}} + f_Q(I + \frac{1}{2})$, where $f_Q = \omega_Q/2\pi$ as defined in Section 2.3.2. The pulses are swept in frequency towards the CT, stopping just before the CT at $f_{\mathrm{CT}} \pm f^{\mathrm{Sw}}_{\mathrm{End}}$ to prevent population change between $I_z = \pm 1/2$, and is illustrated in Fig 3.14. The rate at which the frequency is swept across the STs, f^{Sw}_{Rate}, is carefully tuned in order to ensure the conditions for adiabatic transfer is met. The result is the $I_z = \pm I$ states transferring population to the CT states, increasing the number of potential nuclei to be rotated and creating a greater shift in the Overhauser field for pulsed NMR experiments. Typical values for the frequency offsets and rates are starting frequencies of $f^{\mathrm{Sw}}_{\mathrm{Start}} \sim 5$ - 10 MHz, end frequencies of $f^{\mathrm{Sw}}_{\mathrm{End}} \sim 20$ - 100 kHz and rate of frequency change $f^{\mathrm{Sw}}_{\mathrm{Rate}} \sim 1$ - 15 MHz/s. The strength of the adiabatic NMR magnetic field B_1 varied up to a maximum of ≈ 1 mT to prevent excessive heat generation. Sweeps are applied as an additional step after optical spin pumping and before coherent nuclear spin rotation to enhance the signal for pulsed NMR measurements.

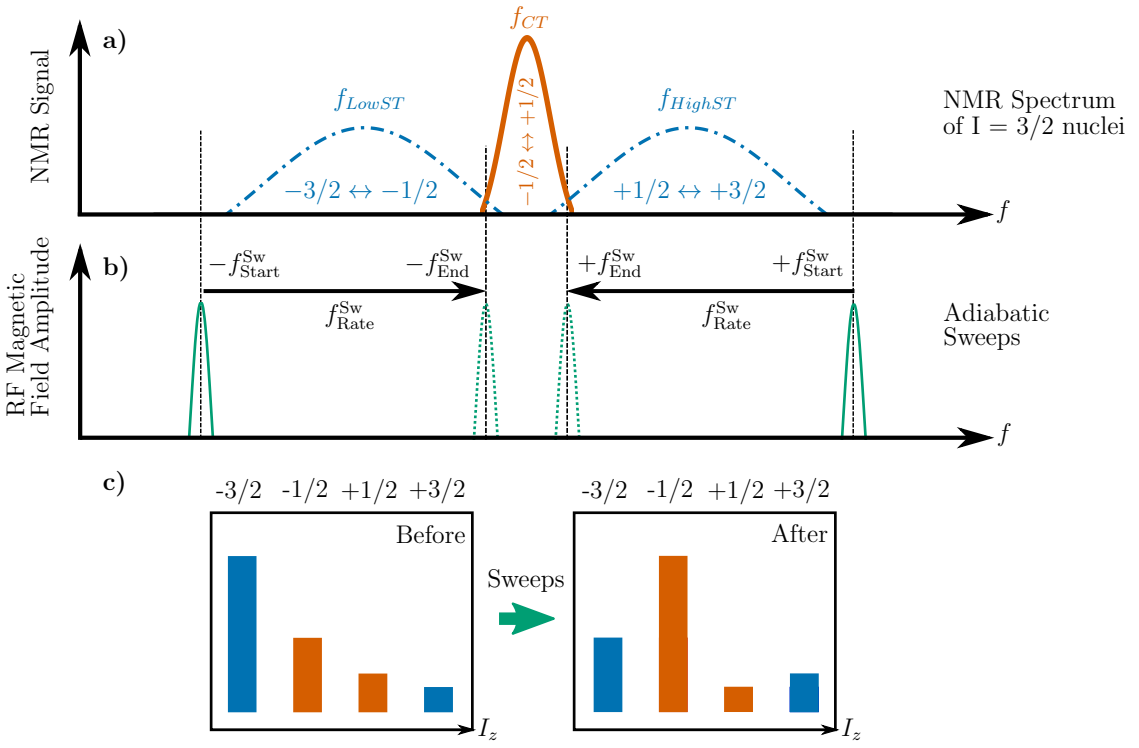

Figure 3.14: Illustration of adiabatic sweep NMR. a) An idealised NMR spectrum of a spin-3/2 nuclei in InGaAs, with three distinct transitions. The CT (solid) is a spectrally narrow transition $\Delta f_{\mathrm{CT}} \approx 1$ - 10 kHz, in contrast to the broad STs (dashed). InGaAs STs have broad spectra on the scale of MHz due to quadrupolar interaction effects as seen in Section 2.3.2. b) Adiabatic sweeps are carried out as two RF signals are swept from above/below the STs, $f_{\mathrm{CT}} \pm f^{Sw}_{Start}$, to just before the CT, $\pm f^{Sw}_{End}$, at a rate of f^{Sw}_{Rate}. c) Populations of I = 3/2 nuclear spin states before and after adiabatic sweeps. The nuclear spin population from the ST states, $I_z = \pm 3/2$, is transferred to the CT states $I_z = \pm 1/2$, increasing number of available nuclei that can be rotated during the application of pulsed RF to the CT.

3.6.5 NMR set-up

Generation of a transverse radio frequency magnetic field is achieved through transmitting an oscillating voltage to a copper coil. Strength of the magnetic field B_1 some distance x along the central axis of the coil can be calculated using the following equation,

$$B_1(x) = \frac{\mu_0}{4\pi} \frac{2nI\pi R^2}{(x^2 + R^2)^{3/2}} \tag{3.1}$$

where μ_0 is the permittivity of free space, R is the radius of the coil, I is the current through the coil and n is the number of turns in the coil. From this equation, we can see that for

the point in the centre of the coil $x = 0$, the smallest radius of the coil R, will generate the largest B_1. In our experimental NMR set-up the centre of the coil is aligned perpendicular to the sample and positioned to be in close proximity with the sample such that $x \approx 0.5$ mm (Fig 3.4), resulting in an optimal radius of $R \approx 0.65$ mm. The small gap is required between the sample and the coil in order to limit heating of the sample, in addition to reducing the risk of collision of the sample and coil during translation of the piezo stages. The RF coil used in experiments is made of enamelled copper wire with thickness 0.1 mm looped with a radius of ≈ 0.5 mm, with $n = 10$ turns for increased B_1.

RF pulses are created by a signal generator and then passed through an amplifier in order to achieve the desired strength of the transverse magnetic field B_1. We use two primary types of RF signal, precise single frequency NMR pulse bursts or broadband NMR signals. Pulsed NMR can be used to coherently rotate the nuclear spins by applying a single frequency pulse at high power. Probing the broad frequency distribution of nuclear resonances requires a wide range of frequencies.

Pulsed NMR waveforms are generated by an arbitrary waveform generator as a pulse burst train of different length sine waves in order to provide precise control of nuclear spin state. The frequency of the sine waves corresponds to the resonant frequency of the desired transition, which is typically the CT for the desired isotope within InGaAs quantum dots. Amplitude of output waveforms can be set at a given value. Waveforms are then sent to a 1 kW Tomco pulsed class-AB amplifier. Amplifier gain is constant so control over the power of applied RF pulses is adjusted through the amplitude of the outputted waveform from the generator. The strongest amplitude RF bursts can create rotating frame magnetic fields of up to $B_1 \approx 10$ mT. Applied RF amplitudes P_{RF} are limited by the 1 kW amplifier compression regime at which amplification of pulses becomes non-linear, $P_{\mathrm{RF}} \approx 59$ dBm, increasing potentially damaging reflections due to amplification of higher order harmonics. Efficiency of the RF coil can be defined by the ratio of rotating frame amplitude to the amplitude of outputted RF from the amplifier, $B_1/\sqrt{P_{\mathrm{RF}}}$, giving a value of 0.35 $\times 10^{-3}$ T

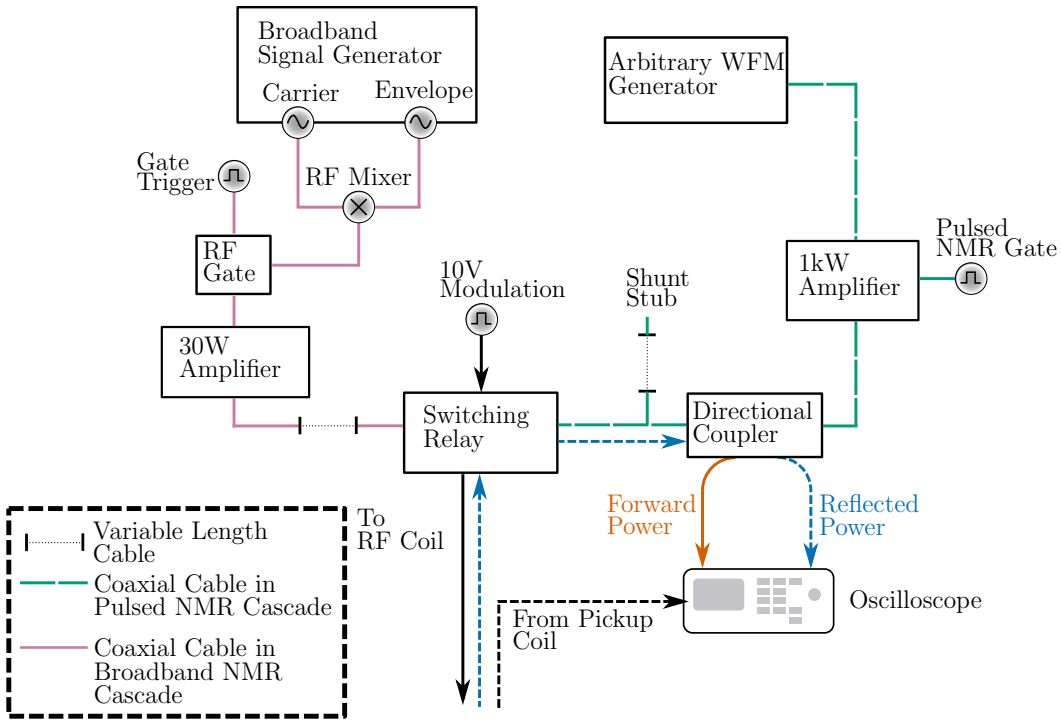

Figure 3.15: Schematic of NMR circuitry used for broadband (pink, solid) and pulsed (green, wide dashed) NMR measurements. Both circuits have signals created by separate signal generators. Carrier and envelope signals are passed through an RF mixer to create the desired signal. High power pulsed RF pulses are monitored by an oscilloscope connected to the forward and reverse channels of the bidirectional coupler in order to ensure no damage to the sample or amplifier. The pickup coil can also be used for RF monitoring of both pulsed and broadband signals. Variable cable lengths are indicated by dashed lines and allow tuning of the impedance matching of each circuit to ensure efficient RF transmission from the coil.

$\mathrm{W}^{-1/2}$.

High power RF pulses are passed through a bidirectional coupler and then are sent down a $1.5 + l$ BNC cable to be converted to B_1 by the RF coil, where l is the length of a "shunt stub". To ensure maximum power is delivered to the RF coil at the desired frequency f_{RF}, it is important to consider the impedance matching of the load (RF coil) to the source (amplifier). A mismatch of loads is present in the circuit by default due to the 50 Ω impedance amplifier sending signal to the the RF coil, which acts approximately as an inductor with a small series resistance such that impedence Z is less than 50 Ω. Effective transmission of f_{RF} frequency pulses can be enabled by the addition of a "shunt stub" cable of length l to allow alteration of the impedance of the cascade (see Fig 3.15). The shunt stub acts as a resonant transformer

by which change in the shunt stub cable length l achieves impedence matching at a fixed frequency. A change in the desired f_{RF} requires alteration of the shunt stub length l. A more detailed description of impedance matching and the use of shunt stubs can be found in Chapter 5 of Microwave Engineering [152].

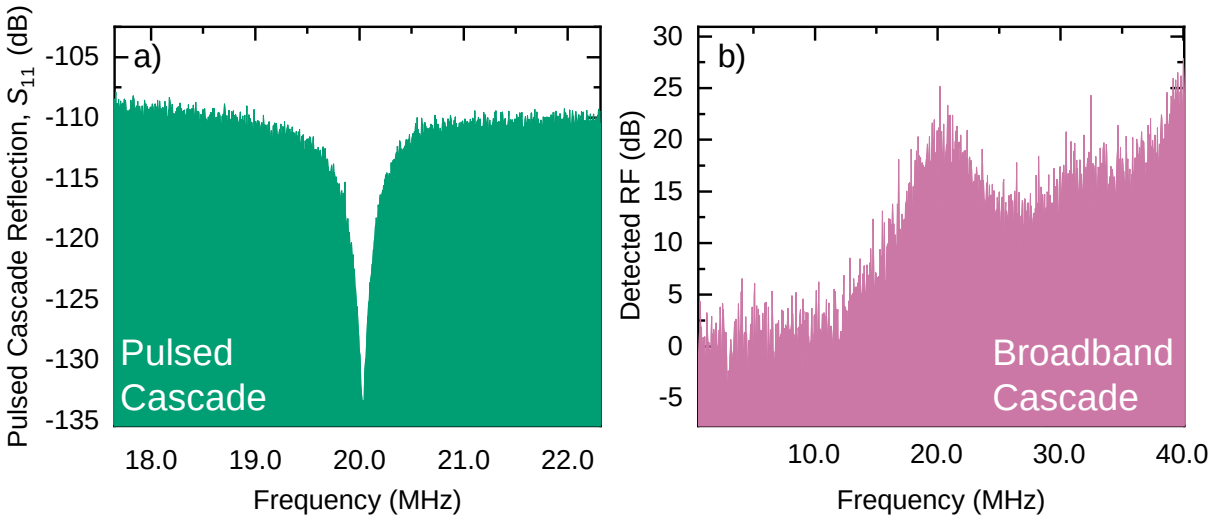

Figure 3.16: a) Reflection spectrum of pulsed NMR cascade circuit optimized to transmit ∼20 MHz RF. Reflection obtained from the reverse port of the directional coupler while applying broadband white noise to the pulsed NMR circuit. Adjustment of shunt stub length l will alter the central frequency of reflection dip. Dip in reflection indicates successful absorption of RF energy by the NMR coil, while high reflection sidebands are demonstrating impedance mismatched frequencies. b) Detected RF signal on the pickup coil generated by broadband white noise applied to the broadband NMR circuit and transmitted by the RF coil. Peak at target ∼20 MHz indicates efficient generation of RF magnetic field B_1 for CW NMR applications.

Scattering parameters (S-parameters) between ports in a distributed network describe the input-output relationship between each port. Outputted signal from port 1 (amplifier) to port 2 (RF Coil) is partially reflected back to port 1 and quantified by the S_{11} parameter. The S_{11} parameter of the pulsed cascade network can be observed by applying low power broadband white noise and monitoring the reflection on the reverse channel of the bidirectional coupler, as shown in Fig 3.16a. Dips in S_{11} provide an indicator of frequencies absorbed by the RF coil, and the width of the transmission spectrum gives a measure of the range of frequencies

that can be applied, which for Fig 3.16a is $\sim$ 0.8 MHz. This information is critical to ensure most efficient generation of RF signals at frequency f_{RF} and to safely protect the 1 kW amplifier. Pulses sent at non-transmissive frequencies will reflect back to the amplifier, causing a mismatch and potentially damaging the amplifier.

For measurements that require a wide range of frequencies, such as inverse NMR or adiabatic sweeps, a different set-up is used. Broadband RF signal is transmitted to a Class-A 30 W broadband amplifier, separate from the 1 kW pulsed amplifier. It is not possible to create transmission profiles valid for the many required frequencies for the desired frequency bands f_{Band}. We instead use a separate broadband matching circuit with no stub and simply change the length of cable between the 30 W amplifier and a switching relay. As a consequence of inefficient transmission over the wide range of desired frequencies for CW NMR, reflections are inevitable when applying broadband RF. The 30 W amplifier used for broadband signals is capable of withstanding full reflection of waveforms over a wide range of frequencies, removing any concerns with potentially high power RF reflections.

To set up broadband matching over a wide range of frequencies, we use the detection spectrum of broadband white noise measured by the pickup coil placed on the opposite side of the RF coil to the sample (shown in Fig 3.15). A variation in the transmission profile of the RF coil over broadband frequency ranges is observed. Adjustment of the broadband matching circuit attempts to mitigate this variation in transmission through changing cable length. It is usually possible to achieve a cascade where conversion of RF power to B_1 is sufficiently uniform ($\pm$5 dB) within the required frequency range of $\pm$5 - 10 MHz. An example of detection of broadband white noise is shown in Fig 3.16b.

Broadband RF signals are created through mixing of a carrier and envelope signal allowing creation of wide band CW RF. The inverse NMR technique introduced in Section 3.6.2 requires wide bandwidth CW RF. A full range of frequencies for the desired $\pm$12 MHz frequency band would require sophisticated generators and would provide challenges in maintaining consistent power across the spectrum. Instead we use a techinque called frequency

combs, where many discrete frequencie modes of RF are generated with a small mode spacing $f_{MS} \approx 120$ Hz. The frequency combs work approximately as a white noise continuum of frequencies provided the mode spacing is less than the homogeneous NMR linewidth and will efficiently depolarise the nuclei based on the strength of B_1 [153].

We cannot meet the requirements for the two types of RF signals in a single impedance matched cascade, as it impossible to achieve perfect and broadband impedance matching [152]. Consequently we create two separate cascades and combine the signal to allow both broadband and pulsed NMR techniques to be used in a single experiment. In order to combine both cascade set-ups for use during automated measurements, the cascades are input to a fast mechanical switching relay. The switching relay multiplexes the two RF signals, the broadband inverse NMR and the pulsed NMR bursts, into a single load. In the "Off" state (0 V), the relay allows the signal from the broadband cascade to be transmitted to the sample. When a voltage of 10 V is applied, the relay will switch to the "On" state, transmitting RF from the pulsed cascade. Automated measurements synchronise relay switching and pulsed NMR gating in order to create a short window for any pulsed NMR sequences that are to be applied to the sample.

4

Fundamental limits of electron and nuclear spin qubit lifetimes in an isolated self-assembled quantum dot

We require any "stationary" qubit to possess long-lasting states to allow the initialisation, manipulation and readout of the system, as introduced in Chapter 1. In order to improve the overall quality of the quantum dot spin qubits, and to open up opportunities for us to attempt electron spin resonance in QDs in the future, we must consider closely how design and operating conditions of QD structures affect the lifetimes and coherence times of both the electron and nuclear spins.

In this chapter, we focus on the spin lifetimes T_1 within InGaAs/GaAs quantum dots. Spin lifetimes define the timescale at which longitudinal magnetization is lost, and the spin system returns to the thermal equilibrium magnetization, as described by the Bloch equations introduced in Section 2.4.2. Practically, for the electron lifetime $T_{1,\mathrm{e}}$ this means that in the case of a spin initialised to $|\uparrow\rangle$, relaxation to the $|\downarrow\rangle$ state will occur on a time scale of $T_{1,\mathrm{e}}$. Similarly, in a nuclear spin bath optically polarised to achieve a spin polarisation degree of $\approx$ 60 - 80 %, nuclear spin lifetime $T_{1,\mathrm{N}}$ is a measure of how long it takes the average nu-

clear spin bath polarisation to return to its unpolarised thermal equilibrium. Understanding the mechanisms limiting T_1 is a critical component of selecting qubit candidates. Previous independent studies of nuclear [140] and electron [144] lifetimes in InGaAs QDs have been carried out with great success, but no systematic set of measurements for the electron $T_{1,e}$ and the nuclear $T_{1,\mathrm{N}}$ spin systems have been made.

Our first investigation into self-assembled quantum dots set out to fully characterise the effect of magnetic field, charging bias and tunnelling coupling to the electron Fermi reservoir on the lifetimes T_1 of spins within the quantum dot. We study a series of InGaAs/GaAs QDs Schottky diode structures with a varying tunnelling barrier thickness, t_B = 37, 42, 52 nm, intending to investigate the effect of tunnel coupling between the QD and the Fermi reservoir on spin lifetimes. Here, we used time-resolved resonance fluorescence and pump-probe measurements to measure electron and nuclear lifetimes respectively. Fidelity of electron spin initialisation is studied for varying t_B, with a thicker barrier causing a reduction due to Auger recombination effects. Bias dependant measurement of lifetimes reveals the expected single charging plateau arising due to the Coulomb blockade, while magnetic field dependant measurements allowed us to create a model for prediction of electron and nuclear T_1. The models ultimately lead to an estimate on the fundamental limits of spin lifetimes within the quantum dot system, which applies universally to all self-assembled QDs.

The results in this chapter are presented in the form of a paper for which I am first author and was published on 24th February 2021:

G. Gillard, I. M. Griffiths, G. Ragunathan, A. Ulhaq, C. McEwan, E. A. Chekhovich. "Fundamental limits of electron and nuclear spin qubit lifetimes in an isolated self-assembled quantum dot". *npj Quantum Information*, **7**, 43 (2021), doi:10.1038/s41534-021-00378-2.

npj | Quantum Information

www.nature.com/npjqi

ARTICLE OPEN

Check for updates

Fundamental limits of electron and nuclear spin qubit lifetimes in an isolated self-assembled quantum dot

George Gillard[1], Ian M. Griffiths[1], Gautham Ragunathan[1], Ata Ulhaq[1,3], Callum McEwan[1], Edmund Clarke[2] and Evgeny A. Chekhovich[1]✉

Combining external control with long spin lifetime and coherence is a key challenge for solid state spin qubits. Tunnel coupling with electron Fermi reservoir provides robust charge state control in semiconductor quantum dots, but results in undesired relaxation of electron and nuclear spins through mechanisms that lack complete understanding. Here, we unravel the contributions of tunnelling-assisted and phonon-assisted spin relaxation mechanisms by systematically adjusting the tunnelling coupling in a wide range, including the limit of an isolated quantum dot. These experiments reveal fundamental limits and trade-offs of quantum dot spin dynamics: while reduced tunnelling can be used to achieve electron spin qubit lifetimes exceeding 1 s, the optical spin initialisation fidelity is reduced below 80%, limited by Auger recombination. Comprehensive understanding of electron-nuclear spin relaxation attained here provides a roadmap for design of the optimal operating conditions in quantum dot spin qubits.

npj Quantum Information (2021)7:43 ; https://doi.org/10.1038/s41534-021-00378-2

INTRODUCTION

Semiconductor quantum dots (QDs) offer excellent quantum optical properties and well-defined quantum states of individual spins—an attractive combination for quantum information processing devices[1]. Recent proof-of-concept demonstrations with QDs include heralded entanglement of two remote spins[2], generation of photonic cluster states[3], spin-controlled photon switching[4] as well as implementation of electron–nuclear quantum spin interfaces[5] and nuclear spin quantum computing[6]. The stability of the spin states, measured by their lifetimes, is crucial in all these applications.

Quantum dot is described by a central spin of a single charge (electron or hole) coupled to $N \approx 10^3 - 10^5$ nuclear spins via hyperfine interaction[7]. The lack of translational motion combined with the mismatch in electron and nuclear spin energies suppresses relaxation[8], providing long spin lifetimes required for spin qubits. However, thorough understanding of spin relaxation is complicated by the multitude and complexity of the residual environment couplings, which include electron–phonon interactions[9–12], quadrupolar coupling of nuclear spins to strain[13], nuclear spin diffusion, and electron cotunneling[14,15] arising from proximity of the Fermi reservoir. Moreover, impurity charge traps[16,17] adjacent to QDs degrade spin qubit lifetimes. Thus, it remains an open question to establish the maximum (intrinsic) spin lifetimes that can be achieved at any given magnetic field and temperature, as opposed to spin relaxation arising from QD device design and imperfections.

Phonon-assisted electron spin relaxation enabled by spin–orbit interaction is a dominant mechanism[9,10,18] at high magnetic field $B_z \gtrsim 2$ T, but the limit to electron spin lifetime $T_{1,e}$ at low fields remains unexplored. In case of nuclear spins, cotunneling-mediated relaxation was identified as dominant mechanism[15], while direct verification is lacking, since bias control of cotunneling is restricted to a narrow range compatible with single-electron QD state.

Here we study a series of structures where electron cotunneling is controlled directly by the thickness t_B of the tunnel barrier separating the dot from the Fermi reservoir. We find that at $B_z \gtrsim 2$ T and temperatures $\theta > 4.2$ K nuclear spin relaxation is dominated by a higher-order process assisted by phonons[19,20] and noncollinear hyperfine interaction[13], rather than by cotunneling, which is dominant only at low fields $B_z \lesssim 2$ T. Electron spin lifetimes exceeding $T_{1,e} > 1$ s are found at $B_z \approx 0.4$ T, with a fundamental maximum $T_{1,e} \approx 20$ s estimated for an isolated dot at $\theta = 4.2$ K, bounded by phonon relaxation and direct hyperfine interaction at high and low magnetic fields, respectively. While coupling to Fermi reservoir degrades $T_{1,e}$, it is shown to play a crucial role in counteracting Auger recombination[21] and enabling electron spin initialisation with near-unity fidelity[22].

RESULTS

Quantum dot structures and experimental techniques

Figure 1a sketches conduction band energy profile which is controlled with external bias V_S to tune an InAs QD into Coulomb blockade regime, where it is charged deterministically[23] with a single electron (1*e*). The trion state with two electrons and one hole can be accessed through resonant optical excitation, and observed in resonance fluorescence (ResFl). Magnetic field B_z along the sample growth axis splits the electron spin-up $|\uparrow\rangle$ and spin-down $|\downarrow\rangle$ energies (Fig. 1b), enabling selective excitation of the optically allowed transition between $|\uparrow\rangle$ electron and the trion $|\uparrow\downarrow\Uparrow\rangle$ with a spin-up hole $|\Uparrow\rangle$. Weak recombination enabled by hyperfine and heavy–light hole mixing $\beta \ll 1$ can 'shelve' the dot[14] into $|\downarrow\rangle$ state, quenching ResFl intensity I_{ResFl} until electron returns to $|\uparrow\rangle$ through a spin flip with rate $\xi_{\uparrow\downarrow}$. Such shelving provides an efficient way both for initialisation and readout of the electron spin[14,22]. Furthermore, hyperfine interaction $\hat{\mathcal{H}}_{\mathrm{hf}} \propto (\hat{\mathbf{I}}\mathbf{s})$ of electron spin **s** with nuclear spins **I** enables electron–nuclear flip–flops, so that repeated electron spin initialisation creates a net

[1]Department of Physics and Astronomy, University of Sheffield, Sheffield S3 7RH, UK. [2]Department of Electronic and Electrical Engineering, University of Sheffield, Sheffield S1 3JD, UK. [3]Present address: Physics department, SBA School of Science and Engineering, Lahore University of Management Sciences, Sector U, DHA 54792 Lahore, Pakistan. ✉email: e.chekhovich@sheffield.ac.uk

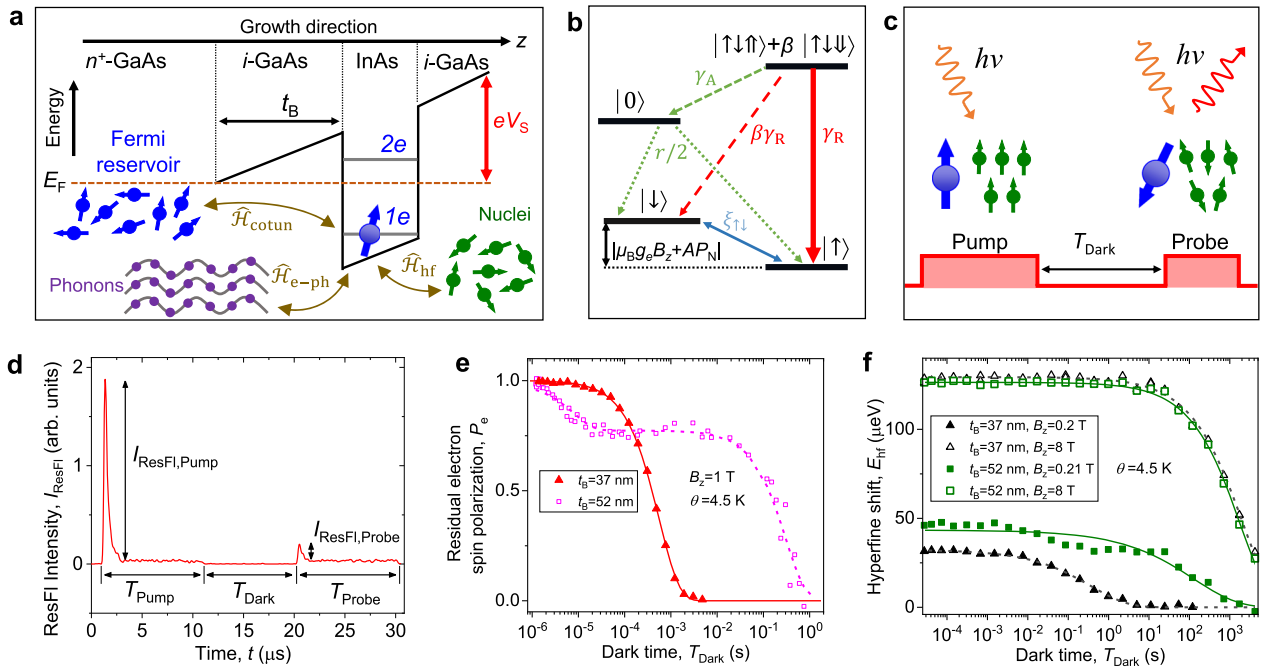

Fig. 1 Electron and nuclear spins in a quantum dot. a Schematic of an InAs quantum dot embedded in a *n*–*i*–Schottky diode structure. Electron spin is coupled to nuclei via hyperfine interaction ($\hat{\mathcal{H}}_{hf}$) and to phonons ($\hat{\mathcal{H}}_{e-ph}$). Tunnel barrier thickness t_B controls the cotunneling interaction ($\hat{\mathcal{H}}_{cotun}$). Quantum dot charge state is controlled with bias V_S, which tunes the energies of one-electron (1*e*) and two-electron (2*e*) states with respect to Fermi energy E_F. **b** Energy levels of an empty dot $|0\rangle$, electron with spin up ($|\uparrow\rangle$, $s_z = +1/2$) or down ($|\downarrow\rangle$, $s_z = -1/2$), and a trion $|\uparrow\downarrow\Uparrow\rangle$ with hole moment $j_z = +3/2$, which has a small admixture $\beta \ll 1$ of a trion $|\uparrow\downarrow\Downarrow\rangle$ with opposite hole moment $j_z = -3/2$. Arrow labels show the rates of radiative recombination γ_R, Auger recombination γ_A, recharging r, and electron spin flip $\xi_{\uparrow\downarrow}$. Electron spin splitting is due to Zeeman effect ($\mu_B g_e B_z$, where g_e is electron *g*-factor and μ_B is Bohr magneton) and nuclear hyperfine shift $E_{hf} \propto A_{hf} P_N$. **c** Timing diagram of a pump-delay-probe experiment where optical excitation is used to initialise and probe the spins of either the electron or nuclei. **d** Time-resolved resonance fluorescence (ResFl) in a pump-probe experiment. Resonance fluorescence pulses of intensities $I_{ResFl,Pump}$ and $I_{ResFl,Probe}$ indicate electron spin pumping and are used to calculate the residual (i.e. relative to initial) electron spin polarisation $P_e = (I_{ResFl,Pump} - I_{ResFl,Probe})/I_{ResFl,Pump}$ after time T_{Dark}. **e** Electron spin decay measured in Coulomb blockade regime as $P_e(T_{Dark})$ in diode sample structures with different t_B (symbols). Lines show exponential (solid) or rate-equation (dashed) fitting. **f** Nuclear spin decay obtained by measuring hyperfine shift E_{hf} as a function of dark time T_{Dark} in a pump-delay-probe experiment. Lines show fitting with stretched exponential function.

nuclear spin polarisation P_N, which can be monitored through optically measured hyperfine shifts E_{hf} in the splitting of the $|\uparrow\rangle$ and $|\downarrow\rangle$ states[7,17].

Electron and nuclear spin dynamics are measured using a pump-delay-probe protocol (Fig. 1c). The decay of optically pumped electron [nuclear] spin polarisation over dark period T_{Dark} is probed by measuring I_{ResFl} [E_{hf}]. Figure 1d shows an example of time-resolved ResFl, which is used to derive the residual electron spin polarisation P_e after a delay T_{Dark} (see the "Methods" section). Measurements of P_e at different T_{Dark} reveal electron spin relaxation (symbols in Fig. 1e), while examples of nuclear spin relaxation $E_{hf}(T_{Dark})$ are shown in Fig. 1f. Fitting (lines in Fig. 1e, f) is used to derive the intrinsic spin-relaxation rates of electron $\Gamma_e = 1/T_{1,e} = 2\xi_{\uparrow\downarrow}$ and nuclei $\Gamma_N = 1/T_{1,N}$.

Effect of Auger recombination on spin initialisation

We make a systematic comparison of spin dynamics in a thin-barrier sample ($t_B = 37$ nm, Fig. 2a–c), similar to structures used previously[10,14,15], and a thick-barrier structure ($t_B = 52$ nm, Fig. 2d–f), approximating a QD isolated from the Fermi reservoir. Examining the bias dependence of continuous excitation resonance flourescence intensity I_{ResFl} in a thin-barrier sample, we observe a 1*e* plateau at $B_z = 0$ T (triangles in Fig. 2a), while at high B_z (circles and squares in Fig. 2a) ResFl is strongly suppressed, indicating spin 'shelving'[10,14]. A striking difference is observed in a thick-barrier sample (Fig. 2d), where fluorescence intensity and spin 'shelving' contrast are reduced (Fig. 2a), which may at first suggest the lack of electron spin initialisation. However, this is ruled out by time-resolved ResFl (e.g. Fig. 1d), which reveals spin-pumping fluorescence pulses of similar intensity for all t_B. We ascribe the reduction in I_{ResFl} and the peculiar two-stage electron spin decay in a thick-barrier sample (squares in Fig. 1e) to the Auger process[21,24], where electron–hole recombination ejects the second electron with a rate γ_A (Fig. 1b). Following the ejection, an empty QD does not contribute to ResFl, hence $P_e \approx 1$ observed initially. During T_{Dark} an unpolarised electron can return from the Fermi reservoir with recharging rate r, giving rise to the fast component of the $P_e(T_{Dark})$ decay (squares in Fig. 1e at $T_{Dark} <$ 100 μs), whereas the slow component corresponds to resident electron spin relaxation with rate Γ_e.

Using rate equation modelling (see details in the "Methods" section) of the four-level system shown in Fig. 1b, we find good description of the experiments (dashed line Fig. 1e) and derive $r \approx 1.26 \times 10^5\ s^{-1}$, $\Gamma_e = T_{1,e}^{-1} \approx 3.3\ s^{-1}$. Importantly, the level $P_e \approx 0.77$ reached after dot recharging ($T_{Dark} \approx 100$ μs) gives a direct measure of the electron spin initialisation fidelity in a thick-barrier sample, revealing the fundamental limitations arising in an isolated ($t_B \to \infty$) QD. In a thin-barrier sample, Auger recombination is counteracted by fast recharging: the resulting spin initialisation fidelity is higher, but can never reach unity. The maximum spin initialisation fidelity is an algebraic function of QD properties such as relaxation rates and heavy-light hole mixing. (The exact expression can be found in Supplementary Note 2.) Analysis shows that fidelity is improved for faster recharging r, larger trion mixing β and slower spin flip $\xi_{\uparrow\downarrow}$. Conversely, in the limit of infinitely slow recharging $r \to 0$ spin initialisation becomes

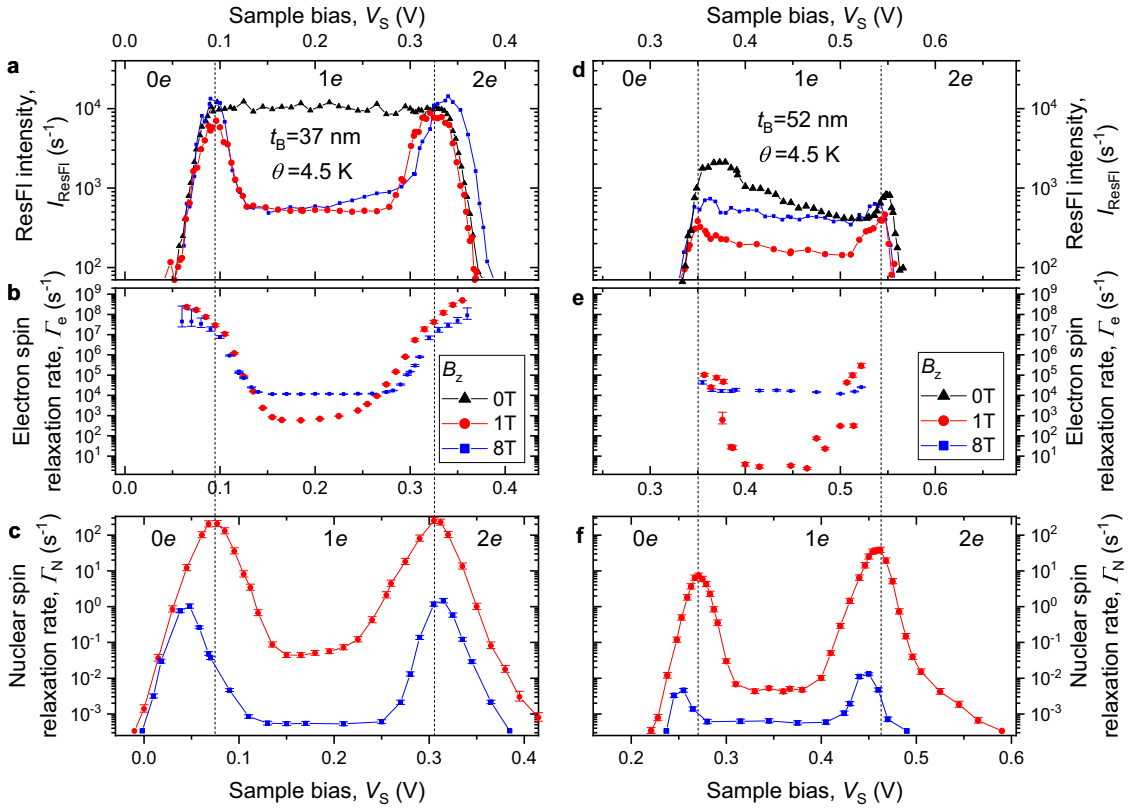

Fig. 2 Bias dependence of electron and nuclear spin dynamics. a Bias dependence of resonance fluorescence (ResFl) intensity I_{ResFl} in a QD sample with $t_B = 37$ nm. At $B_z = 0$ T (triangles) a clear Coulomb blockade (1*e* plateau) is observed, with I_{ResFl} decreasing when the dot is emptied (0*e*, $V_S \lesssim 0.1$ V) or filled with a second electron (2*e*, $V_S \gtrsim 0.33$ V). At non-zero $B_z = 1$ T (circles) and $B_z = 8$ T (squares) the centre of the 1*e* plateau is suppressed due to spin 'shelving', leaving two peaks arising from resonant tunnel coupling to the Fermi reservoir. **b** Bias dependence of the electron spin relaxation rate measured at $B_z = 1$ T (circles) and $B_z = 8$ T (squares). **c** Bias dependence of the nuclear spin relaxation rate measured for the same QD as in **a** and **b**. Note the offset in the horizontal axis, which is likely due to additional electric fields arising from the optically generated trapped charges near the QD. Vertical dashed lines separate different charge states 0*e*, 1*e*, 2*e*. **d**–**f** Same as **a**–**c** but for a QD from a thick-barrier sample ($t_B = 52$ nm). All error bars are 95% confidence intervals.

impossible ($P_e \to 0$), imposing a practical lower limit on the tunnel coupling with the Fermi reservoir.

Fundamental limits of electron spin lifetimes

Figure 2 shows that electron (Fig. 2b, e) and nuclear (Fig. 2c, f) spin relaxation rates are reduced at the centre of the 1*e* plateau[15,25]. This Coulomb blockade regime is of most interest, as it corresponds to a stable electron spin qubit, and is examined in more detail in Fig. 3. The dependence of Γ_e on magnetic field is well described (solid lines in Fig. 3a) by

$$\Gamma_e = \Gamma_{e,cotun} + \Gamma_{e,ph} B_z^{k_{ph}} \quad (1)$$

where for the field-dependent mechanism assisted by spin–orbit interaction and phonons we find $\Gamma_{e,ph} \approx 2.27 \pm 0.48\ s^{-1} \times T^{-k_{ph}}$ and $k_{ph} \approx 4.1 \pm 0.13$ in both samples. The exponent is in good agreement with $k_{ph} = 4$ predicted[26] and observed experimentally[9] for this mechanism in high-temperature regime $\mu_B g_e B_z \lesssim k_B \theta$, where phonon thermal occupation factor gives rise to an additional $\propto B_z^{-1}$ factor in Γ_e. This condition is well satisfied for our experiments at $B_z \leq 8$ T, $\theta \geq 4.5$ K and typical *g*-factor values $|g_e| \approx 0.4$. By contrast, in previous studies at $B_z \leq 12$ T, $\theta \approx 1$ K the onset of low-temperature regime was observed[9], where phonon thermal occupation factor is ≈1, resulting in $k_{ph} = 5$.

Cotunneling involves virtual injection of a second electron into the dot, followed by return of a spin-flipped electron to the Fermi reservoir[14,27]. The fitted cotunneling-induced relaxation rate in a thin-barrier ($t_B = 37$ nm) sample $\Gamma_{e,cotun} \approx 532 \pm 65\ s^{-1} = (0.0019 \pm 0.0002\ s)^{-1}$ is larger than $\Gamma_{e,cotun} \approx (1.65 \pm 0.21\ s)^{-1}$ found for a thicker $t_B = 52$ nm. Since $\Gamma_{e,cotun}$ is field independent, the increase in Γ_e at very low $B_z \lesssim 0.2$ T (squares in Fig. 3a) is likely due to energy-conserving electron–nuclear flip–flops, which become allowed when electron Zeeman energy is comparable to nuclear quadrupolar energy. By extrapolating the phonon (dotted line) and hyperfine (dash-dotted line) mechanisms we roughly estimate the fundamental minimum of the electron spin relaxation rate in an isolated ($t_B \to \infty$) QD as $\Gamma_{e,min} \gtrsim (20\ s)^{-1}$, expected to occur at $B_z \approx 0.4$ T for $\theta \approx 4.5$ K. Similarly slow electron spin relaxation rates were reported in strain-free III–V QDs[28], although at lower temperatures $\theta < 0.1$ K.

Figure 3b shows Γ_e measured in cotunneling-dominated low-field regime in samples with different barriers. A considerable variation between individual dots for the thin barrier $t_B = 37$ nm can be due to random atomic-scale positioning of the individual Si dopants[29] and Si segregation[30] at the interface between tunnel barrier and Fermi reservoir. By contrast, in a thick-barrier sample ($t_B = 52$ nm) the dot is coupled to a large number of dopants, smoothing out atomic-scale variations and leading to consistent Γ_e.

In low-field regime the barrier thickness t_B controls both the electron spin relaxation rate Γ_e and recharging rate *r*, but we find that *r* exceeds Γ_e by approximately five orders of magnitude, as exemplified in Fig. 1e. The recharging of an empty QD is a first-order tunnelling process, whereas cotunneling in a charged QD is a second-order process[31,32], which qualititatively explains the difference in rates. Moreover, the charge state of the dot itself may affect the conduction band energy profile, altering the tunnel

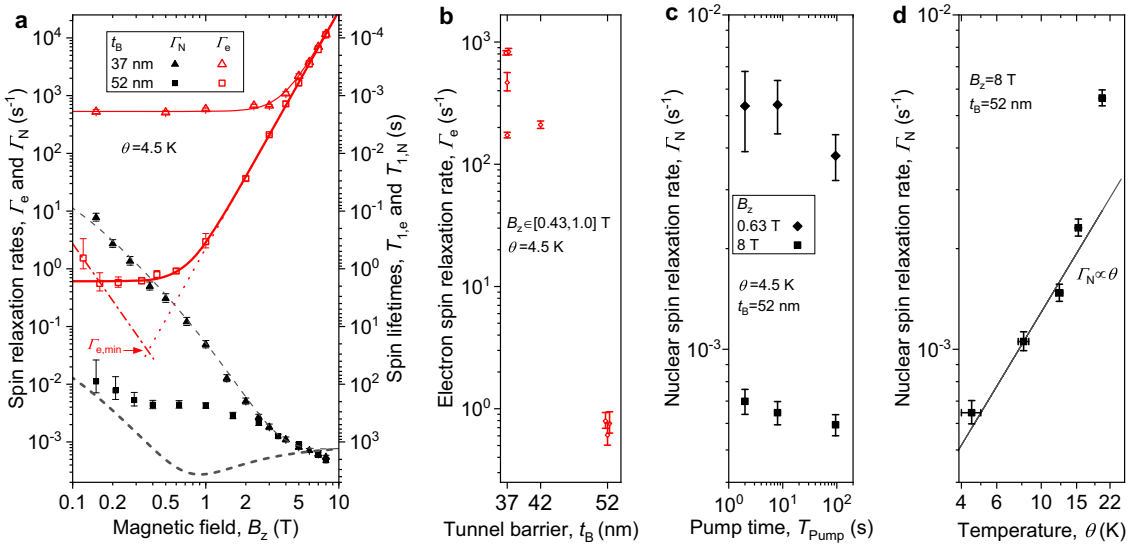

Fig. 3 Electron and nuclear spin dynamics in Coulomb blockade regime. a Magnetic field dependence of the electron (Γ_e, open symbols) and nuclear (Γ_N, solid symbols) spin relaxation rates measured in a thin-barrier (triangles, $t_B = 37$ nm) and thick-barrier (squares, $t_B = 52$ nm) samples at base temperature $\theta \approx 4.5$ K. Tabulated experimental data can be found in Supplementary Note 3. Spin pumping time in nuclear spin relaxation experiments is $T_{Pump} = 8$ s. Modelling is shown by the solid (electron) and dashed (nuclei) thin ($t_B = 37$ nm) and thick ($t_B = 52$ nm) lines. Dotted and dash-dotted lines show power-law extrapolations of the low-field and high-field regimes to estimate the minimum electron spin relaxation rate $\Gamma_{e,min} \approx (20\,s)^{-1}$. **b** Γ_e for several QDs in samples with $t_B = 37$, 42 and 52 nm measured in low-field regime $B_z \leq 1$ T, where spin relaxation is dominated by cotunneling. Small horizontal offsets are added to prevent points from overlapping. **c** Γ_N measured as a function of the pump time in a thick-barrier sample at $B_z = 0.63$ T (diamonds) and $B_z = 8$ T (squares). **d** Γ_N measured as a function of sample temperature in a thick-barrier sample at $B_z = 8$ T (symbols). Line shows linear dependence. All error bars are 95% confidence intervals.

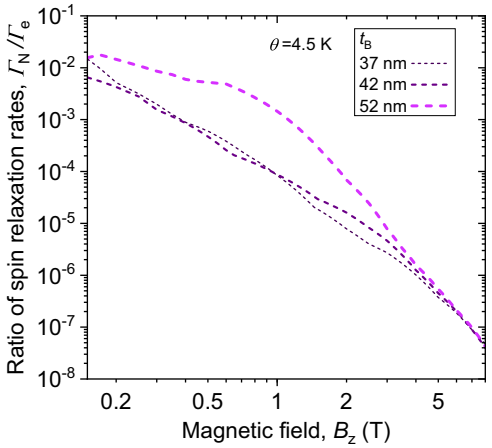

Fig. 4 Ratio of nuclear and electron spin relaxation rates. Γ_N/Γ_e as a function of magnetic field B_z is plotted by taking linear interpolations of the logarithms of experimentally measured nuclear and electron spin relaxation rates. The results are shown for individual quantum dots in three samples with different tunnel barriers $t_B = 37$, 42 and 52 nm.

coupling. An accurate first-principle quantitative description of the rates would require development of a detailed theoretical model.

Nuclear spin relaxation mechanisms

The marked difference in nuclear spin relaxation rate Γ_N (solid symbols in Fig. 3a) of the two samples at low magnetic fields suggest cotunneling as the dominant channel, whereas at $B_z \gtrsim 2$ T cotunneling is negligible. This is in contrast to previous studies under similar conditions ($t_B = 35$ nm, $B_z = 5$ T), which identified cotunneling and nuclear spin diffusion[15] as dominant mechanisms. We examine diffusion by varying the spin pumping time (squares in Fig. 3c): Taking the difference in Γ_N at short and long pumping, the diffusion rate is estimated to be as small as $\Gamma_{N,diff} \lesssim 10^{-4}\,s^{-1}$ (at $B_z = 8$ T). Slow diffusion is due to quadrupolar freezing of nuclear spin flip–flops[15,17]. Moreover, optical pumping through wetting layer states used in this work (as opposed to resonant optical pumping in ref. [15]), is likely to polarise nuclear spins not only in the dot but also in its vicinity, further suppressing the diffusion. Thus cotunneling and spin diffusion alone do not account for all the relevant nuclear spin relaxation mechanisms.

To explain the entire $\Gamma_N(B_z)$ dependence, we treat the average spin of the QD electron as a random process. Uniquely for self-assembled QDs, noncollinear hyperfine interaction permits nuclear spin relaxation without electron spin flip[13]—this mechanism is expected to be more efficient than direct electron–nuclear spin flips[15]. The transition rate $\Gamma_{N,ij}$ between states $|i\rangle$ and $|j\rangle$ of a single nuclear spin is proportional to spectral power density[33] of the fluctuating electron spin $s_z(t)$ at the nuclear spin transition frequency ν_{ij}. Using first-order perturbation theory[13] we have

$$\Gamma_{N,ij} = \left(\frac{A_{hf}}{N\hbar}\right)^2 \frac{2|M_{ij}|^2\tau_e}{1 + 4\pi^2\tau_e^2\nu_{ij}^2} \quad (2)$$

where A_{hf} is the hyperfine constant, $M_{ij} = \langle i|\hat{I}_z|j\rangle$ is the matrix element of the nuclear spin operator $\hat{I}_z$, and electron spin correlation time is approximated by $\tau_e \approx 1/\Gamma_e$. This model describes a higher-order nuclear spin relaxation process, mediating by electron spin relaxation, which in turn is dominated by phonons at high fields or cotunneling at low fields. In the high field limit $|M_{ij}|^2 \propto B_z^{-2}$, $\Gamma_e \propto B_z^4$ and $\nu_{ij}^2 \propto B_z^2$ (see the "Methods" section) leading to $\Gamma_N \propto$ const, which agrees with the weak field dependence of Γ_N observed for both samples at $B_z \gtrsim 4$ T (solid symbols in Fig. 3a). Moreover, temperature dependence at high field (Fig. 3d) is close to linear $\Gamma_N \propto \theta$ at $\theta \lesssim 15$ K, matching the $\Gamma_e \propto \theta$ dependence[34] of the underlying phonon-mediated electron spin relaxation process. Superlinear growth of Γ_N at $\theta \gtrsim 15$ K is likely due to two-phonon processes[26,35], with scaling predicted to range between $\propto\theta^2$ and $\propto\theta^9$.

For quantitative description (see the "Methods" section) we use experimentally measured Γ_e and estimate ν_{ij} and M_{ij} from

magnetic resonance spectra[36,37]. The results (dashed lines in Fig. 3a) are in good agreement for the thin barrier ($t_B = 37$ nm), where electron correlation time is short. The discrepancy for the thick-barrier sample ($t_B = 52$ nm) is most prominent at $B_z \lesssim 2.5$ T, revealing the limitations of the electron-spin fluctuation model (Eq. (2)) in the previously unexplored regime of a nearly isolated long-lived electron spin. To examine the cause, we note that $\tau_e^2 \nu_{ij}^2 \gg 1$ except for possible quadrupolar anti-crossings of the nuclear spin levels[37,38], so that Eq. (2) can be rewritten as

$$\Gamma_{N,ij}\tau_e = \left(\frac{A_{hf}|M_{ij}|}{\sqrt{2}\pi N\hbar\nu_{ij}}\right)^2 \quad (3)$$

The right side of this equation is a function of magnetic field and quantum dot structural properties, such as chemical composition and strain inhomogeneity, but it does not depend on tunnel coupling to Fermi reservoir. If $\tau_e = 1/\Gamma_e$, the equation predicts independence of Γ_N/Γ_e on tunnel barrier. This is seen to be the case in Fig. 4 for samples with $t_B = 37$ and 42 nm, whereas the thick barrier sample ($t_B = 52$ nm) shows excessive Γ_N/Γ_e.

The exact reason for the increased Γ_N/Γ_e in the thick barrier sample is not clear. One likely possibility is additional nuclear spin relaxation mechanisms where hyperfine interaction fluctuates without electron spin flips, resulting in $\tau_e < 1/\Gamma_e$. For example, modulation of the hyperfine interaction can occur through electron wavefunction density shifts, arising from fluctuating electric fields of the itinerant carriers in the Fermi reservoir[33,39], or charge traps[16]. Charge noise in the studied structures is indeed present and evidenced, e.g. by fluctuating electron spin relaxation rates at the edges of 1e plateau (circles in Fig. 3e). Future experiments using, e.g. bias modulation spectroscopy may elucidate the roles of different nuclear spin relaxation mechanisms and lead to more accurate theoretical models. Further improvements to nuclear spin relaxation description can be sought through a microscopic model that takes into account quadrupolar anti-crossings of the individual nuclear spin levels[37,38], which may accelerate relaxation and reenable frozen spin diffusion. A contribution of direct nuclear–phonon interaction[33,40] is also possible, as its rate $\Gamma_N \approx 10^{-4}$–10^{-3} s^{-1} is comparable to the lowest Γ_N observed here in electron-charged QDs.

DISCUSSION

Experiments presented here establish a comprehensive picture of electron–nuclear spin relaxation in self-assembled QDs in a wide range of practically accessible conditions. Present experiments require $B_z \gtrsim 0.15$ T to initialise the spins[22] and resolve the Zeeman-split optical transitions for spin probing. Extension to lower fields could shed light on the less explored regime where electron spin relaxation abruptly slows down from $\Gamma_e \approx 10^9$ s^{-1} at zero field[8,41] to $\Gamma_e \approx 1$ s^{-1} observed here at 0.15 T. For the practically interesting range $B_z \gtrsim 0.15$ T, electron spin relaxation is fundamentally limited by phonon coupling, which is similar in other types of QDs. Hence, electron spin lifetimes exceeding 1 s should be achievable in GaAs electrostatic[28] and epitaxial[42] QDs, as well as in II–VI QDs[43,44]. By contrast, nuclear spin relaxation studied here is specific to self-assembled III–V QDs, and is governed by noncollinear hyperfine interaction. All experiments here were conducted in Faraday geometry, whereas noncollinear interaction is expected to be even stronger for magnetic field tilted away from the sample growth axis[37], which may lead to faster nuclear spin relaxation in Voigt geometry. The techniques employed here, can also be applied to establish the less explored fundamental limits of nuclear spin dynamics in electron-charged strain-free QDs[28,42], where noncollinear interaction will be small, but nuclear spin diffusion might be more prominent.

METHODS

Samples and experimental techniques

The samples are low-density InAs self-assembled QDs ($\lesssim$1 QD per μm^2) grown on a GaAs substrate. The dot layer is positioned at the centre of a $\lambda/2$ optical cavity formed by a bottom Bragg mirror consisting of 15 GaAs/AlAs pairs and a top reflector with 2 pairs (estimated quality factor $Q \approx 60$). Cavity mode is centred at 950 nm, which matches the long-wavelength tail of the QD wavelength distribution. The Fermi reservoir is formed by a doped GaAs layer (Si concentration of 1.1×10^{18} cm^{-3}, thickness ≈ 80 nm). The doped layer is located beneath QDs and is separated by a GaAs layer of thickness $t_B = 37$–52 nm, depending on the structure. Each sample is processed into a Schottky diode structure with an Au/(In–Ge) ohmic back contact[45] annealed from the top surface, and a 5 nm-thick semitransparent Ti Schottky top contact. External bias is applied to the top contract and controls the charge states of QDs. In order to form an electron spin qubit, the dot is charged deterministically with one electron (1e). This is achieved by tuning the energy of the 1e state to ≈10 meV below the Fermi energy E_F (Fig. 1a), while the two-electron (2e) state remains depopulated, since its energy exceeds E_F by ≈10 meV, which is $\gtrsim$20 times the thermal energy $k_B\theta$ at liquid helium temperature $\theta \approx 4.2$ K (Boltzmann constant $k_B \approx 86.17$ μeV K^{-1}). The dot is then charged by an electron tunnelling from the Fermi reservoir.

The sample is mounted in a bath cryostat equipped with a superconducting coil producing magnetic field up to 8 T in Faraday geometry (field parallel to sample growth direction and optical axis z). An aspheric lens mounted near the sample is used for optical excitation of the QD and for light collection. Photoluminescence (PL) spectroscopy (see Supplementary Fig. 1) is used for initial QD characterisation. In nuclear spin dynamics experiments the dot is excited using diode lasers operating at 850 nm (resonant with InGaAs wetting layer). Nuclear spin polarisation (cooling) is achieved with a circularly polarised high power ($\gtrsim$100 times the power of ground state exciton saturation) laser, with typical pump pulse duration of $T_{Pump} \approx 8$ s. A short ($T_{Probe} \approx 10$ ms) low power (approximately corresponding to ground state exciton saturation) probe pulse is used to excite PL, which is then analysed on a double grating spectrometer to derive the hyperfine shifts E_{hf} in the splitting of a QD Zeeman doublet. The relaxation of the nuclear spin polarisation is derived by measuring E_{hf} in the probe as a function of delay T_{Dark} between the pump and the probe. The resulting $E_{hf}(T_{Dark})$ dependencies (e.g. Fig. 1f) are fitted with stretched or compressed exponentials $\propto e^{-(T_{Dark}/T_{1,N})^{\eta}}$, where η is the parameter describing stretching ($\eta < 1$) or compression ($\eta > 1$).

In ResFl experiments the dot is excited with a linearly polarised single-mode tunable diode laser. The scattered laser is rejected using cross-polarised detection[46], and the collected fluorescence is directed to an avalanche photodiode detector, whose photon-counting pulses are measured with a pulse counter and a digital oscilloscope. Typical linewidths measured in continuous excitation ResFl spectra on a negatively charged trion are ≈0.5 GHz at low power (non-saturating excitation). Electron spin initialisation at finite magnetic field is witnessed through ResFl intensity I_{ResFl}, which is significantly reduced when electron is initialised into the $|\downarrow\rangle$ state, taking the dot out of resonance with optical driving of the $|\uparrow\rangle \leftrightarrow |\uparrow\downarrow\Uparrow\rangle$ transition (compare squares and circles with triangles in Fig. 2a). Electron spin relaxation is accelerated and spin shelving is destroyed when the bias is tuned to the level where Fermi reservoir is resonantly tunnel-coupled with 1e ($V_S \approx 0.1$ V in Fig. 2a) or 2e ($V_S \approx 0.33$ V in Fig. 2a) quantum dot state, resulting in two peaks in the $I_{ResFl}(V_S)$ dependence (squares and circles in Fig. 2a).

In electron spin dynamics measurements pulsing of the resonant laser is achieved with acousto-optical modulators providing on/off ratio better than 10^7. The power of the pump and probe pulses is close to ResFl saturation conditions and typical duration is $T_{Pump} \approx T_{Probe} \approx 5$–$10$ μs, which is significantly longer than the spin pumping time. As a result, time-resolved ResFl exhibits short pulses (Fig. 1d) with amplitudes $I_{ResFl,Pump}$ and $I_{ResFl,Probe}$. At the start of each measurement cycle, and prior to optical pump pulse, the bias is adjusted for resonant electron tunnelling in order to counteract optical nuclear spin pumping and depolarise the electron (see further details in Supplementary Note 1). The rising edge of the fluorescence pulse corresponds to the rise time of the laser intensity in a pulse that pumps the initially depolarised electron. The exponentially decaying falling edge of the fluorescence pulse traces the gradual shelving (initialisation) of the dot into the $|\downarrow\rangle$ electron spin state. The loss of electron spin polarisation during the delay T_{Dark} results in partial recovery of the fluorescence intensity measured in the probe pulse. The residual polarisation P_e (i.e. electron spin polarisation at the start of the probe

normalised by polarisation at the end of the pump pulse) is then derived as $P_e = (I_{\mathrm{ResFl,Pump}} - I_{\mathrm{ResFl,Probe}})/I_{\mathrm{ResFl,Pump}}$. This way complete loss of electron polarisation ($P_e = 0$) is observed as $I_{\mathrm{ResFl,Probe}} = I_{\mathrm{ResFl,Pump}}$, while $I_{\mathrm{ResFl,Probe}} = 0$ implies no loss ($P_e = 1$) or Auger recombination that empties the dot. By measuring P_e at different T_{Dark} the decay of electron spin polarisation is obtained as shown in Fig. 1e by the symbols.

Unless stated otherwise, all error estimates in the text and error bars in figures are 95% confidence intervals.

Modelling of the electron spin relaxation dynamics

We simulate the dynamics of the four-level system shown in Fig. 1b using a simplified noncoherent rate equation model. The relaxation rates of all possible transitions are shown in Fig. 1b, and when resonant optical pumping is present we add a transition $|\uparrow\rangle \rightarrow |\uparrow\downarrow\Uparrow\rangle$ with rate P. We assume symmetric rates in electron spin flips $|\uparrow\rangle \leftrightarrow |\downarrow\rangle$, which is justified when electron Zeeman energy is smaller than the thermal energy $k_B\theta$. The system of first-order differential rate equations is

$$\frac{\partial}{\partial t}\begin{pmatrix} p_{|0\rangle}(t) \\ p_{|\uparrow\rangle}(t) \\ p_{|\downarrow\rangle}(t) \\ p_{|\uparrow\downarrow\Uparrow\rangle}(t) \end{pmatrix} = \mathbf{R}\begin{pmatrix} p_{|0\rangle}(t) \\ p_{|\uparrow\rangle}(t) \\ p_{|\downarrow\rangle}(t) \\ p_{|\uparrow\downarrow\Uparrow\rangle}(t) \end{pmatrix} \tag{4}$$

$$\mathbf{R} = \begin{pmatrix} -r & 0 & 0 & \gamma_A \\ r/2 & -P-\xi_{\uparrow\downarrow} & \xi_{\uparrow\downarrow} & \gamma_R \\ r/2 & \xi_{\uparrow\downarrow} & -\xi_{\uparrow\downarrow} & \beta\gamma_R \\ 0 & P & 0 & -(1+\beta)\gamma_R - \gamma_A \end{pmatrix} \tag{5}$$

In simulations we set $\gamma_R = 10^9\ \mathrm{s}^{-1}$, which is typical for InAs/GaAs QDs[47]. In order to simulate the pump-delay-probe experiment we use initial population probabilities $(p_{|0\rangle}, p_{|\uparrow\rangle}, p_{|\downarrow\rangle}, p_{|\uparrow\downarrow\Uparrow\rangle}) = (0, 1/2, 1/2, 0)$, and propagate the equations numerically over pump pulse (with $P \neq 0$), dark delay ($P = 0$), and probe ($P \neq 0$). The values of γ_A, P, β, r, $\xi_{\uparrow\downarrow}$ are used as fitting parameters. The evolution of the trion state population $p_{|\uparrow\downarrow\Uparrow\rangle}(t)$ reproduces the experimentally measured time-resolved ResFl (e.g. Fig. 1d). The simulated $p_{|\uparrow\downarrow\Uparrow\rangle}(t)$ traces are integrated over pump and probe intervals and are used to calculate the residual electron polarisation P_e in the same way $I_{\mathrm{ResFl,Pump}}$ and $I_{\mathrm{ResFl,Probe}}$ are used to calculate P_e from experimental data (e.g. Fig. 1e). The fitting parameters are adjusted to achieve two-objective optimisation: one objective is to minimise the root mean square difference between simulated and experimental $P_e(T_{\mathrm{Dark}})$ traces, the other objective is to match the characteristic exponential time in the falling edge of the ResFl intensity produced by the pump pulse. An example of the Pareto-optimal fitted $P_e(T_{\mathrm{Dark}})$ is shown by the dashed line in Fig. 1e, in good agreement with experiment (squares). The calculated falling edge time (87 ns) is also in good agreement with the experimental value ≈91 ns.

From fitting we find $r \approx 1.26 \times 10^5\ \mathrm{s}^{-1}$ (95% confidence interval [$0.47 \times 10^5\ \mathrm{s}^{-1}$, $3.34 \times 10^5\ \mathrm{s}^{-1}$]) and $\xi_{\uparrow\downarrow} \approx 1.65\ \mathrm{s}^{-1}$ [$1.16\ \mathrm{s}^{-1}$, $2.34\ \mathrm{s}^{-1}$], which correspond to the characteristic timescales of the fast and slow components, respectively, in the two-stage decay (squares in Fig. 1e). For Auger rate we obtain $\gamma_A \approx 1.09 \times 10^7\ \mathrm{s}^{-1}$ [$0.66 \times 10^7\ \mathrm{s}^{-1}$, $3.11 \times 10^7\ \mathrm{s}^{-1}$]. This is approximately five times higher than $\gamma_A \approx 0.23 \times 10^7\ \mathrm{s}^{-1}$ reported previously from time-resolved ResFl experiments[21]. The discrepancy could be due to the difference in QD structures, high optical pump power used in our experiments, limitations of a non-coherent rate equation model, and uncertainty in the fitted parameters. The uncertainty is increased by the interdependence of the fitting parameters γ_A, P, β, r, $\xi_{\uparrow\downarrow}$, which is inevitable since five parameters are used to fit essentially four degrees of freedom (fast and slow rates of the two stage $P_e(T_{\mathrm{Dark}})$ decay, P_e following fast decay and the characteristic time of the falling edges in fluorescence pulses). This uncertainty can also be understood to arise from the limited information provided by the ResFl measurement, which does not distinguish between spin shelving into the $|\downarrow\rangle$ state and Auger recombination into the $|0\rangle$ state, restricting the ability to monitor the full dynamics of the four-level system. The remaining best fit values are $P \approx 2.5 \times 10^9\ \mathrm{s}^{-1}$ [$0.34 \times 10^9\ \mathrm{s}^{-1}$, $3.16 \times 10^9\ \mathrm{s}^{-1}$] and $\beta \approx 5.2 \times 10^{-3}$ [0.75×10^{-3}, 20.1×10^{-3}].

Modelling of the nuclear spin relaxation rate

We start by noting that at all magnetic fields used in this study (B_z = 0.15–8 T) nuclear spin relaxation in an empty dot (0*e*) is at least an order of magnitude slower than at the centre of the 1*e* charging plateau. (In 0*e* regime we measure $\Gamma_N \approx 6.0 \times 10^{-4}\ \mathrm{s}^{-1}$ at $B_z = 0.15$ T, which reduces at higher fields below the minimum measurable level of $\Gamma_N < 10^{-4}\ \mathrm{s}^{-1}$.) This suggests that electron is the dominant mediator of nuclear spin relaxation in a Coulomb blockade regime (1*e*). Electron–nuclear coupling is given by the hyperfine Hamiltonian

$$\hat{\mathcal{H}}_{\mathrm{hf}} = \sum_k A_{\mathrm{hf},k}(\hat{s}_x\hat{I}_{x,k} + \hat{s}_y\hat{I}_{y,k} + \hat{s}_z\hat{I}_{z,k}), \tag{6}$$

where the summation goes over all nuclei, $A_{\mathrm{hf},k}$ is the hyperfine constant of the kth nucleus, $(\hat{s}_x, \hat{s}_y, \hat{s}_z)$ are the components of the electron spin-1/2 operator and $(\hat{I}_{x,k}, \hat{I}_{y,k}, \hat{I}_{z,k})$ are the components of the spin operator of the kth nucleus. The flip–flop term $\propto (\hat{s}_x\hat{I}_x + \hat{s}_y\hat{I}_y)$ of this interaction permits spin exchange between nuclear spin **I** and electron spin **s**, but at sufficiently large magnetic field, where electron Zeeman energy significantly exceeds nuclear Zeeman and quadrupolar spin splitting, such flip–flops are strongly suppressed. For a depolarised nuclear spin ensemble in an InAs QD, this threshold field would be on the order of 0.03 T, corresponding to statistical fluctuation $\propto A_{\mathrm{hf},k}\sqrt{N}$ of the nuclear hyperfine field acting on the electron. However, in self-assembled QDs the principal strain axis is generally misaligned[36,37] from the growth axis z, resulting in nuclear eigenstates which are superpositions of $\hat{I}_z$ eigenstates. Under these conditions nuclear spin states are mixed by the non-flip–flop part of the hyperfine interaction $A_{\mathrm{hf},k}\hat{I}_{z,k}\hat{s}_z$. This noncollinear interaction enables transitions between nuclear spin states $|i\rangle$ and $|j\rangle$ without transfer of spin to the electron. Using first-order perturbation and Weisskopf–Wigner approximation one arrives to Eq. (2) for nuclear spin relaxation rate between the pair of states $|i\rangle$ and $|j\rangle$, where we have assumed the same hyperfine constant $A_{\mathrm{hf},k} = A_{\mathrm{hf}}/N$ for all nuclei.

In order to calculate matrix element M_{ij} of $\hat{I}_z$ we consider spin $I = 3/2$ and assume that the principal component of electric field gradient is characterised by quadrupolar shift frequency ν_Q, and is tilted by angle α from the z-axis. Using first-order perturbation approach we calculate M_{ij} in the opposite limits of small magnetic field ($\gamma_N B_z \ll \nu_Q$, where γ_N is the nuclear gyromagnetic ratio) and high magnetic field ($\gamma_N B_z \gg \nu_Q$). For each individual nucleus the pair ($|i\rangle$, $|j\rangle$) with the largest off-diagonal matrix element is then selected leading to:

$$|M|^2_{B_z\to 0} = \frac{3}{4}\cos^2\alpha\sin^2\alpha \tag{7}$$

$$|M|^2_{B_z\to\infty} = \frac{3\pi\nu_Q^2}{8\gamma_N^2 B_z^2}\sin^4\alpha, \tag{8}$$

For intermediate fields we interpolate the matrix element with a monotonic function: $|M(B_z)|^2 = 1/(|M|^{-2}_{B_z\to 0} + |M|^{-2}_{B_z\to\infty})$, and the nuclear spin transition frequency is taken to be $\nu_{ij}^2 = (\gamma_N/2\pi)^2(B_z^2 + B_{z,\mathrm{min}}^2)$, where non-zero $B_{z,\mathrm{min}}$ reflects the fact that at $B_z = 0$ the spin states are split by nuclear quadrupolar effects. This model is a simplification since nuclear spin levels (anti)cross[38] at $B_z \approx 2\pi\nu_Q/\gamma_N$, where nucleus experiences a nearly zero effective magnetic field. The perturbative approach breaks down as M_{ij} is enhanced and $\nu_{ij} \approx 0$ at these anticrossing points (typically occurring at $B_z \approx 1$ T)[37], hence the introduction of $B_{z,\mathrm{min}}$ which softens the singularities in Eq. (2). While spin relaxation would be enhanced in such resonant nuclei, it would also prevent their optical polarisation, thus we effectively neglect their contribution to the overall measured nuclear spin decay in our simplified model.

In order to calculate the nuclear spin decay rate according to Eq. (2), we take $\tau_e = \Gamma_e^{-1}$, equivalent to assuming that electron spin flips are the only source of noise acting on the nuclear spins. For Γ_e we use Eq. (1) taking best fit parameters for each QD sample. Based on NMR spectroscopy of similar QDs[36,37], we model strain inhomogeneity within the quantum dot by considering a uniformly distributed quadrupolar shift $\nu_Q \in [0, 16]$ MHz with principal axis uniformly distributed on a part of a sphere with $\alpha \in [0°, 76°]$. The large values of $\alpha \approx 76°$ account for As nuclei, whose quadrupolar shifts are dominated by atomic scale disorder, arising from Ga and In alloying[36]. The gyromagnetic ratio is also varied uniformly $\gamma_N/2\pi \in [7.4, 9.2]$ MHz T^{-1} to account for five different isotopes[48] present in the dot (^{113}In, ^{115}In, ^{69}Ga, ^{71}Ga, ^{75}As). We take $B_{z,\mathrm{min}} = 0.06$ T and use an average value $A_{\mathrm{hf}} = 50$ μeV for all the isotopes[49]. The number of nuclei is taken to be $N = 4 \times 10^4$. The nuclear spin relaxation rate at a given magnetic field B_z is then calculated by averaging over all parameter distributions to take into account the contributions of the individual nuclei in a QD.

Despite the simplifications, the model is in good agreement with experimental dependence $\Gamma_N(B_z)$ in the $t_B = 37$ nm sample (thin dashed line in Fig. 3a) and $t_B = 42$ nm sample (Supplementary Fig. 2). Qualitative

comparison with Eq. (2) is possible in the high field limit where $\Gamma_e \propto B_z^4$, $|M_{ij}|^2 \propto B_z^{-2}$ and $v_{ij}^2 \propto B_z^2$ leading to $\Gamma_N \propto$ const, which agrees with the weak field dependence observed for all samples at $B_z \gtrsim 4$ T. By contrast, at fields $B_z \lesssim 4$ T, nuclear spin relaxation rate is determined by a combination of different factors prohibiting simple analytical description. Better description of the $\Gamma_N(B_z)$ dependence, including the discrepancies with the thick-barrier ($t_B = 52$ nm) sample experiments, would require a more detailed model, which takes into account hyperfine fluctuations unrelated to electron spin flips, contributions of both noncollinear and direct hyperfine interaction, electron–nuclear spin feedback[17], quadrupolar anticrossings[36,37] of the individual nuclear spin levels and electron-mediated nuclear–nuclear interactions[15].

DATA AVAILABILITY

The data that support the findings of this study are available from the corresponding authors upon reasonable request.

Received: 31 October 2020; Accepted: 26 January 2021;
Published online: 24 February 2021

REFERENCES

1. Kimble, H. J. The quantum internet. *Nature* **453**, 1023 (2008).
2. Delteil, A. et al. Generation of heralded entanglement between distant hole spins. *Nat. Phys.* **12**, 218 (2016).
3. Schwartz, I. et al. Deterministic generation of a cluster state of entangled photons. *Science* **354**, 434–437 (2016).
4. Javadi, A. et al. Spin–photon interface and spin-controlled photon switching in a nanobeam waveguide. *Nat. Nanotechnol.* **13**, 398–403 (2018).
5. Gangloff, D. A. et al. Quantum interface of an electron and a nuclear ensemble. *Science* **364**, 62–66 (2019).
6. Chekhovich, E. A., da Silva, S. F. C. & Rastelli, A. Nuclear spin quantum register in an optically active semiconductor quantum dot. *Nat. Nanotechnol.* **15**, 999–1004 (2020).
7. Urbaszek, B. et al. Nuclear spin physics in quantum dots: An optical investigation. *Rev. Mod. Phys.* **85**, 79–133 (2013).
8. Merkulov, I. A., Efros, A. L. & Rosen, M. Electron spin relaxation by nuclei in semiconductor quantum dots. *Phys. Rev. B* **65**, 205309 (2002).
9. Kroutvar, M. et al. Optically programmable electron spin memory using semiconductor quantum dots. *Nature* **432**, 81–84 (2004).
10. Lu, C.-Y. et al. Direct measurement of spin dynamics in InAs/GaAs quantum dots using time-resolved resonance fluorescence. *Phys. Rev. B* **81**, 035332 (2010).
11. Linpeng, X. et al. Longitudinal spin relaxation of donor-bound electrons in direct band-gap semiconductors. *Phys. Rev. B* **94**, 125401 (2016).
12. Vaughan, M. P. & Rorison, J. M. Model expressions for the spin-orbit interaction and phonon-mediated spin dynamics in quantum dots. *Semicond. Sci. Technol.* **33**, 014001 (2017).
13. Huang, C.-W. & Hu, X. Theoretical study of nuclear spin polarization and depolarization in self-assembled quantum dots. *Phys. Rev. B* **81**, 205304 (2010).
14. Dreiser, J. et al. Optical investigations of quantum dot spin dynamics as a function of external electric and magnetic fields. *Phys. Rev. B* **77**, 075317 (2008).
15. Latta, C., Srivastava, A. & Imamoglu, A. Hyperfine interaction-dominated dynamics of nuclear spins in self-assembled InGaAs quantum dots. *Phys. Rev. Lett.* **107**, 167401 (2011).
16. Houel, J. et al. Probing single-charge fluctuations at a GaAs/AlAs interface using laser spectroscopy on a nearby InGaAs quantum dot. *Phys. Rev. Lett.* **108**, 107401 (2012).
17. Chekhovich, E. A. et al. Dynamics of optically induced nuclear spin polarization in individual InP/GaInP quantum dots. *Phys. Rev. B* **81**, 245308 (2010).
18. Heiss, D. et al. Observation of extremely slow hole spin relaxation in self-assembled quantum dots. *Phys. Rev. B* **76**, 241306 (2007).
19. Kim, J. H., Vagner, I. D. & Xing, L. Phonon-assisted mechanism for quantum nuclear-spin relaxation. *Phys. Rev. B* **49**, 16777–16780 (1994).
20. Dahan, P. & Vagner, I. D. Nuclear spin relaxation rate of magnetic impurities in quantum Hall effect systems. *Phys. Rev. B* **72**, 115328 (2005).
21. Kurzmann, A., Ludwig, A., Wieck, A. D., Lorke, A. & Geller, M. Auger recombination in self-assembled quantum dots: quenching and broadening of the charged exciton transition. *Nano Lett.* **16**, 3367–3372 (2016).
22. Atatüre, M. et al. Quantum-dot spin-state preparation with near-unity fidelity. *Science* **312**, 551–553 (2006).
23. Warburton, R. J. et al. Optical emission from a charge-tunable quantum ring. *Nature* **405**, 926–929 (2000).
24. Löbl, M. C. et al. Radiative Auger process in the single-photon limit. *Nat. Nanotechnol.* **15**, 558–562 (2020).
25. Lyanda-Geller, Y. B., Aleiner, I. L. & Altshuler, B. L. Charging effects on nuclear spin relaxation in quantum dots. *J. Supercond. Nov. Magn.* **16**, 751–761 (2003).
26. Khaetskii, A. V. & Nazarov, Y. V. Spin–flip transitions between Zeeman sublevels in semiconductor quantum dots. *Phys. Rev. B* **64**, 125316 (2000).
27. Smith, J. M. et al. Voltage control of the spin dynamics of an exciton in a semiconductor quantum dot. *Phys. Rev. Lett.* **94**, 197402 (2005).
28. Camenzind, L. C. et al. Hyperfine-phonon spin relaxation in a single-electron GaAs quantum dot. *Nat. Commun.* **9**, 3454 (2018).
29. Kleemans, N. A. J. M. et al. Many-body exciton states in self-assembled quantum dots coupled to a Fermi sea. *Nat. Phys.* **6**, 534–538 (2010).
30. Cunningham, J. E., Chiu, T. H., Tell, B. & Jan, W. Atomic diffusion and surface segregation of Si in δ-doped GaAs grown by gas source molecular beam epitaxy. *J. Vac. Sci. Technol. B* **8**, 157–159 (1990).
31. De Franceschi, S. et al. Electron cotunneling in a semiconductor quantum dot. *Phys. Rev. Lett.* **86**, 878–881 (2001).
32. Küng, B. et al. Quantum dot occupation and electron dwell time in the cotunneling regime. *New J. Phys.* **14**, 083003 (2012).
33. Lu, J. et al. Nuclear spin-lattice relaxation in *n*-type insulating and metallic GaAs single crystals. *Phys. Rev. B* **74**, 125208 (2006).
34. Erlingsson, S. I. & Nazarov, Y. V. Hyperfine-mediated transitions between a Zeeman split doublet in GaAs quantum dots: The role of the internal field. *Phys. Rev. B* **66**, 155327 (2002).
35. Woods, L. M., Reinecke, T. L. & Lyanda-Geller, Y. Spin relaxation in quantum dots. *Phys. Rev. B* **66**, 161318 (2002).
36. Chekhovich, E. A. et al. Structural analysis of strained quantum dots using nuclear magnetic resonance. *Nat. Nanotechnol.* **7**, 646–650 (2012).
37. Bulutay, C. Quadrupolar spectra of nuclear spins in strained $In_xGa_{1-x}As$ quantum dots. *Phys. Rev. B* **85**, 115313 (2012).
38. Maletinsky, P., Kroner, M. & Imamoglu, A. Breakdown of the nuclear-spin-temperature approach in quantum-dot demagnetization experiments. *Nat. Phys.* **5**, 407–411 (2009).
39. Vladimirova, M. et al. Nuclear spin relaxation in *n*-GaAs: from insulating to metallic regime. *Phys. Rev. B* **95**, 125312 (2017).
40. McNeil, J. A. & Clark, W. G. Nuclear quadrupolar spin-lattice relaxation in some III–V compounds. *Phys. Rev. B* **13**, 4705–4713 (1976).
41. Bechtold, A. et al. Three-stage decoherence dynamics of electron spin qubits in an optically active quantum dot. *Nat. Phys.* **11**, 1005–1008 (2015).
42. Zhai, L. et al. Low-noise GaAs quantum dots for quantum photonics. *Nat. Commun.* **11**, 4745 (2020).
43. Akimov, I. A., Feng, D. H. & Henneberger, F. Electron spin dynamics in a self-assembled semiconductor quantum dot: the limit of low magnetic fields. *Phys. Rev. Lett.* **97**, 056602 (2006).
44. Ragunathan, G. et al. Direct measurement of hyperfine shifts and radio frequency manipulation of nuclear spins in individual CdTe/ZnTe quantum dots. *Phys. Rev. Lett.* **122**, 096801 (2019).
45. Grovenor, C. Metallurgical reactions in Au/(In–Ge) ohmic contacts to GaAs. *Thin Solid Films* **104**, 409–418 (1983).
46. Kuhlmann, A. V. et al. A dark-field microscope for background-free detection of resonance fluorescence from single semiconductor quantum dots operating in a set-and-forget mode. *Rev. Sci. Instrum.* **84**, 073905 (2013).
47. Dalgarno, P. A. et al. Coulomb interactions in single charged self-assembled quantum dots: radiative lifetime and recombination energy. *Phys. Rev. B* **77**, 245311 (2008).
48. Harris, R. K., Becker, E. D., de Menezes, S. M. C., Goodfellow, R. & Granger, P. NMR nomenclature. nuclear spin properties and conventions for chemical shifts (IUPAC Recommendations 2001). *Pure Appl. Chem.* **73**, 1795–1818 (2001).
49. Checkhovich, E. A. et al. Element-sensitive measurement of the hole-nuclear spin interaction in quantum dots. *Nat. Phys.* **9**, 74–78 (2013).

ACKNOWLEDGEMENTS

I.M.G. processed samples into Schottky diodes with input and advice from S. Kumar, B. Royal, I. Farrer, N. Babazadeh, K. Kennedy, A.U., and B. Harrison. E.C. acknowledges P. Patil, I. Farrer and J. Heffernan. Royal Society provided funding support to E.A.C. through University Research Fellowship and grant RGF\EA\180117, and to G.G. and E. A.C. through grant RG150465. Experimental costs were part-funded through EPSRC grant EP/N031776/1.

AUTHOR CONTRIBUTIONS

G.G., E.A.C. and A.U. developed time-resolved resonance fluorescence techniques. G. G., G.R., and E.A.C. developed nuclear spin lifetime measurement techniques. G.G. and E.A.C. conducted spin lifetime measurements. I.M.G., C.M. and E.A.C. conducted photoluminescence experiments. E.C. grew the samples. G.G. and E.A.C. analysed the data and wrote the manuscript. E.A.C. coordinated the project.

COMPETING INTERESTS

The authors declare no competing interests.

ADDITIONAL INFORMATION

Supplementary information The online version contains supplementary material available at https://doi.org/10.1038/s41534-021-00378-2.

Correspondence and requests for materials should be addressed to E.A.C.

Reprints and permission information is available at http://www.nature.com/reprints

Publisher's note Springer Nature remains neutral with regard to jurisdictional claims in published maps and institutional affiliations.

Supplementary Information: Fundamental limits of electron and nuclear spin qubit lifetimes in an isolated self-assembled quantum dot

G. Gillard, I. M. Griffiths, G. Ragunathan, A. Ulhaq, C. McEwan, E. Clarke, and E. A. Chekhovich

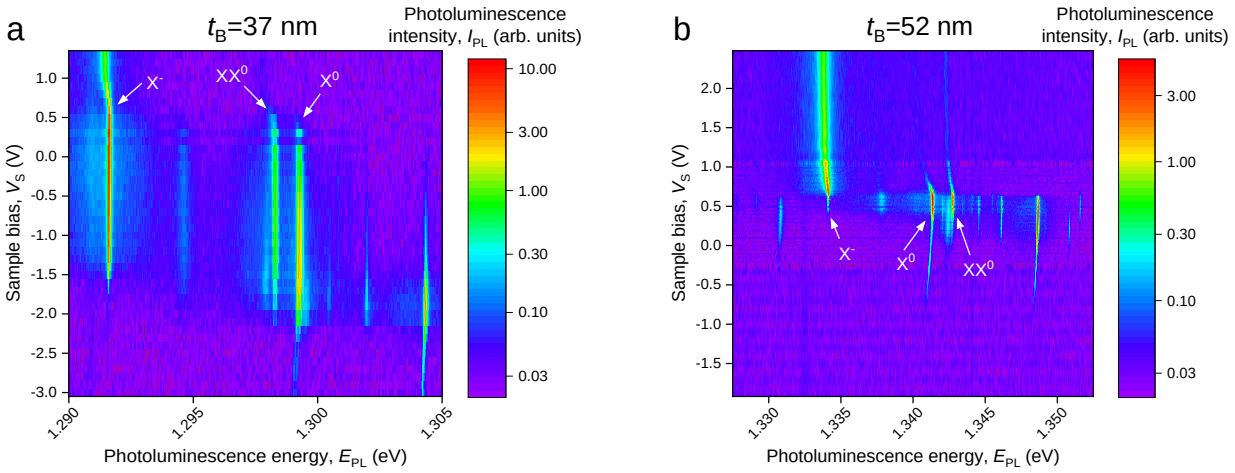

Supplementary Figure 1. **Photoluminescence (PL) spectroscopy of quantum dots. a,** Photoluminescence spectra of an individual quantum dot in a sample with tunnel barrier thickens $t_B = 37$ nm. Color plots show spectra measured at different values of sample bias V_S. **b,** Same for a sample with $t_B = 52$ nm. All spectra are taken at a temperature of $\theta \approx 6$ K using 850 nm laser excitation, resonant with the wetting layer states. The neutral exciton X^0 and biexciton XX^0 states are identified from the doublet structure (visible in **a**) and additional measurements with linearly polarised luminescence detection. The emission of a negatively charged trion X^- is redshifted from X^0 by ≈ 7 meV, which is typical for InAs/GaAs dots[1]. Note that stability conditions of a resident charge are generally different from stability conditions of the corresponding exciton complex with an extra electron-hole pair[1]. As a result of this difference X^- PL is observed in a wide range of biases (from $V_S \approx -1.5$ V to $+1$ V in **a**), while the single-electron state $1e$ is stable in a narrower range (from $V_S \approx +0.1$ V to $+0.3$ V in Fig. 2a-c).

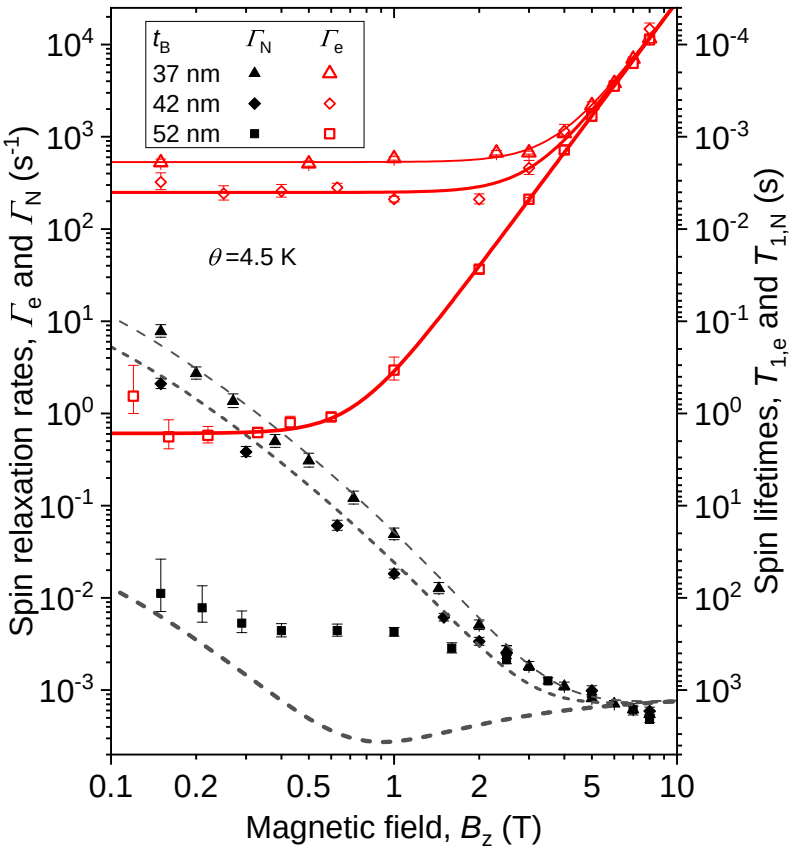

Supplementary Figure 2. **Magnetic field dependence of electron and nuclear spin dynamics in Coulomb blockade regime.** This figure reproduces Fig. 3a with the addition of the data for a sample with an intermediate tunnel barrier $t_B = 42$ nm (diamonds). Electron spin relaxation rate Γ_e is shown by the open symbols (experiment) and solid lines (model fitting). Nuclear spin relaxation rate Γ_N is shown by the solid symbols (experiment) and dashed lines (model fitting). For each sample Γ_e and Γ_N are measured on the same individual quantum dot at a base temperature $\theta \approx 4.5$ K.

Supplementary Note 1. DESIGN OF THE SPIN DYNAMICS EXPERIMENTS

A. Electron spin dynamics

In order to observe QD electron spin dynamics, we employ time-resolved resonance fluorescence. Pump and probe laser pulses that produce fluorescence signal are synchronized with sample bias V_S pulses, which control the state of the dot and the tunnel coupling to Fermi reservoir (Supplementary Fig. 3a).

Between the measurement cycles the dot is 'flushed' under bias V_{Flush} over time $T_{Flush} = 2000$ μs. We choose V_{Flush} to match one of the resonance fluorescence intensity peaks at the edges of the

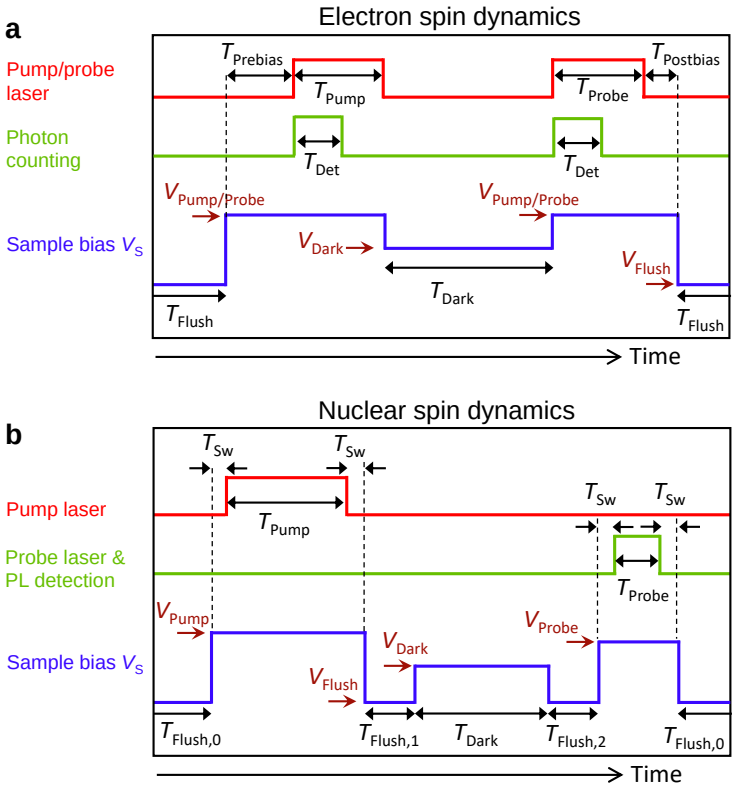

Supplementary Figure 3. **Design of the spin dynamics experiments. a,** Timing diagram of one cycle of the electron spin dynamics measurements. The lines show (from top to bottom): resonant laser pulses, photon counting gating, sample bias V_S. **b,** Cycle diagram in a nuclear spin decay experiment showing (from top to bottom): nonresonant pump laser pulse, nonresonant probe laser pulse and PL gating, sample bias V_S. See discussion in Supplementary Note 2

1e plateau (e.g. $V_S = 0.1$ V or $V_S = 0.32$ V in Fig. 2a). Under these conditions fast resonant tunneling of the electron depolarises the nuclear spin bath of the quantum dot and suppresses the undesired fluctuations of the optical transition energy due to 'dragging' effects[2]. After flushing, the bias is changed to $V_{\mathrm{Pump/Probe}}$, corresponding to the centre of the 1e plateau (e.g. $V_S = 0.2$ V in Fig. 2a), and kept for $T_{\mathrm{Prebias}} = 300$ μs to ensure the dot achieves a steady-state charging with one electron prior to optical spin pumping. After the resonant laser pump pulse with duration in the range $T_{\mathrm{Pump}} = 5 - 10$ μs, the bias is switched to V_{Dark}, which can be stepped over the 1e plateau in bias dependent experiments (e.g. Fig. 2b,e). Following the dark delay T_{Dark}, the bias is once again switched to $V_{\mathrm{Pump/Probe}}$ and a probe laser pulse identical to the pump is applied. Finally, after a short delay $T_{\mathrm{Postbias}} = 10$ μs, the bias is tuned to flush and experiment proceeds to the next cycle. Photon counting pulses of the resonance fluorescence signal are recorded on a digital oscilloscope and, when averaged, produce traces such as in Fig. 1d. Delays in the triggering

system of the oscilloscope mean that only a fraction of experimental cycles can be collected. For that reason the pulses are additionally accumulated over the initial time windows $T_{\mathrm{Det}} = 0.5$ μs of the pump and probe pulses using gated digital counters. While the counters do not provide temporal resolution, the signal is collected in full, providing accurate measurement of the residual electron spin polarisation P_{e} (e.g. Fig. 1e).

B. Nuclear spin dynamics

The timing of a nuclear spin decay measurement cycle is shown in Supplementary Fig. 3b. The sample bias is synchronized with pump and probe pulses. Nuclear spins are polarised with a high power optical pump with duration in the range $T_{\mathrm{Pump}} = 3 - 90$ s. During the pump the bias V_{Pump} is kept in the range from -1.0 V to $+1.3$ V, depending on the sample and individual QD. V_{Pump} is chosen from additional calibration experiments to maximize the nuclear spin polarisation and in some QDs corresponds to forward bias of the structure. Optical illumination under forward bias generates trapped charges, which quench PL and may affect the spin dynamics. To avoid this, the dot is flushed in the dark for $T_{\mathrm{Flush,1}} = 0.1$ s at $V_{\mathrm{Flush}} = -1.5$ V after each optical pump to remove the charges. Nuclear spin relaxation is very slow at $V_{\mathrm{Flush}} = -1.5$ V, so the flush has minimal effect on the measured nuclear spin decay. After the flush, the bias is switched to the desired level V_{Dark} for time T_{Dark}. Before the optical probe, the sample is flushed once again for $T_{\mathrm{Flush,2}} = 0.02$ s. The bias of the probe pulse $V_{\mathrm{Probe}} = 0.6 - 0.65$ V is chosen to maximize PL intensity of the negatively charged trion X^{-}, and its duration $T_{\mathrm{Probe}} = 0.01 - 0.015$ s coincides with the time window for PL collection and spectral analysis. Between the measurement cycles the dot is kept under flush bias for $T_{\mathrm{Flush,0}} = 0.015$ s. Optical pump and probe pulses, as well as gating of PL collection are implemented using mechanical shutters. To account for their finite switching time, a short delay $T_{\mathrm{Sw}} = 0.008$ s is introduced between fast bias switching and electrical pulses controlling the shutters.

Supplementary Note 2. FIDELITY OF ELECTRON SPIN INITIALISATION

We analyse the effect of Auger recombination and quantum dot recharging on the fidelity of electron spin optical initialisation. To this end we derive an analytical steady-state solution of the rate equation (Eq. 4 of the main text). The steady-state solution vector $(p_{|0\rangle}, p_{|\uparrow\rangle}, p_{|\downarrow\rangle}, p_{|\uparrow\downarrow\Uparrow\rangle})$ under resonant optical excitation is found as a null space of the equation matrix (Eq. 5). Once optical

excitation is turned off, the probability $p_{|\uparrow\downarrow\Uparrow\rangle}$ will quickly decay to zero due to trion recombination. This is taken into account by redistributing $p_{|\uparrow\downarrow\Uparrow\rangle}$ into the remaining probabilities $p_{|0\rangle}, p_{|\uparrow\rangle}, p_{|\downarrow\rangle}$ with weights given by the rates of the corresponding processes $\gamma_{\mathrm{A}}, \gamma_{\mathrm{R}}, \beta\gamma_{\mathrm{R}}$. After that, if the dot is emptied by Auger recombination, recharging takes place, which corresponds to redistributing $p_{|0\rangle}$ with equal weights into $p_{|\uparrow\rangle}$ and $p_{|\downarrow\rangle}$. This completes the process of electron spin optical initialisation, which leaves electron in either of the two spin states $|\uparrow\rangle$ or $|\downarrow\rangle$. The fidelity of initialisation is then given by the electron spin polarisation degree:

$$P_{\mathrm{e}} = p_{|\uparrow\rangle} - p_{|\downarrow\rangle} = \frac{rP\left(-\left(\gamma_A + 2\beta\gamma_R\right)\left(\gamma_A + (\beta+1)\gamma_R\right) - 2(\beta-1)\xi_{\uparrow\downarrow}\gamma_R\right)}{\left(\gamma_A + (\beta+1)\gamma_R\right)\left(\gamma_A(P(2\xi_{\uparrow\downarrow}+r) + 4\xi_{\uparrow\downarrow}r) + 2r\left(\xi_{\uparrow\downarrow}P + \gamma_R(2(\beta+1)\xi_{\uparrow\downarrow} + \beta P)\right)\right)} \tag{S1}$$

The fidelity depends on different relaxation rates and the expression is somewhat bulky. However, by analyzing the derivatives it is possible to show that for all practically relevant cases faster recharging rate r gives better fidelity (larger absolute value $|P_{\mathrm{e}}|$). Moreover, fidelity is generally improved by slower electron spin relaxation $\xi_{\uparrow\downarrow}$ and larger trion state admixture parameter β. On the other hand, the effect of the Auger rate γ_{A} depends on the values of other relaxation rates. According to Eq. S1 spin initialisation becomes impossible ($P_{\mathrm{e}} \to 0$) in the absence of reliable recharging ($r \to 0$): indeed, to form a qubit the QD needs to be charge with an electron in the first place either from a Fermi reservoir or from a nearby semiconductor impurity.

Supplementary Note 3. TABULATED DATA

Here we present tabulated data, including the raw data used in the figures.

A. Electron spin lifetimes

Here we present electron spin lifetimes $T_{1,\mathrm{e}}$ measured as a function of magnetic field B_z in quantum dot samples with different tunnel barriers t_{B}. The numbers are obtained from exponential fitting of the measured electron spin depolarisation. Error estimates are 95% confidence intervals.

Results for $t_{\mathrm{B}} = 37$ nm (open triangles in Supplementary Fig. 2):

B_z (T)	$T_{1,\mathrm{e}}$ (s)
0.15	$0.00189869 \pm 0.000151588$
0.5	$0.00195518 \pm 0.000126302$
1	$0.00171756 \pm 0.0000744649$
2.3	$0.00148989 \pm 0.00008131$
3	$0.00148683 \pm 0.000053571$
4	$0.000916972 \pm 0.0000599$
5	$0.000457006 \pm 0.0000389$
6	$0.000262523 \pm 0.0000115$
7	$0.00014334 \pm 0.00000748$
8	$0.0000860168 \pm 0.00000806$

(S2)

Results for $t_{\mathrm{B}} = 42$ nm (open diamonds in Supplementary Fig. 2):

B_z (T)	$T_{1,\mathrm{e}}$ (s)
0.15	$0.00309782 \pm 0.000640384$
0.25	$0.0041252 \pm 0.000722782$
0.4	$0.00389998 \pm 0.000614786$
0.63	$0.00355091 \pm 0.000362972$
1	$0.00475734 \pm 0.000327926$
2	$0.00475795 \pm 0.000590551$
3	0.00218 ± 0.000377752
4	$0.000864482 \pm 0.000131119$
8	$0.0000675538 \pm 0.000009148$

(S3)

Results for $t_{\mathrm{B}} = 52$ nm (open squares in Supplementary Fig. 2):

B_z (T)	$T_{1,\mathrm{e}}$ (s)
0.12	0.650457 ± 0.349529
0.16	1.79786 ± 0.623995
0.22	1.73346 ± 0.350849
0.33	1.61519 ± 0.199896
0.43	1.25995 ± 0.186163
0.6	1.09469 ± 0.0987524
1	0.339526 ± 0.0952452
2	0.0273806 ± 0.00243508
3	$0.00477182 \pm 0.00021804$
4	$0.00138957 \pm 0.00012975$
5	$0.000596735 \pm 0.00008352$
6	$0.000282641 \pm 0.00003359$
7	$0.000159886 \pm 0.00001909$
8	$0.0000888053 \pm 0.00000608$

(S4)

B. Nuclear spin lifetimes

Here we present nuclear spin lifetimes $T_{1,\mathrm{N}}$ measured as a function of magnetic field B_z in quantum dot samples with different tunnel barriers t_{B}. Error estimates are 95% confidence intervals.

Results for $t_{\mathrm{B}} = 37$ nm (solid triangles in Supplementary Fig. 2):

B_z (T)	$T_{1,\mathrm{N}}$ (s)
0.15	0.128887 ± 0.0200696
0.2	0.36857 ± 0.0559658
0.27	0.738735 ± 0.126206
0.38	2.01091 ± 0.320033
0.5	3.25741 ± 0.553301
0.72	8.28599 ± 1.33143
1	20.4342 ± 2.93934
1.44	79.1195 ± 10.882
2	196.939 ± 23.6121
2.5	371.864 ± 40.8411
3	550.259 ± 61.2703
4	907.88 ± 89.556
5	1226.49 ± 106.751
6	1405.36 ± 106.601
7	1620.3 ± 122.295
8	1830.19 ± 130.303

(S5)

Results for $t_{\mathrm{B}} = 42$ nm (solid diamonds in Supplementary Fig. 2):

B_z (T)	$T_{1,\mathrm{N}}$ (s)
0.15	0.476704 ± 0.060443
0.3	2.60955 ± 0.328726
0.63	16.4288 ± 2.04592
1	54.6469 ± 5.89249
1.5	162.594 ± 15.5768
2	296.841 ± 29.4867
2.5	390.403 ± 62.7901
5	1012.91 ± 113.703
8	1689.63 ± 157.518

(S6)

Results for $t_{\mathrm{B}} = 52$ nm (solid squares in Supplementary Fig. 2):

B_z (T)	$T_{1,\mathrm{N}}$ (s)
0.15	89.4321 ± 51.4728
0.21	128.526 ± 54.506
0.29	188.409 ± 49.8251
0.4	227.143 ± 37.287
0.63	225.879 ± 33.7603
1	234.635 ± 25.3402
1.6	351.177 ± 44.1603
2.5	468.241 ± 49.8137
3.5	794.271 ± 59.6212
5	1100.9 ± 87.0357
7	1632.23 ± 225.801
8	2082.21 ± 172.213

(S7)

Here we present nuclear spin lifetimes $T_{1,\mathrm{N}}$ measured as a function of sample temperature θ at magnetic field $B_z = 8$ T in a quantum dot sample with tunnel barrier thickness $t_{\mathrm{B}} = 52$ nm. Error estimates of $T_{1,\mathrm{N}}$ are 95% confidence intervals. The uncertainty in sample temperature is ± 0.5 K. Results are shown by the symbols in Fig. 3d of the main text:

θ (K)	$T_{1,\mathrm{N}}$ (s)
4.5 ± 0.5	1547.79 ± 123.901
8.17 ± 0.5	947.942 ± 61.6851
12.3 ± 0.5	678.778 ± 40.066
15.3 ± 0.5	433.259 ± 25.4814
20.1 ± 0.5	177.321 ± 9.73723

(S8)

SUPPLEMENTARY REFERENCES

[1] Dalgarno, P. A. *et al.* Coulomb interactions in single charged self-assembled quantum dots: Radiative lifetime and recombination energy. *Phys. Rev. B* **77**, 245311 (2008).

[2] Latta, C. *et al.* Confluence of resonant laser excitation and bidirectional quantum-dot nuclear-spin polarization. *Nat. Phys.* **5**, 758–763 (2009).

5

Using nuclear spins for millisecond coherence storage and single-shot readout of an electron spin qubit

So far we have studied the loss of energy of the spin states to the environment, quantified by T_1. Now we must consider the loss of phase information of a coherent state, defined by the coherence time T_2. To investigate T_2, we require the ability to coherently rotate the spin projection into the equatorial plane of the Bloch sphere, allowing us to perform the necessary spin echo sequences for measurement of T_2. As highlighted previously, coherent control of the electron can be carried out using either optical [31] or magnetic resonance [32] techniques. The use of magnetic resonance techniques for coherent electron spin control has proven challenging, however, there is extensive work on pulsed nuclear magnetic resonance which allows us to investigate the coherence of the nuclear spin ensemble $T_{2,\mathrm{N}}$. Understanding the mechanisms limiting nuclear coherence will provide a more complete description of the environment of the electron spin qubit, in addition to exploring the possibility of using the nuclear spins as a quantum resource. We have briefly covered the limiting factors of nuclear spin ensemble coherence $T_{2,\mathrm{N}}$ in Section 2.4.2. The constituent nuclei of the $I > 3/2$

nuclear spin bath within the InGaAs/GaAs QD system are coupled via dipole-dipole interaction, fundamentally limiting coherence time $T_{2,N}$ to $\approx$ 1 - 10 ms in an uncharged QD [112]. Extension to $T_{2,N}$ through dynamical decoupling techniques is successful in uncharged QDs [114], however, the charging of a QD with an electron complicates the nuclear spin bath coherence as the system takes the form of the central spin model. Here, a central spin with a large magnetic moment interacts with a bath of spins with comparatively smaller magnetic moments, ultimately limiting the coherence of both systems. Previous investigations have found that nuclear spin ensemble coherence time for a charged QD, $T_{2,\mathrm{N}}^{(1e)}$, is dramatically reduced to $T_{2,\mathrm{N}}^{(1e)} \approx 20\ \mu$s. The reduction was attributed to a hyperfine-mediated decoherence mechanism [136], which would vary depending on both hyperfine coupling strength and magnetic field $T_{2,\mathrm{N}}^{(1e)} \propto B_z^2 A^{-3}$. Ultimately, these results led to the conclusion that long nuclear spin coherence in the presence of an electron would prove challenging.

The promising long lifetime results from Chapter 4 opened up a new opportunity to investigate charged QD nuclear spin coherence in the limit of slow electron spin fluctuations ($\Gamma_e = 1/T_{1,e} \approx 1\ \mathrm{s}^{-1}$). Here, we investigate the dynamics of the nuclear spin ensemble in the transverse plane using pulsed NMR. We measure pure dephasing $T_{2,\mathrm{N}}^{*}$ through free induction decay measurements for both a charged and uncharged QD, in addition to the coherence $T_{2,\mathrm{N}}$ from Hahn echo pulse sequences. From the study of $T_{2,\mathrm{N}}$ in a charged QD at a variety of static magnetic fields B_z, we can develop a spectral diffusion model describing the effect of a fluctuating electron spin on the nuclear spin ensemble. In addition to this, we demonstrate for the first time that the recently developed CHASE dynamical decoupling sequence [114] is successful in extending nuclear spin ensemble coherence in a charged QD. Further investigation into the effect of the fluctuating electron spin enabled us to develop a novel single-shot electron spin readout technique utilising the Knight shift to encode the electron spin state onto the nuclear spin bath collective coherence.

The results in this chapter are presented in the form of a manuscript that has been submitted for peer review.

Using nuclear spins for millisecond coherence storage and single-shot readout of an electron spin qubit

George Gillard,[1,*] Edmund Clarke,[2] and Evgeny A. Chekhovich[1,†]

[1] *Department of Physics and Astronomy, University of Sheffield, Sheffield S3 7RH, United Kingdom*
[2] *Department of Electronic and Electrical Engineering, University of Sheffield, Sheffield S1 3JD, UK*

(Dated: December 5, 2021)

The original approach to quantum dot spin qubits viewed the environment nuclear spins as a decoherence source [1–3]. Recently, attention shifted to hybrid approaches, where nuclear spins are interfaced to the electron spin qubit [4, 5] and used as quantum memory [6] or qubit registers [7]. These approaches require long-term collective nuclear spin coherence, which proved to be evasive due to the decoherence induced by the electron spin [8]. Here we successfully address this problem by demonstrating millisecond long nuclear spin coherence in InGaAs semiconductor quantum dots, which can be extended further using dynamical decoupling [9]. Similarly long coherence is achieved when quantum dot is empty or charged with a single electron, which we explain in terms of spectral diffusion theory [10, 11]. These results provide understanding of the many-body coherence in central spin systems, required for development of electron-nuclear spin qubits – as a demonstration, we implement here a conditional gate that encodes electron spin state onto collective nuclear spin coherence, and use it for a single-shot readout of the electron spin qubit with $> 99.8\%$ fidelity.

Central spin model describes a single electron spin $\mathbf{s}$ whose hyperfine interaction with an ensemble of nuclear spins $\mathbf{I}_j$ is characterized by coupling constants A_j (Fig. 1a). Magnetic interactions between the nuclei with pairwise coupling constants $b_{j,k}$, together with inhomogeneity in A_j, result in complex spin dynamics [3, 12]. This problem is of interest, as it describes solid-state qubit systems developed for quantum information processing. Nuclear spins offer uniquely long coherence storage, making them attractive as buffer memories in photonic quantum information processing systems [13]. In group IV materials, such as diamond and silicon, nuclear spins can be diluted, allowing quantum states of individual nuclei to be addressed in point defects [14] and gate-defined quantum dots (QDs) [4]. In the optically active III-V QDs all nuclei have spins – understanding their collective dynamics, characterised by coherence time $T_{2,\mathrm{N}}$, is crucial for the design of qubits.

In a typical epitaxial device (Fig. 1a) a Fermi reservoir of electrons is introduced, and electric field is applied through the gate voltage V_G, to control the charge state of the QD. In an empty ($0e$) InGaAs QD the nuclear-nuclear interactions limit the coherence time to a few millisecond range [8, 9] ($T_{2,\mathrm{N}}^{(0e)} \propto 1/\max(h|b_{j,k}|)$, where h is Planck's constant). The spin of a single electron ($1e$) induces hyperfine shifts in precession frequencies, ranging from $\max(|A_j|)/h \approx 100$ kHz for nuclei at the centre of the QD to zero. These shifts, known as Knight shifts, result in short nuclear spin dephasing times $T_{2,\mathrm{N}}^{*,(1e)} \approx 3$ μs. Refocusing this inhomogeneity with spin echo [15] previously gave little improvement [8], with nuclear coherence limited to $T_{2,\mathrm{N}}^{(1e)} \approx 20$ μs. However, to fully understand the QD coherence, one must take into account the effects of the electron Fermi reservoir.

By minimizing the tunnel coupling between QD and the Fermi reservoir, we achieve isolated-qubit regime, with a two orders of magnitude improvement in collective nuclear spin coherence, exceeding milliseconds. For a wide range of magnetic fields $B_z = 0.25 - 8$ T, nuclear spin coherence is well described as spectral diffusion induced by a randomly fluctuating electron central spin. Our results show that electron central spin is not an obstacle for long nuclear spin ensemble coherence, enabling a variety of nanoscale designs using quantum states of electron and nuclear spins.

We study diode structures (Fig. 1a) with tunnel barrier $t_\mathrm{B} = 37$ or 52 nm, thick enough to ensure long single electron spin lifetimes $T_{1,\mathrm{e}}$ of ≈ 1 ms or ≈ 1 s, respectively [16]. We investigate spin-3/2 nuclei of ^{75}As, ^{69}Ga and ^{71}Ga. With magnetic field B_z applied along the sample growth axis, nuclear states with spin projections $I_\mathrm{z} = \pm 1/2$ form effective spin-1/2 ensembles that we focus on. Hyperfine interaction between the electron spin and nuclear spins (see Supplementary Note 1) provides a tool both for hyperpolarisation of the nuclei via optical pumping, and for detection of the nuclear ensemble polarisation via hyperfine shifts E_hf in the optical emission spectra of the QD electrons [17]. The reciprocal hyperfine effect of the electron spin is characterised by the Knight shifts in the nuclear magnetic resonance (NMR) frequencies.

We examine the collective coherence of the QD nuclear spins using optically detected NMR protocol (Fig. 1b). Figure 1c shows the result of an NMR experiment, where a single resonant radio-frequency (rf) burst of duration t_rf induces coherent Rabi oscillations between the $I_\mathrm{z} = -1/2$ and $+1/2$ nuclear spin states. The inhomogeneous Knight shifts $\nu_{\mathrm{e},j} \propto A_j$ induced by the electron

* ggillard1@sheffield.ac.uk
† e.chekhovich@sheffield.ac.uk

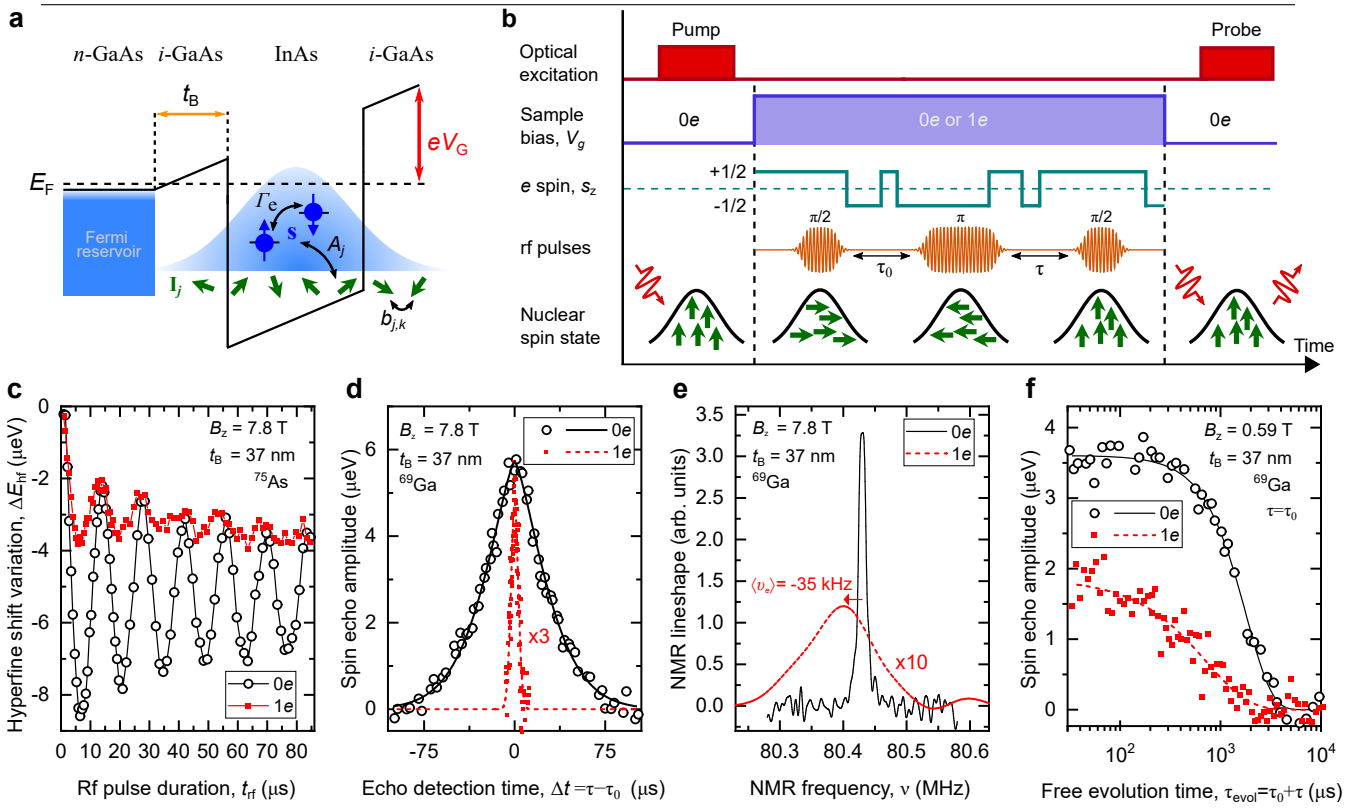

FIG. 1. **Coherent control of nuclear spins coupled to quantum dot electron spin qubit. a,** Schematic of a conduction band edge in an n-i-Schottky diode structure containing InGaAs QDs, separated from the electron Fermi reservoir by a tunnel barrier of thickness t_B. Gate voltage V_G is adjusted with respect to Fermi energy E_F to achieve single-electron ($1e$) QD charging. The electron spin **s** (ball and arrow) couples to the nuclear spin ensemble $\mathbf{I}_j$ (small arrows) via inhomogeneous hyperfine interaction. Relaxation between electron spin-up ($\uparrow$, $s_z = +1/2$) and spin-down ($\downarrow$, $s_z = -1/2$) states is characterized by rate Γ_e. **b,** NMR experiment timing diagram showing optical pump and probe pulses, used to polarise and measure polarization of the nuclear spins, respectively. Radio frequency (rf) pulses implementing coherent nuclear spin control at an arbitrary V_G are sketched for spin echo sequence $(\pi/2)_x - \tau_0 - (\pi)_x - \tau - (\pi/2)_x$. The electron spin s_z undergoes random transitions between its two states. **c,** Rabi oscillations of the ^{69}Ga nuclear spins induced by a resonant rf pulse of variable duration t_{rf} in an empty ($0e$, circles) and charged ($1e$, squares) QD in the $t_B = 52$ nm sample at $B_z = 7.8$ T. Lines are a guide to the eye. **d,** Spin echo evolution as a function of the second delay τ in the $t_B = 37$ nm sample at $B_z = 7.8$ T, revealing free induction decay in $0e$ (circles, $\tau_0 = 150$ μs) and $1e$ states (squares, $\tau_0 = 7.5$ μs, data multiplied by 3). Lines show compressed exponential fits used to derive the nuclear spin dephasing times $T^*_{2,N}$. **e,** Fourier transform of **d**, showing spectral broadening and the average Knight shift $\langle \nu_e \rangle \approx -35$ kHz induced by equilibrium electron spin polarisation. Data for $1e$ is multiplied by 10. **f,** Spin echo decay measured by varying the total free evolution times $\tau_{evol} = \tau_0 + \tau$ at $\tau_0 = \tau$. Lines show fitting used to derive the nuclear spin coherence times $T_{2,N}$.

($1e$) result in faster damping of coherent nuclear spin rotations compared to an empty QD ($0e$). To characterise this inhomogeneity we use a spin echo sequence (Fig. 1b), where the initial $\pi/2$ pulse transforms nuclear spin polarization into collective coherence, followed by free evolution over time τ_0, a refocusing π pulse, and a further free evolution time τ, before the final $\pi/2$ pulse converts the remaining coherence back into optically detectable nuclear spin polarization. The width of the spin echo peak observed around $\tau = \tau_0$ (Fig. 1d) is proportional to dephasing time, which reduces from $T^{*,(0e)}_{2,N} \approx 35$ μs to $T^{*,(1e)}_{2,N} \approx 4.3$ μs when QD is charged with a single electron. This corresponds to spectral broadening from ≈ 13 kHz in an empty QD, to ≈ 126 kHz in presence of inhomogeneous Knight shifts (Fig. 1e).

By fixing $\tau = \tau_0$ we remove the dephasing and examine pure nuclear spin decoherence by measuring spin echo amplitude decay with increasing total free evolution time $\tau_{evol} = \tau_0 + \tau$ (Fig. 1f). From exponential fitting we find the coherence time $T^{(0e)}_{2,N} \approx 1.8$ ms in a bare ^{69}Ga nuclear spin ensemble, in good agreement with previous studies [8, 9]. By contrast, the coherence time $T^{(1e)}_{2,N} \approx 0.7$ ms in presence of a single QD electron is a factor of ≈ 30 longer than reported earlier [8]. By varying the gate bias V_G (Fig. 2a) we observe a clear plateau in $T_{2,N}$ around $V_G \approx 0.42$ V, confirming that QD is in single electron ($1e$) Coulomb blockade. Nuclear coherence time $T^{(1e)}_{2,N}$ in this regime is measured as a function of magnetic field B_z

(solid symbols in Fig. 2b). At low fields $T_{2,\mathrm{N}}^{(1e)}$ is nearly independent of B_z, but changes over to $T_{2,\mathrm{N}}^{(1e)} \propto B_\mathrm{z}^{-4}$ scaling at $B_\mathrm{z} \gtrsim 4$ T, in stark contrast to $T_{2,\mathrm{N}}^{(1e)} \propto B_\mathrm{z}^2 A^{-3}$ law predicted previously for hyperfine-mediated nuclear spin decoherence mechanism [8]. Furthermore, at high field $B_\mathrm{z} \approx 7.8$ T we find similar $T_{2,\mathrm{N}}^{(1e)} \approx 130$ μs for ^{75}As and ^{71}Ga nuclei, despite a factor of ≈ 1.8 difference in their hyperfine constants A.

To explain the observed $T_{2,\mathrm{N}}^{(1e)}$ values we invoke the spectral diffusion model, where the fluctuating environment is the single central electron spin, making uncorrelated random jumps between the $s_\mathrm{z} = \pm 1/2$ states as sketched in Fig. 1b. The rate of electron spin flips $1/(2T_{1,\mathrm{e}}) \lesssim 6000$ s^{-1} in the studied QDs is small compared to root mean square Knight shift $\Delta\nu_\mathrm{e} \approx 30$ kHz, derived from NMR spectra of Fig. 1e. In this regime of slow fluctuations, the nuclear spin decoherence time due to spectral diffusion approximately equals the electron spin lifetime $T_{2,\mathrm{N,SD}} \approx 1.38 T_{1,\mathrm{e}}$ (see derivation in Supplementary Note 2). Spectral diffusion dominates nuclear spin decoherence at high magnetic fields where electron spin lifetimes shorten as $T_{1,\mathrm{e}} \propto B_\mathrm{z}^{-4}$. In an empty QD nuclear dipole-dipole interaction causes nuclear spin ensemble decoherence on a timescale $T_{2,\mathrm{N}}^{(0e)}$ – including this mechanism, we find the following approximation for nuclear spin coherence time in presence of the electron central spin:

$$1/T_{2,\mathrm{N}}^{(1e)} = 1/T_{2,\mathrm{N}}^{(0e)} + 1/(1.38 T_{1,\mathrm{e}}). \qquad (1)$$

This model fully describes the experimental dependence of $T_{2,\mathrm{N}}^{(1e)}$ on B_z (lines in Fig. 2b), as well as isotope-independent $T_{2,\mathrm{N}}^{(1e)}$ at high B_z. In the $t_\mathrm{B} = 52$ nm sample $T_{1,\mathrm{e}}$ is very long at $B_\mathrm{z} \lesssim 3$ T, making the dipole-dipole mechanism dominant – and indeed we find $T_{2,\mathrm{N}}^{(1e)} \approx T_{2,\mathrm{N}}^{(0e)}$ in that case.

Qualitative understanding of spectral diffusion is found by considering two scenarios: In the absence of electron spin flips, the static inhomogeneous Knight shifts are fully refocused to form nuclear spin echo. By contrast, even a single electron spin flip unbalances the phases acquired by the nuclei before and after the refocusing π pulse (except for those rare flips occurring within a short interval $\approx T_{2,\mathrm{N}}^{*,(1e)}$ at the start or the end or the spin echo sequence). The probability to have zero electron flips in an increasing time interval decreases exponentially, and with it decays exponentially the average nuclear spin coherence on a timescale $T_{2,\mathrm{N,SD}} \approx 1.38 T_{1,\mathrm{e}}$. A direct observation of this process is shown in Fig. 3a, where we plot histograms of the spin echo amplitude ΔE_hf detected with single shot probe pulses, as opposed to averaging over multiple pump-rf-probe cycles used for the data of Figs. 1, 2. At long evolution times $\tau_\mathrm{evol} \approx 1300$ μs the echo is destroyed by decoherence, resulting in a single peak at $\Delta E_\mathrm{hf} \approx 0$. At short $\tau_\mathrm{evol} \approx 0.4$ μs the nuclear coherence is preserved in most cases, leading to a peak at $\Delta E_\mathrm{hf} \approx 1.9$ μeV. At intermediate τ_evol a bimodal distribution is observed, demonstrating the two discrete possibilities of nuclear spin echo preservation or destruction, if electron spin does not or does flip, respectively.

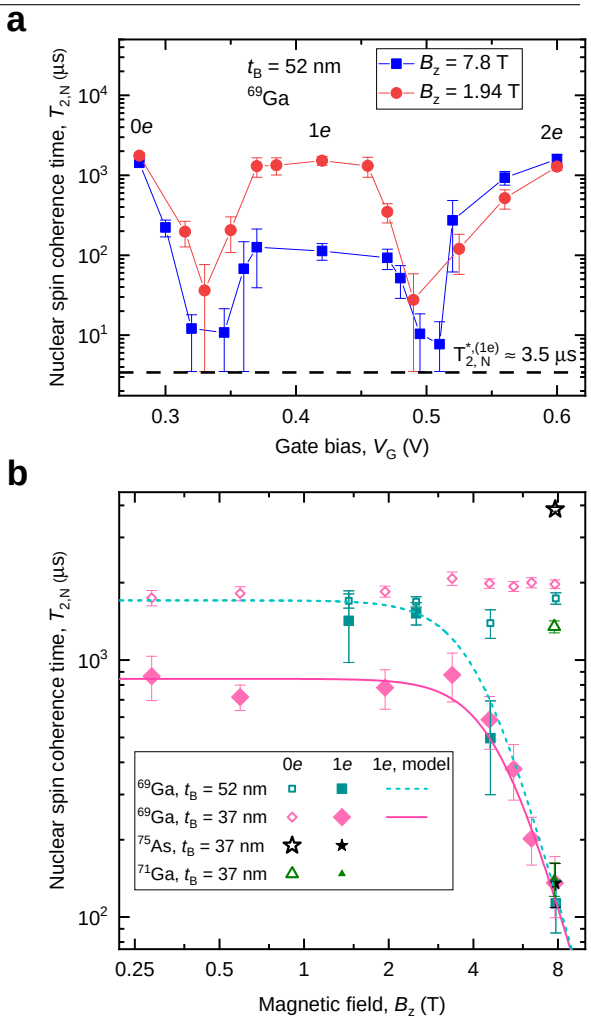

FIG. 2. **Coherence time of the nuclear spins coupled to quantum dot electron spin qubit. a,** Gate bias (V_G) dependence of the ^{69}Ga nuclear spin echo decay time $T_{2,\mathrm{N}}$ in the $t_\mathrm{B} = 52$ nm sample at $B_\mathrm{z} = 1.94$ T (circles) and $B_\mathrm{z} = 7.8$ T (squares). Solid lines are a guide to the eye. Resonant cotunneling between QD and the Fermi reservoir leads to reduction of $T_{2,\mathrm{N}}$ down to dephasing time $\approx T_{2,\mathrm{N}}^{*,(1e)}$ (dashed line), observed as dips at $V_\mathrm{G} \approx 0.33$ V and ≈ 0.5 V, which separate the Coulomb blockade plateaus corresponding to stable QD charge states $0e$, $1e$ and $2e$. **b,** Nuclear spin coherence in an empty QD ($T_{2,\mathrm{N}}^{(0e)}$, open symbols) and electron-charged QD ($T_{2,\mathrm{N}}^{(1e)}$ solid symbols) measured as a function of magnetic field B_z for spin-3/2 isotopes in samples with different t_B. Lines show $T_{2,\mathrm{N}}^{1e}$ of ^{69}Ga calculated according to the model of Eq. 1 for $t_\mathrm{B} = 37$ nm (solid line) and $t_\mathrm{B} = 52$ nm (dashed line) samples. Error bars are 95% confidence intervals.

Figures 3b, c show single shot NMR measurement with a sequences $(\pi/2)_\mathrm{x} - \tau_\mathrm{evol} - (\pi/2)_\mathrm{y}$, which generates col-

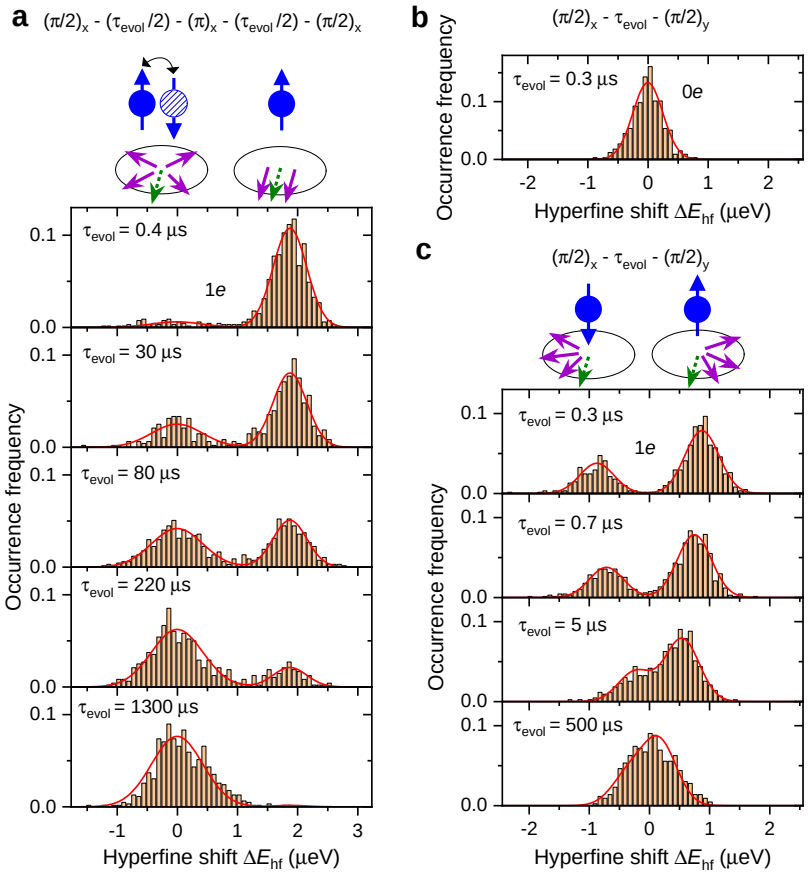

FIG. 3. **Single shot NMR detection of the electron spin state. a,** Spin echo of ^{75}As nuclei in a $t_B = 37$ nm sample at $B_z \approx 7.8$ T measured with single shot detection of the resulting hyperfine shift variation ΔE_{hf}. Measurement sequence is $(\pi/2)_x - (\tau_{evol}/2) - (\pi)_x - (\tau_{evol}/2) - (\pi/2)_x$ with several values of the total free evolution time $\tau_{evol} = 0.4 - 1300$ μs. Results are shown as histograms of the detected spin echo amplitudes ΔE_{hf}. Lines show double Gaussian fits. Schematic shows electron spin in an $s_z = +1/2$ or $-1/2$ states (balls with up or down arrows). After the initial $(\pi/2)_x$ pulse all nuclear spins point along the same axis orthogonal to z (dashed small arrow) and then precess around the z axis to point along generally different directions prior to the final $(\pi/2)_x$ pulse (solid small arrows). An electron spin flip during the nuclear spin precession dephases the spins, resulting in $\Delta E_{hf} \approx 0$, whereas in the absence of electron flips, nuclear spin echo is formed, resulting in $\Delta E_{hf} \approx 1.9$ μeV. **b,** Single shot measurement of the free induction decay in an empty QD ($0e$), using sequence $(\pi/2)_x - (\tau_{evol}) - (\pi/2)_y$, where subscripts x, y denote the equatorial axes in the rotating frame towards which the spins are flipped by the rf pulses. Line shows Gaussian fit. **c,** Same sequence as in **b** applied to a charged QD ($1e$). For a sufficiently short evolution time $\tau_{evol} \lesssim T_{2,N}^{*,(1e)}$ the spin $s_z = -1/2$ ($s_z = +1/2$) of a single electron pointing down (up) gives rise to a negative (positive) quadruature nuclear spin polarisation ΔE_{hf}, observed as a bimodal distribution of the detected ΔE_{hf}. Lines show double Gaussian fits.

lective nuclear spin coherence and probes its quadrature component ΔE_{hf} following the free evolution time τ_{evol}. In an empty QD ($0e$, Fig. 3b) the distribution of detected ΔE_{hf} is unimodal with a width given by the optical readout noise. By contrast, a clear bimodal distribution is observed with a single electron in a QD ($1e$, Fig. 3c) at $\tau_{evol} \approx 0.3$ μs. The two modes correspond to the two discrete electron spin qubit states $s_z = \pm 1/2$, that add positive or negative phase $\propto \tau_{evol}$ to the nuclear spin coherence, thus implementing a controlled phase (CPHASE) quantum logic gate in the hybrid electron-nuclear spin system. The $(\pi/2)_y$ pulse converts this phase into the optically detected hyperfine shift, thus implementing a single-shot readout of the electron spin qubit, which is a key ingredient in quantum information processing. The readout is achieved using a small fraction ($< 13\%$, see Methods) of the QD nuclei, so that the remaining nuclear spins can be used as a quantum resource. Using Gaussian fitting (lines in Fig. 3c) to calculate the overlap (see Methods) of the two modes, we estimate the readout fidelity $> 99.8\%$, which can be improved further by optimizing the collection efficiency of the QD optical emission. Our method of qubit readout via spin environment offers notable improvement over previously achieved fidelities in solid state spin systems ($80 - 95\%$, Refs. [18–21]) and superconducting qubits ($> 97 - 99\%$, Refs. [22, 23]). The relative weights of the two modes in Fig. 3c reveal the electron spin polarization degree

$\rho_e \approx 0.35$, corresponding to equilibrium of an electron with $g_e \approx -0.63$, in good agreement with electron g-factors found in similar QDs [24]. At long evolution times $\tau_{evol} \gg T_{2,N}^{*,(1e)}$ the coherence imprinted by the electron spin is dephased, resulting in a unimodal distribution around $\Delta E_{hf} \approx 0$ (e.g. at $\tau_{evol} \approx 500$ μs).

Using the long nuclear spin coherence $T_{2,N}$ and fast (bang-bang) rf control we implement dynamical decoupling [25] protocols, which increase $T_{2,N}$ by filtering out the unwanted interactions under an increasing pulse repetition rate. Applying a 5-pulse sequence CHASE-5 (Ref. [9]) to ^{69}Ga nuclei in the low field regime ($B_z = 2.5$ T), where $T_{1,e}$ is long, we find an improved coherence $T_{2,N}^{(1e)} \approx 2.2$ ms compared to a single-pulse spin echo $T_{2,N}^{(1e)} \approx 1.5$ ms. Due to the Knight shift broadening, decoupling sequences with more pulses are found to reduce the echo amplitude to unmeasurable levels (see Supplementary Note 5). However, this limitation is technical, and can be addressed by increasing the rf control bandwidth. Since nuclear spin decoherence in both neutral ($0e$) and charged ($1e$) QDs is governed by the same mechanisms of inhomogeneous broadening and nuclear dipolar interactions, we expect that $T_{2,N}^{(1e)}$ can be as large as $T_{2,N}^{(0e)} > 10$ ms, found previously in neutral QDs [7, 9]. We expect that optimal dynamical decoupling would be achieved by synchronizing the control pulses applied to the nuclear spin ensemble and the central spin qubit.

Our results show that spectral diffusion, observed previously in dilute spin systems [26], applies to 100% abundant spin ensembles of III-V semiconductor quantum dots, predicting long spin ensemble coherence required to implement recent proposals for QD spin-photon networks with nuclear spin quantum memories [6] and registers [7]. In contrast to previous studies [8], we find no signature of decoherence arising from hyperfine-mediated nuclear-nuclear interactions down to $B_z \approx 0.25$ T – this however is consistent with earlier estimates [27] that such interactions play a role only for magnetic fields $\lesssim 0.02$ T. While our experiments are conducted on collective, multi-quanta coherent excitations of the nuclear spin ensemble, we expect the same mechanisms and similar coherence times for the low-energy excitations such as magnon modes [5]. The findings of this work on InAs/GaAs QDs are expected to apply to high-quality optically active GaAs/AlGaAs QDs [7], where small intrinsic strain holds a promise for even longer coherence and complete control of the hybrid electron-nuclear spin quantum system. Future work will include development of quantum gates for reversible coherent state transfer between electron and nuclear spins. The detrimental effect of electron-nuclear interaction inhomogeneity on such gates can be alleviated by operating on small nuclear spin sub-ensembles via spectrally-selective rf control pulses [28] – the sensitivity of the techniques demonstrated here is sufficient for that and can be improved further.

[1] Khaetskii, A. V., Loss, D. & Glazman, L. Electron spin decoherence in quantum dots due to interaction with nuclei. *Phys. Rev. Lett.* **88**, 186802 (2002).

[2] Yao, W., Liu, R.-B. & Sham, L. J. Theory of electron spin decoherence by interacting nuclear spins in a quantum dot. *Phys. Rev. B* **74**, 195301 (2006).

[3] Fischer, J. & Loss, D. Dealing with decoherence. *Science* **324**, 1277–1278 (2009).

[4] Hensen, B. *et al.* A silicon quantum-dot-coupled nuclear spin qubit. *Nat. Nanotechnol.* **15**, 13–17 (2020).

[5] Gangloff, D. A. Quantum interface of an electron and a nuclear ensemble. *Science* **364**, 62–66 (2019).

[6] Denning, E. V., Gangloff, D. A., Atatüre, M., Mørk, J. & Le Gall, C. Collective quantum memory activated by a driven central spin. *Phys. Rev. Lett.* **123**, 140502 (2019).

[7] Chekhovich, E. A., da Silva, S. F. C. & Rastelli, A. Nuclear spin quantum register in an optically active semiconductor quantum dot. *Nat. Nanotechnol.* **15**, 999–1004 (2020).

[8] Wüst, G. *et al.* Role of the electron spin in determining the coherence of the nuclear spins in a quantum dot. *Nat. Nanotechnol.* **11**, 885–889 (2016).

[9] Waeber, A. M. *et al.* Pulse control protocols for preserving coherence in dipolar-coupled nuclear spin baths. *Nat. Commun.* **10**, 3157 (2019).

[10] Klauder, J. R. & Anderson, P. W. Spectral diffusion decay in spin resonance experiments. *Phys. Rev.* **125**, 912–932 (1962).

[11] Hu, P. & Hartmann, S. R. Theory of spectral diffusion decay using an uncorrelated-sudden-jump model. *Phys. Rev. B* **9**, 1–13 (1974).

[12] Barnes, E., Cywiński, L. & Das Sarma, S. Nonperturbative master equation solution of central spin dephasing dynamics. *Phys. Rev. Lett.* **109**, 140403 (2012).

[13] Heshami, K. *et al.* Quantum memories: emerging applications and recent advances. *J. Mod. Opt.* **63**, 2005–2028 (2016).

[14] Dutt, M. V. G. *et al.* Quantum register based on individual electronic and nuclear spin qubits in diamond. *Science* **316**, 1312–1316 (2007).

[15] Hahn, E. L. Spin echoes. *Phys. Rev.* **80**, 580–594 (1950).

[16] Gillard, G. *et al.* Fundamental limits of electron and nuclear spin qubit lifetimes in an isolated self-assembled quantum dot. *npj Quantum Inf.* **7**, 43 (2021).

[17] Urbaszek, B. *et al.* Nuclear spin physics in quantum dots an optical investigation. *Rev. Mod. Phys.* **85**, 79–133 (2013).

[18] Elzerman, J. M. *et al.* Single-shot read-out of an individual electron spin in a quantum dot. *Nature* **430**, 431–435 (2004).

[19] Morello, A. *et al.* Single-shot readout of an electron spin in silicon. *Nature* **467**, 687–691 (2010).

[20] Neumann, P. *et al.* Single-shot readout of a single nuclear spin. *Science* **329**, 542–544 (2010).

[21] Zhang, Q. *et al.* High-fidelity single-shot readout of single electron spin in diamond with spin-to-charge conversion. *Nat. Commun.* **12**, 1529 (2021).

[22] Arute, F. *et al.* Quantum supremacy using a programmable superconducting processor. *Nature* **574**, 505–510 (2019).

[23] Dassonneville, R. *et al.* Fast high-fidelity quantum nondemolition qubit readout via a nonperturbative cross-kerr coupling. *Phys. Rev. X* **10**, 011045 (2020).

[24] Prechtel, J. H. *et al.* Electrically tunable hole *g* factor of an optically active quantum dot for fast spin rotations. *Phys. Rev. B* **91**, 165304 (2015).

[25] Viola, L., Knill, E. & Lloyd, S. Dynamical decoupling of open quantum systems. *Phys. Rev. Lett.* **82**, 2417–2421 (1999).

[26] Tyryshkin, A. M. *et al.* Electron spin coherence exceeding seconds in high-purity silicon. *Nature Mater.* **11**, 143 (2012).

[27] Reilly, D. J. *et al.* Exchange control of nuclear spin diffusion in a double quantum dot. *Phys. Rev. Lett.* **104**, 236802 (2010).

[28] Freeman, R. Selective excitation in high-resolution NMR. *Chem. Rev.* **91**, 1397–1412 (1991).

[29] Chekhovich, E. A., Hopkinson, M., Skolnick, M. S. & Tartakovskii, A. I. Suppression of nuclear spin bath fluctuations in self-assembled quantum dots induced by inhomogeneous strain. *Nat. Commun.* **6**, 6348 (2015).

[30] Chekhovich, E. A. *et al.* Pumping of nuclear spins by optical excitation of spin-forbidden transitions in a quantum dot. *Phys. Rev. Lett.* **104**, 066804 (2010).

[31] Ostroff, E. D. & Waugh, J. S. Multiple spin echoes and spin locking in solids. *Phys. Rev. Lett.* **16**, 1097–1098 (1966).

[32] Serrels, K. A. *et al.* Solid immersion lens applications for nanophotonic devices. *J. Nanophotonics* **2**, 1 – 29 (2008).

Supplementary Information is available in the online version of the paper.

Acknowledgements Royal Society provided funding support to E.A.C. through University Research Fellowship and grant RGF\EA\180117, and to G.G. and E.A.C through grant RG150465. The work was supported by EPSRC grant EP/V048333/1.

Author contributions G.G. and E.A.C developed experimental techniques, analysed the data and wrote the manuscript. G.G. conducted experiments. E.C. grew the samples. E.A.C. coordinated the project.

Additional information Supplementary information is available in the online version of the paper. Reprints and permission information is available online at www.nature.com/reprints. Correspondence and requests for materials should be addressed to G.G. and E.A.C.

Data availability The data that support the findings of this study are available from the corresponding authors upon reasonable request.

Competing financial interests: The authors declare no competing financial interests.

METHODS

Sample structures. The studied semiconductor structures have been examined previously [16] using photoluminescence and spin lifetime measurement techniques. The samples are low-density InAs self-assembled QDs grown on a GaAs substrate using molecular beam epitaxy. The dots are placed between two distributed Bragg reflectors consisting of GaAs and AlAs layers and forming a $\lambda/2$ optical cavity. The low temperature ground-state optical emission of the studied QDs is at $\approx$ 950 nm. The Fermi reservoir is a Si doped GaAs layer (Si concentration $\approx 1.1 \times 10^{18}$ cm^{-3}), separated from QDs by a GaAs tunnel barrier layer of thickness $t_{\rm B}$. The samples are processed into planar Schottky diode structure, allowing for the charge state of the dots to be controlled by applying external bias $V_{\rm G}$ to the top metal gate.

Electron spin relaxation rates $\Gamma_{\rm e} = 1/T_{1,\rm e}$ measured at low temperature $T = 4.5$ K are well described by the following model [16]:

$$\Gamma_{\rm e} = \Gamma_{\rm e,cotun} + \Gamma_{\rm e,ph} B_{\rm z}^{k_{\rm ph}} \qquad (2)$$

where the first term $\Gamma_{\rm e,cotun}$ accounts for the field-independent relaxation induced by electron cotunneling and the second term describes the field-dependent relaxation induced by acoustic phonons. Equation 2 is then substituted into Eq. 1 to find a closed form dependence of the nuclear spin coherence time on the external magnetic field $B_{\rm z}$. The phonon mechanism parameters are $\Gamma_{\rm e,ph} \approx 2.27 \pm 0.48$ s^{-1} $\times$ T$^{-k_{\rm ph}}$ and $k_{\rm ph} \approx 4.1 \pm 0.13$ in both samples. Cotunneling depends on the barrier thickness. For the $t_{\rm B} = 52$ nm sample the range of values is $1/\Gamma_{\rm e,cotun} \approx 1.26 - 1.65$ s for different individual QDs. For the $t_{\rm B} = 37$ nm sample the dot-to-dot variation is more pronounced $1/\Gamma_{\rm e,cotun} \approx 1.2 - 5.8$ ms. Electron spin lifetimes have not been measured for the particular QDs used here for nuclear spin coherence studies, and thus we treat $\Gamma_{\rm e,cotun}$ in the $t_{\rm B} = 37$ nm sample as the only adjustable parameter. The best fit value plotted by the solid line in Fig. 2b is $1/\Gamma_{\rm e,cotun} \approx 1.1$ ms, in good agreement with relaxation rates found from direct measurements on other QDs in the same sample.

Experimental techniques. The sample is placed in a liquid helium bath cryostat equipped with a superconducting magnet, providing a field up to $B_{\rm z} = 8$ T, parallel to sample growth direction and optical axis z (Faraday geometry). An aspheric lens is used for optical excitation of the QD and photoluminescence (PL) collection. Diode lasers emitting at 850 nm are used both for optical polarization of the nuclear spins (optical pump pulses) and PL excitation (optical probe pulses). The collected PL is dispersed with a 1 m double grating spectrometer and recorded with a charge-coupled device camera. The changes in the spectral splitting of a negatively charged trion X^-, derived from the PL spectra, are used to measure the hyperfine shifts $E_{\rm hf}$ proportional to the nuclear

spin polarisation degree. The oscillating magnetic field $B_x \perp z$ implementing the coherent control of the collective nuclear spin state is produced by a coil placed at a distance of ≈ 0.5 mm from the QD sample. The coil is made of 10 turns of a 0.1 mm diameter enameled copper wire wound on a ≈ 0.4 mm diameter spool in 5 layers, with 2 turns in each layer. The coil is fed by a 1 kW rf amplifier through a resonant impedance matching network made of 50 Ω coaxial cables.

Optically detected NMR. The details of NMR implementation are given in Supplementary Note 3. Overall the experimental cycle follows the timing diagram shown in Fig. 1b. As in previous work [8, 9, 29], the optically induced nuclear spin state is augmented with adiabatic rf frequency sweeps over the inhomogeneously broadened satellite NMR transitions $-3/2 \leftrightarrow -1/2$ and $+1/2 \leftrightarrow +3/2$. The sweeps exchange the populations of the $I_z = -3/2$ and $-1/2$ pair of states, as well as populations of the $I_z = +1/2$ and $+3/2$ pair. This way the population difference of the $I_z = \pm 1/2$ pair is maximised, prior to coherent manipulation of the $I_z = \pm 1/2$ subspace. The amplitude of the frequency-swept rf excitation is chosen to produce Rabi frequency between $\approx 1 - 4$ kHz, and the typical sweep rates are between $5 - 10$ MHz s^{-1}. In some experiments, such as single-shot measurements of Fig. 3, the same adiabatic sweeps are applied for the second time, after the coherent manipulation, transferring the final populations of the $I_z = \pm 1/2$ states back into $I_z = \pm 3/2$ states. This gives a factor of 3 increase in the variation of the optically detected hyperfine shifts $\Delta E_{\rm hf}$ at the expense of a longer experimental time. In the case such second set of sweeps is used, all the measured $\Delta E_{\rm hf}$ are divided by 3 to obtain the values directly comparable with the measurements where adiabatic sweeps are applied only after the optical pumping. In all experiments, except for single shot measurements, the hyperfine shift $\Delta E_{\rm hf}$ is acquired by averaging over $15 - 60$ pump-rf-probe cycles shown in Fig. 1b to obtain an approximation to a statistical average NMR signal. In echo decay experiments, such as shown in Fig. 1f, the dependence of the echo amplitude on the total free evolution time $\tau_{\rm evol}$ is fitted with stretched or compressed exponentials $\propto {\rm e}^{-(\tau_{\rm evol}/T_{2,\rm N})^{\eta}}$, where η is the parameter describing stretching ($\eta < 1$) or compression ($\eta > 1$).

Coherent control of the nuclear spins is achieved using high power rf pulse bursts with rotating frame amplitude of up to $B_1 \approx 10$ mT, which corresponds to laboratory frame amplitude $B_x \approx 20$ mT and ^{75}As Rabi frequency $\nu_1 = 2\gamma B_1/(2\pi) \approx 140$ kHz, where the additional factor of two is from the matrix element of the spin-3/2 operator projected onto the $I_z = \pm 1/2$ subspace. In order to achieve broadband uniform rotation of a spin ensemble, ν_1 must be larger than the resonance spectral broadening. While larger B_1 can be achieved by increasing the rf power, the practical limitations arise from the parasitic effects of the rf electric field. Above certain level, typically corresponding to $B_1 \approx 5$ mT, high power rf pulses are found to induce electron spin flips, which then disrupt the formation of the nuclear spin echo. In single shot spin echo experiments with short $\tau_{\rm evol}$ the rf-induced electron spin flips are observed as nearly equal weights of the two modes in the histogram. Consequently, experiments shown in Fig. 3a are conducted at a reduced $B_1 \approx 5$ mT, where the probability of parasitic electron spin flipping is estimated to be within < 0.05 from fitting. The downside of a low B_1 is the reduced spectral bandwidth of the control pulses, which leads to incomplete rotation for some of the spins and a reduced spin echo amplitude. In those spin echo experiments where the readout is averaged over multiple pump-probe cycles, the contributions of the cycles where electron spin is flipped by the rf field can be ignored, leading to correct spin echo decay time $T_{2,\rm N}^{(1e)}$ but with a reduced echo amplitude. Future work may include optimisation of rf circuitry with the aim of maximising B_1 while reducing the parasitic rf electric field.

Most of the pulsed nuclear magnetic resonance experiments are conducted on the ^{69}Ga isotope due to its favourable balance between the hyperfine shift amplitude, Knight shift inhomogeneity, and the quadrupolar inhomogeneity. Additional results for ^{75}As isotope can be found in Supplementary Note 4.

Estimate of the number of nuclei used for single shot electron spin detection. The single-shot NMR experiments presented in Fig. 3 are conducted on ^{75}As nuclei, which have 100% natural abundance and thus make up 50% of all the nuclei in a QD, the rest being the group-III Ga, In and possibly some Al nuclei. The nuclear spin polarization degree produced by optical pumping is estimated to be $|\rho_{\rm N}| \approx 0.65$ [30], which corresponds to a dimensionless inverse spin temperature $|\beta| \approx 0.98$ in a Boltzmann distribution of the nuclear spin level population probabilities $p(I_z) \propto \exp(-\beta I_z)$. The nuclei that are initially in the $I_z = \pm 3/2$ states are transferred into the $I_z = \pm 1/2$ states by adiabatic rf frequency sweeps – only these nuclei contribute to NMR signal, and from the $p(I_z)$ distribution their fraction is ≈ 0.67. Finally, the reduced rf amplitude used in single-shot NMR (^{75}As CT Rabi frequency $\nu_1 \approx 70$ kHz) results in selective rf pulses, which excite only the nuclei whose NMR frequencies are within the pulse bandwidth $\propto \nu_1$. In spin echo experiments, such lowering of the rf amplitude results in spin echo amplitude that is a factor of ≈ 0.38 smaller compared to the echo amplitude in experiments conducted with the highest possible rf amplitude. Combining all these factors we find an upper estimate $< 0.5 \times 0.67 \times 0.38 \approx 0.13$ of the fraction of the QD nuclei taking part in a single-shot detection of the electron spin state. With the total number of nuclei estimated to be $N \approx 4 \times 10^4$ in the studied dots [16], this corresponds to ≈ 5000 nuclei participating in electron spin detection.

Estimate of the single-shot electron spin readout fidelity. The histograms of the single-shot quadrature NMR signal $\Delta E_{\rm hf}$ shown in Fig. 3c are fitted with a double Gaussian function $A_{(-)} 2^{-\left(\frac{\Delta E_{\rm hf} + \Delta E_{\rm hf,0}/2}{w/2}\right)^2} + A_{(+)} 2^{-\left(\frac{\Delta E_{\rm hf} - \Delta E_{\rm hf,0}/2}{w/2}\right)^2}$, where $\Delta E_{\rm hf,0}$ is the splitting of

the two modes, w is the full width at half maximum of each mode peak and $A_{(+)}$ ($A_{(-)}$) is the amplitude of the mode corresponding to positive (negative) average hyperfine shift variation $\Delta E_{\rm hf}$. The relative difference of the amplitudes reflects the electron spin polarization degree $\rho_{\rm e} = (A_{(+)} - A_{(-)})/(A_{(+)} + A_{(-)})$. For the measurement at $\tau_{\rm evol} = 0.3$ μs in Fig. 3c we find $\Delta E_{\rm hf,0} \approx 1.75$ μeV and the width $w \approx 0.67$ μeV determined by collection efficiency and spectral resolution of the instruments used to analyze QD PL. When the quadrature NMR signal $\Delta E_{\rm hf}$ is measured it is interpreted as electron spin state $s_{\rm z} = +1/2$ ($s_{\rm z} = -1/2$) for $\Delta E_{\rm hf} > 0$ ($\Delta E_{\rm hf} < 0$). Thus the total probability of correct detection is

$$F = \left((A_{(-)} + A_{(+)}) \int_{-\infty}^{\infty} 2^{-\left(\frac{x}{w/2}\right)^2} {\rm d}x \right)^{-1} \times \left(\int_{-\infty}^{0} A_{(-)} 2^{-\left(\frac{x+\Delta E_{\rm hf,0}/2}{w/2}\right)^2} {\rm d}x + \int_{0}^{\infty} A_{(+)} 2^{-\left(\frac{x-\Delta E_{\rm hf,0}/2}{w/2}\right)^2} {\rm d}x \right).$$

Taking the integrals we find for the readout fidelity:

$$F = \frac{1}{2}\left(1 + {\rm erf}\left[\frac{\sqrt{\ln 2}\Delta E_{\rm hf,0}}{w}\right]\right), \qquad (3)$$

where erf is the standard Gauss error function. Evaluating this for the $\tau_{\rm evol} = 0.3$ μs measurement we find $F \approx 0.9989$. This is the value quoted in the main text above and it is determined by the accuracy with which the collective nuclear spin polarization of the quantum dot is read out optically.

Some additional loss of fidelity can occur if the electron spin flips during the free evolution interval $\tau_{\rm evol}$, which encodes the electron spin state into collective nuclear spin coherence, or during the subsequent $(\pi/2)_{\rm y}$ final rf pulse, whose duration is $t_{\pi/2} = 3.75$ μs for the results shown in Fig. 3c. The Rabi frequency of the rf pulse $\nu_1 \approx 70$ kHz is sufficiently large to dominate over the Knight shift broadening $\Delta\nu_{\rm e} \approx 30$ kHz and cause nuclear spin locking [31]. Under spin locking, electron spin flips during the $(\pi/2)_{\rm y}$ pulse can no longer change the sign of the detected quadrature nuclear spin polarization. Thus we only need to consider the probability $\approx 1 - (\tau_{\rm evol}/T_{1,{\rm e}})$ that the electron spin is preserved during the free evolution time $\tau_{\rm evol}$. This probability is ≈ 0.9967 for the results of Fig. 3c where $\tau_{\rm evol} = 0.3$ μs and $T_{1,{\rm e}} \approx 90$ μs, estimated for high magnetic field $B_{\rm z} = 7.8$ T. Electron spin flips occurring at random times during $\tau_{\rm evol}$ result in quadrature nuclear spin polarization values over the entire range $[-\Delta E_{\rm hf,0}/2, +\Delta E_{\rm hf,0}/2]$. Such signal associated with electron spin flips must appear as broad background in the histograms of Fig. 3c, but in practice is too small to be observed directly. At lower magnetic fields the electron spin lifetimes are considerably longer. For $T_{1,{\rm e}} \geq 10$ ms electron spin flips during the detection sequence become negligible, and the fidelity is governed by the statistical uncertainty in the optically detected hyperfine shift $\Delta E_{\rm hf}$. Increasing the optical probe duration $T_{\rm Probe}$ increases the number of the PL photons collected and reduces w, improving the measurement accuracy of the spectral splitting variation $\Delta E_{\rm hf}$. However, if $T_{\rm Probe}$ is too long, it depolarizes the nuclei and reduces the separation $\Delta E_{\rm hf,0}$ of the histogram modes, reducing the readout fidelity. Thus there is an optimal probe duration $T_{\rm Probe}$ which maximizes the fidelity F. Further improvement of the electron spin readout fidelity can be achieved using e.g. solid immersion lenses [32] in order to increase probe PL photon collection without the need for a longer $T_{\rm Probe}$.

Supplementary Information: Using nuclear spins for millisecond coherence storage and single-shot readout of an electron spin qubit

G. Gillard, E. Clarke, and E. A. Chekhovich

Supplementary Note 1. ELECTRON-NUCLEAR SPIN SYSTEM OF A QUANTUM DOT.

The Hamiltonian of the electron central spin $\mathbf{s}$ and the nuclear spin bath $\mathbf{I}_j$, where $1 \leq j \leq N$ and N is the number of nuclei in the dot, can be written as the following sum of terms:

$$\mathcal{H} = \mathcal{H}_{\mathrm{Z,N}} + \mathcal{H}_{\mathrm{Q,N}} + \mathcal{H}_{\mathrm{DD,N}} + \mathcal{H}_{\mathrm{Z,e}} + \mathcal{H}_{\mathrm{hf}} + \mathcal{H}_{\mathrm{Env,e}} \tag{S1}$$

The first Zeeman term describes interaction of the QD nuclear spins $\mathbf{I}_j$ with the static magnetic field B_z aligned along the z axis:

$$\mathcal{H}_{\mathrm{Z,N}} = -\sum_j \hbar\gamma_j B_\mathrm{z} \hat{I}_{\mathrm{z},j}, \tag{S2}$$

where $\hbar = h/(2\pi)$ is the reduced Planck constant, γ_j is the gyromagnetic ratio of the j-th nuclear spin and $\hat{\mathbf{I}}_j$ is a vector of spin operators with Cartesian components $(\hat{I}_{\mathrm{x},j}, \hat{I}_{\mathrm{y},j}, \hat{I}_{\mathrm{z},j})$. The result of the Zeeman term alone is a spectrum of equidistant single-spin energies $\hbar\gamma_j B_\mathrm{z} I_\mathrm{z}$, corresponding to $2I+1$ eigenstates with nuclear spin z-projections I_z, where $-I \leq I_\mathrm{z} \leq +I$. The interaction of the nuclear electric quadrupolar moment with the electric field gradients is described by the term (Ch. 10 in Ref. [1]):

$$\mathcal{H}_{\mathrm{Q,N}} = \sum_j \frac{q_j}{6}[3\hat{I}^2_{\mathrm{z}',j} - I_j^2 + \eta_j(\hat{I}^2_{\mathrm{x}',j} - \hat{I}^2_{\mathrm{y}',j})], \tag{S3}$$

where q_j and η_j describe the magnitude and asymmetry of the electric field gradient tensor, whose principal axes are $x'y'z'$. In self-assembled QDs the electric field gradients at the nuclear sites are as large as $hq_j \approx 10$ MHz and are dominated by the elastic strains [2, 3]. The strain is inhomogeneous within the QD volume, so that q_j and η_j vary strongly between individual nuclei. The axes $x'y'z'$ are different for each nucleus and generally do not coincide with crystalographic axes or magnetic field direction. At sufficiently strong magnetic fields $|\hbar\gamma_j B_\mathrm{z}| \gg q_j$, quadrupolar effects can be treated perturbatively – the main effect is the nonharmonicity of the nuclear spin energies and the splitting of the NMR spectrum into a quadrupolar multiplet of $2I$ resolved transitions. The $I_\mathrm{z} = \pm 1/2$ states of a half-integer nuclear spin are influenced by quadrupolar effects only in the second order, resulting in a smaller inhomogeneous broadening, compared to the broadening of

the $|I_\mathrm{z}| > 1/2$ state energies. This allows for spectral isolation of the $I_\mathrm{z} = \pm 1/2$ subspaces, which can then be treated as effective spin-1/2 nuclei. Within the $I_\mathrm{z} = \pm 1/2$ subspace, the quadrupolar Hamiltonian is identical to the Zeeman term, so that we can replace $\mathcal{H}_\mathrm{Q,N} \to -\sum_j \hbar\gamma_j \Delta B_\mathrm{z} \hat{I}_{\mathrm{z},j}$, where inhomogeneous quadrupolar shifts q_j are emulated by magnetic field inhomogeneity on the scale of $\Delta B_\mathrm{z,j} \propto q_j^2/(\hbar\gamma_j B_\mathrm{z})$.

Direct interaction between the nuclei is described by the dipole-dipole Hamiltonian:

$$\mathcal{H}_\mathrm{DD} = \sum_{j<k} b_{j,k} \left(3\hat{I}_{j,\mathrm{z}}\hat{I}_{k,\mathrm{z}} - \hat{\mathbf{I}}_j \cdot \hat{\mathbf{I}}_k \right),$$
$$b_{j,k} = \frac{\mu_0}{4\pi} \frac{\gamma_j \gamma_k}{2} \frac{1 - 3\cos^2\theta_{j,k}}{r_{j,k}^3} \tag{S4}$$

Here, $\mu_0 = 4\pi \times 10^{-7}$ NA^{-2} is the magnetic constant and $r_{j,k}$ denotes the length of the vector, which forms an angle θ with the z axis and connects the two spins j and k. The typical magnitude of the interaction constants for the nearby nuclei in InGaAa is $\max(h|b_{j,k}|) \approx 100$ Hz. The Hamiltonian of Eq. S4 has been truncated to eliminate all spin non-conserving terms – this is justified for static magnetic field exceeding $\gtrsim 1$ mT. Due to its bilinear form in terms of spin operators, the dipolar interaction is not refocused by the nuclear spin echo sequences, and is responsible for collective nuclear spin decoherence on a timescale $T_\mathrm{2,N,DD} \propto 1/\max(h|b_{j,k}|)$.

The electron Zeeman term is

$$\mathcal{H}_\mathrm{Z,e} = \mu_\mathrm{B} g_\mathrm{e} B_\mathrm{z} \hat{s}_\mathrm{z}, \tag{S5}$$

where μ_B is the Bohr magneton and g_e is the effective conduction-band electron g-factor, estimated to be $g_\mathrm{e} \approx -0.67$ in the studied QDs.

The interaction of the conduction band electron spin $\mathbf{s}$ with the ensemble of the QD nuclear spins is dominated by the contact (Fermi) hyperfine interaction, with the following Hamiltonian:

$$\mathcal{H}_\mathrm{hf} = \sum_j A_j (\hat{s}_\mathrm{x}\hat{I}_{\mathrm{x},j} + \hat{s}_\mathrm{y}\hat{I}_{\mathrm{y},j} + \hat{s}_\mathrm{z}\hat{I}_{\mathrm{z},j}), \tag{S6}$$

where the hypefine constant of an individual nucleus j is $A_j = A^{(j)}|\psi(\mathbf{r}_j)|^2 v$. Unlike A_j, the $A^{(j)}$ hyperfine constant is a parameter dependent only on the material and the isotope type to which nucleus j belongs, $|\psi(\mathbf{r}_j)|^2$ is the density of the electron envelope wavefunction at the nuclear site $\mathbf{r}_j$, and v is the crystal volume per one cation or one anion. The definitions of the hyperfine constants differ between different sources. With the definition adopted here, a fully polarized isotope with spin I, hyperfine constant A and a 100% abundance (e.g. ^{75}As), would shift the energies of the

electron spin states $s_z = \pm 1/2$ by $\pm AI$, irrespective of the shape of $|\psi(\mathbf{r}_j)|^2$. In that case, the typical values in InGaAs are $A \approx 50$ μeV (Refs. [4–6]).

The three orders of magnitude disparity in the energy scales of $\mathcal{H}_{\mathrm{Z,e}}$ and $\mathcal{H}_{\mathrm{Z,N}}$ suppresses at high magnetic field the direct (first-order) electron nuclear spin flip-flops governed by the $\propto \hat{s}_x\hat{I}_{x,j}+\hat{s}_y\hat{I}_{y,j}$ term. The remaining secular term $\hat{s}_z\hat{I}_{z,j}$ is responsible for the Knight shifts of the nuclear magnetic resonance frequencies and the electron spin hyperfine shift (Overhauser shift) E_{hf}. In the second order perturbation expansion, $\mathcal{H}_{\mathrm{hf}}$ gives rise to hyperfine-mediated nuclear-nuclear spin flip-flops. The effective coupling strength of the two nuclei j and k is $\propto A_jA_k/\Delta E_{\mathrm{Z}}$, where ΔE_{Z} is the energy splitting of the electron spin levels, which includes both the Zeeman splitting $\mu_{\mathrm{B}}g_{\mathrm{e}}B_z$ and the electron hyperfine shifts E_{hf} due to the polarized nuclei [7]. Thus, unlike the Knight shifts, the hyperfine-mediated nuclear-nuclear interaction is field dependent, and is expected to have the most pronounced effect, such as shorter nuclear spin coherence, at low magnetic fields [8].

The coupling of the electron spin to external environments is described by the term $\mathcal{H}_{\mathrm{Env,e}}$ in the total Hamiltonian of Eq. S1. Interaction of the electron spin with phonons, mediated by spin-orbit coupling, induces electron spin relaxation with rate $\Gamma_{\mathrm{e}} \propto B_z^4$ (or $\Gamma_{\mathrm{e}} \propto B_z^5$ at low temperatures), strongly dependent on magnetic field B_z (Ref. [9]). Cotunneling coupling between the quantum dot and the nearby electron Fermi reservoir also gives rise to QD electron spin relaxation, whose rate depends weakly on magnetic field, but is strongly affected by the gate bias V_{G} that controls the energies of the QD states with respect to the Fermi level [9]. Additional electron spin relaxation mechanisms may arise for example from the charge fluctuations of the defects in proximity to the QD. Full description of electron spin dynamics is a complex problem. However, as we show in this work, in order to explain the collective coherence of the QD nuclear spin bath, it is sufficient to use a simplified spectral diffusion model, where environment-driven electron spin flips are treated as random events, described by the experimentally measurable electron spin relaxation rate Γ_{e}.

Supplementary Note 2. SPECTRAL DIFFUSION MODEL.

We consider evolution of the nuclear spin ensemble in the frame rotating at nuclear Larmor frequency determined by the strong static magnetic field B_z. Since all NMR experiments are conducted on the $(I_z = -1/2) \leftrightarrow (I_z = +1/2)$ transitions, the nuclei can be treated for simplicity as spin-1/2 particles. Optical cooling is used to create nonequilibrium longitudinal nuclear spin magnetization along the z axis. The initial $(\pi/2)_x$ rf pulse of the sequence flips the spins, so that magnetization points along the equatorial x axis of the rotating frame. In the absence of any

interactions, the spins remain static in the rotating frame indefinitely, corresponding to unperturbed Larmor precession in the laboratory frame. Various interactions cause dephasing and decoherence of the nuclear spin ensemble – here we focus on the effect of the central electron spin $\mathbf{s}$ coupled to the nuclear spins $\mathbf{I}_j$ via contact hyperfine interaction (see Supplementary Note 1). With large static magnetic field applied, electron-nuclear flip-flops are energetically forbidden, truncating the hyperfine Hamiltonian to $A_j \hat{s}_\mathrm{z} \hat{I}_{j,\mathrm{z}}$. Here A_j is the hyperfine constant of the j-th nucleus, which is proportional to the electron envelope wavefunction density $A_j \propto |\psi(\mathbf{r}_\mathrm{j})|^\mathbf{2}$ at the site $\mathbf{r}_\mathrm{j}$ of the nucleus. We assume that the electron can only occupy two discrete spin states with z-projections $s_\mathrm{z} = +1/2$ ($\uparrow$) or $s_\mathrm{z} = -1/2$ ($\downarrow$). For each nucleus j, the hyperfine field of the electron gives rise to a Knight shift $\nu_{\mathrm{e},j} = A_j s_\mathrm{z}/h$ of the NMR frequency. For a static electron spin and in the absence of nuclear-nuclear interactions, the π pulse of the nuclear spin echo sequence $(\pi/2)_\mathrm{x} - (\tau_\mathrm{evol}/2) - (\pi)_\mathrm{x} - (\tau_\mathrm{evol}/2) - (\pi/2)_\mathrm{x}$ can completely refocus the effect of inhomogeneous ($A_j \neq A_k$) Knight shifts resulting in an echo in transverse nuclear spin magnetization at time τ_evol after the initial $\pi/2$ pulse. It is the temporal evolution of the electron spin $s_\mathrm{z}(t)$ during the nuclear spin evolution that leads to irreversible decay of the echo amplitude through decoherence.

In order to model the time evolution of the electron spin we assume that it is governed by a memoryless random telegraph process. We denote the rate of transition from $\uparrow$ to $\downarrow$ as $w_{\uparrow\to\downarrow} = \Gamma_\mathrm{e}(1-\rho_\mathrm{e})/2$ and the rate of the reverse process as $w_{\downarrow\to\uparrow} = \Gamma_\mathrm{e}(1+\rho_\mathrm{e})/2$. The stationary population probabilities are then $p_\uparrow = (1+\rho_\mathrm{e})/2$ and $p_\downarrow = (1-\rho_\mathrm{e})/2$. Here we express the quantities in terms of the experimentally measurable electron spin relaxation rate Γ_e ($\Gamma_\mathrm{e} = 1/T_{1,\mathrm{e}}$, where $T_{1,\mathrm{e}}$ is the electron spin lifetime) and the equilibrium polarization degree $\rho_\mathrm{e} = \tanh[-\mu_\mathrm{B} g_\mathrm{e} B_\mathrm{z}/(2k_\mathrm{B}T)]$ of an electron spin with g-factor g_e at a temperature T (k_B is the Boltzmann constant). Due to the electron spin flips the Knight shift experienced by each nucleus is a random process $\nu_{\mathrm{e},j}(t) = A_j s_\mathrm{z}(t)/h$. In order to evaluate the relative spin echo amplitude of an individual nuclear spin we consider the total rotation of the magnetization vector in the xy plane of the rotating frame caused by the Knight shift, and find $\cos[2\pi \int_0^{\tau_\mathrm{evol}/2} \nu_{\mathrm{e},j}(t)dt - 2\pi \int_{\tau_\mathrm{evol}/2}^{\tau_\mathrm{evol}} \nu_{\mathrm{e},j}(t)dt]$. The echo amplitude observed in optically detected NMR is a sum of contributions from the individual nuclei, weighted by the electron wavefunction density. Moreover, we take the average over all possible implementations of the random process $s_\mathrm{z}(t)$. The amplitude of the QD nuclear spin echo as a function of free evolution time τ_evol is then modeled as

$$\mathcal{E}(\tau_\mathrm{evol}) = \left(N_\mathrm{hist} \sum_{j=1}^{N} A_j \right)^{-1} \sum_{i=1}^{N_\mathrm{hist}} \sum_{j=1}^{N} A_j \cos[\frac{2\pi A_j}{h} \left(\int_0^{\frac{\tau_\mathrm{evol}}{2}} s_{\mathrm{z},i}(t)dt - \int_{\frac{\tau_\mathrm{evol}}{2}}^{\tau_\mathrm{evol}} s_{\mathrm{z},i}(t)dt \right)], \qquad \text{(S7)}$$

The integral over $t = [\tau_\mathrm{evol}/2, \tau_\mathrm{evol}]$ is taken with a negative sign since the reversal of the nuclear spin

magnetization by the π pulse at $t = \tau_{\rm evol}/2$ changes the direction of the nuclear spin precession. The contributions of the N QD nuclei are weighted by $A_j \propto |\psi(\mathbf{r}_j)|^2$ to describe the optical detection of NMR via electron hyperfine shifts $E_{\rm hf}$. The sum over i implements the averaging over a finite number $N_{\rm hist}$ of electron spin evolution histories $s_{{\rm z},i}(t)$. The ideal echo amplitude at zero free evolution time is $\mathcal{E}(0) = 1$.

There is no universal closed-form solution to Eq. S7. A simple approximation of $E(\tau_{\rm evol})$ can be found in the limiting case, relevant to experimental results of this work. If the rate of electron spin flip events $= \Gamma_{\rm e}/2$ is small compared to a typical Knight shift $\nu_{\rm e}$, then one or more flips of the electron spin are likely to lead to a complete loss of the nuclear spin echo. Indeed, unless the electron spin flip occurs within a short time interval $\Delta t \approx T_{2,{\rm N}}^{*,(1e)} \propto 1/\Delta\nu_{\rm e}$ near the start or the end of the nuclear spin echo sequences, the precession phases acquired by the nuclear spins before and after the electron spin flip do not cancel out, and no echo is observed. The same reasoning holds for multiple electron spin flips during the nuclear spin echo sequence. Thus the formation of the collective nuclear spin echo is conditional on no electron spin flips occurring during the entire nuclear spin evolution. In equilibrium, the probability of having no electron spin flips in a short time period dt is $1 - w_{\uparrow\to\downarrow}p_\uparrow dt - w_{\downarrow\to\uparrow}p_\downarrow dt$. For a finite evolution time $\tau_{\rm evol}$ the probability to have no electron spin flips is then $\lim_{dt\to 0}(1 - w_{\uparrow\to\downarrow}p_\uparrow dt - w_{\downarrow\to\uparrow}p_\downarrow dt)^{\tau_{\rm evol}/dt} = \exp[-(w_{\uparrow\to\downarrow}p_\uparrow + w_{\downarrow\to\uparrow}p_\downarrow)\tau_{\rm evol}] = \exp(-\Gamma_{\rm e}(1-\rho_{\rm e}^2)\tau_{\rm evol}/2)$. For this regime of spectral diffusion under slow electron central spin flips ($\Gamma_{\rm e}/\Delta\nu_{\rm e} \ll 1$), averaging over electron spin-flip histories leads to an exponential decay of the echo amplitude with a characteristic coherence time $T_{2,{\rm N,SD}} \propto 2/(\Gamma_{\rm e}(1-\rho_{\rm e}^2)) = 2T_{1,{\rm e}}/(1-\rho_{\rm e}^2)$, linearly proportional to the central spin lifetime $T_{1,{\rm e}}$.

We perform numerical evaluation of the full Equation S7 to compute $T_{2,{\rm N,SD}}$ for arbitrary $\Gamma_{\rm e}$, $\rho_{\rm e}$ and $\nu_{{\rm e},j}$ without any simplifying assumptions about $\Gamma_{\rm e}$. We use $N_{\rm hist} \geq 10000$ and the set of the Knight shifts $\nu_{{\rm e},j}$ for nuclei within the quantum dot is modeled by taking $N = 1000$ samples from a random distribution. We use uniform or Gaussian distribution – for the practically relevant slow-electron-flip regime the root mean square broadening $\Delta\nu_{\rm e} = \sqrt{\langle\nu_{{\rm e},j}^2\rangle}$ and the actual shape of the distribution make no difference (here, $\langle\rangle$ denotes averaging over QD nuclei). The dependence of $T_{2,{\rm N,SD}}$ on $\Gamma_{\rm e}/\Delta\nu_{\rm e}$ is shown in Supplementary Fig. 1 for the case of uniform distribution. In the slow-electron-flip limit ($\Gamma_{\rm e}/\Delta\nu_{\rm e} \ll 1$), we find $T_{2,{\rm N,SD}} \approx 1.38T_{1,{\rm e}}/(1-\rho_{\rm e}^2)$, in good agreement with a simple estimate presented in the paragraph above. At $\Gamma_{\rm e}/\Delta\nu_{\rm e} \approx 10$, the spin bath decoherence time reaches its minimum $T_{2,{\rm N,SD}} \approx 0.4/\Delta\nu_{\rm e}$. Further increase of the electron spin flip rate $\Gamma_{\rm e}/\Delta\nu_{\rm e} \gg 1$ results in increasing $T_{2,{\rm N,SD}}$: In this motional narrowing regime the electron flips take place faster than it takes the nuclei to make any significant precession under the effect of the Knight shift, so

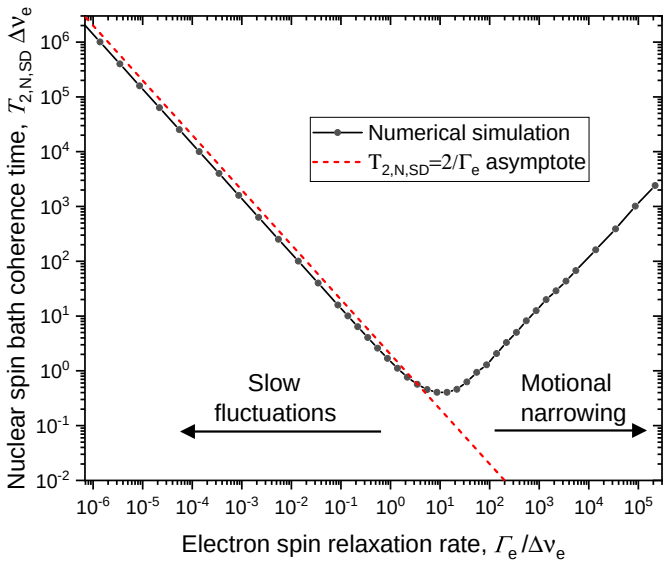

Supplementary Figure 1. **Numerical simulation of decoherence induced by spectral diffusion.** Coherence time $T_{2,\mathrm{N,SD}}$ of the nuclear spin bath as a function of the relaxation rate $\Gamma_\mathrm{e} = 1/T_{1,\mathrm{e}}$ of the central electron spin. Results are for an unpolarized electron $\rho_\mathrm{e} = 0$. The characteristic root mean square width $\Delta\nu_\mathrm{e}$ of the uniform distribution of the Knight shifts is used to scale $T_{2,\mathrm{N,SD}}$ and Γ_e and plot dimensionless values on both axes.

that the Knight shifts are effectively averaged to zero, leading to an extended spin bath coherence time $T_{2,\mathrm{N,SD}}$.

Dipole-dipole coupling between the nuclei of an empty QD ($0e$) itself causes spin bath decoherence [10–12] with a characteristic time $T_{2,\mathrm{N,DD}} \propto 1/\max(h|b_{j,k}|)$. In order to model the experimentally measured nuclear spin coherence time $T_{2,\mathrm{N}}^{(1e)}$ in presence of an electron we combine the dipole-dipole and spectral diffusion decoherence rates $1/T_{2,\mathrm{N}}^{(1e)} = 1/T_{2,\mathrm{N,DD}} + 1/T_{2,\mathrm{N,SD}}$. The dipolar decoherence time $T_{2,\mathrm{N,DD}}$ is taken to be the measured empty-QD ($0e$) time $T_{2,\mathrm{N}}^{(0e)}$, which is nearly independent of magnetic field in the studied structures. We can then write the model equation for $T_{2,\mathrm{N}}^{(1e)}$ in a closed form:

$$1/T_{2,\mathrm{N}}^{(1e)} = 1/T_{2,\mathrm{N}}^{(0e)} + (1 - \tanh^2[-\frac{\mu_\mathrm{B} g_\mathrm{e} B_\mathrm{z}}{2k_\mathrm{B}T}])/(1.38T_{1,\mathrm{e}}), \tag{S8}$$

where all quantities are either measurable (g_e, $T_{1,\mathrm{e}}(B_\mathrm{z})$, $T_{2,\mathrm{N}}^{(0e)}$) or controlled in the experiment (B_z, T). Equation 1 of the main text is a special case of this Eq. S8 in the high-temperature or low-field limit where equilibrium electron spin polarization ρ_e is small. The model plots of Fig. 2b of the main text take into account the electron spin polarization, although the difference with the simplified model of $\rho_\mathrm{e} \approx 0$ is relatively small for the studied range of magnetic fields $B_\mathrm{z} < 8$ T at

$T \approx 4.5$ K.

Supplementary Note 3. DETAILS OF PULSED NMR IMPLEMENTATION

A schematic of the timing sequence used in the pulsed NMR experiments is shown in Supplementary Fig. 2. The gate bias V_{G} applied to the structure is varied together with optical and radio frequency pulses in order to provide optimal charging conditions for each stage. High power ($P_{\mathrm{Pump}} \approx 8$ mW) circularly polarized optical excitation with a wavelength $\lambda \approx 850$ nm, corresponding to the ground states of the InAs wetting layer, is applied for pumping time $T_{\mathrm{Pump}} \approx 8$ s. Such optical pumping produces a state of the QD nuclear spin ensemble that is well described by a Boltzmann distribution [6]. A bias of $V_{\mathrm{Pump}} = -1.5$ V to 1.0 V applied during optical pumping produces large dynamic nuclear polarisation (DNP), characterised by the hyperfine shifts of up to $E_{\mathrm{hf}} \approx \pm 120$ μeV. It is found that negative values of V_{Pump} generate a somewhat reduced DNP but produce the most stable results, whereas V_{Pump} exceeding the single-electron Coulomb blockade bias V_{1e} leads to intermittent ejection of the electron during the application of the high power rf pulses. This undesired effect is found to be particularly pronounced in the thickest barrier sample with $t_{\mathrm{B}} = 52$ nm. In order to avoid this parasitic electron ejection we use $V_{\mathrm{Pump}} = -1.5$ V in all measurements, and the presence of the electron in a QD during the NMR sequences can be verified directly by observing a bimodal distribution in single-shot measurements, such as those shown in Figs. 3c of the main text. A short delay $T_{\mathrm{Del}} \approx 5$ ms is introduced between switching the gate bias and the optical excitation, in order to account for delays of the mechanical shutters implementing the pump and probe laser pulses.

Frequency swept rf excitation is applied after optical pumping to implement adiabatic population transfer [13], which transforms the $I_{\mathrm{z}} = \pm 3/2$ nuclear spin states into the $I_{\mathrm{z}} = \pm 1/2$ states. This increases the difference in the number of $I_{\mathrm{z}} = -1/2$ and $I_{\mathrm{z}} = +1/2$ nuclei that are coherently controlled under pulsed rf excitation that follows. The frequency sweeps start 5 to 10 MHz away from the $-1/2 \leftrightarrow +1/2$ central transition (CT) frequency and end 50 to 200 kHz near the CT frequency, depending on the isotope. These sweep ranges are chosen to fully cover the strain-broadened satellite transitions (STs) $-3/2 \leftrightarrow -1/2$ and $+1/2 \leftrightarrow +3/2$, while maintaining sufficient detuning from the CT frequency. A frequency sweep rate ranging from 5 to 10 MHz s^{-1} is used, depending on the isotope, to achieve adiabatic inversion. Adiabatic sweeps are applied while the sample is kept at large reverse bias $V_{\mathrm{Flush}} = -1.5$ V to ensure any charges generated during optical pumping are flushed out of the QD leaving it empty ($0e$ state). High power radio

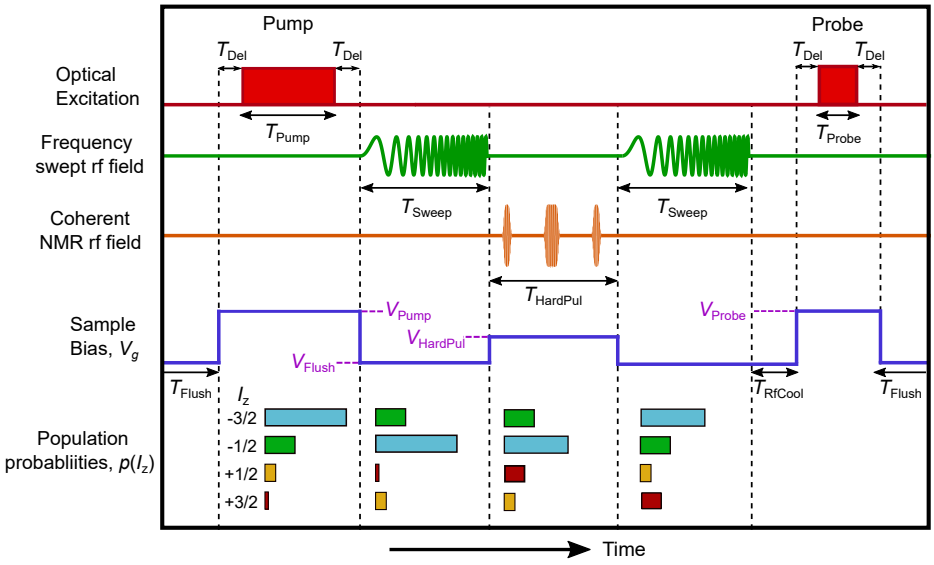

Supplementary Figure 2. **Pulsed NMR measurement timing diagram.** Timing sequence of one cycle used in pulsed NMR experiments on $I_z = \pm 1/2$ spin states of half-integer quadrupolar nuclei. Optical excitation includes pump and probe laser pulses (red), frequency swept rf implementing adiabatic population transfer (green), high power rf pulsed implementing coherent control of the nuclear spins (orange) and applied sample bias V_G controlling the charge state of the QD (blue). The bars in the bottom row sketch the population probabilities $p(I_z)$ of the spin states I_z at the end of each stage of the cycle. For discussion see Supplementary Note 3.

frequency pulses are then applied while the sample is at an arbitrary bias V_{HardPul} to study nuclear spin bath coherence under various QD charge states and tunneling conditions. The same adiabatic sweeps that precede the high power rf sequence are applied in some measurements once again afterwards, transferring the final populations of the $I_z = \pm 1/2$ states back into $I_z = \pm 3/2$ states, respectively. This provides a factor of 3 increase in the optically detected hyperfine shift variations ΔE_{hf} at the expense of a longer experimental cycle. After all the rf excitations have completed, a short delay of $T_{\mathrm{RfCool}} \approx 60$ ms at V_{Flush} is used to ensure dissipation of any rf-induced heat before optical probing is done. Optical probe is a low power ($P_{\mathrm{Probe}} = 1 - 10$ μW) laser pulse of duration $T_{\mathrm{Probe}} = 5 - 20$ ms, at a bias of $V_{\mathrm{Probe}} \approx 0.3 - 0.65$ V, chosen to maximise optical PL intensity of the negatively charged trion X^-. After each cycle the sample is returned to the flush bias V_{Flush} for a time $T_{\mathrm{Flush}} = 30$ ms to remove any residual charges before the next cycle begins.

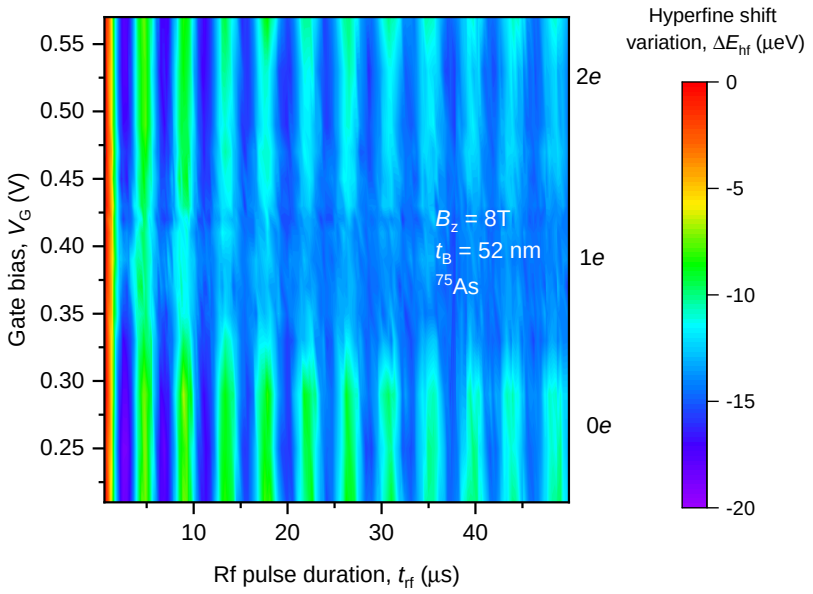

Supplementary Figure 3. **Bias dependant ^{75}As Rabi oscillations**. Rf induced variation of the hyperfine shift $\Delta E_{\rm hf}$ as a function of rf pulse duration $t_{\rm rf}$ measured at $B_z = 8$ T in the $t_{\rm B} = 52$ nm sample for a range of gate biases $V_{\rm G}$ across the single-electron ($1e$) charging plateau centered at $V_{\rm G} \approx 0.4$ V. Each point is obtained by averaging over multiple measurements. Inhomogeneous Knight shifts and electron spin flips occurring during the rf pulse lead to dephasing, resulting in reduced oscillation amplitude in the single electron regime ($1e$). In a doubly charged state ($2e$, $V_{\rm G} > 0.55$ V) Rabi oscillations are similar to oscillations in an empty dot ($0e$, $V_{\rm G} < 0.25$ V) confirming that the damping of the oscillation is due to the unpaired spin of a single electron.

Supplementary Note 4. ADDITIONAL RESULTS FOR ^{75}As NUCLEAR SPINS

Supplementary Fig. 3 shows the results of bias dependent Rabi oscillation measurements. Clear oscillations with a period of ≈ 4.4 μs are observed. At $V_{\rm G} \approx 0.4$ V, corresponding to single-electron charging of the QD, the damping of the Rabi oscillations is accelerated by the inhomogeneous Knight shifts.

Supplementary Fig. 4 shows the results of free induction decay NMR measured using the spin echo sequences with a fixed τ_0 and variable τ. The experiments are similar to those presented in Figs. 1d, e of the main text for ^{69}Ga. The time resolved measurements with a sequence $(\pi/2)_{\rm x} - \tau_0 - (\pi)_{\rm x} - \tau - (\pi/2)_{\rm x}$ shown in Supplementary Fig. 4a provide estimates of the nuclear spin dephasing time $T^*_{2,{\rm N}}$. In order to derive the spectral information we also implement the $(\pi/2)_{\rm x} - \tau_0 - (\pi)_{\rm x} - \tau - (\pi/2)_{\rm y}$ sequence. The rotation by the $(\pi/2)_{\rm y}$ pulse is around the axes orthogonal to the rotation axis of the $(\pi/2)_{\rm x}$ pulse. Thus the sequences with the $(\pi/2)_{\rm y}$ final pulse measures the quadrature

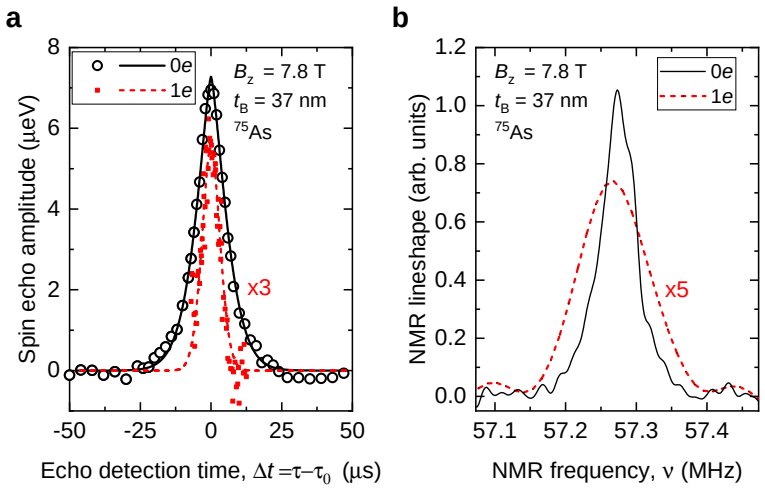

Supplementary Figure 4. **Free induction decay spectroscopy of ^{75}As nuclei in a single quantum dot. a,** Spin echo evolution as a function of the second delay τ in the $t_{\rm B} = 37$ nm sample at $B_{\rm z} = 7.8$ T, revealing free induction decay in $0e$ (circles, $\tau_0 = 150$ μs) and $1e$ charge states (squares, $\tau_0 = 7.5$ μs, data multiplied is by 3). Lines show compressed exponential fitting used to derive the nuclear spin dephasing times $T^*_{2,\rm N}$. **b,** Fourier transform of **a**, data for $1e$ is multiplied by 5.

component of the echo nuclear spin polarization. By performing the Fourier transform on both the in-phase and the quadrature data we obtain the NMR lineshapes such as shown in Supplementary Fig. 4b and Fig. 1e of the main text. The lineshapes are then fitted with compressed exponential profiles to derive the full width at half maximum (FWHM) spectral broadening.

For ^{69}Ga at $B_{\rm z} = 7.8$ T we find $T^{*,(0e)}_{2,\rm N} \approx 34.6$ μs in an empty QD, and a corresponding spectral profile with a FWHM of ≈ 13.3 kHz and a compression parameter $\eta \approx 1.6$ (Figs. 1e, d of the main text). For ^{75}As at $B_{\rm z} = 7.8$ T (Supplementary Fig. 4) we find $T^{*,(0e)}_{2,\rm N} \approx 7.4$ μs, $\eta \approx 1.38$, and a FWHM of ≈ 53.8 kHz. The larger spectral broadening of ^{75}As is due to its larger quadrupolar moment and the stronger second order quadrupolar shifts arising from the lattice constant scale strain, induced by the random alloying of Ga and In atoms [3].

When a single electron is added to the dot we find for ^{69}Ga at $B_{\rm z} = 7.8$ T the dephasing time of $T^{*,(1e)}_{2,\rm N} \approx 4.3$ μs and a spectral profile with $\eta \approx 1.88$, and a FWHM of ≈ 126 kHz. For ^{75}As we find $T^{*,(1e)}_{2,\rm N} \approx 4.5$ μs, $\eta \approx 2.05$, and a FWHM of ≈ 116 kHz. The additional broadening due to electron charging characterises the magnitude and inhomogeneity of the electron-induced Knight shifts of the individual nuclei in the dot. The Knight shifts of ^{75}As are smaller due to its smaller gyromagnetic ratio and smaller hyperfine constant compared to ^{69}Ga.

At a reduced magnetic field of $B_{\rm z} = 1.94$ T (data not shown) we find for ^{69}Ga the dephasing

times of $T_{2,\mathrm{N}}^{*,(0e)} \approx 13.6$ μs and $T_{2,\mathrm{N}}^{*,(1e)} \approx 3.6$ μs. The spectral profile for an empty quantum dot is characterised by $\eta \approx 1.03$, and a FWHM of ≈ 23 kHz, which is twice larger than at high magnetic field, as expected for broadening related to second order quadrupolar effects [10]. For the nuclear spin spectral lineshape in presence of a single electron we find $\eta \approx 2.04$, and a FWHM of ≈ 150 kHz, consistent with the results obtained at high fields. Unlike at high fields, the average Knight shift $\langle \nu_{\mathrm{e}} \rangle$ is very small at $B_{\mathrm{z}} = 1.94$ T due to the small equilibrium electron spin polarization. For ^{75}As at low magnetic fields the quadrupolar induced spectral broadening becomes too large to conduct reliable pulsed NMR spectroscopy.

Supplementary Note 5. DYNAMICAL DECOUPLING OF THE NUCLEAR SPIN ENSEMBLE IN PRESENCE OF A SINGLE ELECTRON SPIN.

Dynamical decoupling is a technique used to suppress decoherence arising from unwanted interactions of a quantum system. A commonly used implementation relies on a series of short (bang-bang) control pulses [14, 15] that transform the effective Hamiltonian governing the interactions in the free evolution intervals following each pulse. The control sequence can be chosen to selectively remove some of the interactions or can be chosen to implement 'time-suspension' where all the interactions are suppressed. Here we discuss experimental results on dynamical decoupling of the nuclear spins in an individual quantum dot in presence of a single electron ($1e$). The methodology follows the previous work [12] conducted on neutral QDs ($0e$ state). Each NMR pulse sequences starts with a $(\pi/2)_{\mathrm{x}}$ or $(\pi/2)_{\mathrm{y}}$ pulse creating transverse nuclear spin polarization along the x or y axis of the rotating frame, respectively (sequences labeled as -X and -Y, respectively). A dynamical decoupling sequence of rf pulses is then applied, followed by a final $\pi/2$ pulse of the same phase (same rotation axis) as the initial pulse to convert the preserved fraction of the nuclear spin coherence into an optically detectable longitudinal nuclear spin polarization. The decay of coherence as a function of the total free evolution time τ_{evol} between the initial and the final pulses is fitted with a stretched or compressed exponent to derive the coherence time $T_{2,\mathrm{N}}$.

We start by examining ^{69}Ga nuclei in the low field regime ($B_{\mathrm{z}} = 2.5$ T) where electron spin flips, characterised by $T_{1,\mathrm{e}} \approx 10$ ms, are slow compared to dipolar-dominated nuclear spin coherence time $T_{2,\mathrm{N}}^{(0e)} \approx 1.69$ ms in an empty QD. For each decoupling sequence the resulting $T_{2,\mathrm{N}}$ is shown in Supplementary Fig. 5a as a function of the total duration of the control pulses, excluding the initial and final pulses, and measured in units of a π-pulse duration t_π. The Carr Purcell sequence (CP-X) consists of a train of periodic π pulses with the same phase as the initial and final pulses

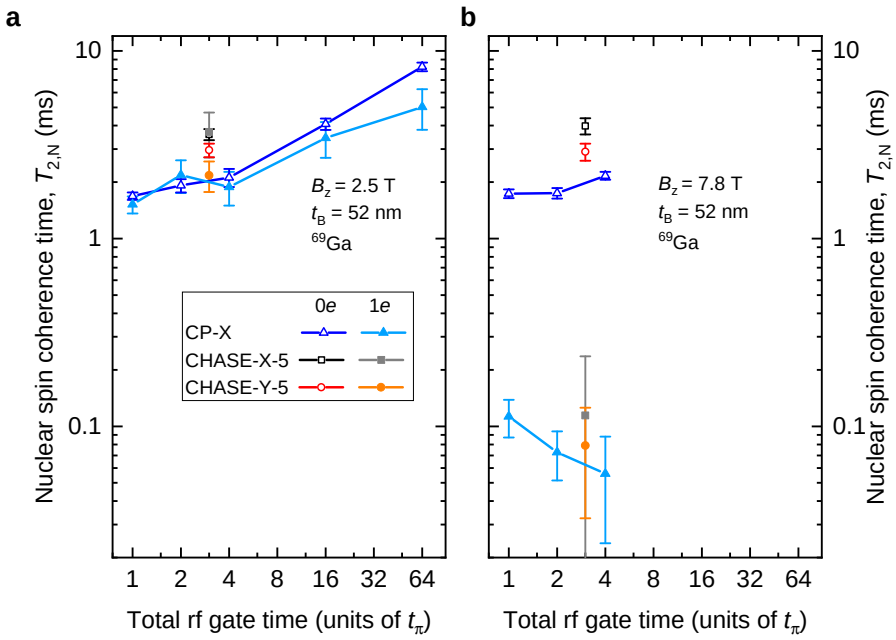

Supplementary Figure 5. **Coherence of ^{69}Ga nuclear spins under dynamical decoupling. a,** Measurements of $T_{2,\mathrm{N}}^{(0e)}$ (open symbols) and $T_{2,\mathrm{N}}^{(1e)}$ (solid symbols) on a QD in the $t_\mathrm{B} = 52$ nm sample at $B_\mathrm{z} = 2.5$ T. The coherence times are plotted as a function of the total rf sequence gate time in units of π-pulse duration t_π with initial and final pulses excluded. **b,** Same as **a** but for $B_z = 7.8$ T.

[12]. Spin echo is a particular case with just one π pulse. The CP sequence removes the dephasing induced by inhomogeneous broadening, but does not affect the dipolar nuclear-nuclear interactions. For ideal (infinitely fast) control pulses and a static inhomogeneous broadening, $T_{2,\mathrm{N}}$ is expected to be constant for any number of π pulses. By contrast, in experiment on an empty QD ($0e$, open triangles) we find an increase in $T_{2,\mathrm{N}}$ with an increasing number of π pulses applied during the τ_evol interval. This increase in $T_{2,\mathrm{N}}$ is a pulsed spin locking effect [12, 16] resulting from coherent evolution of the interacting nuclear spins during the non-ideal (finite-duration) rf control pulses. In presence of an electron ($1e$, solid triangles) spin locking is observed as well, although the maximum $T_{2,\mathrm{N}}$ is smaller than in the $0e$ case, most likely limited by $T_{2,\mathrm{N}}$ approaching the $T_{1,\mathrm{e}}$, when it becomes probable that the nuclear spin decoupling echo is destroyed by an electron spin flip occurring during the τ_evol interval.

To implement the time-suspension we use CHASE-5 sequence [12], which suppresses both the ensemble inhomogeneous broadening and the nuclear-nuclear interactions. Unlike the spin locking, which preserves the coherence only along the preferential direction of the rotating frame, the CHASE sequence is designed to preserve a coherent state with an arbitrary phase. This is verified

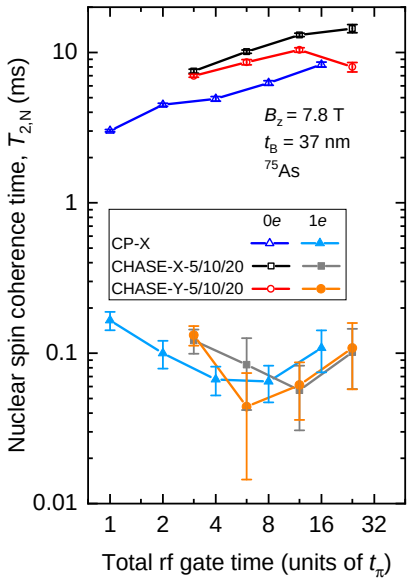

Supplementary Figure 6. **Coherence of ^{75}As nuclear spins under dynamical decoupling. a,** Measurements of $T_{2,\mathrm{N}}^{(0e)}$ (open symbols) and $T_{2,\mathrm{N}}^{(1e)}$ (solid symbols) on a QD in the $t_\mathrm{B} = 37$ nm sample at $B_\mathrm{z} = 7.8$ T. The coherence times are plotted as a function of the total rf sequence gate time in units of π-pulse duration t_π with initial and final pulses excluded. The points at 3π correspond to one cycle of CHASE-5 sequence, the points at 6π correspond to one cycle of CHASE-10 and the points at $\geq 12\pi$ are for integer numbers of CHASE-20 cycles.

by measuring the decay of the echo initialised either along the x or the y axis of the rotating frame, with results shown in Supplementary Fig. 5a by the squares and circles, respectively. In agreement with previous studies [12], in an empty QD ($0e$) CHASE-5 leads to approximately a factor of 2 increase in coherence time, from $T_{2,\mathrm{N}}^{(0e)} \approx 1.69 \pm 0.085$ ms for spin echo to $T_{2,\mathrm{N}}^{(0e)} \approx 3.59 \pm 0.24$ ms and $T_{2,\mathrm{N}}^{(0e)} \approx 2.96 \pm 0.24$ ms for CHASE-X-5 and CHASE-Y-5 sequences, respectively. In presence of the electron spin ($1e$) CHASE-X-5 is equally effective in improving the spin echo coherence time $T_{2,\mathrm{N}}^{(1e)} \approx 1.50 \pm 0.15$ ms to $T_{2,\mathrm{N}}^{(1e)} \approx 3.7 \pm 1.0$ ms (solid square in Supplementary Fig. 5a). In the worst case scenario of a coherent state with polarisation along the y axis of the rotating frame (CHASE-Y-5, solid circle in Supplementary Fig. 5a) the observed $T_{2,\mathrm{N}}^{(1e)} \approx 2.2 \pm 0.4$ ms is still a significant improvement over the single-pulse spin echo. Longer decoupling sequences, such as CHASE-10 and CHASE-20 lead to accumulation of pulse control errors, and reduction of the echo amplitude which prevents reliable $T_{2,\mathrm{N}}^{(1e)}$ measurement. Nevertheless, the CHASE-5 results confirm that the central spin is not a fundamental obstacle for dynamical decoupling of the nuclear spin bath.

In the high field regime (B_z = 7.8 T, Supplementary Fig. 5b) the addition of the electron spin to the quantum dot results in a pronounced reduction of the ^{69}Ga nuclear spin coherence. This is expected since the significantly shortened $T_{1,e} \approx 90$ μs makes spectral diffusion mechanism dominant over the intrinsic dipolar-induced decoherence. The accuracy is not sufficient to evaluate the trends in $T_{2,N}^{(1e)}$ as a function of the rf gate time, but it can be seen that neither CP nor CHASE sequences provide any reliable improvement in $T_{2,N}^{(1e)}$, suggesting that both the pulsed spin locking and time-suspension are disrupted. The mechanism is similar to the one that governs the spin echo decoherence under spectral diffusion in the limit of slow fluctuations (see details in Supplementary Note 2). Owing to the strong Knight shift inhomogeneity, characterised by short dephasing time $T_{2,N}^{*,(1e)}$, the probability that a single electron flip destroys the nuclear spin echo $\approx 1 - T_{2,N}^{*,(1e)}/T_{2,N}^{(0e)}$ is close to unity. This is also the case for CP and CHASE sequences: just as for spin echo, these dynamical decoupling sequences rely on rf pulses periodically transforming the instantaneous interaction Hamiltonian to converge the average Hamiltonian to zero. A single electron flip is sufficient to disrupt the decoupling by breaking the balance of phases accumulated by spins in the free evolution intervals of the sequence. As a result, nuclear spin coherence is essentially limited by the electron spin lifetime $T_{2,N}^{(1e)} \lesssim 1.38 T_{1,e}$. Under these conditions, an improvement of $T_{2,N}^{(1e)}$ with CHASE can be expected only if a large number of decoupling pulses is applied with intervals much shorter than the timescale $T_{1,e}$ of the electron spin flips. This regime is currently not achievable in our experiments on ^{69}Ga, and would require improvement of the echo amplitude through optimisation of the rf circuits to attain larger rf magnetic field while reducing the parasitic rf electric field.

We also examine dynamical decoupling of ^{75}As nuclei in the high field regime (B_z = 7.8 T). The results shown in Supplementary Fig. 6 are consistent with the high field results for ^{69}Ga (Supplementary Fig. 5b), showing that dynamical decoupling provides no reliable improvement when nuclear spin decoherence is dominated by random electron spin flips rather than by the nuclear spin-spin interactions. Due to the 100% natural abundance, ^{75}As gives a larger NMR signal making it possible to measure $T_{2,N}^{(1e)}$ under longer decoupling sequences than in ^{69}Ga. From these measurements shown in Supplementary Fig. 6 we observe a non-monotonic dependence of $T_{2,N}^{(1e)}$ on the number of CP-X cycles (solid triangles). The coherence time first decreases to $T_{2,N}^{(1e)} \approx 65$ μs under a sequence with 4 and 8 π-pulses. Such decrease can be ascribed to the heating of the spins by frequent control pulses, which reenables the dipolar flip-flops, otherwise frozen by inhomogeneous quadrupolar shifts [12]. The coherence is then seen to increase to $T_{2,N}^{(1e)} \approx 110$ μs under 16 π-pulses. This increase would be consistent with dynamical decoupling overcoming the random electron spin

flips by periodically inverting the nuclear spins faster than $T_{1,\mathrm{e}}$. However, validation of these trends in $T_{2,\mathrm{N}}^{(1e)}$ would require further studies with improved measurement accuracy.

[1] Slichter, C. P. *Principles of Magnetic Resonance* (Springer, 1990).

[2] Bulutay, C. Quadrupolar spectra of nuclear spins in strained $In_xGa_{1-x}As$ quantum dots. *Phys. Rev. B* **85**, 115313 (2012).

[3] Chekhovich, E. A. *et al.* Structural analysis of strained quantum dots using nuclear magnetic resonance. *Nat. Nanotechnol.* **7**, 646–650 (2012).

[4] Gueron, M. Density of the conduction electrons at the nuclei in indium antimonide. *Phys. Rev.* **135**, A200–A205 (1964).

[5] Gotschy, B., Denninger, G., Obloh, H., Wilkening, W. & Schnieder, J. Overhauser shift and dynamic nuclear polarization in InP. *Solid State Commun.* **71**, 629–632 (1989).

[6] Chekhovich, E. A. *et al.* Measurement of the spin temperature of optically cooled nuclei and GaAs hyperfine constants in GaAs/AlGaAs quantum dots. *Nat. Mater.* **16**, 982 (2017).

[7] Klauser, D., Coish, W. A. & Loss, D. Nuclear spin dynamics and Zeno effect in quantum dots and defect centers. *Phys. Rev. B* **78**, 205301 (2008).

[8] Reilly, D. J. *et al.* Exchange control of nuclear spin diffusion in a double quantum dot. *Phys. Rev. Lett.* **104**, 236802 (2010).

[9] Gillard, G. *et al.* Fundamental limits of electron and nuclear spin qubit lifetimes in an isolated self-assembled quantum dot. *npj Quantum Inf.* **7**, 43 (2021).

[10] Chekhovich, E. A., Hopkinson, M., Skolnick, M. S. & Tartakovskii, A. I. Suppression of nuclear spin bath fluctuations in self-assembled quantum dots induced by inhomogeneous strain. *Nat. Commun.* **6**, 6348 (2015).

[11] Wüst, G. *et al.* Role of the electron spin in determining the coherence of the nuclear spins in a quantum dot. *Nat. Nanotechnol.* **11**, 885–889 (2016).

[12] Waeber, A. M. *et al.* Pulse control protocols for preserving coherence in dipolar-coupled nuclear spin baths. *Nat. Commun.* **10**, 3157 (2019).

[13] Haase, J. & Conradi, M. S. Sensitivity enhancement for NMR of the central transition of quadrupolar nuclei. *Chem. Phys. Lett.* **209**, 287–291 (1993).

[14] Waugh, J. S., Huber, L. M. & Haeberlen, U. Approach to High-Resolution NMR in Solids. *Phys. Rev. Lett.* **20**, 180–182 (1968).

[15] Viola, L., Knill, E. & Lloyd, S. Dynamical decoupling of open quantum systems. *Phys. Rev. Lett.* **82**, 2417–2421 (1999).

[16] Li, D. *et al.* Intrinsic origin of spin echoes in dipolar solids generated by strong π pulses. *Phys. Rev. B* **77**, 214306 (2008).

6

Fast microwave control of electron spins

6.1 Introduction

We have so far studied the dynamics of spins in self-assembled quantum dots, determining the ideal operating conditions for long-lasting spin states. We have also demonstrated coherent control of nuclear isotopes within the quantum dots, allowing the use of the nuclear spin bath as a quantum computing resource. We now turn to coherent control of an electron spin, which as discussed previously (Section 2.4.2), can be achieved through optical control in Voigt [31] or electron spin resonance (ESR) in Faraday geometry [32].

Electron spin resonance on quantum dots would coherently control the electron spin in a charged QD, allowing rotation of the spin state between $|\uparrow\rangle$ and $|\downarrow\rangle$. Similar to NMR measurements, electron spin resonance requires a rotating magnetic field B_1 oscillating at a frequency equal to the splitting of the electron spin states $f_{\mathrm{ESR}} = \Delta E_{\mathrm{Zeeman}} = g_e \mu_B B_z$, where g_e is the electron g-factor. For an electron residing in a charged InGaAs quantum dot, the g-factor can vary from $g_e^{(\mathrm{QD})} \approx -0.7$ to -0.3 [89, 137, 138]. We observed a value of $g_e^{(\mathrm{QD})} = -0.67$ for the QD measured in Chapter 5, which in a moderate magnetic field of

$B_z = 0.5$ - 1 T results in an estimate of $f_{\mathrm{ESR}} \approx 4.5$ - 9.5 GHz, corresponding to the X-band of microwave (MW) frequencies.

The rate of coherent control is defined by the Rabi frequency f_{Rabi}, and to allow coherent control must meet the condition that the Rabi frequency is less than the frequency of the spin state transition $f_{\mathrm{Rabi}} < f_{\mathrm{ESR}}$. We desire the fastest possible spin control to allow an increase in the number of gate operations that can be performed before the electron spin state decoheres. As such, operating ESR measurements at a higher f_{ESR} is desirable to allow the opportunity to provide faster rotations through increased f_{Rabi}.

The high-frequency requirement for electron spin control can not be generated from a simple copper coil as we used for NMR experiments. Broadband linear conductors can produce the required frequencies but have to be geometrically small and close to the target spin [154]. This is not a suitable solution for the ODMR protocols used on QD structures throughout this thesis, nor any other system that requires optical access. In addition to limited optical access, the simple antenna can also cause parasitic electric fields and heating effects which will destroy the coherence of a charged QD spin [33].

To mitigate these issues we require a microwave source that can be operated at a reasonable separation to the sample, as for the RF coil described in Chapter 3. To achieve this we use resonator structures that can produce a sufficiently strong oscillating magnetic field B_1 to compensate for the separation. Resonators operate at fixed resonant frequencies f_{Res} and require careful design to achieve the desired frequency. The requirements for the resonators are the need to efficiently generate and propagate microwave pulses at a high power P_{MW}, with minimal electric field $\vec{E}$ generation to prevent disturbing the quantum dot charge state. There is also the additional requirement to operate at cryogenic temperatures for use in the bath cryostat set-up described in Chapter 3.

In this chapter we set out to test keyhole resonators (KHR) [33] designed to operate at $f_{\mathrm{Res}} = 8$ GHz, selected to allow sufficiently fast Rabi oscillations f_{Rabi} of the QD electron spin resonance. Testing of the KHR resonator design was carried out recently at low microwave

powers ($P_{\mathrm{MW}} = 3$ W) on silicon carbide (SiC) vacancies, with reasonable success [33]. Here, we test a further optimisation to the previously successful KHR designs in order to push the resonator frequency mode to $f_{\mathrm{Res}} = 8$ GHz and more importantly test their ability to operate at higher microwave powers (up to $P_{\mathrm{MW}} = 250$ W), allowing for fast electron spin control. We test the resonators on a benchmark sample of NV centres in diamond at room temperature. NV Centres in diamond provide a system with non-degenerate spin states allowing coherent control through optically detected magnetic resonance techniques (ODMR) at room temperature and is well studied through the literature [155, 156]. Room temperature operation allows ease of access to the set-up for iterative improvement, which is preferable to the time-consuming process of loading test resonators into the bath cryostat used in the QD studies (Section 3.2). We present a basic characterisation of the resonator properties and of the NV centres, followed by magnetic field dependence of ESR and finally present Rabi oscillations from pulsed ESR of the NV^- spin states.

6.2 Microwave resonator design for pulsed ESR measurements

A microwave resonator to be used in coherent control of electron spins has several critical requirements as laid out in Ref [33], and are used to design the keyhole resonators used in this chapter. To summarise some of the key requirements, we desire a resonator that can efficiently generate a strong oscillating magnetic field B_1 at $f_{\mathrm{Res}} \approx 8$ GHz, while producing minimal parasitic electric fields $\vec{E}$. We also require the ability to generate short bursts of B_1 to allow coherent control of electron spins and thus require lower Q-factor cavities. The resonator also must allow optical excitation to reach the sample, or in other words, must not obscure the sample surface in any way.

6.2.1 Loop-gap resonators

Before discussing the keyhole resonator design, we can first discuss more established resonator designs. Simple high Q-factor rectangular microwave resonators are undesirable for pulsed coherent control techniques, as the high Q limits the operational bandwidth, preventing short pulses from being generated. A solution to this was developed known as the loop-gap resonator (LGR). These were designed with pulsed electron spin resonance measurements in mind by providing moderate Q-factors while maintaining a strong conversion of microwave power P_{MW} to emitted magnetic field B_1 [157]. A simple schematic of an LGR is displayed in Fig 6.1.

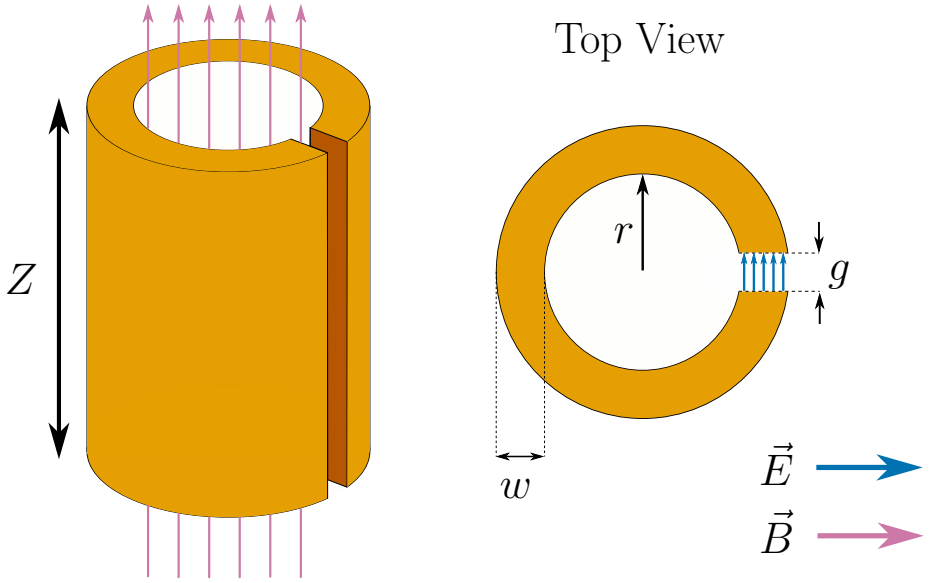

Figure 6.1: Schematic of a typical loop gap resonator (LGR). Dimensions of the LGR are defined by the inner bore radius r, the conducting loop width w, the gap width g and the resonator height Z. Electric field $\vec{E}$ (blue arrows) is confined to the gap region which acts as a capacitor, while magnetic field $\vec{B}$ (pink arrows) propagates parallel to the central axis of the conducting loop.

The resonator can be considered as two primary components, a loop with inductance L and a gap with capacitance C. Both L and C are determined by the geometry and material

properties of the resonator, as defined by the following equations.

$$C = \frac{(\epsilon_0 \epsilon_r) w Z}{g} \qquad L = \frac{\mu_0 \pi r^2}{Z} \tag{6.1}$$

where Z, w, r and g are defined by the various dimensions of the LGR, Fig 6.1, μ_0 is the permeability of free space, ϵ_0 is the permittivity of free space. The medium within the conductive gap g has dielectric constant ϵ_r, which can be an air gap $\epsilon_r \approx 1$, or filled with a dielectric material $\epsilon_r > 1$. For simplicity we use a lumped circuit approximation, which neglects the effect of distance on the circuitry, instead assuming that the dimensions of the circuit are much smaller than the wavelength of the microwaves. The resonant mode frequency of the LGR can thus be approximated by $2\pi f_{\text{Res}} = 1/\sqrt{LC}$, effectively demonstrating that careful selection of the LGR dimensions is required to produce a resonator capable of generating microwaves at the desired frequency. Real resonant frequency modes will be different, but can only be calculated from solving Maxwell's equations or testing the system experimentally.

Continuing to use the lumped circuit approximation, we can make a simple estimate for the Q-factor of the LGR:

$$Q \approx \frac{r}{\delta} \quad \text{where} \quad \delta = \sqrt{\frac{2\rho}{(2\pi f_{\text{Res}})\mu_0}} \tag{6.2}$$

where r is defined as in Fig 6.1, δ is the skin depth of the conductive material defined by resistivity ρ, and the resonant frequency of the LGR f_{Res} [157, 158]. Practically, this is an overestimate of Q due conductive losses in the capacitor and loss of magnetic field to free space, the latter of which can be limited by surrounding the LGR in a cylindrical cavity to act as a shield [157].

In order to design a resonator for a specific scenario, there are several key properties that need to be considered in the design phase. The frequency of the resonant mode f_{Res} and the Q-factor of the cavity are critical, in addition to efficient conversion of input microwave power P_{MW} to outputted microwave magnetic field B_1, which can be quantified by the microwave

conversion factor $B_1/\sqrt{P_{\mathrm{MW}}}$.

For the work in this chapter, we require the resonators to have resonant frequencies of $f_{\mathrm{Res}} \approx 8$ GHz to achieve fast electron spin control. The geometry of the structure must then be designed to operate at the target frequency f_{Res} in addition to providing maximum $B_1/\sqrt{P_{\mathrm{MW}}}$. Both the Q-factor and the resonator mode volume can affect the microwave conversion efficiency. However, there is an upper limit on Q, imposed due to the need for sufficient bandwidth to allow generation of the short bursts of microwaves required to achieve coherent control of electron spins. Generating a rectangular pulse of 10 ns requires a bandwidth of $f_{\mathrm{BW}} \approx 88$ MHz according to the Mims' criterion [159, 160]. This results in an upper limit of $Q = \dfrac{f_{\mathrm{Res}}}{f_{\mathrm{BW}}} \approx 90$. Consequently, once the desired Q has been achieved, minimising the mode volume is the primary method of improving the microwave conversion factor $B_1/\sqrt{P_{\mathrm{MW}}}$ of the resonators [33].

For the simple LGR described so far, the reduction of mode volume is achievable by reducing the height of the LGR. To take this to its extreme, surface LGRs can be created through deposition of conductive material on a dielectric substrate, allowing thin LGRs of $Z \sim 0.1$ to 1 μm [161]. Reduction of resonator height z will alter both L and C. As the frequency of the resonator is determined by $\approx 1/\sqrt{LC}$, appropriate adjustment of the other resonator dimensions is required to prevent unwanted deviation from the desired frequency. Results from Ref. [161] demonstrate successful surface LGRs with varying geometries, the simplest of which is an LGR with a small Z and large w, while other designs incorporate more complex Ω-shaped structures. Further research into surface LGRs and other surface resonators can be found in Refs. [162–164].

6.2.2 Keyhole resonator

The surface LGRs discussed so far solve two of the four critical conditions for the desired resonator design by providing moderate Q-factors and strong conversion of P_{MW} to B_1. We now also need to consider minimising the electric field $\vec{E}$ to prevent unwanted electrostatic

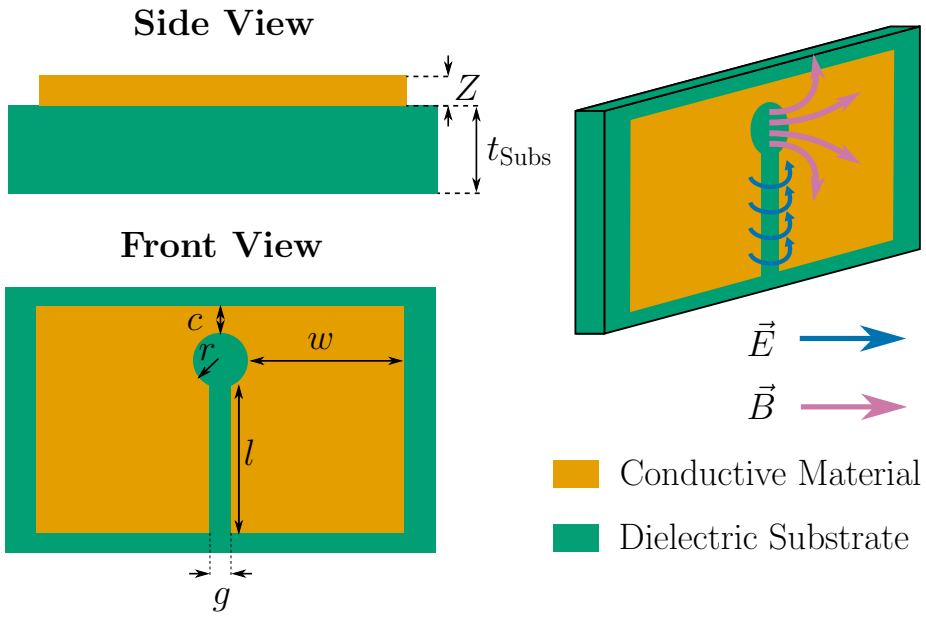

Figure 6.2: Schematic of the keyhole resonator (KHR). Dimensions of the KHR are defined by the inner loop radius r and gap height l, forming the characteristic keyhole shape in the conductor (orange). Width of the conductor either side of the resonator loop is quantified by w, while the distance between the loop and top of the conductive material is c. The capacitive gap width is defined by g. Conductor thickness is a constant, $Z = 35$ μm, while the dielectric substrate has a thickness of $t_{\text{Subs}} = 0.254$ mm. Similar to the LGR, the electric field $\vec{E}$ (blue arrows) is confined to the gap region which acts as a capacitor. The magnetic field $\vec{B}$ (pink arrows) propagates parallel to the central axis of the conducting loop, out of plane of the resonator.

interaction with the spin qubits, and creating a resonator that will allow optical access to the sample to allow hybrid optical-microwave studies of electron spin systems. This can be achieved through a design of resonator known as the keyhole resonator (KHR). A full description of the design, modelling and initial tests of the KHRs can be found in [33]. Here we provide a brief summary of the key characteristics of the KHRs.

A schematic of a KHR is shown in Fig 6.2. The resonator is designed to be used at some separation L_{MW} from the optically excited area. This both allows the desired optical access and limits heating effects from high power microwaves. With regards to the KHR geometry, there are three key differences when compared to the surface LGRs introduced in the previous section. Firstly, the conducting loop is now not just a simple ring, but a rectangular conductor, with asymmetric distances along the sides w and top c of the loop

radius r. The rectangular shape is easier to fabricate and allows for a simpler mounting and shielding system to be used. Secondly, the length of the gap is large, much greater than the resonator radius r. A large gap length moves the electric field $\vec{E}$ away from the centre of the resonator loop, reducing the overlap between magnetic field $\vec{B}$ and $\vec{E}$, ensuring minimal electric field fluctuations are felt by the target of the microwave magnetic field. Finally, the position of the centre of the resonator is close to the top of the substrate instead of placed at the centre, which allows the resonator to be placed closer to the aspheric lens typically used in confocal microscope set-ups designed for microphotoluminescence.

The KHRs used in this chapter are printed circuit board (PCBs) designs made by depositing $Z = 35$ μm (1 oz) of copper cladding (conductor) on to a Rogers laminate RO3003 dielectric substrate, which was $t_{\text{Subs}} = 0.254$ mm thick and has a dielectric constant $\epsilon_r = 3 \pm 0.04$. The conducting area of the PCBs had an Immersion Silver finish to maximise conductivity. A series of keyhole resonators (LGR) were designed to provide a range of frequencies from 7.5 to 8.5 GHz. Testing was required to verify the frequency of the resonator modes under practical operating conditions, as opposed to the theoretically predicted frequency from the modelling and design phase. Resonators are referred to by their theoretically expected resonator frequency from the design phase of the structures.

Several different types of KHR were used in the characterisation of the new KHR designs, but for all ESR work we use a 7.58 GHz KHR resonator shown in Fig 6.2. The parameters of the structure are: conductive thickness $Z = 35$ μm, substrate thickness $t_{\text{Subs}} = 0.254$ mm, gap width $g = 0.559$ mm, gap length $l = 2.382$ mm and loop radius $r = 0.878$ mm. The width between side of rectangular metallization and the side of the circle has thickness $w = 3.088$ mm and width between circle and top of metallization has thickness $c = 0.861$ mm. The thickness of the dielectric around the edges of the conductive face varies as the substrate is a fixed size while metallisation size varies.

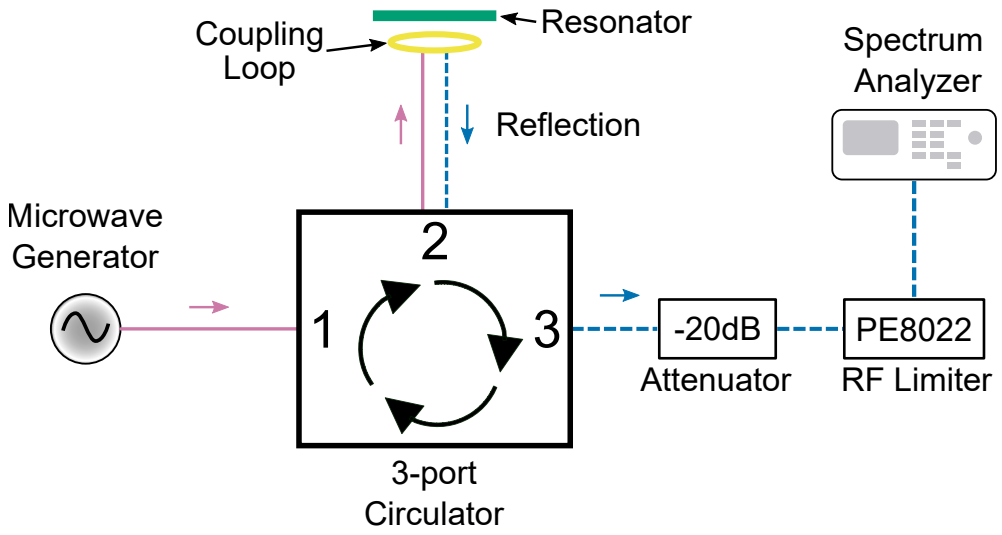

Figure 6.3: Circuit diagram for microwave reflectometry testing of resonators. A microwave generator (SMB100) generates sinusoidal microwave signals of frequency f_{MW} which is passed into a circulator. Unidirectional circulator ensures signal only travels to the next numbered port ($1 \rightarrow 2 \rightarrow 3 \rightarrow 1$). Microwaves are sent to the coupling loop driving a resonator, which absorbs microwaves matching the frequency of the resonator mode. Reflections indicate partial or no coupling of the frequency applied, which can be measured by a spectrum analyzer after being passed sufficient attenuation (-20dB) and a fail-safe RF limiter.

6.3 Resonator testing

In order to experimentally measure the properties of the KHRs, microwave reflectometry measurements were used. Microwave reflectometry measurements were carried out by generating a sinusoidal MW signal at a particular frequency f_{MW}, transmitting the MW to the resonator and measuring the amplitude of reflection at the MW frequency on a spectrum analyser. Repeating this sequence over a range of frequencies f_{MW} gives a detailed spectra of the KHR's reflection profile and allows the properties of the resonator mode to be observed.

In order to carry out microwave reflectometry measurements, we use the circuit shown in Fig 6.3. A microwave generator (SMB100) is used to generate arbitrary waveforms with a frequency of up to 40 GHz. Sinusoidal microwave signal of frequency f_{MW} is passed into port 1 of a 3-port circulator. RF circulators are unidirectional, and thus transmit signal in only one direction ($1 \rightarrow 2 \rightarrow 3 \rightarrow 1$), preventing any reflections of microwaves back to the generator. Port 2 of the circulator is connected to a single loop copper coil, acting as

a coupling loop which will drive the resonator at f_{MW}. The resonator coupling to applied microwaves varies with f_{MW}, where the strongest coupling is at the resonator mode frequency f_{Res}. Frequencies outside the mode are partially or completed uncoupled to the resonator resulting in reflection. All reflected microwave signals are directed to port 3 of the circulator. Port 3 outputs reflected microwaves through a -20 dB attenuator, an RF limiter (PE8022, 2 - 18 GHz) and then to a spectrum analyser (N9010). The limiter acts as a fail-safe for high amplitude microwave reflections, and prevents spikes in amplitude that may damage the sensitive spectrum analyser. The spectrum analyser allows measurement of reflection spectra to characterise the resonator modes, which will appear as a characteristic dip indicative of the resonator mode frequency and bandwidth.

6.3.1 Critical coupling of coupling loop and resonator

Testing of LGR resonator modes was carried out by attaching a KHR to a copper resonator mount, a schematic of which is shown in Fig 6.4. Inside the resonator mount resides a single loop of copper wire soldered to a coaxial cable which acts as the coupling loop for the resonator. The coaxial cable is connected to port 2 of the MW circulator, as described previously. Once the resonator is attached, the coupling loop is completely enclosed by both the copper mount and thin conductive surface on the resonator, minimising the effects of spurious electric fields generated by the coupling loop.

Careful positioning of the copper coil is required in order to critically couple the electromagnetic field from the coupling loop to the resonator. Critical coupling corresponds to maximal energy transfer from the coupling loop to the resonator [152]. The distance between the coupling loop and the resonator can be adjusted by loosening a screw on the side of the resonator mount and moving the coaxial cable to shift the coil. Coupling is most efficient (critically coupled) when the resonator mode provides the strongest absorption of the coupling loop microwaves, which is detected as the largest dip in reflection spectra measurements.

To investigate the coupling of the coupling loop and resonator, reflection spectra were

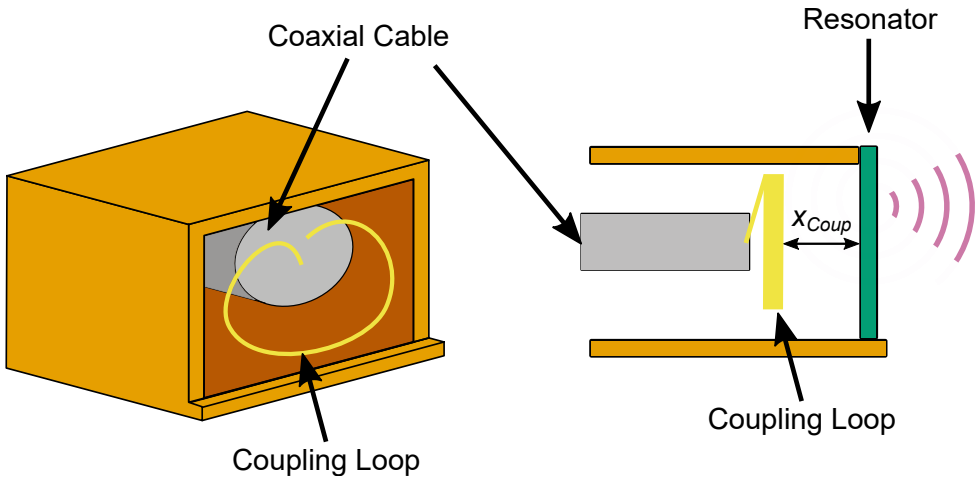

Figure 6.4: Schematic of copper resonator mounting block. A coupling loop connected to a coaxial cable is fed into the mounting block and secured with a screw (not shown), while the resonator is positioned on the front of the mount. Critical coupling of the coupling loop to the resonator can be adjusted through alteration of the spacing between the loop and the resonator, quantified by x_{Coup}. The copper block and resonator form a container around the coupling loop, acting as a shield from additional electrical fields generated by the coupling loop, minimising the effect of the coupling loop on any sample undergoing microwave excitation.

measured as the position of the coupling loop was iterated until the ideal conditions were met. The ideal conditions required for this work is a compromise between the critical coupling of the coupling loop and keyhole resonator and ensuring the resonator mode frequency is close to the specified frequency of our high power pulsed amplifier, $f_{\mathrm{Amp}} = 8$ GHz. Once the ideal position of the coil was found, the coil was fixed in place to be used for the rest of the experiments. Some representative results demonstrating the effect of the distance x_{Coup} between the coupling loop and the resonator on the resonator modes are shown in Fig 6.5. Coupling configuration 3 is close to critical coupling, as indicated by the low reflection (high transmission) of the resonator mode. However, in the final configuration (thick, black) we chose to slightly increase the coupling loop separation in order to match the resonator mode to the pulsed amplifier frequency f_{Amp}. Analysis of the width of the transmission dip at -3 dB in Fig 6.5 gives an estimate of the bandwidth $f_{\mathrm{BW}} \approx 102$ MHz. This allows an estimate of the loaded Q-factor of the resonator, which is calculated to be $Q = \dfrac{f_{\mathrm{Res}}}{f_{\mathrm{BW}}} \approx 79$, demonstrating

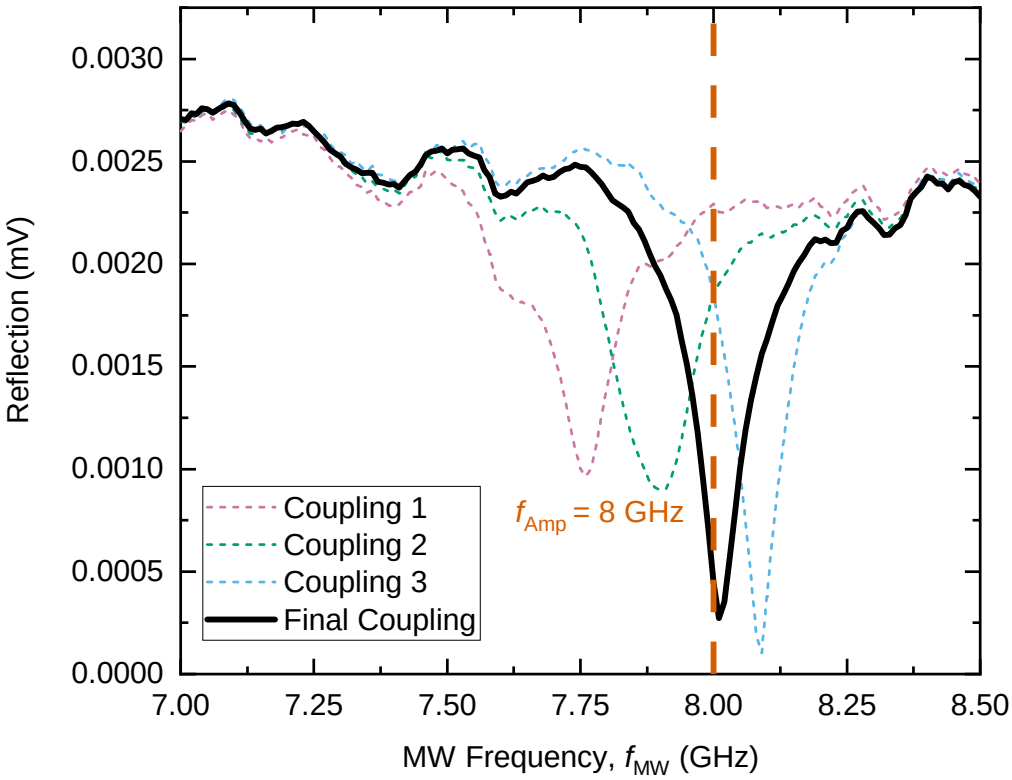

Figure 6.5: Reflection spectrum of a 7.75 GHz keyhole resonator with different iterations of drive coil position inside the resonator mount. Resonant mode is required to be as close to the pulsed amplifier's peak operation frequency at $f_{\mathrm{Amp}} = 8$ GHz (dashed line).

the resonator meets the requirement laid out in Section 6.2.1 for a 10 ns pulses at 8 GHz.

6.3.2 Effect of nearby conductors on resonator modes

In an ideal scenario, the resonator generates electromagnetic fields into the free space in front of the resonator. However, in reality, there are likely to be nearby objects that may impede the efficiency of MW transmission and may distort the shape of the magnetic field in the resonant mode. The set-up used for ESR measurements places the resonator close to the conducting copper sample mount in addition to the cage system supporting the optical components.

In order to test the effect of nearby conductive objects, we first test a simple scenario where a copper block was placed in front of the resonator, as shown in Fig 6.6, simulating

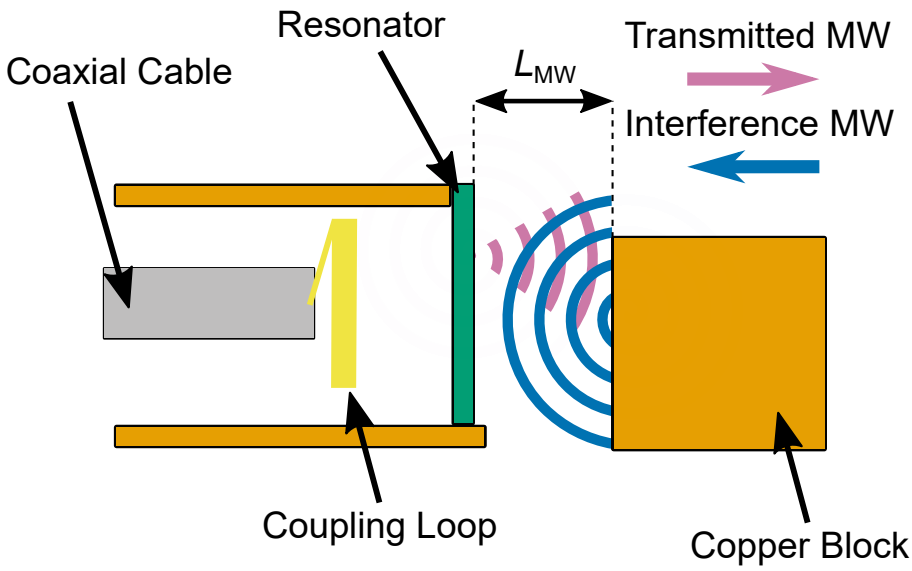

Figure 6.6: Schematic of set up for investigating effect of nearby conductor on resonator modes. Microwave reflectometry measurements were carried out for a range of separations L_{MW} between the KHR (green) and a copper block. The copper block interferes with the transmission (pink) of microwave magnetic field and alters the properties of the resonator.

the effect of a semi-infinite conductor. The separation between the block and resonator was changed to observe the effect on the resonator modes. Microwave reflectometry spectra were measured between 7 - 9 GHz for a range of separations, and are presented in Fig 6.7. Above 1.5 mm separation, there is no change in the frequency of the resonator mode, indicating the copper block has minimal effect on the behaviour of the resonator. Below 1.5 mm the resonator mode is shifted to lower frequencies until even small changes in L_{MW} cause a significant shift in the resonator frequency mode f_{Res}. These tests suggest that separation of $L_{\mathrm{MW}} = 1.5$ mm between the resonator and nearby conductors is sufficient to limit change in the resonator mode. Calculation of the loaded Q-factor of the resonator modes as L_{MW} is stepped demonstrates an approximate value of $Q \approx 80$. Constant Q-factor is an indication that the copper block absorbs a minimal amount of microwave energy.

The geometry of the experimental set-up is more complex than a simple metal block, and as such, it was important to characterise the shift in f_{Res} for the keyhole resonator design

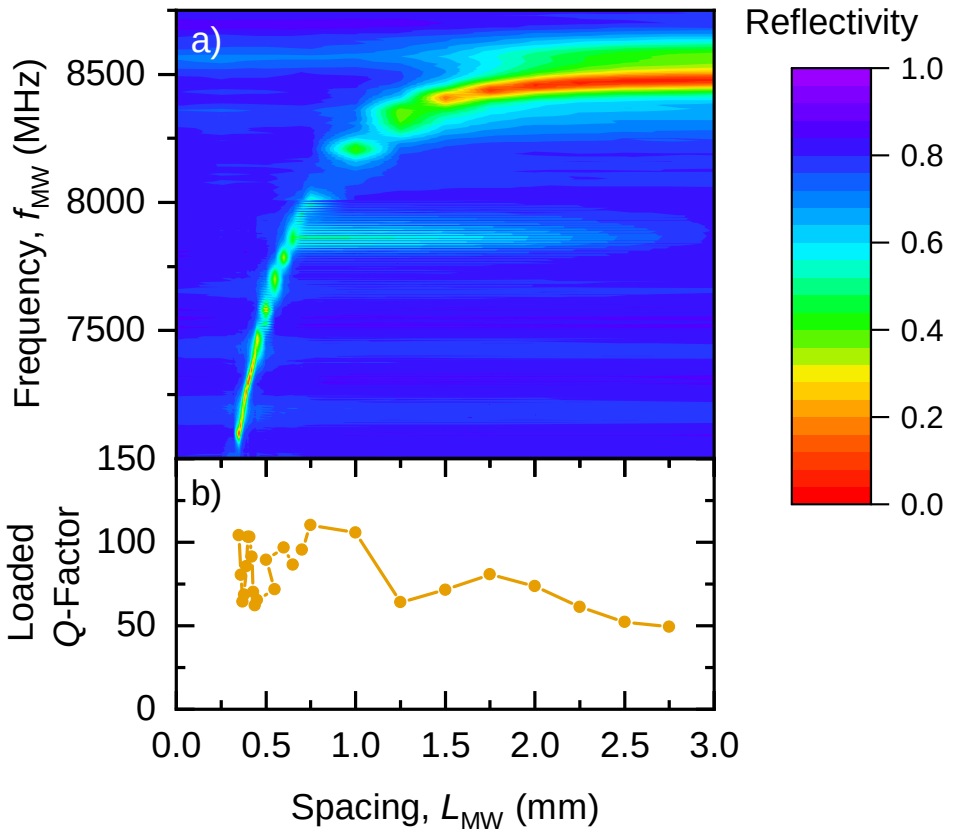

Figure 6.7: a) Microwave reflectometry spectra for a range of L_{MW}. Nearly constant resonator modes at $\approx$ 8450 MHz above 1.5 mm separation indicates the copper block has minimal effect in this regime and coincides with a reduction in resonator loaded Q-factor. The block strongly affects resonator frequencies f_{Res} below this regime, with sharp resonance modes experiencing strong frequency shifts for small changes to L_{MW}. b) Loaded Q-factor values of resonator mode for different separations L_{MW} of an 8.1 GHz KHR to a copper block.

when positioned for ESR experiments. Quantifying the shift between free space transmission and transmission in presence of the set-up components (sample mount, lens, magnets) was key to selecting the correct resonator geometry, as testing every resonator design is time-consuming. As such, we made a comparison of the resonator mode for transmission into free space versus the resonator mode while mounted to the full ESR set-up described in Section 6.5. The resonator was not critically coupled for either measurement, but coupling was not altered between the two configurations. We observed a minor shift of resonator mode frequency of $\approx$ 10 MHz indicating the set-up has minimal effect on the KHR resonator mode.

6.3.3 Effect of cryogenic temperatures on resonator modes

For the purpose of measuring ESR on NV centres in diamond, the resonators have been sufficiently characterised and can be used for experiments at $f_{\mathrm{MW}} \approx 8$ GHz at room temperature ($T = 293$ K). However, to use the resonators for their future intended purpose of ESR on quantum dots, we need to understand the effect of cryogenic temperatures on the resonator modes. Temperature alters the dielectric properties of the keyhole resonator substrate, and therefore the resonance properties will also be altered. The coupling between the coupling loop and resonator may also change due to thermal contraction as a result of the reduced temperature.

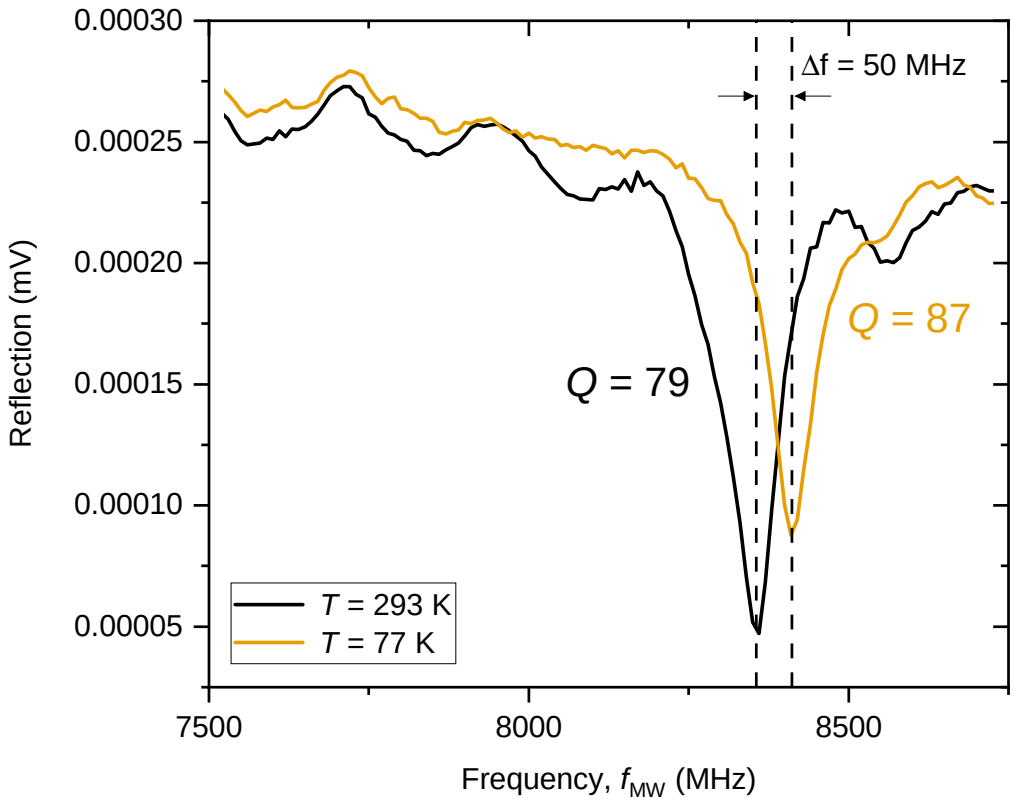

Figure 6.8: Microwave reflectometry of an 8.1 GHz keyhole resonator at temperatures $T = 273$ K (black) and $T = 77$ K (orange). An increase in the resonance mode frequency is observed at lower temperature, with the frequency shifting by $\Delta f = 50$ MHz. Increase in the reflection at the peak of the mode for $T = 77$ K indicates critical coupling may have been lost due to reduced resistance of conductive components in the coupling loop and resonator.

A simple temperature test was carried out on a resonator design to operate at 8.1 GHz with no conductors nearby. Two microwave reflectometry spectra were measured, one at room temperature ($T = 293$ K) and one after the resonator had been cooled to $T = 77$ K. We achieved a stable thermal equilibrium at $T = 77$ K by submerging a screw attached to the resonator mount in liquid nitrogen for 10 minutes. This allowed the cooling of the resonator without direct contact with the liquid nitrogen, which may have affected the reflection spectra.

Results of the thermal testing are shown in Fig 6.8, demonstrating an increase in resonator mode frequency of $\Delta f = 50$ MHz. A shift of the resonator mode frequency is observed and is attributed to the temperature-dependent dielectric constant of the KHR substrate, altering the resonator mode as the temperature changes. It is also clear that the coupling efficiency has deviated from the critical condition observed at $T = 293$ K, in addition to a $\sim 10\%$ increase in resonator Q-factor. Both of these effects likely arise from the reduced resistance of conductive components in the circuit due to temperature change. Quantum dot ESR experiments will be carried out at $T = 4$ K, where we would expect even stronger effects of temperature on the resonators. However, the $T = 77$ K results allow us to better anticipate the shifts in resonator properties and coupling efficiency, which is critical due to the time-consuming process of iterating resonator configuration in the quantum dot set-up.

6.4 NV centres in diamond

Once preliminary characterisation of the keyhole resonators had been carried out, we needed to test the resonators ability to be used in coherent control measurements on spin qubits. Initial investigations for these types of resonators were carried out on the vacancies found in SiC, with successful ESR measurement up to 6.5 GHz at microwave powers of up to 3 W [33]. We set out to test updated designs of the keyhole resonator developed to operate at $f_{\mathrm{Res}} = 8$ GHz on the nitrogen vacancy (NV) defect in diamond, using a 300 W pulsed amplifier to

allow fast coherent control. NV centres were selected due to the predicted increase in optically detected magnetic resonance signal compared to the previously tested SiC vacancies.

NV centres are a point defect occurring within the lattice of diamond and are formed from a Carbon-12 vacancy site adjacent to a Nitrogen-14 (^{14}N) site. Diamond samples fabricated through chemical vapour deposition (CVD) can be additionally implanted with nitrogen atoms, which bond with carbon vacancy sites to form the NV centres [165]. The neutral NV centre, NV^0, is formed entirely of dangling bonds from the surrounding three carbon and one nitrogen lattice sites, resulting in the vacancy being occupied by five electrons (one for each ^{12}C and two for the ^{14}N) [155, 166, 167]. An additional charge can occupy the vacancy through a nearby donor lattice site, generally another nitrogen atom, or through the use of charge-tunable structures, forming the negatively charged nitrogen-vacancy centre NV^-. The NV centre defect axis typically forms in equal densities along one of four orientations [111], $[1\bar{1}\bar{1}]$, $[\bar{1}1\bar{1}]$, $[\bar{1}\bar{1}1]$, resulting in only 25% of NV centres being accessible in most experiments [168]. However, there have been some successful attempts at controlling the growth of the NV centres to orientate the defect axis along only one of the 4 crystallographic directions, allowing full access to the entire population of NV centres [169, 170].

The additional charge in the NV^- forms a spin triplet ground state $S = 1$ of the form $^3A_2$, with the three spin projections $m_s = 0, \pm 1$ [155, 156, 171]. An energy level diagram of the NV^- is shown in Fig 6.9. An intrinsic splitting of the $m_s = 0$ and $m_s = \pm 1$ occurs due to spin-spin interaction between the electrons in the vacancy, and is referred to as the zero-field splitting, quantified by $D^{\mathrm{GS}}_{\mathrm{ZFS}} \approx 2.87$ GHz at room temperature [155]. Additional strain and electric field effects can cause mixing between the $m_s = \pm 1$ states, which can be quantified by the E_{ZFS} parameter and is usually on the order of several MHz [172].

The excited state of the NV^- is also a spin triplet state of the form ^3E, and lies ~ 1.9 eV above the ground state, allowing optical transitions in the visible band to occur. The radiative recombination rate of the NV^- is approximately $\approx (12\ \mathrm{ns})^{-1}$, and transitions are generally spin conserving, resulting in the triplet returning to the original state after optical

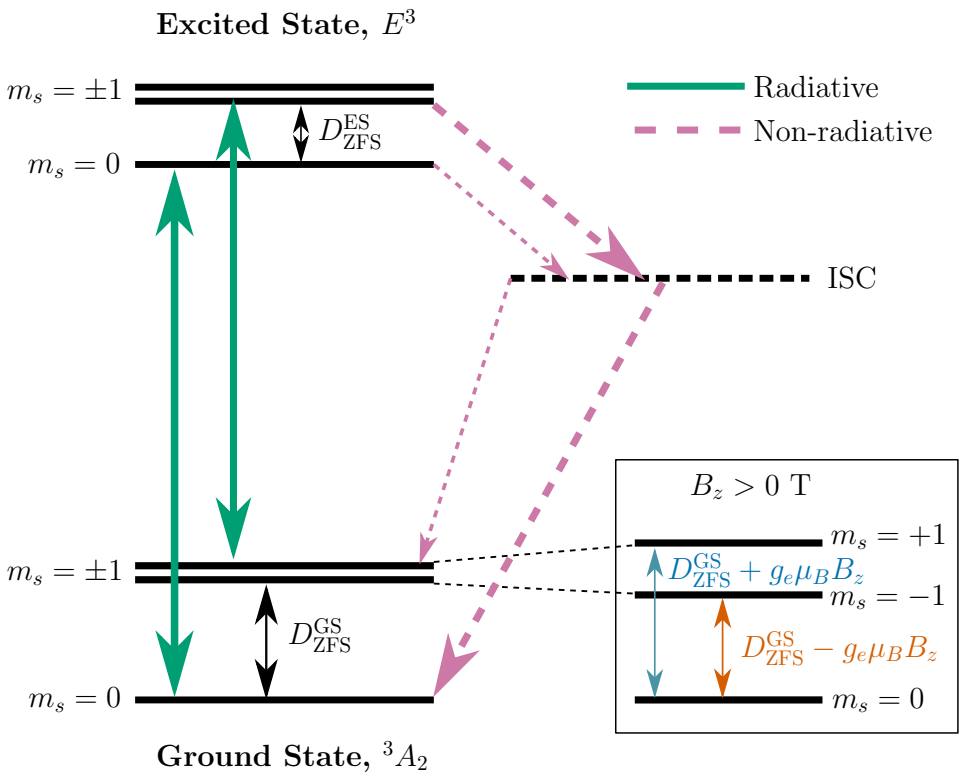

Figure 6.9: Energy Level diagram of NV^- centres in diamond. Optical excitation promotes electrons to the $^3A_2$ state, which radiatively recombines on the scale of $\sim (12\ \mathrm{ns})^{-1}$. Alternatively, relaxation can occur to a cascade of singlet states that are treated as one metastable state known as the inter-state crossing (ISC). Ground state ^3E spin triplet ($S = 1$) has a zero-field splitting of $D_{\mathrm{ZFS}}^{\mathrm{GS}} = 2.870$ GHz, splitting the $m_s = 0$ and $m_s = \pm 1$ states. For $B_z > 0$ T, the $m_s = \pm 1$ degeneracy is lifted allowing excitation of specific transitions ($m_s = 0 \leftrightarrow +1$ or $m_s = 0 \leftrightarrow -1$) as a two-level spin system.

excitation [173, 174]. A secondary relaxation pathway occurs through a series of spin singlet states, which are generally considered as a single metastate known as the inter-system crossing (ISC). The ISC has comparatively slow relaxation on the scale of 200 - 400 ns as the electrons cascade through the series of spin singlet states via infrared optical and/or non-radiative vibronic recombination [175, 176].

Relaxation to the ISC is strongly coupled to the $m_s = \pm 1$ levels in the excited state (^3E), while relaxation from the ISC has strong probability to return to the $m_s = 0$ level in the ground state ($^3A_2$). Consequently, repeated cycles of optical excitation can preferentially populate the $m_s = 0$ state. Spins in the $m_s = 0$ are likely to return after an optical

excitation/recombination cycle, while spins in the $m_s = \pm 1$ state are likely to recombine through the ISC, and thus into the ground state $m_s = 0$, providing a mechanism for optical initialisation of the NV centre spins [177]. The energy level diagram in Fig 6.9 provides a schematic of the various transitions and relative coupling strengths in the optical initialisation scheme.

Zero field splitting between the spin states $m_s = 0$ and $m_s = \pm 1$ within the NV^- allows selective microwave excitation of the spin transition [166, 172, 178]. However, it can be more useful to address a pure two-level system, which can be achieved through the application of a static magnetic field B_0. The Zeeman effect splits the $m_s = \pm 1$ states by $\pm g_e \mu_B \boldsymbol{B}$, providing two addressable transitions of $m_s = 0 \leftrightarrow +1$ and $m_s = 0 \leftrightarrow -1$, allowing a two-level spin qubit to created. It is by using a static magnetic field that allows us to tune the NV^- centre transition energies to 8 GHz, allowing us to use it as a test structure for optically detected electron spin resonance measurements with the keyhole resonator design.

6.5 Room temperature experimental set-up

In order to test the resonators on NV^- centres in diamond, we require a set-up allowing close proximity of the keyhole resonator (KHRs) to a diamond sample under optical excitation. The sample used in these experiments is an Element 6 DNV-B1 diamond sample, with dimensions 3 mm x 3 mm x 0.5 mm and was grown using chemical vapour deposition (CVD). The sample has a 1.1% abundance of ^{13}C and an NV centre density of 300 parts per billion.

The experimental set-up is comprised of two main sections, the optics required for microphotoluminescence (μ-PL) and the hardware for microwave generation and resonator positioning, both of which are critical to perform optically detected electron spin resonance experiments. Both parts of the set up are controlled synchronously with a four channel TGA1244 signal generator. An overall schematic is shown in Fig 6.10.

Optical excitation of the diamond sample is carried out using a μ-PL set-up operating

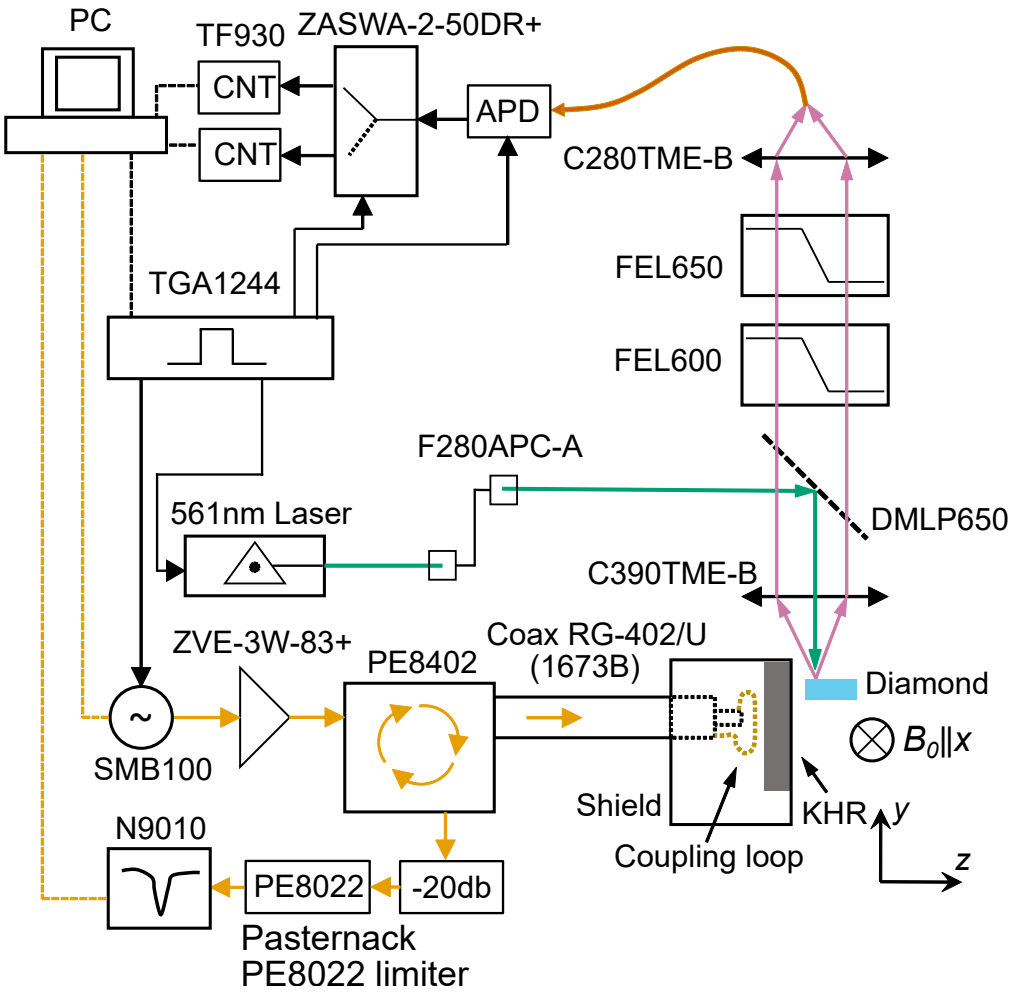

Figure 6.10: Schematic of ESR set-up, a modified version of the set-up described in Ref [33]. A PC using LabView sets up the various components in the system. Triggers for each component is generated by a master generator TGA1244. Microwave circuitry is indicated in orange (full description in text) and allows the generation of microwave magnetic fields from the coupling loop, which in turn can drive the keyhole resonators studied in this chapter. The coupling loop can be replaced with a simple single loop coil for microwave generation below the KHR frequency range $f_{\mathrm{Res}} < 6.5$ GHz. Microwaves are directed along the z-axis towards the diamond sample for optically detected electron spin resonance. The diamond sample is positioned below a μ-PL set-up to allow optical excitation and measurement. Digital laser modulation is controlled by TGA1244, allowing fast pulses of optical excitation to be sent to the sample. Signal collection routes detectable photons to the APD after filtering unwanted wavelengths (FEL650, FEL600). APD detection signal is passed through an SPDT demultiplexer (ZASWA-2-50D+) to allow rapid alternating of signal detection between two pulse counters (TF930) to allow differential microwave "On" and "Off" measurements.

under a similar principle to the set-up used for quantum dots described in Chapter 3, without the requirement for a cryostat. We use a $\lambda = 561$ nm laser to perform optical excitation, which is coupled to the set-up via single-mode fibre. A dichroic mirror (DMLP650) with a threshold wavelength of 650 nm is used in order to provide maximum reflection of laser down to the sample, and maximum transmission of signal ($\lambda > 650$ nm) up to the collection coupler. Optical excitation is focused with an aspheric lens (C390TME-B), with the lens aligned so the focal point resides below the sample surface in the centre of the sample thickness. Photoluminescent emission is collimated by the aspheric lens and is then transmitted through the dichroic mirror into a fibre coupler for signal detection. The optical signal is measured either with a single spectrometer connected to an electrically cooled CCD, or an avalanche photodiode (APD).

The diamond sample is attached to a custom made mount that allows rotation of the sample around the z-axis to align the NV^- defect axis with the static magnetic field applied along the x-axis (Fig 6.11). The sample's y-axis position is adjusted so the centre of the loop in the KHR is level with the part of the sample under optical excitation for maximum absorption of microwave magnetic field, and is then fixed for the duration of experiments. Density of NV centres in the diamond sample and the size of the laser spot (≈ 1 μm^2) is high enough that optical illumination will provide PL signal regardless of the position on the sample, eliminating the need for control of sample position after the initial alignment.

Application of the microwaves required for ESR is achieved through the circuitry described in Section 6.3, with the addition of a microwave amplifier before the circulator port 1. To quickly summarise, a microwave generator (SMB100) generates arbitrary waveforms to be sent to a microwave amplifier. The amplifier can be either a 3 W continuous wave (CW) amplifier (ZVE-3W-83+) or a 300 W pulsed amplifier (AM61-7.5-8.5-55-55). For the 3 W amplifier, we use a broadband 4 - 8 GHz circulator (PE8402), while for the 300 W pulsed amplifier we use the amplifier's internal narrow-band high power circulator. The amplified signal is passed into port 1 of the circulator, transmitting microwaves to the coupling loop

and resonator out of port 2. Port 2 is configured to drive a KHR through a coupling loop for experiments at $f_{\mathrm{ESR}} \approx 8$ GHz. For experiments at $f_{\mathrm{MW}} \leq 6.5$ GHz, we used a bare copper coil as a mismatched broadband microwave antenna for microwave generation. Port 3 outputs any reflected microwave signal to be monitored on the spectrum analyser.

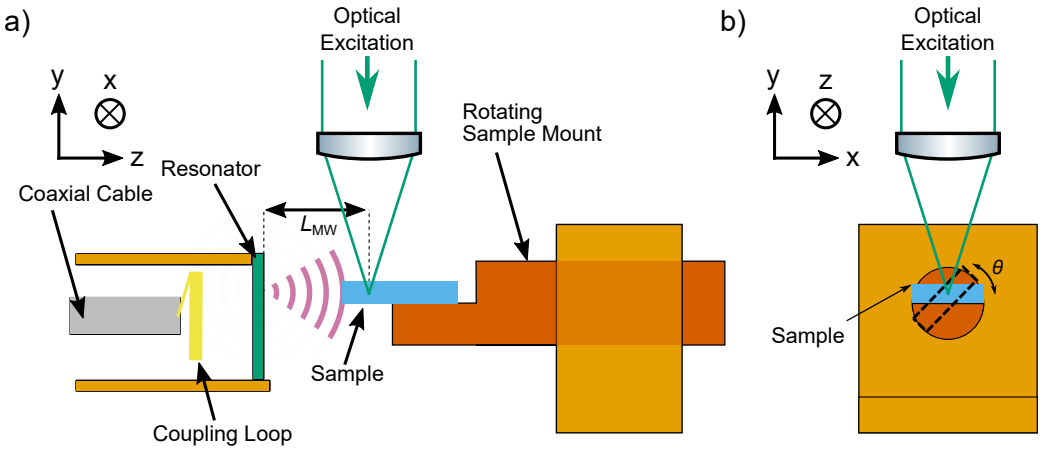

Figure 6.11: Schematic of full experimental set-up for electron spin resonance measurements. a) Side view of the resonator mount where a cylinder (dark orange) rests inside a mounting block (orange) to allow rotation of the diamond. Optical excitation (green) is focused on to the diamond sample (blue) with an aspheric lens. Spacing L_{MW} between the resonator and the sample is as small as possible to increase the strength of microwave field B_1 at the focal point of optical excitation within the crystal, resulting in maximum detectable ESR signal. b) View of the sample mount along z-axis. Rotation of the diamond sample is quantified by θ.

6.6 Photoluminescence of NV^- centres in diamond

Optically detected ESR required understanding of the PL signal emitted by the NV^- ensemble, and as such we first had to characterise the optical emission of the sample through a series of PL investigations. For this, we used the μ-PL set-up introduced in Section 6.5, allowing the sample to be illuminated with $\lambda = 561$ nm optical excitation, where the subsequent signal can be sent to a spectrometer for data acquisition.

Initial characterisation spectra were measured with optical excitation orthogonal to the sample surface $\theta = 0°$, as shown in Fig 6.12. The charged NV centre optical zero phonon

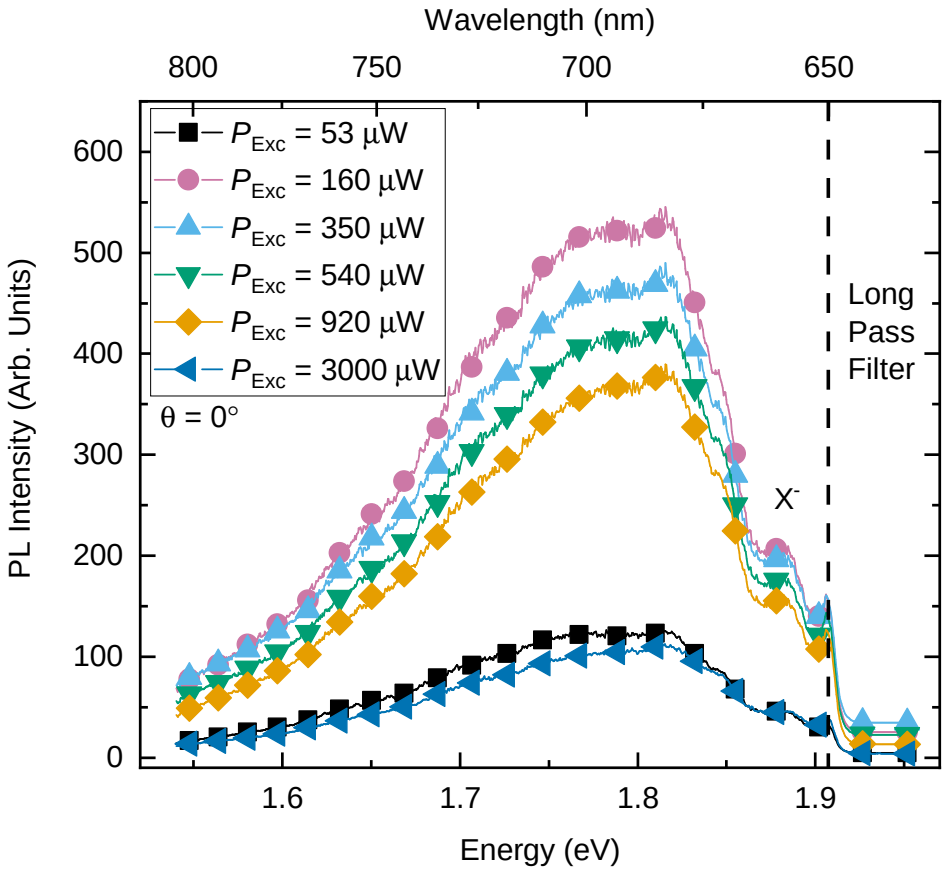

Figure 6.12: Optical power (P_{Exc}) dependant photoluminescent (PL) spectra of NV centres in diamond. Excitation of $\lambda = 561$ nm was applied orthogonal to the sample surface $\theta = 0°$, providing strong PL amplitude. Saturation of PL signal occurs at $P_{\text{Exc}} \approx 160$ μW. The small peak at ~ 1.88 eV (~ 660 nm) is the NV$^-$ optical zero phonon line emission X^-, with the NV$^-$ vibronic band vacancy making up the bulk of the broad signal 1.6 - 1.9 eV (~ 680 - 780 nm). The sudden drop in signal at 1.92 eV (650 nm) is due to the 650 nm long pass filter placed in the collection arm of the μ-PL set-up

line (ZPL) is visible at ~ 1.88 eV, with a broad spectrum at lower energies representing the vibronic band of the NV$^-$ centre [179]. Saturation occurs at an optical power of $P_{\text{Exc}} = 160$ μW, which allows maximum signal to be collected.

As introduced in Section 6.4, NV$^-$ defects in the diamond lattice can be orientated in four ways [168]. In order to maximise the population of addressable electron spin states to provide the strongest ESR signal, we must align one of the four defect axes along the static magnetic field. A schematic of diamond sample orientation with respect to the sample rotation θ axis z and static magnetic field $\vec{\boldsymbol{B}}$ axis x is shown in Fig 6.13. Sample cleaving orientates the

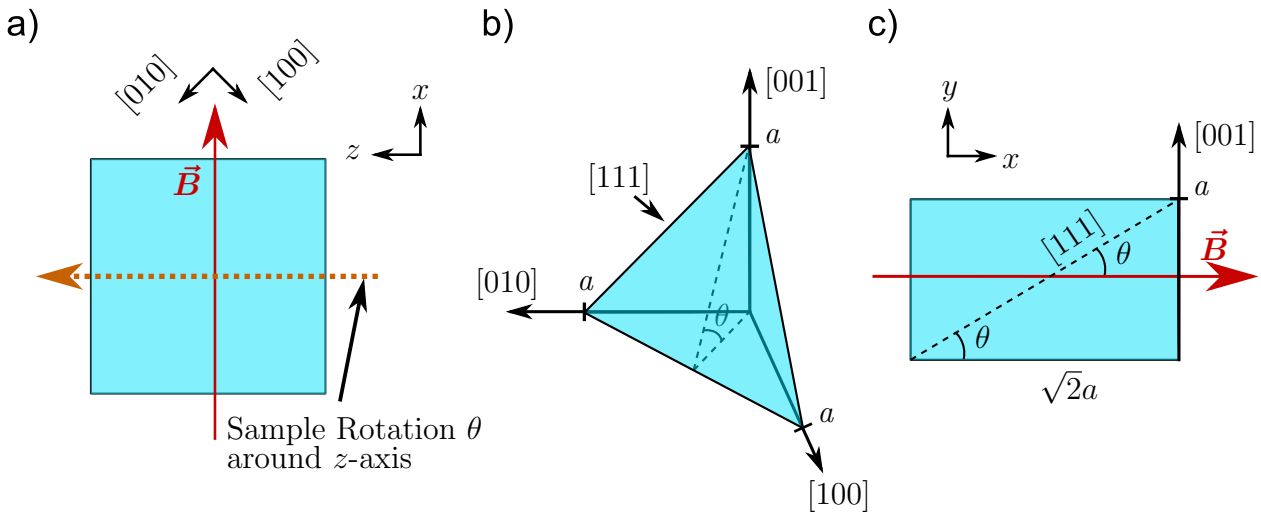

Figure 6.13: Schematic of diamond sample orientation with respect to the sample rotation θ axis z and static magnetic field $\vec{B}$ axis x. a) Top view (y-axis) of diamond sample. Sample cleaving orientates the [100] and [010] crystal axes at a 45° angle to the edges of the sample. b) A crystallographic projection of the target [111] NV^- defect demonstrates the angle θ between the [001] axis and the defect axis. c) View of θ from the z-axis, where it is clear that θ can be calculated from $\tan(\theta) = 1/\sqrt{2}$, giving a sample rotation value of $\theta = 35.3°$.

[100] and [010] crystal axes at a 45° angle to the edges of the sample. Orientating the sample so that one of the four NV^- orientations is parallel to the static field requires alteration of θ.

We arbitrarily chose the [111] orientation NV^-, whose crystallographic projection is shown in Fig 6.13b. The bottom edge ([010]-[100] plane) of the unit cell shown creates a 45° angle with the crystal axes [010] and [100], and as such the direction of the NV^- in this plane aligns parallel with the edges of the cleaved sample. Consequently, alignment of the [111] NV^- centre can be achieved purely through rotation of the sample around the z-axis. Fig 6.13c shows the sample layout from the rotation axis perspective (z-axis), demonstrating how θ describes the angle between the [111] plane and the static magnetic field along the x-axis. A simple calculation $\tan\theta = a/(\sqrt{2}a) = 1/\sqrt{2}$ gives us the desired sample rotation of $\theta = 35.3°$.

We measure PL of the NV centres at the desired sample rotation $\theta = 35.3°$, shown in Fig 6.14. The primary disadvantage of rotating the sample is loss of optical signal as the cone of emission from NV centres orthogonal to the sample surface becomes misaligned with

the cone of collection of the aspheric lens due to the $\theta = 35.3°$ rotation. This effect can be observed by the factor of ~ 20 reduction in PL amplitude seen in the $\theta = 35.3°$ spectra (Fig 6.14) when compared to the $\theta = 0°$ spectra (Fig 6.12).

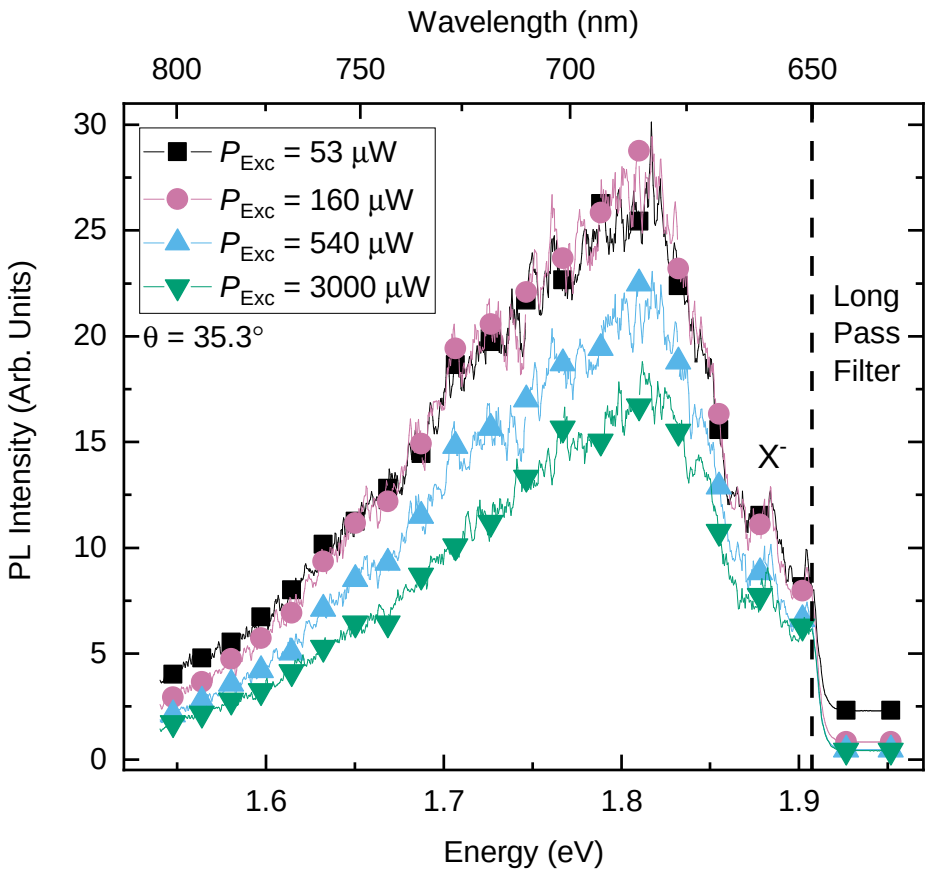

Figure 6.14: Optical power (P_{Exc}) dependant photoluminescent (PL) spectra of NV centres in diamond, where excitation was applied at $\theta = 35.3°$ to the sample surface, demonstrating similar but weaker PL spectra when compared to the $\theta = 0°$ spectra Fig 6.12. Saturation of PL signal occurs at $P_{\text{Exc}} = 50$ - 160 μW.

6.7 Electron spin resonance

We have shown that our set-up is capable of photoluminescence measurements on NV centres, and that the KHR design provides modes at the targeted $f_{\text{Res}} \sim 8$ GHz. Now we can bring both of these components together to measure electron spin resonance of the NV^- centres in the diamond sample, and characterise the strength of the microwave magnetic field produced

by the KHR. We achieve this through optically detected magnetic resonance (ODMR), where change in the optical signal is observed as a result of microwave control of electron spins in the NV centres.

Measurement of ESR requires us to follow the three steps for coherent control of spins laid out in Chapter 2, which are initialisation, manipulation and readout. The spin state of the $S = 1$ triplet in the ground state of the NV^- can be optically addressed to initialise the spin to the $m_s = 0$ state. Optical excitation promotes the electron to the E^3 state, where it optically recombines generating a photon with a high probability. There is also a small probability of non-radiative relaxation through the ISC. Relaxation from the ISC has a higher probability of relaxation to the $m_s = 0$ state than the $m_s = \pm 1$ states. As a consequence, repeated optical excitation cycles will populate the $m_s = 0$ state, achieving the state initialisation part of the spin control process [156, 177].

In order to control the spins within the NV^- centres, microwave radiation of frequency f_{MW} is applied resonant with the splitting between $m_s = 0$ and either one of the $m_s = \pm 1$ states, manipulating the electron spins through electron spin resonance. As introduced in Section 6.4, the transition energies are determined by the zero-field splitting D_{ZFS} and the Zeeman effect $\Delta E_{Zeeman} = g_e \mu_B B_z$. Successful application of microwave magnetic field results in manipulation of the electron spin states which can be detected by optical readout of the electron spin state.

Readout of the NV^- electron spin state is possible due to the difference in radiative recombination rates for the $m_s = 0$ and $m_s = \pm 1$ states. Once the system is optically excited to the ^3E state, relaxation to the ISC is dependant on the spin state. The $m_s = \pm 1$ states couple more strongly to the non-radiative relaxation via the ISC, reducing optical recombination rate when the $m_s = \pm 1$ is optically excited. In contrast, $m_s = 0$ is only weakly coupled with the non-radiative ISC relaxation, resulting in more frequent optical recombination of the $m_s = 0$ state. Enhanced rates of $m_s = 0$ radiative recombination increases the optical emission from the sample. Therefore, high optical signal is an indicator

that the ensemble is in the $m_s = 0$ state and can be used as a readout technique for the spin state.

6.7.1 Continuous wave electron spin resonance

For initial ESR investigations, we carry out continuous wave (CW) ESR measurements in order to determine the frequency of ESR resonance f_{ESR} of the NV^- centres. The expected resonance of the NV^- centres at $B = 0$ T is $D_{\mathrm{ZFS}} = 2.87$ GHz, and acts as benchmark to test the CW ESR measurement scheme. The resonators will not be suitable for MW generation at 2.87 GHz, and so we instead we used a simple coil as a broadband microwave emitter for measurements at $B = 0$ T, and any other ESR measurements below 6.5 GHz. For ESR measurements close to 8 GHz, we use a nominal 7.58 GHz KHR which is fully described in Section 6.2.2.

A full schematic of the measurement cycle for CW ESR is shown in Fig 6.15. CW ESR measurements require differential measurement to accurately determine the optically detected signal. We use an avalanche photodiode (APD) for precise photon counting. Detection signal from the APD is routed to a SPDT demultiplexer switch that alternates between two pulse counters, which allow measurement of optical intensity I. The differential measurement modulates microwave signal on and off whilst the gate synchronously switches between the two pulse counters, allowing data acquisition of both MW On and MW Off components of the measurement cycle. Change in optical signal is proportional to variation of electron spin polarization degree induced by microwave pulses, and therefore is the ODMR signal. Enhanced rates of radiative recombination from the $m_s = 0$ state results in application of ESR reducing optical signal as the spins transfer to the $m_s = \pm 1$ state. As such, we expect the "MW On" signal to be lower than the "MW Off" for successful ESR. Differential measurements comparing MW "On" and "Off" gives the optically detected magnetic resonance signal. In order to account for drift in optical signal due to optical excitation power or collection alignment, we normalise the difference in "On" and "Off" signal with respect to the total counts during

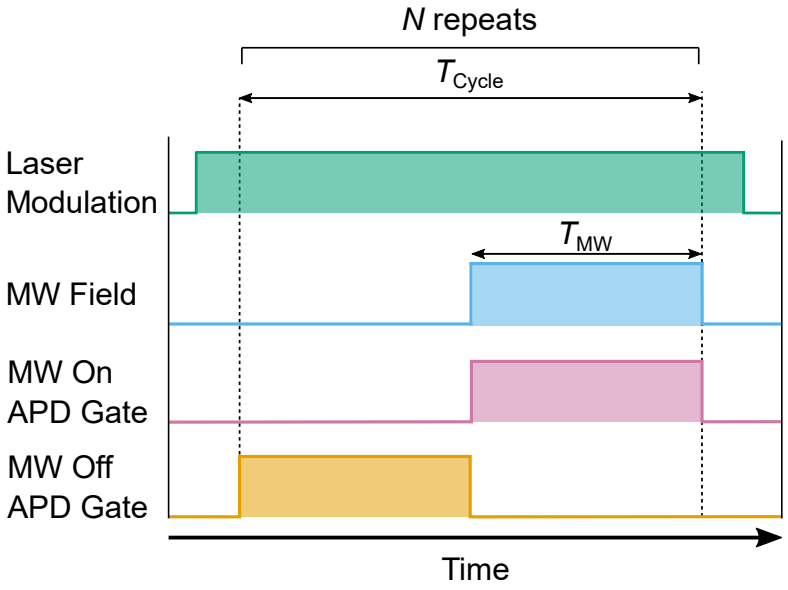

Figure 6.15: Experimental sequences for CW ESR. Optical excitation is continuously applied to the sample, populating the $m_s = 0$ state of the NV^- ensemble, providing maximum radiative recombination. A burst of microwave field excitation is applied for T_{MW} to depolarise the $m_s = 0$ state, reducing overall optical intensity. The duty cycle of T_{MW} compared to T_{Cycle} is altered to limit heating of the resonator, with a duty cycle of 50% for the 3 W amplifier, and 10% for the 300 W amplifier. Optical signal collection switches between two photon pulse counters depending on whether MW excitation is being applied, allowing relative differential signal $(I_{Off} - I_{On})/(I_{Off} + I_{On})$ to be calculated, which quantifies the final electron spin polarization degree. The sequence is repeated N times for a desired acquisition time T_{Acq} such that $N = T_{Acq}/T_{Cycle}$.

the acquisition window:

$$I_{ODMR} = \frac{I_{Off} - I_{On}}{I_{On} + I_{Off}} \tag{6.3}$$

We average over many measurement cycles in order to provide an accurate measurement. In the case of CW ESR spectra, the microwave frequency f_{MW} is stepped for each acquisition window, allowing measurement of the ESR spectrum.

The first measurements studied the NV^- centre ESR spectrum at $B = 0$ with no sample rotation $\theta = 0°$, and is shown in Fig 6.16. We can clearly see two multiplets, with the centre of the two at the expected $f_{MW} = D_{ZFS}$. It is also clear that there is a fine structure present, with 4 distinct peaks being observed in both multiplets. This is the result of hyperfine interaction of the NV^- electron spin with the constituent ^{14}N and neighbouring ^{13}C nuclear

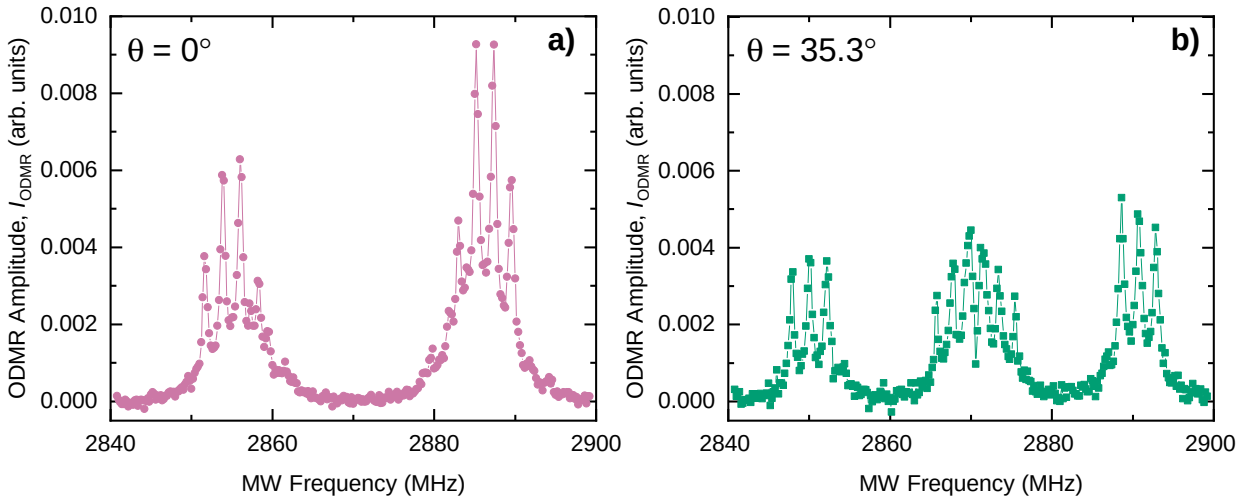

Figure 6.16: Continuous wave ESR measurements of NV^- centres in diamond at $B = 0$ T for two sample orientations. a) 0 T ESR with sample orientation $\theta = 0°$. Two clear multiplets are present, equally offset from the expected $D_{ZFS} = 2780$ MHz resonance. Both multiplets consist of 4 fine structure peaks, which likely arise from hyperfine interaction between the NV^- electron and nearby nuclear spins (^{14}N and ^{13}C nuclei). b) 0 T ESR with sample orientation $\theta = 35.3°$. A primary multiplet consisting of 6 fine structure peaks occurs at the zero field splitting value $D_{ZFS} = 2870$ MHz, with two satellite multiplets consisting of 3 peaks each.

spins. The presence of two multiplets split by ≈ 25 MHz suggest additional effects are present, as only six peaks are predicted due to hyperfine interaction when the $m_s = 0 \leftrightarrow -1$ and $m_s = 0 \leftrightarrow +1$ transitions are degenerate. The symmetry of the two multiplets around 2870 MHz suggests the $m_s = \pm 1$ states are non-degenerate, indicating presence of a combination of a small residual magnetic field and strain [180].

Due to the 4 possible orientations of the NV^- centres, we rotate the sample by $\theta = 35.3°$, as described in Section 6.6, to ensure the applied magnetic field acts parallel to the defect axis of the [111] NV centre. Despite reduced PL amplitude (Fig 6.14), we still can clearly see ODMR signal as shown in Fig 6.16. The two multiplets observed at $\theta = 0°$ have now separated into three multiplets, with the satellites having 3 fine structure peaks, and the central resonance displaying 6.

At low magnetic fields ($B_z < 5$ mT), additional splitting of the spin states occurs due to the hyperfine interaction present within the NV^- centre [181]. Electron spins $\boldsymbol{S}$ within

the vacancy can interact with nearby nuclear spins $\boldsymbol{I}$, arising from the constituent $I = 1$ ^{14}N site, or with nearby I = 1/2 ^{13}C sites. Results from the scenario where the sample is oriented at $\theta = 35.3°$ (Fig 6.16b) can be explained through the hyperfine interaction. A Hamiltonian predicting hyperfine transitions energies from the $m_s = 0$ states to the $m_s = \pm 1$ states is presented in Ref [181]. We show a modified version here, in which we replace the Zeeman splitting with a more general splitting term F that will encapsulate any splitting of the $m_s = \pm 1$ states as a result of strain, magnetic field and electric field.

$$H = D_{\mathrm{ZFS}} S_z^2 + P(I_z^{(N)})^2 + \left(\frac{F}{2} \cdot \boldsymbol{S}\right) + \boldsymbol{S} \cdot (\boldsymbol{A}_N \cdot \boldsymbol{I}^{(\boldsymbol{N})} + \boldsymbol{A} \cdot \boldsymbol{I}) \tag{6.4}$$

where $\boldsymbol{S}$ is the spin operator of the NV$^-$ ground state spin triplet, with S_z as the projection operator in the z-direction (parallel to defect axis [111]), μ_B is the Bohr magneton, g_e is the free electron g-factor, $\boldsymbol{I}^{(N)}$ ($\boldsymbol{I}$) is the spin of the consituent ^{14}N (neighbouring ^{13}C) nuclei with a gyromagnetic ratio of γ_N (γ) and a hyperfine coupling of $\boldsymbol{A}_N$ ($\boldsymbol{A}$). The first term describes the zero field splitting previously introduced. The second term is a correction to the zero field splitting that arises from quadrupolar interaction of the ^{14}N nuclei, with a quadrupolar moment of $P \approx 5$ MHz [181]. The third term is a general term quantifying the splitting F of the electron spin states $m_s = \pm 1$. The final term is the hyperfine interaction of the NV$^-$ spin triplet with the ^{13}C and ^{14}N nuclei, with the strength of the interactions defined by the hyperfine constants $\boldsymbol{A}$ ($\boldsymbol{A}^{(\boldsymbol{N})}$).

Evaluating Eqn 6.4 for all permutations of the NV$^-$ electron spin $\boldsymbol{S} \in [-1, +1]$, the ^{13}C nuclear spin $\boldsymbol{I} \in [-\frac{1}{2}, +\frac{1}{2}]$ and the ^{14}N nuclear spin $\boldsymbol{I}^{(\boldsymbol{N})} \in [-1, 0, 1]$ allows us to create a series of 12 transitions matching the observed peaks found in Fig 6.16b. We fit the CW ESR spectra with a function defined by the summation of Gaussian peaks $y = \sum_{i=1}^{N} A_i e^{-((x-x_i)/w_i)^2}$. The central frequency of the peaks are all related through Eqn 6.4, allowing us to find optimal values, which are summarised in Table 6.1. The result of the fit is shown in Fig 6.17.

Fitted value of the ^{14}N quadrupolar splitting $P = -4$ MHz slightly deviated from the

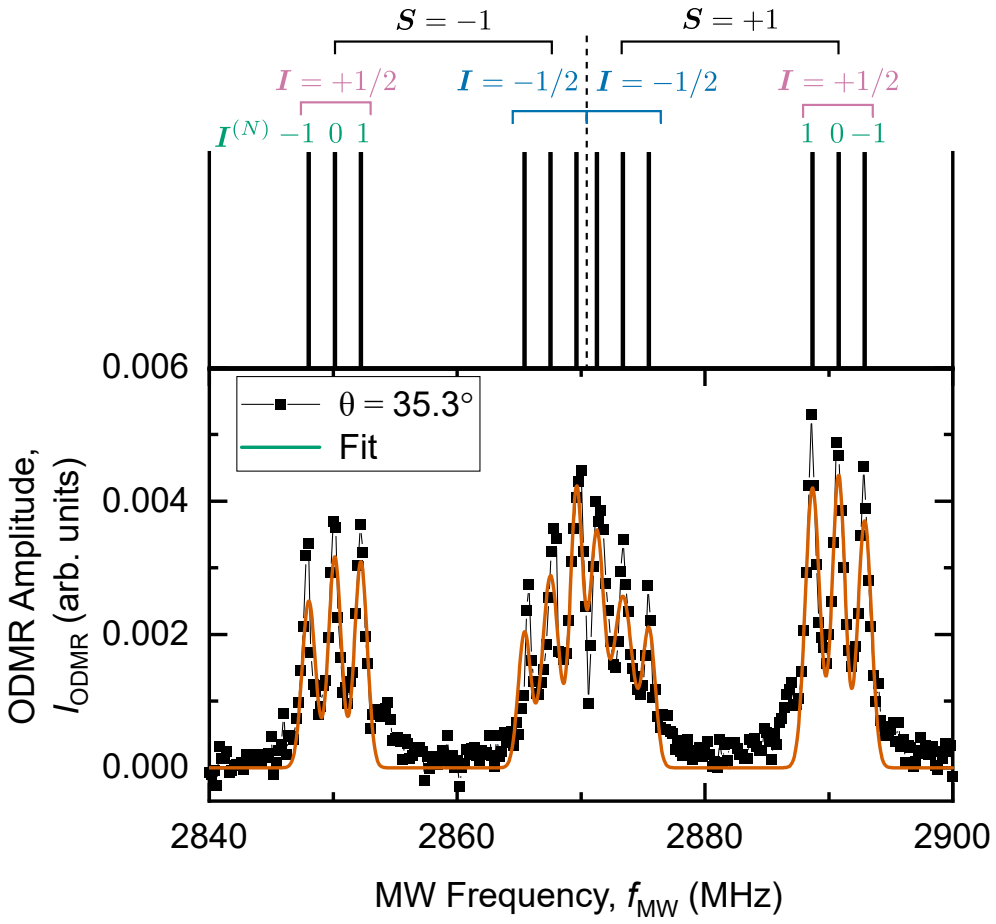

Figure 6.17: Fitting of $\theta = 35.3°$ CW ESR data with a function of the summation of 12 Gaussian peaks $y = \sum_{i=1}^{N=12} A_i e^{-((x-x_i)/w_i)^2}$, defined by shared constants and different spin permutations of Eqn 6.4. Fitted parameters are the hyperfine constants $\boldsymbol{A^{(N)}}$, $\boldsymbol{A}$, splitting F of the $m_s = \pm 1$, zero field splitting D_{ZFS} and the nitrogen quadrupole interaction strength P, the values of which are found in Table 6.1. The top schematic demonstrates how all valid permutations of $\boldsymbol{I^{(N)}}, \boldsymbol{I}$ and $\boldsymbol{S}$ create 12 distinct energetic transitions.

known value of $P = -5$ MHz [181, 182]. The hyperfine splitting from ^{14}N ($\boldsymbol{A}^{(N)} = -2.16$ MHz) matches well with previous work [182] and the ^{13}C hyperfine shift ($\boldsymbol{A} = 17.4$ MHz) falls within the region of expected values 2 - 20 MHz [181]. Zero field splitting $D_{\mathrm{ZFS}} = 2874.5$ MHz was higher than the widely accepted $D_{\mathrm{ZFS}} \approx 2870$ MHz [155], likely due to the unaccounted effect of strain on the zero field splitting, characterised by a shift E_{ZFS}, typically in the range usually 1 - 10 MHz [172]. The electron spin state splitting F of the ground state spin triplet can arise from a combination of local strain and magnetic field splitting. The earth's

Parameter	Fitted Value	Units
$\boldsymbol{A}^{(N)}$	-2.07	MHz
$\boldsymbol{A}$	17.4	MHz
P	-4.07	MHz
D_{ZFS}	2874.5	MHz
F	23.2	MHz

Table 6.1: Values for fitted parameters fitting Eqn 6.4 to the $\theta = 35.3°$ CW ESR scan in Fig 6.17.

magnetic field is ≈ 0.05 mT, which would correspond to a Zeeman splitting of $2g_e\mu_B B \approx 2$ MHz, and so cannot fully explain the observed splitting. Local strain has been reported to cause splitting on the order of tens of MHz [180], and so we conclude this is the cause of the additional splitting.

Experiments have been carried out in the literature providing a full description of the $m_s = \pm 1$ electron spin state splitting F, considering applied electric field, magnetic field and local strain [180]. A full investigation of these features would require systematic study of magnetic field strength $\boldsymbol{B}$, orientation θ and applied electric field $\boldsymbol{E}$ on the NV^- ESR resonance, and was not required for testing of the keyhole resonator designs. Detection of the hyperfine effects is promising as it demonstrates the possibility of using the NV^- centres as a test structure for the design of the hybrid electron-nuclear coherent control measurements using both NMR and ESR techniques, which has been previously demonstrated on up to 27 nuclear spins in diamond [18].

6.7.2 Magnetic field dependence of NV^- CW ESR

In order to test keyhole resonators for ESR measurements, we require the application of a static magnetic field along the defect axis of NV^- to fully exploit the Zeeman effect and increase the frequency of one of the NV^- ESR transitions to $f_{\mathrm{ESR}} \approx 7.5$ - 8.5 GHz. As shown in Fig 6.9, the splitting of the $m_s = \pm 1$ states results in an increase in the $m_s = 0 \leftrightarrow 1$ frequency, whereas the $m_s = 0 \leftrightarrow -1$ transition decreases in frequency until the $m_s = -1$

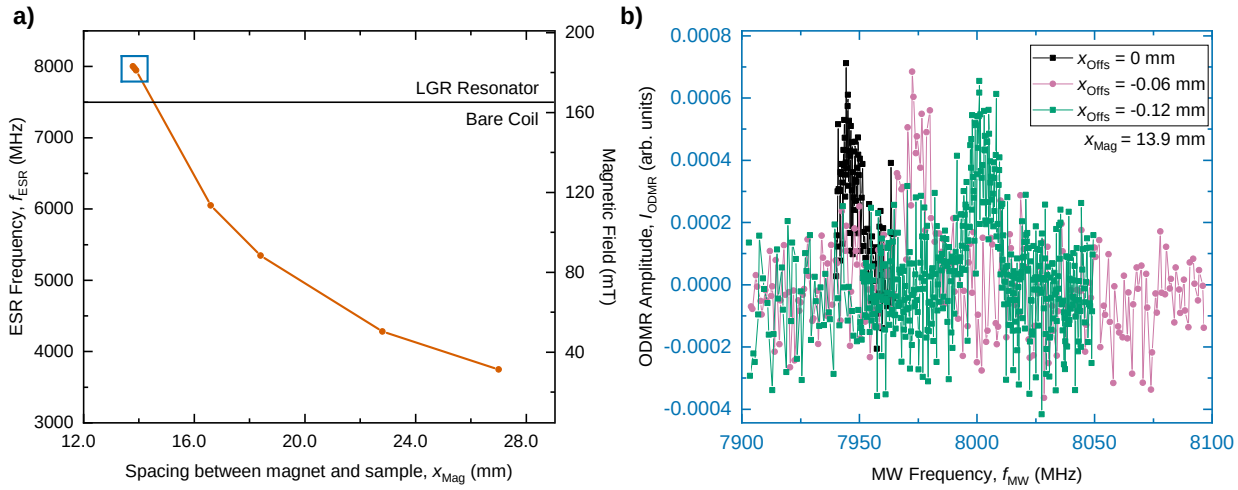

Figure 6.18: a) ESR frequencies f_{ESR} of the NV^- ensemble for increasing magnetic field B_x (decreasing magnet position x_{Mag}). Frequencies were calculated from fitting ESR peaks with a Gaussian. Microwave excitation below 6.5 GHz are generated by a bare copper coil, and above 6.5 GHz were measured using an 7.75 GHz KHR resonator. b) ESR spectra for points in blue box found in a). Fine tuning of magnetic field using a motor-driven translation stage for small adjustments x_{Offs} to the position of one of the magnets. Incrementing x_{Offs} allows tuning of NV^- resonance to match resonator frequency mode $f_{\mathrm{Res}} = 8006$ MHz.

state crosses the $m_s = 0$ state. To minimise the required magnetic field, all results for ESR where $B > 0$ T are performed on the $m_s = 0 \leftrightarrow +1$ transition.

Once the defect axis has been aligned parallel to the x-axis, magnetic field is introduced by placing two neodymium permanent magnets on a sliding rail either side of the sample at $x_{\mathrm{Mag}} > 0$ and $x_{\mathrm{Mag}} < 0$, where x_{Mag} is the spacing between the excited area of the sample and a magnet. The spacing between both magnets is $2x_{\mathrm{Mag}}$, and the sample is kept directly in the centre to keep the spacing between the sample and either magnet symmetric. This preserves static field homogeneity, limiting the effects of field inhomogeneities on the NV centre ensemble. Local variation in magnetic field results in different NV centres experiencing different magnetic fields, thus broadening the ESR resonance. We systematically decrease the spacing of the magnets x_{Mag} to increase the magnetic field experienced by the NV centre ensemble, and measure ESR spectra at each magnet spacing. Results from the gradual increase in field are shown in Fig 6.18a, where a clear increase in frequency with magnetic field is observed. The ESR frequency of each field is calculated through fitting of the ESR

spectra with a Gaussian function.

Once the ESR frequency is close to the resonator mode frequency f_{Res}, small adjustments to the field are required to tune f_{ESR} into resonance with the resonator mode. Minor adjustments to the magnetic field were made by attaching one magnet to a motor-driven translation stage with a 0.01 mm accuracy. We could then systematically measure ESR spectra for small changes in the magnet position, x_{Offs}, as shown in Fig 6.18b. As we know the resonator mode frequency f_{Res} from microwave reflectometry, we can ensure the ESR frequency is optimally tuned such that $f_{\text{ESR}} = f_{\text{Res}}$. When correctly tuned, microwave transmission will be most efficient at the NV^- centre resonance.

6.8 Pulsed electron spin resonance

Experiments so far have used CW ESR to non-coherently depolarise the electron spin. In order to provide coherent rotation of the NV^- electron spin, we must use short pulses of microwave excitation. The underlying theory of electron spin control is much the same as for pulsed NMR measurements, for which a detailed description can be found in Section 3.6.3.

In order to provide a quick breakdown of coherent control of the electron spins in NV^-, we can consider the $m_s = 0 \leftrightarrow +1$ as a two level spin system [113, 183]. The spin system in a static magnetic field B_0 with an applied alternating perpendicular driving field $B_1(t)$ can be studied in the rotating frame with a frequency $\omega_L = g_e \mu_B B_0$. In this rotating frame, the alternating magnetic field $B_1(t)$ becomes static and causes the spin projection to oscillate between the $m_s = 0$ and $m_s = +1$ state. This process is what is referred to as a Rabi oscillation and occurs at rate defined by the previously introduced Rabi frequency $f_{\text{Rabi}} = \left|\frac{\gamma_e}{2\pi}\right| B_1/\sqrt{2}$, where $\left|\frac{\gamma_e}{2\pi}\right| = 28\,024$ MHz T^{-1} is the free electron gyromagnetic ratio. The $1/\sqrt{2}$ term arises from the S_x matrix elements for a spin-1 system [183]. Consequently, it can be seen how increased strength of the oscillating magnetic field will increase the rate of coherent spin control. It is worth noting that B_1 amplitude in the rotating frame

corresponds to an oscillating magnetic field in the lab frame with an amplitude of $2B_1$ due to decomposition of rotating and corotating components in the rotating frame [113].

Faster rotation of spins allows more quantum gate operations to be performed in a fixed time window, and so it is desirable to apply the strongest microwave field possible. In order to achieve this, we use a customized 300 W pulsed microwave amplifier (AM61-7.5-8.5-55-55) specified to produce maximum amplification at 8 GHz with a 1 GHz bandwidth. As a consequence, it is vital to use a keyhole resonator with f_{Res} as close to 8 GHz as possible in order to fully utilise both the amplifier and resonator for maximum P_{MW}. We can define the efficiency of the resonator as the ratio of applied microwave power to the strength of the resulting microwave magnetic field $2B_1$. The strength of the oscillating field is related to the microwave power through $2B_1 \propto \sqrt{P_{\mathrm{MW}}}$, and as such, the efficiency can be quantified by the microwave conversion factor $2B_1/\sqrt{P_{\mathrm{MW}}}$. We can also quantify the microwave conversion factor in terms of Rabi frequency $f_{\mathrm{Rabi}}/\sqrt{P_{\mathrm{MW}}}$, demonstrating the amount of microwave power converted to coherent rotation of the NV^- spin ensemble. In this section, we measure Rabi oscillations of the NV^- ensemble in order to measure the efficiency of the keyhole resonator designs and compare them with other designs used in the literature.

6.8.1 Optical pump and probe pulse length calibrations

A schematic of the timing sequence used for pulsed ESR is shown in Fig 6.19. The measurement is differential, with a microwave "On" sequence and "Off" sequence within a full measurement cycle T_{Cycle}. For an acquisition window T_{Acq}, the full measurement cycle is then repeated N times such that $N = T_{\mathrm{Acq}}/T_{\mathrm{Cycle}}$, to ensure a sufficient amount of signal is detected.

To carry out pulsed ESR measurements, we can no longer use continuous optical excitation as this may destroy the coherent spin state. Instead, we switch to an optical pump-probe scheme where short optical pulses initialise (readout) the spin state before (after) coherent spin rotation. In order to optimise the length of the optical pulses for maximum ESR signal

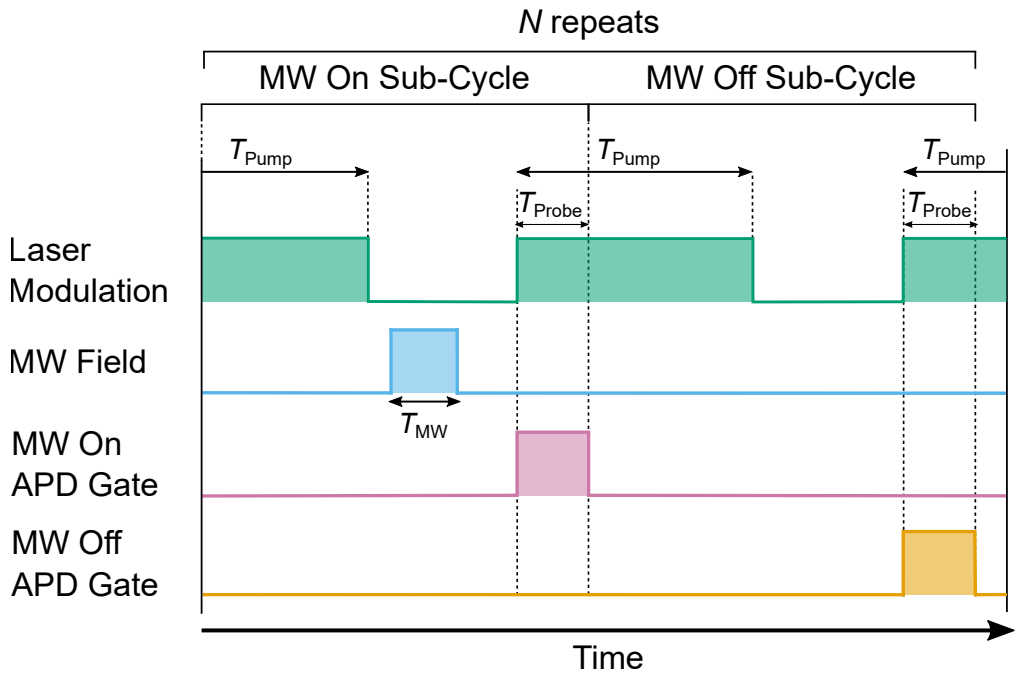

Figure 6.19: Timing diagram for pump-probe pulsed ESR measurements. A single optical pulse of length T_{Pump} is repeated twice for a full cycle. The first sub-cycle starts with a pump pulse T_{Pump}, after which a MW pulse of length T_{MW} is applied to the sample, coherently exciting the electron spin in the NV^- ensemble. The second pump pulse starts in sync with the APD gate for MW On. The APD gate remains open for T_{Probe}, acting as a probe pulse by capturing signal from a portion of the optical pump pulse. The ratio of pump and probe duration is kept at a constant $T_{\text{Pump}}/T_{\text{Probe}} = 30$. Once APD gating has stopped, a new sub-cycle is started where no MW field is applied, with optical signal being sent to the other APD detection channel. Comparison of signal from MW On (Pink) and MW Off (Orange) gives the differential optical signal and therefore the ODMR signal. For pump-probe time calibrations, a small modification to this scheme using long T_{MW} is used to non-coherently depolarise the electron spins.

from the NV^-, we carried out a calibration of the pump and probe time. ODMR signal was measured for a range of pump, T_{Pump}, and probe, T_{Probe}, times. The ratio of T_{Pump} to T_{Probe} is fixed to 30. We require a differential measurement with "On" and "Off" microwave excitation for this calibration to allow us to determine the change in PL as a result of electron spin polarisation. Efficient optical pumping will increase ensemble electron spin polarisation and therefore we will observe a stronger change in PL with a differential MW measurement.

Several measurements were carried out, with the first series investigating the effect of optical excitation power on ODMR signal at $B_z = 0$ T using a bare copper coil as the

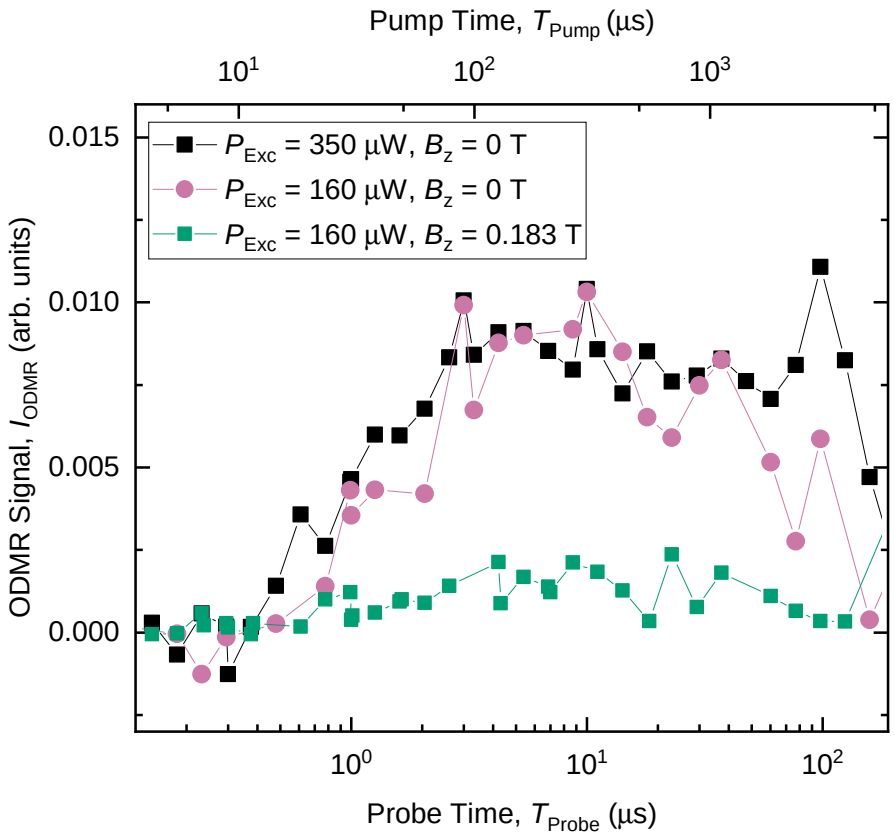

Figure 6.20: Optical pump time T_{Pump} and probe time T_{Probe} calibration. A range of probe times $T_{\text{Probe}} \sim 0.1$ - 400 μs were tested to observe the effect on ODMR signal. Pump time T_{Pump} was also altered to maintain a fixed ratio of $T_{\text{Pump}}/T_{\text{Probe}} = 30$. Measurements were carried out at $B_z = 0$ (red, black) and $B_z = 0.183$ T (where $f_{\text{ESR}} = 8$ GHz) to ensure no change in the optical pulse lengths as field changes. Maximum ODMR was found to occur with $T_{\text{Probe}} \sim 7$ μs ($T_{\text{Pump}} \sim 210$ μs), with a clear reduction in ODMR signal at higher field. Saturation of optical excitation due to excitation power P_{Exc} must occur between 160 - 350 μW as the ODMR signal is similar for both.

microwave source. As shown in Fig 6.20, the increase in optical power makes no difference to detected ODMR signal. As such, we use $P_{\text{Exc}} = 160$ μW for all pump-probe measurements. Signal is maximum at approximately $T_{\text{Probe}} \sim 7$ μs ($T_{\text{Pump}} \sim 210$ μs), providing optimal pulse lengths for maximum ODMR signal. These values match well with the literature, which show typical values $T_{\text{Probe}} \sim 0.5$ - 10 μs ($T_{\text{Pump}} \sim 50$ - 300 μs) [176, 184, 185].

Additional investigation was required to see if the pump-probe parameters remained the same in the presence of applied magnetic field. A measurement was made at a magnetic field of $B = 0.183$ T, which corresponds to the frequency $f_{\text{ESR}} = 8$ GHz at which the KHR was

used for microwave generation. As shown in Fig 6.20, ODMR signal is significantly reduced, but follows the same trend as the $B = 0$ T measurements, allowing us to use the same pump-probe parameters for pulsed ESR with the keyhole resonators as used for the bare coil.

6.8.2 Hardware limitations

Before performing pulsed experiments, we need to increase the power generated by the set-up for fast coherent spin rotation. We replace the 3 W amplifier with a 300 W pulsed amplifier and set out to investigate the maximum power that could be generated by the KHR. Firstly, we test long bursts of $f_{\mathrm{MW}} = 8$ GHz microwaves with $T_{\mathrm{MW}} = 1000$ ns to investigate the maximum continuous driving power that can be used. A fraction of the reflected pulse was passed through an RF detector, a device that demodulates the microwave signal and allows observation of changes in amplitude. As power was increased, we observed an intermittent but dramatic increase in reflected amplitude as the input power reached $P_{\mathrm{MW}} = 51.5$ dBm. Further increase of the power caused the effect to occur consistently. We attribute these sporadic and sudden jumps in amplitude to an arcing effect, whereby electrical breakdown occurs in the volumes with the highest electric field. For the KHR structures, this will occur in the conductive gap, which can be seen by electric field distribution simulations in Ref. [33].

The presence of arcing effects are unwanted side effects of the strong electric fields generated by the resonator, potentially causing damage to studied samples through heating or sudden electrical discharges, and thus need to be avoided. It is also worth considering that these resonators are designed to work in the low pressure helium insert used in the bath cryostat system described in Chapter 3. Low density helium exchange gas will have a lower threshold for arcing to occur, and so understanding the practical limits of the arcing effects to arise is critical for future use.

For pulsed ESR experiments, we require the use of pulses much shorter than the $T_{\mathrm{MW}} = 1000$ ns used in the previous test. Consequently, the total dissipated energy per pulse is reduced, potentially allowing higher powers to be used for the shorter pulses. It is important

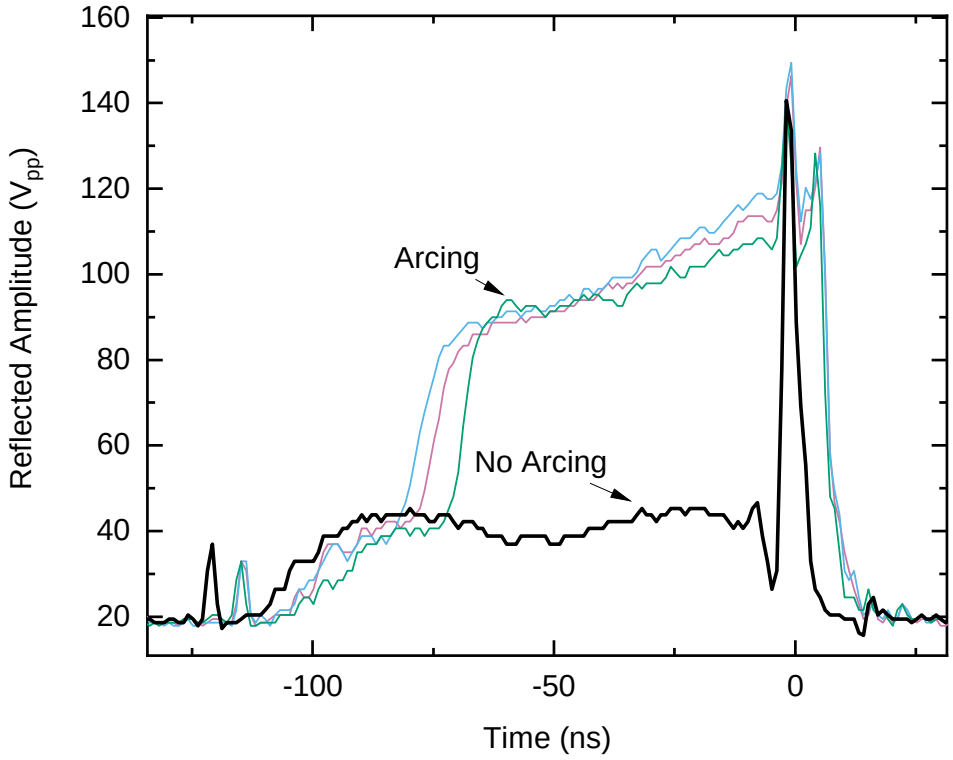

Figure 6.21: Time trace of reflected MW amplitude from an RF detector attached to reflected channel of pulsed amplifier. This test is for a pulse length of $T_{\mathrm{MW}} = 120$ ns. There is a significant increase in amplitude in the coloured curves at ≈ 40 ns when compared to the standard pulse (black), which is attributed to arcing effects.

to note that the 300 W pulsed amplifier has a maximum output of 54 dBm, and so we wanted to find the longest pulse T_{MW} that can be operated at $P_{\mathrm{MW}} = 54$ dBm. Gradual increase of T_{MW} for a fixed $P_{\mathrm{MW}} = 54$ dBm reveals that arcing effects occur once $T_{\mathrm{MW}} \geq 120$ ns. Interestingly, arcing effects begin at ≈ 40 ns during the $T_{\mathrm{MW}} = 120$ ns pulse test (as seen by arcing curves in Fig 6.21) despite tests of $T_{\mathrm{MW}} = 40$ ns pulses showing no signs of arcing. This is explained through the repeated application of the microwave pulse for a fixed measurement cycle period T_{Period} with increased T_{MW}, effectively increasing the duty cycle $T_{\mathrm{MW}}/T_{\mathrm{Period}}$ of applied MW. Subsequently, pulse duration at $P_{\mathrm{MW}} = 54$ dBm could likely be improved with a longer measurement cycle, at the cost of increased experimental time.

An alternative solution to increasing the measurement period is the alteration of the

resonator design in order to minimise the strength of the electric field generated by high P_{MW} and transmitted towards the sample. Modifications to the current KHR design could include the introduction of a "bridge" across the conductive gap, creating a bridged LGR (BLGR). The conductive bridge acts as an electrical shield, limiting the generation of electric field into free space [186], and thus limiting the voltage that the gas is exposed to.

6.8.3 Fast coherent control of electron spins

Coherent rotation of the electron spin projection between the $m_s = 0 \leftrightarrow +1$ states is quantified by $\theta = T_{\mathrm{MW}}/f_{\mathrm{ESR}}$. We measured pulsed ESR by varying microwave pulse length T_{MW}, which allows us to observe Rabi oscillations as seen in Fig 6.22. Microwave power of $P_{\mathrm{MW}}^{\mathrm{In}} = -25$ dBm was selected to be as high as possible while ensuring no arcing effects occurred during longer pulses, corresponding to an output power of $P_{\mathrm{MW}} = 44.1$ dBm. The Rabi oscillation data was fitted with a damped sine wave fit of the form:

$$A\cos(\frac{2\pi t}{T_{\mathrm{Rabi}}})\exp(-\frac{t}{T_2^{\mathrm{Rabi}}})$$

where the first term is a simple cosine function, and the second introduces an exponential decay to account for loss of amplitude over time. Oscillation period is described by T_{Rabi}, while the oscillation amplitude is determined by the scaling factor A. The rate at which the oscillations are damped is characterised by the driven coherence time $T_2^{\mathrm{Rabi}} \approx 400$ ns, and arises due to both inhomogenities in applied B_1 and inhomogenous broadening of the NV^- ensemble [187, 188]. We obtain a Rabi oscillation period of $T_{\mathrm{Rabi}} = 40.3$ ns, corresponding to a Rabi frequency of $f_{\mathrm{Rabi}} = 24.8$ MHz, which allows us to calculate the strength of the oscillating magnetic field in the lab frame $2B_1$ through $f_{\mathrm{Rabi}} = \left|\frac{\gamma_e}{2\pi}\right| B_1/\sqrt{2}$. This yields a value of $2B_1 = 2.5$ mT, where the factor of 2 accounts for the transformation from the rotating frame to lab frame. Calculation of the microwave conversion factor for an input power of $P_{\mathrm{MW}} = 44.1$ dBm (25.9 W) gives a value of $2B_1/\sqrt{P_{\mathrm{MW}}} = 0.49 \times 10^{-3}$ T $\mathrm{W}^{-1/2}$

(4.89 MHz $W^{-1/2}$).

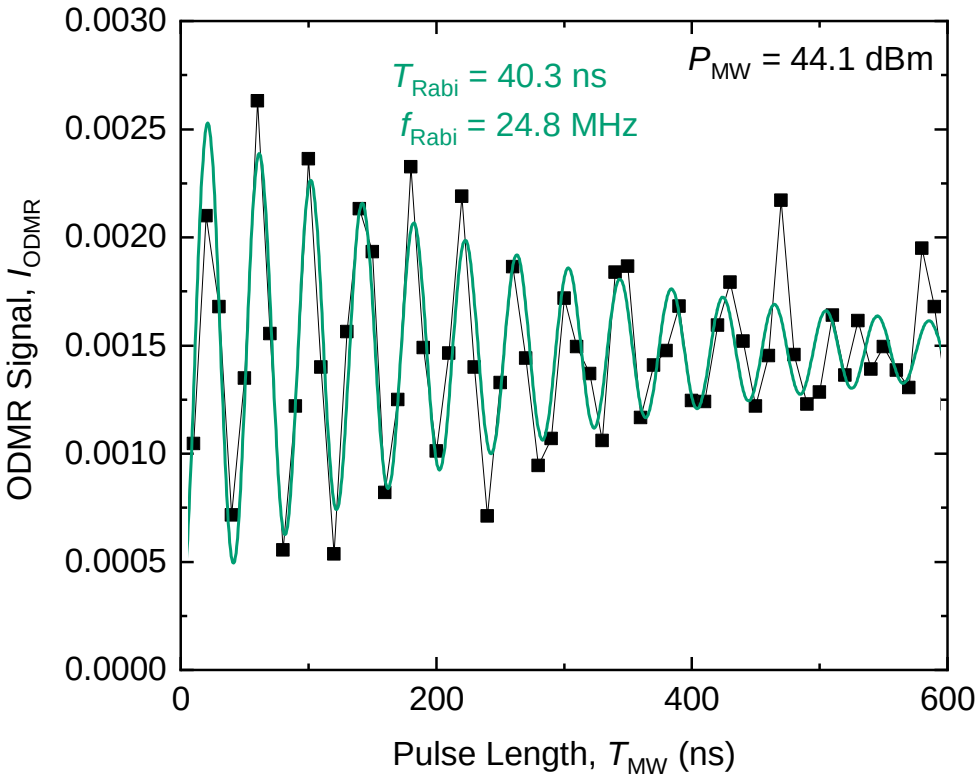

Figure 6.22: Rabi oscillations (black, squares) of the $m_s = 0 \leftrightarrow +1$ transition in the NV^- ensemble by varying length of MW pulses T_{MW} for a fixed power P_{MW}. MW pulses were applied at $f_{MW} = 8.006$ GHz to match the resonator mode f_{Res}, at a power of $P_{MW} = 44.1$ dBm. Fitting the data (green) with a damped exponential function gives a Rabi period of $T_{Rabi} = 40.3$ ns, which can also be expressed as the Rabi frequency $f_{Rabi} = 1/T_{Rabi} = 24.8$ MHz.

Low resolution of the T_{MW} time varied measurement was limited by the microwave generator (SMB100) resolution of 10 ns. In order to circumvent this, we ran another measurement with a fixed T_{MW} and varied P_{MW}. This allows much more detailed oscillations to be measured due to the precise control over microwave waveform power. Variation in P_{MW} will change the rate at which coherent control of the spin occurs, which for a fixed T_{MW} will result in the spin projection rotating as P_{MW} changes. Results from this measurement are shown in Fig 6.23, and show Rabi oscillation curves for several different T_{MW}. Above -10 dBm, a clear plateauing of the ODMR signal is observed, arising from the compression of

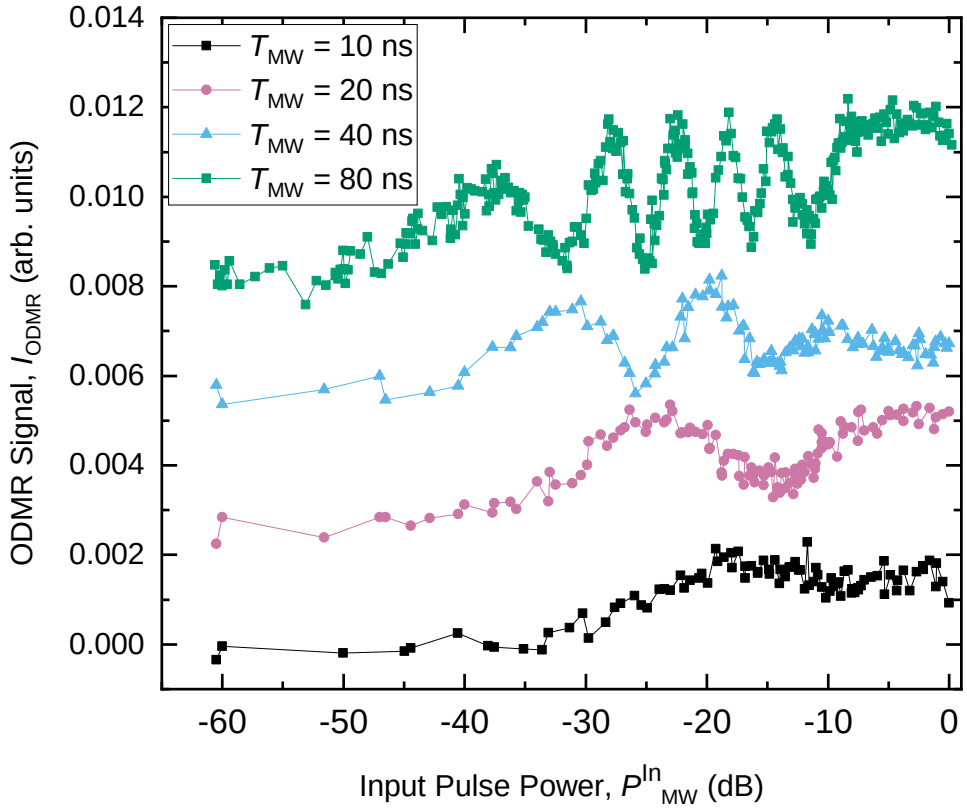

Figure 6.23: Rabi oscillations of the $m_s = 0 \leftrightarrow +1$ transition in the NV$^-$ ensemble by varying the power of MW excitation P_{MW} for fixed length MW pulses T_{MW}. MW pulses were applied at $f_{\mathrm{MW}} = 8.006$ GHz, as for Fig 6.22. A clear reduction in coherent rotation rate is present for decrease pulse lengths due to the reduced microwave energy input.

the amplifier when maximum output power is reached.

Compression is the limiting factor in maximum power output from an amplifier. The amplifier adds power to an input waveform, and is quantified by gain G. Under standard operating conditions and considering input power $P^{\mathrm{In}}_{\mathrm{MW}}$ in dBm, the gain is simply added to the input power such that $P_{\mathrm{MW}} = P^{\mathrm{In}}_{\mathrm{MW}} + G$. Conversion between microwave power in Watts to dBm is achieved through $P^{\mathrm{dBm}}_{\mathrm{MW}} = 10\log_{10}(P^{\mathrm{Watts}}_{\mathrm{MW}}/1\mathrm{mW})$. However, as the input power approaches the compression point of the amplifier, the gain regime becomes nonlinear, resulting in imperfect amplification of the input signal [152]. Measurement of the change in gain for higher input powers is critical for accurate calibration of the outputted microwave power P_{MW}. As such, we ran calibrations measuring the gain G of the input microwave

signal $P_{\mathrm{MW}}^{\mathrm{In}}$ through the 300 W pulsed amplifier. The measurement was carried out by using an RF detector to measure the time trace of the amplified signal and calculating the area under the curve. Area under the curve corresponds to the pulse area, defined by the product of the pulse length and pulse amplitude $A_{\mathrm{PA}} = T_{\mathrm{MW}} V_{\mathrm{p-p}}$. The ratio of input pulse area to outputted pulse area gives a measurement of the effective amplitude gain G_{Eff} of the amplifier for a given input T_{MW} and P_{MW}, the results of which are shown in Fig 6.24. A clear reduction in effective gain G_{Eff} occurs from $P_{\mathrm{MW}}^{\mathrm{In}} = -20$ dBm, with shorter pulses experiencing an even stronger reduction in G_{Eff}.

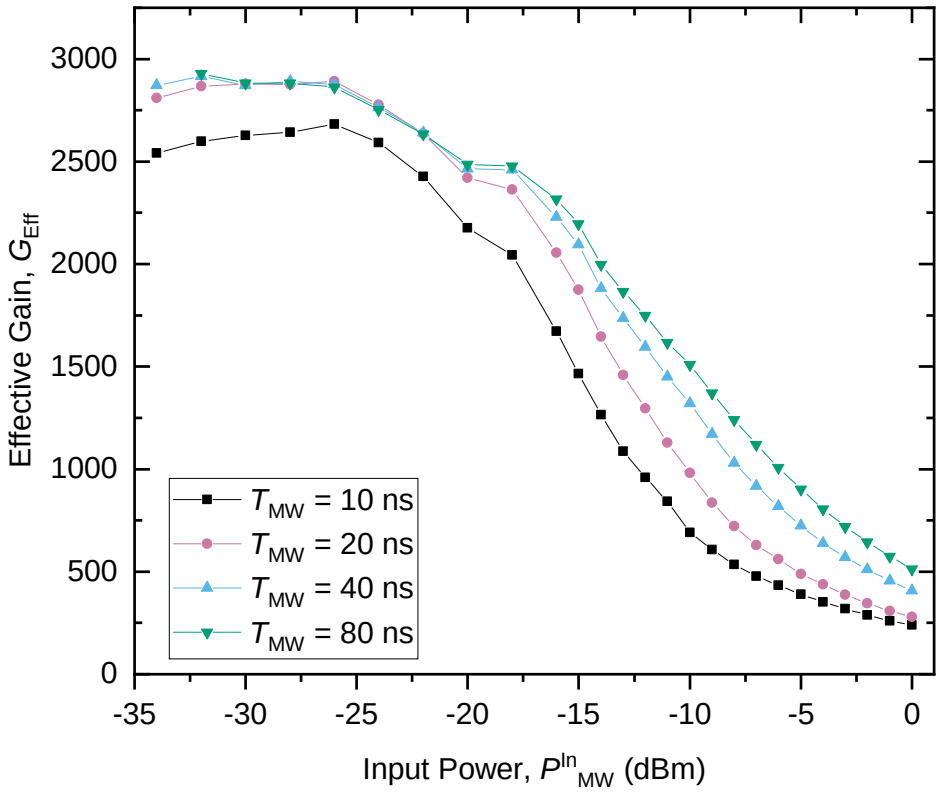

Figure 6.24: Effective gain of 300 W pulsed amplifier for a range of microwave pulse powers $P_{\mathrm{MW}}^{\mathrm{In}}$ and pulse lengths T_{MW}. Effective gain is calculated by taking the ratio of the amplifier microwave output pulse area $A_{\mathrm{PA}}^{\mathrm{Out}}$ to the input pulse area $A_{\mathrm{PA}}^{\mathrm{In}} = V_{\mathrm{p-p}}^{\mathrm{In}} T_{\mathrm{MW}}$. A clear reduction in amplifier gain is observed for higher input power pulses $P_{\mathrm{MW}}^{\mathrm{In}}$. It is also clear from reduced gain for shorter T_{MW} that the amplifier is less efficient as the pulse length approaches the minimum pulse length of $T_{\mathrm{MW}} = 10$ ns.

Considering the reduction in gain above $P_{\mathrm{MW}}^{\mathrm{In}} = -20$ dBm, it is important to adjust

the results in Fig 6.23 to reflect the actual microwave power emitted. To achieve this, we convert the input power to outputted pulse area through the following expression $A_{\mathrm{PA}}^{\mathrm{In}} = G_{\mathrm{Eff}}(T_{\mathrm{MW}}^{\mathrm{In}} V_{\mathrm{MW}}^{\mathrm{In}})$, where $V_{\mathrm{MW}}^{\mathrm{In}}$ is the input microwave peak-to-peak amplitude measures and $V_{\mathrm{MW}}^{\mathrm{In}} \propto \sqrt{P_{\mathrm{MW}}^{\mathrm{In}}}$. Fig 6.25 shows the results of Rabi oscillations with fixed T_{MW} and varying P_{MW} in terms of pulse area A_{PA}.

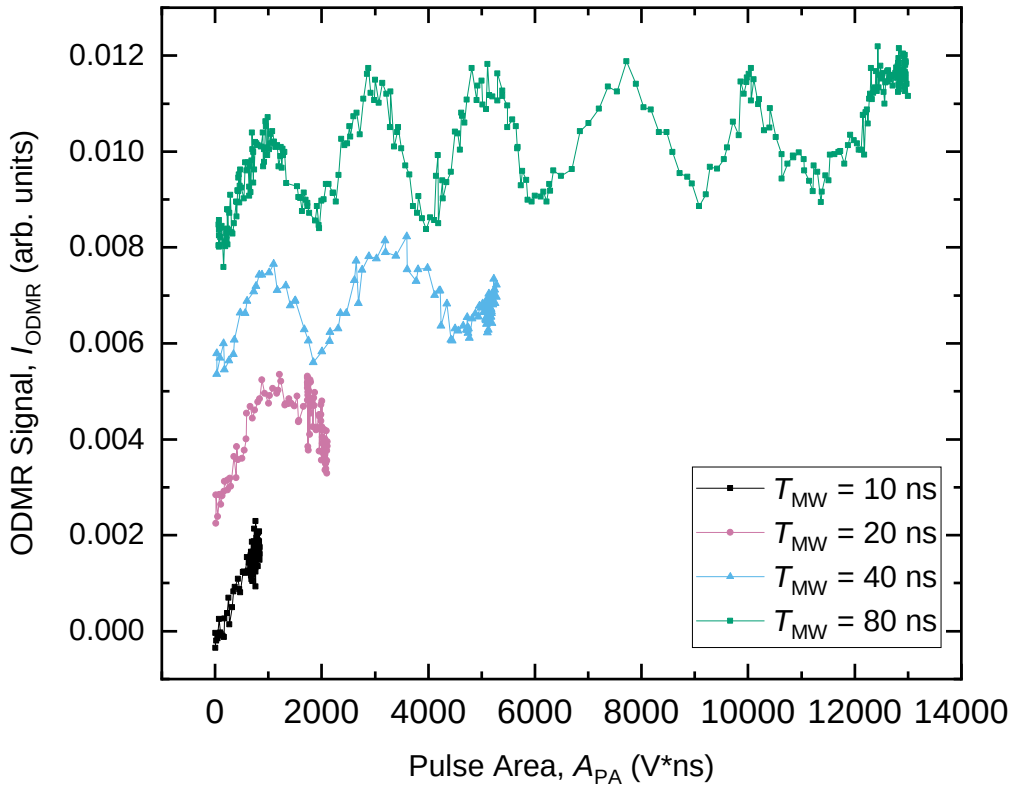

Figure 6.25: Rabi oscillations of the $m_s = 0 \leftrightarrow +1$ transition in the NV^- ensemble as function of pulse area $A_{\mathrm{PA}} = P_{\mathrm{MW}} * T_{\mathrm{MW}}$ by varying the power of MW excitation P_{MW} for fixed length MW pulses T_{MW}. MW pulses were applied at $f_{\mathrm{MW}} = 8.006$ GHz, as for Fig 6.22. A clear reduction in coherent rotation rate is present for decrease pulse lengths due to the reduced energy input.

There are two factors that limit number of electron spin rotations that can be achieved with our current set-up. Firstly, the non-linear regime of the pulse amplifier ultimately limits the maximum power that can be outputted with the current hardware configuration. This can be seen most clearly in the $T_{\mathrm{MW}} = 20$ ns results in Fig 6.25, where the data appears to "reflect" at a critical pulse area of $A_{\mathrm{PA}} \approx 2200$ V ns. Here, measurements with power

$P_{\mathrm{MW}}^{\mathrm{In}} > -15$ dBm have smaller pulse areas A_{PA} due to compression effects, reducing the amount of rotation during the 20 ns pulse. As a result, we can see for the $T_{\mathrm{MW}} = 20$ ns curve that measurements above the -15 dBm limit effectively repeat the lower pulse area measurements. This is indicated by the high density of data points in Fig 6.25, and can also be seen in the other T_{MW} curves.

We observe a single π-pulse for the $T_{\mathrm{MW}} = 10$ ns pulse at the maximum power $P_{\mathrm{MW}} = 54$ dBm (Fig 6.25), which allows us to calculate a new Rabi frequency of $f_{\mathrm{Rabi}} = 1/(2t_{\pi}) \approx 50$ MHz. We can then calculate a new microwave conversion efficiency of 0.32×10^{-3} T $\mathrm{W}^{-1/2}$ for the fastest coherent control of the electron spin achieved in these experiments. A hard limit on the amount of power P_{MW} that can be generated by the amplifier means increased pulse length is required for an increased number of spin rotations. However, as described in Section 6.8.2, a second limit on rotations arises due to arcing effects that arise for pulse lengths above $T_{\mathrm{MW}} \geq 120$ ns, acting as hard limit for the pulse length T_{MW}. Consequently, the maximum amount of continuous rotation that can be generated using the current KHR design is shown in the $T_{\mathrm{MW}} = 80$ ns in Fig 6.25, where we observe 11 π-pulse rotations. In order to increase the number of π rotations that can be achieved in our set-up, we require improvements to the maximum P_{MW} by modifying the KHR design to limit arcing effects for longer pulses and higher powers (e.g BLGRs introduced in Sec 6.8.2). It is worth noting that 11 continuous rotations is the worst-case scenario, as most coherent control schemes such as dynamical decoupling sequences that are formed of a train of π-pulses. As a result, the interpulse delays between each π-pulse may allow more pulses to be applied before approaching the arcing limit.

6.8.4 Comparison to alternative resonator designs

The microwave conversion factor introduced in Section 6.8 can be used to compare the effectiveness of the KHR against other work in the literature. A summary of the comparisons can be found in Table 6.2.

Reference	Type	Approx. Size	L_{MW} (mm)	f_{Res} (GHz)	f_{Rabi}^{Max} (MHz)	$2B_1/\sqrt{P_{MW}}$ (T W$^{-1/2}$)	Limiting Condition of f_{Rabi}^{Max}
This work	KHR	5 mm × 10 mm	≈ 0.5	8.0	50	0.32×10^{-3}	Arcing Effects
Chekhovich [33]	KHR	5 mm × 10 mm	≈ 0.5	6.58	14.2	1.04×10^{-3}	Limited source power
Childress et al. [185]	Thin copper wire	20 μm diameter	< 0.05	2.87	15	1.0×10^{-3}	Limited source power
Gaebel et al. [189]	Miniaturized loop	Not Provided	< 0.05	2.87	16.7	0.4×10^{-3}	Limited source power
Fuchs et al. [154]	CPW	Not Provided	< 0.05	0.49	440	87.8×10^{-3}	Breakdown of RWA due to low f_{Res}
de Lange et al. [190]	CPW	Not Provided	< 0.05	0.3	20.5	4.9×10^{-3}	Limited source power
Aslam et al. [191]	CPW	0.1 mm × 1 mm	< 0.05	66 to 70 (Broadband)	< 1	2.7×10^{-3}	Limited source power
Jia et al. [192]	CPW	80 μm × 0.4 mm	< 0.05	0.5 to 17 (Broadband)	6 - 12	0.68×10^{-3}	Limited source power

Table 6.2: Summary of resonator characteristics of this work compared to alternative resonator designs found in the literature.

Firstly, we can compare our result 0.32×10^{-3} T W$^{-1/2}$ with the previous iteration of KHR design tested on SiC vacancies, which yielded a conversion factor of 1.04×10^{-3} T W$^{-1/2}$, demonstrating a factor ≈ 3 reduction in microwave conversion. The KHR tested in this work successfully operated at $f_{Res} = 8$ GHz, an improvement on the Ref [33] $f_{Res} = 6.58$ GHz. Both the SiC and NV$^-$ KHR tests were carried out at similar separations of $L_{MW} \approx 0.5$ mm. While a decrease in conversion efficiency was observed compared to the previous design in Ref [33], the KHR design tested in this chapter was shown to operate up to microwave powers of $P_{MW} = 54$ dBm, while SiC testing on the older design only was tested to powers

of $P_{\mathrm{MW}} \approx 30$ dBm. This was an important step, as high power operation is critical to future applications on quantum dots, where the lower quantum dot electron g-factor, $g_e^{(\mathrm{QD})} \approx 0.25 g_e$ results in a factor of ≈ 4 times higher power requirements for similar Rabi frequencies.

The microwave conversion efficiency can also be compared to other resonator designs used for ODMR on NV^- spins in the literature. One simple design is a copper wire stretched across the surface of a diamond sample, which allowed a maximum Rabi frequency of $f_{\mathrm{Rabi}}^{\mathrm{Max}} = 15$ MHz to be achieved with a conversion factor of 1.0×10^{-3} T $\mathrm{W}^{-1/2}$ [185], similar to that of first work with the KHR design [33]. Another example using a sample resting on a miniaturized loop yielded similar values with $f_{\mathrm{Rabi}}^{\mathrm{Max}} = 16.7$ MHz, but with a reduced conversion efficiency of 0.4×10^{-3} T $\mathrm{W}^{-1/2}$ [189]. Both of these examples are positioned close to the sample such that the separation is $L_{\mathrm{MW}} < 50$ μm, and so does not appropriately address the generation of parasitic electric fields.

The most common type of microwave source used for solid-state ODMR measurements are coplanar waveguides (CPW) [154, 190–192]. The CPW resonators are fabricated on to the surface of the sample, and are also in close proximity to the target spin, $L_{\mathrm{MW}} < 0.05$ mm, similar to the copper wire and miniaturized loop examples discussed so far. The typical CPW structure sizes is approximately 0.1 to 1 mm.

Some of the fastest demonstrations of coherent control of NV^- spins in the literature used a coplanar waveguide fabricated on to the surface of a diamond sample [154]. The $m_s = 0 \leftrightarrow -1$ NV^- transition was shifted with magnetic field such that the resonance frequency was $f_{\mathrm{Res}} = 0.49$ GHz, and allowed generating Rabi frequencies of $f_{\mathrm{Rabi}} = 109$ MHz at an input power of $P_{\mathrm{MW}} = 12$ dB, yielding a conversion factor of 87.8×10^{-3} T $\mathrm{W}^{-1/2}$ (865.8 MHz $\mathrm{W}^{-1/2}$) [154]. Rabi frequencies of up to 440 MHz were achieved, but with significant non-linear behaviour as f_{Rabi} approaches the small transition frequency $f_{\mathrm{Res}} = 0.49$ GHz, resulting in the rotating wave approximation ($f_{\mathrm{Rabi}} \ll f_{\mathrm{Res}}$) no longer being valid. Breakdown of the RWA can be avoided by operating at a higher f_{Res}, allowing linear Rabi oscillations to be observed at a higher f_{Rabi} at the cost of increased difficulty in achieving high

microwave conversion factor. Another example of CPW use for ODMR on NV^- achieved fast rotations with a higher transition frequency of $f_{\text{Res}} \approx 3$ GHz, but was less efficient with a microwave conversion factor of 4.9×10^{-3} T $W^{-1/2}$ [190].

Broadband coplanar waveguide (CPW) designs have also been shown to be operable from 0 to 15.8 GHz, resolving the issue with small f_{Res}, and demonstrating a conversion factor of 0.68×10^{-3} T $W^{-1/2}$ (6.8 MHz $W^{-1/2}$) at $f_{Res} \approx 7.3$ GHz. The highest power tested was only 1 W, and as such Rabi frequencies of only $f_{\text{Rabi}} = 6.8$ Mhz were achieved [192]. Similar results were found with CPW designs operating in the range 60 - 90 GHz [191], where a conversion factor of 2.7×10^{-3} T $W^{-1/2}$ (0.85 MHz $W^{-1/2}$) was measured at $f_{\text{Res}} \approx 68$ GHz. Achieving strong microwave power at high frequencies (E-band, 60 - 90 GHz) is difficult, with amplifiers only being able to operate up to 28 dBm (≈ 0.6 W), yielding Rabi frequencies of $f_{\text{Rabi}} < 1$ MHz.

The CPW designs do provide optical access to the samples measured, but are fabricated directly onto the sample or positioned nearby, giving resonator-sample separations of $L_{\text{MW}} \approx$ 1 - 50 μm. As mentioned for the non-CPW designs, small L_{MW} means that these resonator designs are likely to create the parasitic electric fields that we are trying to avoid. The KHR design used in this work provides microwave conversion factors similar to CPW designs, but with the addition of a large $L_{\text{MW}} \approx 0.5$ mm, allowing global control of many electron spins within a device. The limiting factor of Rabi frequencies from the KHRs are arcing effects that begin to occur at high microwave powers. These can be eliminated in principle by operating the KHR in a vacuum, allowing a strong voltage to be applied, increasing microwave power and therefore Rabi frequency.

6.9 Summary

In this chapter we have introduced the keyhole resonator (KHR) design first introduced in Ref. [33], a planar structure designed to amplify microwave frequency oscillating magnetic

fields for use in pulsed electron spin resonance experiments. We experimentally tested an improved KHR design and verify that the resonator mode is at the targeted $f_{\mathrm{Res}} = 8$ GHz, in addition to studying the effect of nearby conductors and temperature on the resonator mode frequency. The experimentally measured loaded Q-factor of ≈ 80 demonstrated the viability of the resonator to produce high power microwave pulses as short as $T_{\mathrm{MW}} = 10$ ns.

Optically detected electron spin resonance measurements were successfully performed with the KHR design on the NV^- ensemble found in diamond. The KHR was separated from the diamond sample by a distance $L_{\mathrm{MW}} \approx 0.5$ mm to minimise parasitic electric fields while maintaining strong microwave conversion. A static magnetic field of $B_0 = 0.183$ T shifted the $m_s = 0 \leftrightarrow +1$ transition in the $^3A_2$ ground state to 8 GHz, allowing coherent control of the electron spins in the ensemble using the KHR.

High power testing revealed the resonator produces arcing effects through electrical breakdown of the air occupying the space between the resonator and sample. Continuous wave testing revealed the resonator could be operated without arcing at $P_{\mathrm{MW}} = 51.5$ dBm, while the longest pulse at the highest available $P_{\mathrm{MW}}^{\mathrm{In}} = 54$ dBm was $T_{\mathrm{MW}} = 100$ ns. This resulted in a maximum achievable Rabi frequency of $f_{\mathrm{Rabi}} = 50$ MHz, and the shortest π-pulse length of ≈ 10 ns. Taking in to account $g_e^{\mathrm{QD}} \approx 0.25 g_e$, we can expect electron spin π-pulse lengths of approximately 40 ns, which is much less than the longest measured electron spin state decoherence time $T_{2,e} \approx 4$ μs [104, 146], allowing many gate operations to be performed on QD electron spin qubits before decoherence.

A Rabi frequency of $f_{\mathrm{Rabi}} = 50$ MHz with $P_{\mathrm{MW}} = 54$ dBm corresponds to a microwave conversion factor of 0.32×10^{-3} T $\mathrm{W}^{-1/2}$. This is comparable with other designs in the literature (e.g CPWs) but with the added advantage of a large L_{MW}, validating the design as a strong choice to be used in quantum computing protocols. More specifically, the KHR has demonstrated it can fulfill the requirements for a microwave resonator to be used in ESR experiments on the InGaAs QDs measured throughout the rest of this thesis, or other suitable systems such as strain-free GaAs QDs [29, 33].

7

Conclusion

The quantum dot spin qubit addresses many of the requirements described in Chapter 1 to be a viable choice for the building blocks of a quantum computer. Much research has gone into techniques to initialise and readout both the electron spin qubit and the rich nuclear spin bath through optical and magnetic resonance control schemes. One of the major requirements is longevity of any state used as a quantum resource, and in this thesis we have endeavoured to explore the mechanisms involved in relaxation and decoherence of the self-assembled QD spin states. A major driving component for this investigation into spin dynamics was determining the conditions required for a long-lasting electron spin state for future experiments of coherent control using magnetic resonance techniques. In this thesis we have presented several key findings that demonstrate steady progress towards a long lasting controllable QD spin qubit.

The development of a series of charge-tunable samples with varying tunnel coupling allowed investigation in to the effect of a proximal doped layer on the quantum dot spin lifetimes, as presented in Chapter 4. We showed that the quantum dot is effectively isolated in the $t_B = 52$ nm sample, with the longest demonstrated electron spin lifetime $T_1 \approx 1$ s in self-assembled quantum dots. Extended electron lifetime came at the cost of reduced electron spin state preparation fidelity due to Auger recombination effects. We found that a coupling dependant cotunnelling process $\Gamma_{e,\mathrm{cotun}}$ combined with the previously measured

[143, 144] phonon-assisted spin orbit mechanism $\Gamma_{e,\mathrm{ph}}$ gave an accurate description of electron spin lifetimes in a wide range of magnetic fields B_z. Extrapolation of the modelled relaxation mechanisms allowed estimation of a fundamental lower limit $\Gamma_{\mathrm{e,min}} \geq (20\ \mathrm{s})^{-1}$ of electron spin flip rate in the case of an isolated quantum dot ($t_B = \infty$). Nuclear lifetimes $T_{1,\mathrm{N}}$ variation for a range of magnetic fields is explained through a process mediated by electron spin relaxation, resulting in a field-independent lifetime at high magnetic field and t_B dependant nuclear lifetime at low field.

An isolated quantum dot with long electron lifetimes gave the opportunity to study nuclear ensemble coherence in a charged quantum dot, which we presented in Chapter 5. Electron spin fluctuations occurred at a much slower rate to similar work [136], which allowed us to measure millisecond length nuclear ensemble coherence times $T_{2,\mathrm{N}}$, demonstrating charged QD nuclear ensemble coherence times similar to that of an uncharged quantum dot. In this regime, the electron is no longer the primary source of decoherence, and the nuclear spin ensemble coherence is instead limited by direct nuclear dipole-dipole interaction. Further investigation in the form of a magnetic field and tunnel coupling dependence allowed a model to be developed to quantify the effect of a fluctuating electron spin on $T_{2,\mathrm{N}}$. Spectral diffusion accurately describes the effect observed and led us to the conclusion that a single electron spin flip will result in complete loss of nuclear coherence. Stated conversely, the nuclear spin ensemble is limited only by nuclear-nuclear interactions in the presence of a static electron, allowing reliable single shot measurement of the ensemble spin state. Development of the single shot measurement technique allowed us to use the directionality of the Knight field $\pm\nu_e$ (due to electron spin $S_e = \pm 1/2$) to encode the state of the electron spin onto the nuclear spin ensemble collective coherence. This allowed measurement of the electron spin state S_e with a fidelity of above 99.7% - demonstrating improvement when compared to other solid state systems showing fidelities 80 - 95 % [193–195], and superconducting qubits with fidelities 97 - 99 % [9, 196] that includes Google's 53-qubit Sycamore processor introduced in Chapter 1.

Long-lasting coherent spin states are only one of the major requirements laid out in

Chapter 1. The improvements in spin lifetimes and coherence time made in Chapter 4 and Chapter 5 addressed one of the major challenges for attempting coherent control of the electron spin state using magnetic resonance. Another technical hurdle that lay in the way of coherent electron control was the generation of microwave frequency oscillating magnetic fields, a higher frequency version of the NMR pulse discussed in detail within this thesis. Developments of a new type of resonator with minimal electric field generation were recently made [33], and we set out to investigate their suitability for generating high power short pulses of microwave magnetic fields for use in fast coherent electron spin control. A test bed sample of diamond was used to exploit well-studied NV^- electron spins for ESR experiments at room temperature, allowing easy iterative improvements to the ESR configuration. Electron spin resonance was successful, demonstrating high power microwave generation at a frequency similar to that of the Zeeman splitting of the electron in InGaAs quantum dots. The keyhole resonator design provides high power microwaves with minimal parasitic electric field, which when used on the QD system will prevent unwanted ejection of the electron spin.

Combining the advancements in understanding of ideal operating conditions for long lived spin lifetimes and coherence with the keyhole resonator platform places us in a strong position to attempt electron spin resonance on QDs, something that has remained elusive since the first and only demonstration of ESR by Kroner et al. [32]. Placement of the keyhole resonator within the setup described in this thesis, with the pulsed amplifier described in Chapter 6 should allow strong enough microwave pulses to be generated for ESR measurements. Coherent control via this method would be a major step in realising the quantum dot spin qubit. While the work we have presented here considers self-assembled InGaAs/GaAs quantum dots, it has become apparent that the inhomogeneous strain present due to the self assembly process is ultimately a limiting factor of using these QDs as spin qubits [29, 31, 104]. Promising research from strain-free droplet GaAs quantum dots reveals well defined nuclear spin state transitions, allowing full access to the $I = 3/2$ state space present in both Gallium and Arsenic, and has been successfully used to create a nuclear qubit register [29]. State

preparation and readout of the electron spin have been demonstrated in droplet-etched GaAs QDs, with electron lifetimes of $T_1 \approx 50$ μs that may be limited by cotunnelling effects [197]. Additional $T_{1,e}$ measurements close to the fundemental limit ($\Gamma_{\mathrm{e,min}}$) predicted in Chapter 4 have been measured in gate-defined GaAs QDs [198]. Despite the recent shift in focus away from the InGaAs QD system, the results concerning spin dynamics in this thesis are not limited to InGaAs QDs and as such are likely to still play a critical role in the future of III-V semiconductor QD spin qubit design.

Bibliography

[1] R. P. Feynman, "Simulating physics with computers," *International Journal of Theoretical Physics*, vol. 21, pp. 467–488, Jun 1982. doi:10.1007/BF02650179.

[2] R. P. Feynman, "Quantum mechanical computers," *Foundations of Physics*, vol. 16, no. 6, pp. 507–531, 1986. doi:10.1007/BF01886518.

[3] D. Deutsch and R. Penrose, "Quantum theory, the Church-Turing principle and the universal quantum computer," *Proceedings of the Royal Society of London. A. Mathematical and Physical Sciences*, vol. 400, no. 1818, pp. 97–117, 1985. doi:10.1098/rspa.1985.0070.

[4] P. Benioff, "The computer as a physical system: A microscopic quantum mechanical Hamiltonian model of computers as represented by Turing machines," *Journal of Statistical Physics*, vol. 22, pp. 563–591, May 1980. doi:10.1007/BF01011339.

[5] P. Benioff, "Quantum mechanical hamiltonian models of turing machines," *Journal of Statistical Physics*, vol. 29, pp. 515–546, Nov. 1982. doi:10.1007/BF01342185.

[6] D. Deutsch and R. Jozsa, "Rapid solution of problems by quantum computation," *Proceedings of the Royal Society of London. Series A: Mathematical and Physical Sciences*, vol. 439, no. 1907, pp. 553–558, 1992. doi:10.1098/rspa.1992.0167.

[7] L. K. Grover, "A fast quantum mechanical algorithm for database search," in *Proceedings of the Twenty-Eighth Annual ACM Symposium on Theory of Computing*, STOC '96, (New York, NY, USA), p. 212–219, Association for Computing Machinery, 1996.

[8] P. W. Shor, "Polynomial-time algorithms for prime factorization and discrete logarithms on a quantum computer," *SIAM J. Comput.*, vol. 26, p. 1484–1509, oct 1997. doi:10.1137/S0097539795293172.

[9] F. Arute, *et al.*, "Quantum supremacy using a programmable superconducting processor," *Nature*, vol. 574, pp. 505–510, Oct 2019. doi:10.1038/s41586-019-1666-5.

[10] D. P. DiVincenzo, "The physical implementation of quantum computation," *Fortschritte der Physik*, vol. 48, no. 9-11, pp. 771–783, 2000. doi:https://doi.org/10.1002/1521-3978(200009)48:9/11¡771::AID-PROP771¿3.0.CO;2-E.

[11] H.-L. Huang, D. Wu, D. Fan, and X. Zhu, "Superconducting quantum computing: a review," *Science China Information Sciences*, vol. 63, p. 180501, Jul 2020. doi:10.1007/s11432-020-2881-9.

[12] I. Siddiqi, "Engineering high-coherence superconducting qubits," *Nature Reviews Materials*, vol. 6, pp. 875–891, Oct 2021. doi:10.1038/s41578-021-00370-4.

[13] M. Kjaergaard, M. E. Schwartz, J. Braumüller, P. Krantz, J. I.-J. Wang, S. Gustavsson, and W. D. Oliver, "Superconducting qubits: Current state of play," *Annual Review of Condensed Matter Physics*, vol. 11, no. 1, pp. 369–395, 2020. doi:10.1146/annurev-conmatphys-031119-050605.

[14] J. M. Pino, *et al.*, "Demonstration of the trapped-ion quantum CCD computer architecture," *Nature*, vol. 592, pp. 209–213, Apr 2021. doi:10.1038/s41586-021-03318-4.

[15] J. I. Cirac and P. Zoller, "Quantum computations with cold trapped ions," *Phys. Rev. Lett.*, vol. 74, pp. 4091–4094, May 1995. doi:10.1103/PhysRevLett.74.4091.

[16] C. D. Bruzewicz, J. Chiaverini, R. McConnell, and J. M. Sage, "Trapped-ion quantum computing: Progress and challenges," *Applied Physics Reviews*, vol. 6, no. 2, p. 021314, 2019. doi:10.1063/1.5088164.

[17] B. E. Kane, "A silicon-based nuclear spin quantum computer," *Nature*, vol. 393, pp. 133–137, May 1998. doi:10.1038/30156.

[18] M. H. Abobeih, J. Randall, C. E. Bradley, H. P. Bartling, M. A. Bakker, M. J. Degen, M. Markham, D. J. Twitchen, and T. H. Taminiau, "Atomic-scale imaging of a 27-nuclear-spin cluster using a quantum sensor," *Nature*, vol. 576, pp. 411–415, Dec 2019. doi:10.1038/s41586-019-1834-7.

[19] J. R. Weber, W. F. Koehl, J. B. Varley, A. Janotti, B. B. Buckley, C. G. Van de Walle, and D. D. Awschalom, "Quantum computing with defects," *Proceedings of the National Academy of Sciences*, vol. 107, no. 19, pp. 8513–8518, 2010. doi:10.1073/pnas.1003052107.

[20] J. R. Weber, W. F. Koehl, J. B. Varley, A. Janotti, B. B. Buckley, C. G. Van de Walle, and D. D. Awschalom, "Defects in SiC for quantum computing," *Journal of Applied Physics*, vol. 109, no. 10, p. 102417, 2011. doi:10.1063/1.3578264.

[21] D. Loss and D. P. DiVincenzo, "Quantum computation with quantum dots," *Physical Review A*, vol. 57, pp. 120–126, Jan. 1998. doi:10.1103/physreva.57.120.

[22] A. Zrenner, "A close look on single quantum dots," *The Journal of Chemical Physics*, vol. 112, no. 18, pp. 7790–7798, 2000. doi:10.1063/1.481384.

[23] J. Claudon, J. Bleuse, N. S. Malik, M. Bazin, P. Jaffrennou, N. Gregersen, C. Sauvan, P. Lalanne, and J.-M. Gérard, "A highly efficient single-photon source based on a quantum dot in a photonic nanowire," *Nature Photonics*, vol. 4, pp. 174–177, Mar 2010. doi:10.1038/nphoton.2009.287x.

[24] X. Ding, *et al.*, "On-demand single photons with high extraction efficiency and near-unity indistinguishability from a resonantly driven quantum dot in a micropillar," *Phys. Rev. Lett.*, vol. 116, p. 020401, Jan 2016. doi:10.1103/PhysRevLett.116.020401.

[25] O. Gazzano, S. Michaelis de Vasconcellos, C. Arnold, A. Nowak, E. Galopin, I. Sagnes, L. Lanco, A. Lemaître, and P. Senellart, "Bright solid-state sources of indistinguishable single photons," *Nature Communications*, vol. 4, p. 1425, Feb 2013. doi:10.1038/ncomms2434.

[26] R. J. Warburton and C. Schflein, "Optical emission from a chargetunable quantum ring," *Nature*, vol. 405, pp. 926–929, Jun 2000. doi:10.1038/35016030.

[27] A. V. Khaetskii, D. Loss, and L. Glazman, "Electron spin decoherence in quantum dots due to interaction with nuclei," *Phys. Rev. Lett.*, vol. 88, p. 186802, Apr 2002. doi:10.1103/PhysRevLett.88.186802.

[28] I. A. Merkulov, A. L. Efros, and M. Rosen, "Electron spin relaxation by nuclei in semiconductor quantum dots," *Phys. Rev. B*, vol. 65, p. 205309, Apr 2002. doi:10.1103/PhysRevB.65.205309.

[29] E. A. Chekhovich, S. F. C. da Silva, and A. Rastelli, "Nuclear spin quantum register in an optically active semiconductor quantum dot," *Nature Nanotechnology*, vol. 15, pp. 999–1004, Dec 2020. doi:10.1038/s41565-020-0769-3.

[30] G. Éthier-Majcher, D. Gangloff, R. Stockill, E. Clarke, M. Hugues, C. Le Gall, and M. Atatüre, "Improving a solid-state qubit through an engineered mesoscopic environment," *Phys. Rev. Lett.*, vol. 119, p. 130503, Sep 2017. doi:10.1103/PhysRevLett.119.130503.

[31] D. A. Gangloff, G. Éthier Majcher, C. Lang, E. V. Denning, J. H. Bodey, D. M. Jackson, E. Clarke, M. Hugues, C. L. Gall, and M. Atatüre, "Quantum interface of an electron and a nuclear ensemble," *Science*, vol. 364, no. 6435, pp. 62–66, 2019. doi:10.1126/science.aaw2906.

[32] M. Kroner, *et al.*, "Optical detection of single-electron spin resonance in a quantum dot," *Phys. Rev. Lett.*, vol. 100, p. 156803, Apr 2008. doi:10.1103/PhysRevLett.100.156803.

[33] E. Chekhovich, "Keyhole resonators for subwavelength focusing of microwave magnetic fields in optically detected electron spin resonance," *Phys. Rev. Applied*, vol. 15, p. 034082, Mar 2021. doi:10.1103/PhysRevApplied.15.034082.

[34] L. Esaki and R. Tsu, "Superlattice and negative differential conductivity in semiconductors," *IBM Journal of Research and Development*, vol. 14, no. 1, pp. 61–65, 1970. doi:10.1147/rd.141.0061.

[35] K. v. Klitzing, G. Dorda, and M. Pepper, "New method for high-accuracy determination of the fine-structure constant based on quantized hall resistance," *Physical Review Letters*, vol. 45, pp. 494–497, Aug. 1980. doi:10.1103/physrevlett.45.494.

[36] J. Faist, F. Capasso, D. L. Sivco, C. Sirtori, A. L. Hutchinson, and A. Y. Cho, "Quantum cascade laser," *Science*, vol. 264, pp. 553–556, Apr. 1994. doi:10.1126/science.264.5158.553.

[37] C. Kloeffel and D. Loss, "Prospects for spin-based quantum computing in quantum dots," *Annual Review of Condensed Matter Physics*, vol. 4, no. 1, pp. 51–81, 2013. doi:10.1146/annurev-conmatphys-030212-184248.

[38] L. Goldstein, F. Glas, J. Y. Marzin, M. N. Charasse, and G. Le Roux, "Growth by molecular beam epitaxy and characterization of InAs/GaAs strained-layer superlattices," *Applied Physics Letters*, vol. 47, no. 10, pp. 1099–1101, 1985. doi:10.1063/1.96342.

[39] O. Gywat, H. J. Krenner, and J. Berezovsky, *Spins in Optically Active Quantum Dots*. Wiley, 2009.

[40] K. Brunner, U. Bockelmann, G. Abstreiter, M. Walther, G. Böhm, G. Tränkle, and G. Weimann, "Photoluminescence from a single GaAs/AlGaAs quantum dot," *Phys. Rev. Lett.*, vol. 69, pp. 3216–3219, Nov 1992. doi:10.1103/PhysRevLett.69.3216.

[41] J. Y. Marzin, J. M. Gérard, A. Izraël, D. Barrier, and G. Bastard, "Photoluminescence of single InAs quantum dots obtained by self-organized growth on GaAs," *Phys. Rev. Lett.*, vol. 73, pp. 716–719, Aug 1994. doi:10.1103/PhysRevLett.73.716.

[42] F. C. Frank and J. H. van der Merwe, "One-dimensional dislocations. i. static theory," *Proceedings of the Royal Society of London. Series A. Mathematical and Physical Sciences*, vol. 198, pp. 205–216, Aug. 1949. doi:10.1098/rspa.1949.0095.

[43] M. Volmer and A. Z. Weber, "Nucleus formation in supersaturated systems," *Zeitschrift für Physikalische Chemie*, vol. 119, pp. 277–301, Aug. 1926.

[44] I. N. Stranski and L. Krastanow, "Zur theorie der orientierten ausschei- dung von ionenkristallen aufeinander," *Monatshefte für Chemie/ChemicalMonthly*, vol. 71, p. 351–364, 1937.

[45] P. Michler, *Single Semiconductor Quantum Dots (NanoScience and Technology)*. Springer, 2010.

[46] R. J. Warburton, "Single spins in self-assembled quantum dots," *Nature Materials*, vol. 12, pp. 483–493, Jun 2013. doi:10.1038/nmat3585.

[47] D. Leonard, M. Krishnamurthy, C. M. Reaves, S. P. Denbaars, and P. M. Petroff, "Direct formation of quantum-sized dots from uniform coherent islands of InGaAs on GaAs surfaces," *Applied Physics Letters*, vol. 63, pp. 3203–3205, Dec. 1993. doi:10.1063/1.110199.

[48] D. Leonard, K. Pond, and P. M. Petroff, "Critical layer thickness for self-assembled InAs islands on GaAs," *Physical Review B*, vol. 50, pp. 11687–11692, Oct. 1994. doi:10.1103/physrevb.50.11687.

[49] A. Rastelli, S. Ulrich, E.-M. Pavelescu, T. Leinonen, M. Pessa, P. Michler, and O. Schmidt, "Self-assembled quantum dots for single-dot optical investigations," *Superlattices and Microstructures*, vol. 36, pp. 181–191, July 2004. doi:10.1016/j.spmi.2004.08.024.

[50] Q. Q. Wang, A. Muller, P. Bianucci, E. Rossi, Q. K. Xue, T. Takagahara, C. Piermarocchi, A. H. MacDonald, and C. K. Shih, "Decoherence processes during optical manipulation of excitonic qubits in semiconductor quantum dots," *Phys. Rev. B*, vol. 72, p. 035306, Jul 2005. doi:10.1103/PhysRevB.72.035306.

[51] A. K. Rai, S. Gordon, A. Ludwig, A. D. Wieck, A. Zrenner, and D. Reuter, "Spatially indirect transitions in electric field tunable quantum dot diodes," *physica status solidi (b)*, vol. 253, no. 3, pp. 437–441, 2016. doi:https://doi.org/10.1002/pssb.201552591.

[52] M. C. Löbl, S. Scholz, I. Söllner, J. Ritzmann, T. Denneulin, A. Kovács, B. E. Kardynał, A. D. Wieck, A. Ludwig, and R. J. Warburton, "Excitons in InGaAs quantum dots without electron wetting layer states," *Communications Physics*, vol. 2, p. 93, Aug 2019. doi:10.1038/s42005-019-0194-9.

[53] P. B. Joyce, T. J. Krzyzewski, G. R. Bell, B. A. Joyce, and T. S. Jones, "Composition of InAs quantum dots on GaAs(001): Direct evidence for (In,Ga)As alloying," *Phys. Rev. B*, vol. 58, pp. R15981–R15984, Dec 1998. doi:10.1103/PhysRevB.58.R15981.

[54] R. Songmuang, S. Kiravittaya, and O. Schmidt, "Shape evolution of InAs quantum dots during overgrowth," *Journal of Crystal Growth*, vol. 249, no. 3, pp. 416–421, 2003. doi:https://doi.org/10.1016/S0022-0248(02)02222-4.

[55] G. Costantini, A. Rastelli, C. Manzano, P. Acosta-Diaz, R. Songmuang, G. Katsaros, O. G. Schmidt, and K. Kern, "Interplay between thermodynamics and kinetics in the capping of InAs/GaAs(001) quantum dots," *Phys. Rev. Lett.*, vol. 96, p. 226106, Jun 2006. doi:10.1103/PhysRevLett.96.226106.

[56] A. Badolato, K. Hennessy, M. Atatüre, J. Dreiser, E. Hu, P. M. Petroff, and A. Imamoğlu, "Deterministic coupling of single quantum dots to single nanocavity modes," *Science*, vol. 308, no. 5725, pp. 1158–1161, 2005. doi:10.1126/science.1109815.

[57] P. Senellart, G. Solomon, and A. White, "High-performance semiconductor quantum-dot single-photon sources," *Nature Nanotechnology*, vol. 12, pp. 1026–1039, Nov. 2017. doi:10.1038/nnano.2017.218.

[58] C. Schneider, *et al.*, "Single site-controlled In(Ga)As/GaAs quantum dots: growth, properties and device integration," *Nanotechnology*, vol. 20, p. 434012, oct 2009. doi:10.1088/0957-4484/20/43/434012.

[59] J. Große, M. von Helversen, A. Koulas-Simos, M. Hermann, and S. Reitzenstein, "Development of site-controlled quantum dot arrays acting as scalable sources

of indistinguishable photons," *APL Photonics*, vol. 5, no. 9, p. 096107, 2020. doi:10.1063/5.0013718.

[60] A. V. Kuhlmann, J. H. Prechtel, J. Houel, A. Ludwig, D. Reuter, A. D. Wieck, and R. J. Warburton, "Transform-limited single photons from a single quantum dot," *Nature Communications*, vol. 6, p. 8204, Sep 2015. doi:10.1038/ncomms9204.

[61] M. C. Löbl, *et al.*, "Narrow optical linewidths and spin pumping on charge-tunable close-to-surface self-assembled quantum dots in an ultrathin diode," *Phys. Rev. B*, vol. 96, p. 165440, Oct 2017. doi:10.1103/PhysRevB.96.165440.

[62] C. Kittel, *Introduction to Solid State Physics, 8th Edition*. Wiley, 2007.

[63] I. Vurgaftman, J. R. Meyer, and L. R. Ram-Mohan, "Band parameters for iii–v compound semiconductors and their alloys," *Journal of Applied Physics*, vol. 89, no. 11, pp. 5815–5875, 2001. doi:10.1063/1.1368156.

[64] P. W. Fry, *et al.*, "Photocurrent spectroscopy of InAs/GaAs self-assembled quantum dots," *Phys. Rev. B*, vol. 62, pp. 16784–16791, Dec 2000. doi:10.1103/PhysRevB.62.16784.

[65] J. Berezovsky, O. Gywat, F. Meier, D. Battaglia, X. Peng, and D. D. Awschalom, "Initialization and read-out of spins in coupled core–shell quantum dots," *Nature Physics*, vol. 2, pp. 831–834, Nov. 2006. doi:10.1038/nphys458.

[66] A. Wojs, P. Hawrylak, S. Fafard, and L. Jacak, "Electronic structure and magneto-optics of self-assembled quantum dots," *Phys. Rev. B*, vol. 54, pp. 5604–5608, Aug 1996. doi:10.1103/PhysRevB.54.5604.

[67] J. J. Finley, *et al.*, "Observation of multicharged excitons and biexcitons in a single InGaAs quantum dot," *Phys. Rev. B*, vol. 63, p. 161305, Apr 2001. doi:10.1103/PhysRevB.63.161305.

[68] W. Porod and D. K. Ferry, "Modification of the virtual-crystal approximation for ternary III-V compounds," *Phys. Rev. B*, vol. 27, pp. 2587–2589, Feb 1983. doi:10.1103/PhysRevB.27.2587.

[69] E. A. Chekhovich, K. V. Kavokin, J. Puebla, A. B. Krysa, M. Hopkinson, A. D. Andreev, A. M. Sanchez, R. Beanland, M. S. Skolnick, and A. I. Tartakovskii, "Structural analysis of strained quantum dots using nuclear magnetic resonance," *Nature Nanotechnology*, vol. 7, pp. 646–650, Aug. 2012. doi:10.1038/nnano.2012.142.

[70] C. P. Kuo, S. K. Vong, R. M. Cohen, and G. B. Stringfellow, "Effect of mismatch strain on band gap in III-V semiconductors," *Journal of Applied Physics*, vol. 57, no. 12, pp. 5428–5432, 1985. doi:10.1063/1.334817.

[71] S. Paul, J. B. Roy, and P. K. Basu, "Empirical expressions for the alloy composition and temperature dependence of the band gap and intrinsic carrier density in $Ga_xIn_{1x}As$," *Journal of Applied Physics*, vol. 69, no. 2, pp. 827–829, 1991. doi:10.1063/1.348919.

[72] M. Bayer, O. Stern, P. Hawrylak, S. Fafard, and A. Forchel, "Hidden symmetries in the energy levels of excitonic 'artificial atoms'," *Nature*, vol. 405, pp. 923–926, June 2000. doi:10.1038/35016020.

[73] O. Krebs and P. Voisin, "Giant optical anisotropy of semiconductor heterostructures with no common atom and the quantum-confined pockels effect," *Physical Review Letters*, vol. 77, pp. 1829–1832, Aug. 1996. doi:10.1103/physrevlett.77.1829.

[74] D. N. Krizhanovskii, A. Ebbens, A. I. Tartakovskii, F. Pulizzi, T. Wright, M. S. Skolnick, and M. Hopkinson, "Individual neutral and charged $In_xGa_{1-x}As-GaAs$ quantum dots with strong in-plane optical anisotropy," *Phys. Rev. B*, vol. 72, p. 161312, Oct 2005. doi:10.1103/PhysRevB.72.161312.

[75] T. Belhadj, *et al.*, "Impact of heavy hole-light hole coupling on optical selection rules in GaAs quantum dots," *Applied Physics Letters*, vol. 97, p. 051111, Aug. 2010. doi:10.1063/1.3473824.

[76] B. Miller, W. Hansen, S. Manus, R. Luyken, A. Lorke, J. Kotthaus, and S. Huant, "Few-electron ground states of charge-tunable self-assembled quantum dots," *Physical Review B - Condensed Matter and Materials Physics*, vol. 56, no. 11, pp. 6764–6769, 1997. doi:10.1103/PhysRevB.56.6764.

[77] R. J. Warburton, B. T. Miller, C. S. Dürr, C. Bödefeld, K. Karrai, J. P. Kotthaus, G. Medeiros-Ribeiro, P. M. Petroff, and S. Huant, "Coulomb interactions in small charge-tunable quantum dots: A simple model," *Physical Review B*, vol. 58, pp. 16221–16231, Dec. 1998. doi:10.1103/physrevb.58.16221.

[78] A. V. Kuhlmann, J. Houel, D. Brunner, A. Ludwig, D. Reuter, A. D. Wieck, and R. J. Warburton, "A dark-field microscope for background-free detection of resonance fluorescence from single semiconductor quantum dots operating in a set-and-forget mode," *Review of Scientific Instruments*, vol. 84, no. 7, p. 073905, 2013. doi:10.1063/1.4813879.

[79] C. Santori, D. Fattal, J. Vuckovic, G. S. Solomon, and Y. Yamamoto, "Single-photon generation with InAs quantum dots," *New Journal of Physics*, vol. 6, pp. 89–89, July 2004. doi:10.1088/1367-2630/6/1/089.

[80] A. Kiraz, M. Atatüre, and A. Imamoğlu, "Quantum-dot single-photon sources: Prospects for applications in linear optics quantum-information processing," *Phys. Rev. A*, vol. 69, p. 032305, Mar 2004. doi:10.1103/PhysRevA.69.032305.

[81] J. J. Finley, A. D. Ashmore, A. Lemaître, D. J. Mowbray, M. S. Skolnick, I. E. Itskevich, P. A. Maksym, M. Hopkinson, and T. F. Krauss, "Charged and neutral exciton complexes in individual self-assembled In(Ga)As quantum dots," *Phys. Rev. B*, vol. 63, p. 073307, Jan 2001. doi:10.1103/PhysRevB.63.073307.

[82] M. Ediger, G. Bester, A. Badolato, P. M. Petroff, K. Karrai, A. Zunger, and R. J. Warburton, "Peculiar many-body effects revealed in the spectroscopy of highly charged quantum dots," *Nature Physics*, vol. 3, pp. 774–779, Oct. 2007. doi:10.1038/nphys748.

[83] N. A. J. M. Kleemans, J. van Bree, A. O. Govorov, J. G. Keizer, G. J. Hamhuis, R. Nötzel, A. Y. Silov, and P. M. Koenraad, "Many-body exciton states in self-assembled quantum dots coupled to a Fermi sea," *Nature Physics*, vol. 6, pp. 534–538, May 2010. doi:10.1038/nphys1673.

[84] P. A. Labud, A. Ludwig, A. D. Wieck, G. Bester, and D. Reuter, "Direct quantitative electrical measurement of many-body interactions in exciton complexes in InAs quantum dots," *Phys. Rev. Lett.*, vol. 112, p. 046803, Jan 2014. doi:10.1103/PhysRevLett.112.046803.

[85] P. A. Dalgarno, J. M. Smith, J. McFarlane, B. D. Gerardot, K. Karrai, A. Badolato, P. M. Petroff, and R. J. Warburton, "Coulomb interactions in single charged self-assembled quantum dots: Radiative lifetime and recombination energy," *Phys. Rev. B*, vol. 77, p. 245311, Jun 2008. doi:10.1103/PhysRevB.77.245311.

[86] M. Bayer, *et al.*, "Fine structure of neutral and charged excitons in self-assembled In(Ga)As(Al)GaAs quantum dots," *Phys. Rev. B*, vol. 65, p. 195315, May 2002. doi:10.1103/PhysRevB.65.195315.

[87] M. Zieliński, "Fine structure of dark and bright excitons in vertical electric fields: Atomistic theory of alloyed self-assembled InGaAs quantum dots," *Physical Review B*, vol. 102, p. 245423, Dec. 2020. doi:10.1103/physrevb.102.245423.

[88] H. W. van Kesteren, E. C. Cosman, W. A. J. A. van der Poel, and C. T. Foxon, "Fine structure of excitons in type-II GaAs\AlAs quantum wells," *Phys. Rev. B*, vol. 41, pp. 5283–5292, Mar 1990. doi:10.1103/PhysRevB.41.5283.

[89] J. Puebla, E. A. Chekhovich, M. Hopkinson, P. Senellart, A. Lemaitre, M. S. Skolnick, and A. I. Tartakovskii, "Dynamic nuclear polarization in InGaAs/GaAs and GaAs/AlGaAs quantum dots under nonresonant ultralow-power optical excitation," *Phys. Rev. B*, vol. 88, p. 045306, Jul 2013. doi:10.1103/PhysRevB.88.045306.

[90] A. S. Bracker, D. Gammon, and V. L. Korenev, "Fine structure and optical pumping of spins in individual semiconductor quantum dots," *Semiconductor Science and Technology*, vol. 23, no. 11, 2008. doi:10.1088/0268-1242/23/11/114004.

[91] H. Drexler, D. Leonard, W. Hansen, J. P. Kotthaus, and P. M. Petroff, "Spectroscopy of quantum levels in charge-tunable InGaAs quantum dots," *Phys. Rev. Lett.*, vol. 73, pp. 2252–2255, Oct 1994. doi:10.1103/PhysRevLett.73.2252.

[92] J. Kim, O. Benson, H. Kan, and Y. Yamamoto, "A single-photon turnstile device," *Nature*, vol. 397, pp. 500–503, Feb. 1999. doi:10.1038/17295.

[93] M. Ghali, K. Ohtani, Y. Ohno, and H. Ohno, "Generation and control of polarization-entangled photons from GaAs island quantum dots by an electric field," *Nature Communications*, vol. 3, p. 661, Feb 2012. doi:10.1038/ncomms1657.

[94] D. A. B. Miller, D. S. Chemla, T. C. Damen, A. C. Gossard, W. Wiegmann, T. H. Wood, and C. A. Burrus, "Band-edge electroabsorption in quantum well structures: The Quantum-Confined Stark Effect," *Phys. Rev. Lett.*, vol. 53, pp. 2173–2176, Nov 1984. doi:10.1103/PhysRevLett.53.2173.

[95] A. Mysyrowicz, D. Hulin, A. Antonetti, A. Migus, W. T. Masselink, and H. Morkoç, ""Dressed excitons" in a multiple-quantum-well structure: Evidence for an optical Stark effect with femtosecond response time," *Physical Review Letters*, vol. 56, no. 25, pp. 2748–2751, 1986. doi:10.1103/PhysRevLett.56.2748.

[96] P. W. Fry, *et al.*, "Inverted electron-hole alignment in InAs-GaAs self-assembled quantum dots," *Phys. Rev. Lett.*, vol. 84, pp. 733–736, Jan 2000. doi:10.1103/PhysRevLett.84.733.

[97] F. Findeis, M. Baier, E. Beham, A. Zrenner, and G. Abstreiter, "Photocurrent and photoluminescence of a single self-assembled quantum dot in electric fields," *Applied Physics Letters*, vol. 78, pp. 2958–2960, May 2001. doi:10.1063/1.1369148.

[98] R. B. Patel, A. J. Bennett, I. Farrer, C. A. Nicoll, D. A. Ritchie, and A. J. Shields, "Two-photon interference of the emission from electrically tunable remote quantum dots," *Nature Photonics*, vol. 4, pp. 632–635, July 2010. doi:10.1038/nphoton.2010.161.

[99] A. Laucht, F. Hofbauer, N. Hauke, J. Angele, S. Stobbe, M. Kaniber, G. Böhm, P. Lodahl, M.-C. Amann, and J. J. Finley, "Electrical control of spontaneous emission and strong coupling for a single quantum dot," *New Journal of Physics*, vol. 11, p. 023034, Feb. 2009. doi:10.1088/1367-2630/11/2/023034.

[100] E. Blackwood, M. J. Snelling, R. T. Harley, S. R. Andrews, and C. T. B. Foxon, "Exchange interaction of excitons in GaAs heterostructures," *Phys. Rev. B*, vol. 50, pp. 14246–14254, Nov 1994. doi:10.1103/PhysRevB.50.14246.

[101] P.-F. Braun, *et al.*, "Direct observation of the electron spin relaxation induced by nuclei in quantum dots," *Phys. Rev. Lett.*, vol. 94, p. 116601, Mar 2005. doi:10.1103/PhysRevLett.94.116601.

[102] Y. G. Semenov and K. W. Kim, "Effect of an external magnetic field on electron-spin dephasing induced by hyperfine interaction in quantum dots," *Phys. Rev. B*, vol. 67, p. 073301, Feb 2003. doi:10.1103/PhysRevB.67.073301.

[103] B. D. Gerardot, D. Brunner, P. A. Dalgarno, P. Öhberg, S. Seidl, M. Kroner, K. Karrai, N. G. Stoltz, P. M. Petroff, and R. J. Warburton, "Optical pumping of a single hole spin in a quantum dot," *Nature*, vol. 451, no. 7177, pp. 441–444, 2008. doi:10.1038/nature06472.

[104] B. Urbaszek, X. Marie, T. Amand, O. Krebs, P. Voisin, P. Maletinsky, A. Högele, and A. Imamoglu, "Nuclear spin physics in quantum dots an optical investigation," *Rev. Mod. Phys.*, vol. 85, pp. 79–133, Jan 2013. doi:10.1103/RevModPhys.85.79.

[105] T. M. Godden, S. J. Boyle, A. J. Ramsay, A. M. Fox, and M. S. Skolnick, "Fast high fidelity hole spin initialization in a single InGaAs quantum dot," *Applied Physics Letters*, vol. 97, p. 061113, Aug. 2010. doi:10.1063/1.3476353.

[106] T. M. Godden, J. H. Quilter, A. J. Ramsay, Y. Wu, P. Brereton, I. J. Luxmoore, J. Puebla, A. M. Fox, and M. S. Skolnick, "Fast preparation of a single-hole spin in an InAs/GaAs quantum dot in a Voigt-geometry magnetic field," *Phys. Rev. B*, vol. 85, p. 155310, Apr 2012. doi:10.1103/PhysRevB.85.155310.

[107] C. Testelin, F. Bernardot, B. Eble, and M. Chamarro, "Hole–spin dephasing time associated with hyperfine interaction in quantum dots," *Phys. Rev. B*, vol. 79, p. 195440, May 2009. doi:10.1103/PhysRevB.79.195440.

[108] E. A. Chekhovich, M. M. Glazov, A. B. Krysa, M. Hopkinson, P. Senellart, A. Lemaître, M. S. Skolnick, and A. I. Tartakovskii, "Element-sensitive measurement of the hole–nuclear spin interaction in quantum dots," *Nature Physics*, vol. 9, pp. 74–78, Feb 2013. doi:10.1038/nphys2514.

[109] J. Fischer, W. A. Coish, D. V. Bulaev, and D. Loss, "Spin decoherence of a heavy hole coupled to nuclear spins in a quantum dot," *Phys. Rev. B*, vol. 78, p. 155329, Oct 2008. doi:10.1103/PhysRevB.78.155329.

[110] D. Paget, "Optical detection of NMR in high-purity GaAs: Direct study of the relaxation of nuclei close to shallow donors," *Phys. Rev. B*, vol. 25, pp. 4444–4451, Apr 1982. doi:10.1103/PhysRevB.25.4444.

[111] A. Abragam, *Principles of Nuclear Magnetism*. Oxford Science Publications, 1961.

[112] E. Chekhovich, M. Hopkinson, M. Skolnick, and A. Tartakovskii, "Suppression of nuclear spin bath fluctuations in self-assembled quantum dots induced by inhomogeneous strain," *Nature Communications*, vol. 6, Feb. 2015. doi:10.1038/ncomms7348.

[113] C. P. Slichter, *Principles of Magnetic Resonance*. Springer Berlin Heidelberg, 1990.

[114] A. M. Waeber, G. Gillard, G. Ragunathan, M. Hopkinson, P. Spencer, D. A. Ritchie, M. S. Skolnick, and E. A. Chekhovich, "Pulse control protocols for preserving coherence in dipolar-coupled nuclear spin baths," *Nature Communications*, vol. 10, July 2019. doi:10.1038/s41467-019-11160-6.

[115] P. Maletinsky, M. Kroner, and A. Imamoglu, "Breakdown of the nuclear spin temperature approach in quantum-dot demagnetization experiments," *Nature Physics*, vol. 5, pp. 407–411, May 2009. doi:10.1038/nphys1273.

[116] E. A. Chekhovich, I. M. Griffiths, M. S. Skolnick, H. Huang, S. F. C. da Silva, X. Yuan, and A. Rastelli, "Cross calibration of deformation potentials and gradient-elastic tensors of GaAs using photoluminescence and nuclear magnetic resonance spectroscopy in GaAs/AlGaAs quantum dot structures," *Phys. Rev. B*, vol. 97, p. 235311, Jun 2018. doi:10.1103/PhysRevB.97.235311.

[117] N. Stone, "Table of nuclear electric quadrupole moments," *Atomic Data and Nuclear Data Tables*, vol. 111-112, pp. 1–28, 2016. doi:https://doi.org/10.1016/j.adt.2015.12.002.

[118] C. Latta, *et al.*, "Confluence of resonant laser excitation and bidirectional quantum-dot nuclear-spin polarization," *Nature Physics*, vol. 5, pp. 758–763, Aug. 2009. doi:10.1038/nphys1363.

[119] W. A. Coish and D. Loss, "Hyperfine interaction in a quantum dot: Non-Markovian electron spin dynamics," *Phys. Rev. B*, vol. 70, p. 195340, Nov 2004. doi:10.1103/PhysRevB.70.195340.

[120] V. Cerletti, O. Gywat, and D. Loss, "Entanglement transfer from electron spins to photons in spin light-emitting diodes containing quantum dots," *Phys. Rev. B*, vol. 72, p. 115316, Sep 2005. doi:10.1103/PhysRevB.72.115316.

[121] D. Gammon, A. L. Efros, T. A. Kennedy, M. Rosen, D. S. Katzer, D. Park, S. W. Brown, V. L. Korenev, and I. A. Merkulov, "Electron and nuclear spin interactions in the optical spectra of single GaAs quantum dots," *Phys. Rev. Lett.*, vol. 86, pp. 5176–5179, May 2001. doi:10.1103/PhysRevLett.86.5176.

[122] S. Brown, T. Kennedy, and D. Gammon, "Optical NMR from single quantum dots," *Solid State Nuclear Magnetic Resonance*, vol. 11, no. 1, pp. 49–58, 1998. doi:https://doi.org/10.1016/S0926-2040(97)00095-7.

[123] E. A. Chekhovich, A. B. Krysa, M. S. Skolnick, and A. I. Tartakovskii, "Direct measurement of the hole-nuclear spin interaction in single InP/GaInP quantum dots using photoluminescence spectroscopy," *Phys. Rev. Lett.*, vol. 106, p. 027402, Jan 2011. doi:10.1103/PhysRevLett.106.027402.

[124] W. A. Coish and J. Baugh, "Nuclear spins in nanostructures," *physica status solidi (b)*, vol. 246, no. 10, pp. 2203–2215, 2009. doi:https://doi.org/10.1002/pssb.200945229.

[125] B. Eble, C. Testelin, P. Desfonds, F. Bernardot, A. Balocchi, T. Amand, A. Miard, A. Lemaître, X. Marie, and M. Chamarro, "Hole–nuclear spin interaction in quantum dots," *Phys. Rev. Lett.*, vol. 102, p. 146601, Apr 2009. doi:10.1103/PhysRevLett.102.146601.

[126] M. Atature, "Quantum-dot spin-state preparation with near-unity fidelity," *Science*, vol. 312, pp. 551–553, Apr. 2006. doi:10.1126/science.1126074.

[127] J. Dreiser, M. Atatüre, C. Galland, T. Müller, A. Badolato, and A. Imamoglu, "Optical investigations of quantum dot spin dynamics as a function of external electric and magnetic fields," *Physical Review B*, vol. 77, Feb. 2008. doi:10.1103/physrevb.77.075317.

[128] E. A. Chekhovich, M. N. Makhonin, J. Skiba-Szymanska, A. B. Krysa, V. D. Kulakovskii, M. S. Skolnick, and A. I. Tartakovskii, "Dynamics of optically induced nuclear spin polarization in individual InP/$Ga_xIn_{1-x}P$ quantum dots," *Phys. Rev. B*, vol. 81, p. 245308, Jun 2010. doi:10.1103/PhysRevB.81.245308.

[129] A. Bracker, *et al.*, "Optical pumping of the electronic and nuclear spin of single charge-tunable quantum dots," *Physical Review Letters*, vol. 94, Feb. 2005. doi:10.1103/physrevlett.94.047402.

[130] B. Urbaszek, P.-F. Braun, T. Amand, O. Krebs, T. Belhadj, A. Lemaítre, P. Voisin, and X. Marie, "Efficient dynamical nuclear polarization in quantum dots: Temperature dependence," *Phys. Rev. B*, vol. 76, p. 201301, Nov 2007. doi:10.1103/PhysRevB.76.201301.

[131] E. A. Chekhovich, A. Ulhaq, E. Zallo, F. Ding, O. G. Schmidt, and M. S. Skolnick, "Measurement of the spin temperature of optically cooled nuclei and GaAs hyperfine constants in GaAs/AlGaAs quantum dots," *Nature Materials*, vol. 16, pp. 982–986, Oct 2017. doi:10.1038/nmat4959.

[132] C. Kloeffel, P. A. Dalgarno, B. Urbaszek, B. D. Gerardot, D. Brunner, P. M. Petroff, D. Loss, and R. J. Warburton, "Controlling the interaction of electron and nuclear spins in a tunnel-coupled quantum dot," *Phys. Rev. Lett.*, vol. 106, p. 046802, Jan 2011. doi:10.1103/PhysRevLett.106.046802.

[133] F. Bloch, W. W. Hansen, and M. Packard, "Nuclear induction," *Phys. Rev.*, vol. 69, pp. 127–127, Feb 1946. doi:10.1103/PhysRev.69.127.

[134] D. Gammon, S. W. Brown, E. S. Snow, T. A. Kennedy, D. S. Katzer, and D. Park, "Nuclear spectroscopy in single quantum dots: Nanoscopic raman scattering and nuclear magnetic resonance," *Science*, vol. 277, pp. 85–88, July 1997. doi:10.1126/science.277.5322.85.

[135] K. Flisinski, I. Y. Gerlovin, I. V. Ignatiev, M. Y. Petrov, S. Y. Verbin, D. R. Yakovlev, D. Reuter, A. D. Wieck, and M. Bayer, "Optically detected magnetic resonance at the quadrupole-split nuclear states in (In, Ga)As/GaAs quantum dots," *Physical Review B*, vol. 82, Aug. 2010. doi:10.1103/physrevb.82.081308.

[136] G. Wüst, M. Munsch, F. Maier, A. V. Kuhlmann, A. Ludwig, A. D. Wieck, D. Loss, M. Poggio, and R. J. Warburton, "Role of the electron spin in determining the coherence of the nuclear spins in a quantum dot," *Nature Nanotechnology*, vol. 11, pp. 885–889, July 2016. doi:10.1038/nnano.2016.114.

[137] M. Bayer, A. Kuther, A. Forchel, A. Gorbunov, V. B. Timofeev, F. Schäfer, J. P. Reithmaier, T. L. Reinecke, and S. N. Walck, "Electron and hole g factors and exchange interaction from studies of the exciton fine structure in $In_{0.60}Ga_{0.40}As$ quantum dots," *Phys. Rev. Lett.*, vol. 82, pp. 1748–1751, Feb 1999. doi:10.1103/PhysRevLett.82.1748.

[138] A. Schwan, B.-M. Meiners, A. B. Henriques, A. D. B. Maia, A. A. Quivy, S. Spatzek, S. Varwig, D. R. Yakovlev, and M. Bayer, "Dispersion of electron g-factor with optical transition energy in (In,Ga)As/GaAs self-assembled quantum dots," *Applied Physics Letters*, vol. 98, no. 23, p. 233102, 2011. doi:10.1063/1.3588413.

[139] P. Maletinsky, M. Kroner, and A. Imamoglu, "Breakdown of the nuclear spin temperature approach in quantum dot demagnetization experiments," *Nature Physics*, vol. 5, pp. 407–411, May 2009. doi:10.1038/nphys1273.

[140] C. Latta, A. Srivastava, and A. Imamoğlu, "Hyperfine interaction-dominated dynamics of nuclear spins in self-assembled InGaAs quantum dots," *Phys. Rev. Lett.*, vol. 107, p. 167401, Oct 2011. doi:10.1103/PhysRevLett.107.167401.

[141] A. Greilich, A. Shabaev, D. R. Yakovlev, A. L. Efros, I. A. Yugova, D. Reuter, A. D. Wieck, and M. Bayer, "Nuclei-induced frequency focusing of electron spin coherence," *Science*, vol. 317, pp. 1896–1899, Sept. 2007. doi:10.1126/science.1146850.

[142] M. N. Makhonin, *et al.*, "Long nuclear spin polarization decay times controlled by optical pumping in individual quantum dots," *Phys. Rev. B*, vol. 77, p. 125307, Mar 2008. doi:10.1103/PhysRevB.77.125307.

[143] A. V. Khaetskii and Y. V. Nazarov, "Spin-flip transitions between Zeeman sublevels in semiconductor quantum dots," *Physical Review B*, vol. 64, no. January, p. 125316, 2000. doi:10.1177/0022034510389179.

[144] C.-Y. Lu, Y. Zhao, A. N. Vamivakas, C. Matthiesen, S. Fält, A. Badolato, and M. Atatüre, "Direct measurement of spin dynamics in InAs/GaAs quantum dots using time-resolved resonance fluorescence," *Phys. Rev. B*, vol. 81, p. 035332, Jan 2010. doi:10.1103/PhysRevB.81.035332.

[145] J. M. Smith, P. A. Dalgarno, R. J. Warburton, A. O. Govorov, K. Karrai, B. D. Gerardot, and P. M. Petroff, "Voltage control of the spin dynamics of an exciton in a semiconductor quantum dot," *Phys. Rev. Lett.*, vol. 94, p. 197402, May 2005. doi:10.1103/PhysRevLett.94.197402.

[146] D. Press, K. D. Greve, P. L. McMahon, T. D. Ladd, B. Friess, C. Schneider, M. Kamp, S. Höfling, A. Forchel, and Y. Yamamoto, "Ultrafast optical spin echo in a single quantum dot," *Nature Photonics*, vol. 4, pp. 367–370, Apr. 2010. doi:10.1038/nphoton.2010.83.

[147] E. L. Hahn, "Spin echoes," *Phys. Rev.*, vol. 80, pp. 580–594, Nov 1950. doi:10.1103/PhysRev.80.580.

[148] A. Muller, E. B. Flagg, P. Bianucci, X. Y. Wang, D. G. Deppe, W. Ma, J. Zhang, G. J. Salamo, M. Xiao, and C. K. Shih, "Resonance fluorescence from a coherently driven semiconductor quantum dot in a cavity," *Phys. Rev. Lett.*, vol. 99, p. 187402, Nov 2007. doi:10.1103/PhysRevLett.99.187402.

[149] W. Yang and L. J. Sham, "Collective nuclear stabilization in single quantum dots by noncollinear hyperfine interaction," *Phys. Rev. B*, vol. 85, p. 235319, Jun 2012. doi:10.1103/PhysRevB.85.235319.

[150] A. Högele, M. Kroner, C. Latta, M. Claassen, I. Carusotto, C. Bulutay, and A. Imamoglu, "Dynamic nuclear spin polarization in the resonant laser excitation of an InGaAs quantum dot," *Phys. Rev. Lett.*, vol. 108, p. 197403, May 2012. doi:10.1103/PhysRevLett.108.197403.

[151] D. Gammon, A. L. Efros, T. A. Kennedy, M. Rosen, D. S. Katzer, D. Park, S. W. Brown, V. L. Korenev, and I. A. Merkulov, "Electron and nuclear spin interactions in the optical spectra of single gaas quantum dots," *Phys. Rev. Lett.*, vol. 86, pp. 5176–5179, May 2001. doi:10.1103/PhysRevLett.86.5176.

[152] D. Pozar, *Microwave Engineering*. Wiley, 2011.

[153] A. M. Waeber, *et al.*, "Few-second-long correlation times in a quantum dot nuclear spin bath probed by frequency-comb nuclear magnetic resonance spectroscopy," *Nature Physics*, vol. 12, pp. 688–693, Mar. 2016. doi:10.1038/nphys3686.

[154] G. D. Fuchs, V. V. Dobrovitski, D. M. Toyli, F. J. Heremans, and D. D. Awschalom, "Gigahertz dynamics of a strongly driven single quantum spin," *Science*, vol. 326, no. 5959, pp. 1520–1522, 2009. doi:10.1126/science.1181193.

[155] M. W. Doherty, N. B. Manson, P. Delaney, F. Jelezko, J. Wrachtrup, and L. C. Hollenberg, "The nitrogen-vacancy colour centre in diamond," *Physics Reports*, vol. 528, no. 1, pp. 1–45, 2013. doi:https://doi.org/10.1016/j.physrep.2013.02.001. The nitrogen-vacancy colour centre in diamond.

[156] S. Pezzagna and J. Meijer, "Quantum computer based on color centers in diamond," *Applied Physics Reviews*, vol. 8, no. 1, p. 011308, 2021. doi:10.1063/5.0007444.

[157] W. Froncisz and J. S. Hyde, "The loop-gap resonator: a new microwave lumped circuit ESR sample structure," *Journal of Magnetic Resonance (1969)*, vol. 47, no. 3, pp. 515–521, 1982. doi:https://doi.org/10.1016/0022-2364(82)90221-9.

[158] W. N. Hardy and L. A. Whitehead, "Split-ring resonator for use in magnetic resonance from 200–2000 MHz," *Review of Scientific Instruments*, vol. 52, no. 2, pp. 213–216, 1981. doi:10.1063/1.1136574.

[159] W. B. Mims, "Electron echo methods in spin resonance spectrometry," *Review of Scientific Instruments*, vol. 36, no. 10, pp. 1472–1479, 1965. doi:10.1063/1.1719359.

[160] G. A. Rinard and G. R. Eaton, *Loop-Gap Resonators*, pp. 19–52. Boston, MA: Springer US, 2005.

[161] Y. Twig, E. Suhovoy, and A. Blank, "Sensitive surface loop-gap microresonators for electron spin resonance," *Review of Scientific Instruments*, vol. 81, no. 10, p. 104703, 2010. doi:10.1063/1.3488365.

[162] Y. Twig, E. Dikarov, and A. Blank, "Ultra miniature resonators for electron spin resonance: Sensitivity analysis, design and construction methods, and potential applications," *Molecular Physics*, vol. 111, no. 18-19, pp. 2674–2682, 2013. doi:10.1080/00268976.2012.762463.

[163] Y. Twig, A. Sorkin, D. Cristea, A. Feintuch, and A. Blank, "Surface loop-gap resonators for electron spin resonance at W-band," *Review of Scientific Instruments*, vol. 88, no. 12, p. 123901, 2017. doi:10.1063/1.5000946.

[164] R. Narkowicz, D. Suter, and I. Niemeyer, "Scaling of sensitivity and efficiency in planar microresonators for electron spin resonance," *Review of Scientific Instruments*, vol. 79, no. 8, p. 084702, 2008. doi:10.1063/1.2964926.

[165] J. Meijer, B. Burchard, M. Domhan, C. Wittmann, T. Gaebel, I. Popa, F. Jelezko, and J. Wrachtrup, "Generation of single color centers by focused nitrogen implantation," *Applied Physics Letters*, vol. 87, no. 26, p. 261909, 2005. doi:10.1063/1.2103389.

[166] J. H. N. Loubser and J. A. v. Wyk, "Electron spin resonance in the study of diamond," *Reports on Progress in Physics*, vol. 41, pp. 1201–1248, Aug 1978. doi:10.1088/0034-4885/41/8/002.

[167] M. S. Barson, E. Krausz, N. B. Manson, and M. W. Doherty, "The fine structure of the neutral nitrogen-vacancy center in diamond," *Nanophotonics*, vol. 8, no. 11, pp. 1985–1991, 2019. doi:doi:10.1515/nanoph-2019-0142.

[168] L. M. Pham, N. Bar-Gill, D. Le Sage, C. Belthangady, A. Stacey, M. Markham, D. J. Twitchen, M. D. Lukin, and R. L. Walsworth, "Enhanced metrology using preferential orientation of nitrogen-vacancy centers in diamond," *Phys. Rev. B*, vol. 86, p. 121202, Sep 2012. doi:10.1103/PhysRevB.86.121202.

[169] J. Michl, *et al.*, "Perfect alignment and preferential orientation of nitrogen-vacancy centers during chemical vapor deposition diamond growth on (111) surfaces," *Applied Physics Letters*, vol. 104, no. 10, p. 102407, 2014. doi:10.1063/1.4868128.

[170] T. Fukui, *et al.*, "Perfect selective alignment of nitrogen-vacancy centers in diamond," *Applied Physics Express*, vol. 7, p. 055201, Apr 2014. doi:10.7567/apex.7.055201.

[171] N. B. Manson, M. Hedges, M. S. J. Barson, R. Ahlefeldt, M. W. Doherty, H. Abe, T. Ohshima, and M. J. Sellars, "NV^--N^+ pair centre in 1b diamond," *New Journal of Physics*, vol. 20, p. 113037, nov 2018. doi:10.1088/1367-2630/aaec58.

[172] A. Gruber, A. Dräbenstedt, C. Tietz, L. Fleury, J. Wrachtrup, and C. von Borczyskowski, "Scanning confocal optical microscopy and magnetic resonance on single defect centers," *Science*, vol. 276, no. 5321, pp. 2012–2014, 1997. doi:10.1126/science.276.5321.2012.

[173] J.-P. Tetienne, L. Rondin, P. Spinicelli, M. Chipaux, T. Debuisschert, J.-F. Roch, and V. Jacques, "Magnetic-field-dependent photodynamics of single NV defects in diamond: an application to qualitative all-optical magnetic imaging," *New Journal of Physics*, vol. 14, p. 103033, oct 2012. doi:10.1088/1367-2630/14/10/103033.

[174] A. Batalov, C. Zierl, T. Gaebel, P. Neumann, I.-Y. Chan, G. Balasubramanian, P. R. Hemmer, F. Jelezko, and J. Wrachtrup, "Temporal coherence of photons emitted by single nitrogen-vacancy defect centers in diamond using optical Rabi-oscillations," *Phys. Rev. Lett.*, vol. 100, p. 077401, Feb 2008. doi:10.1103/PhysRevLett.100.077401.

[175] L. J. Rogers, S. Armstrong, M. J. Sellars, and N. B. Manson, "Infrared emission of the NV centre in diamond: Zeeman and uniaxial stress studies," *New Journal of Physics*, vol. 10, p. 103024, oct 2008. doi:10.1088/1367-2630/10/10/103024.

[176] A. Batalov, V. Jacques, F. Kaiser, P. Siyushev, P. Neumann, L. J. Rogers, R. L. McMurtrie, N. B. Manson, F. Jelezko, and J. Wrachtrup, "Low temperature studies of the excited-state structure of negatively charged nitrogen-vacancy color centers in diamond," *Phys. Rev. Lett.*, vol. 102, p. 195506, May 2009. doi:10.1103/PhysRevLett.102.195506.

[177] L. Rondin, J.-P. Tetienne, T. Hingant, J.-F. Roch, P. Maletinsky, and V. Jacques, "Magnetometry with nitrogen-vacancy defects in diamond," *Reports on Progress in Physics*, vol. 77, p. 056503, may 2014. doi:10.1088/0034-4885/77/5/056503.

[178] F. Jelezko, T. Gaebel, I. Popa, A. Gruber, and J. Wrachtrup, "Observation of coherent oscillations in a single electron spin," *Phys. Rev. Lett.*, vol. 92, p. 076401, Feb 2004. doi:10.1103/PhysRevLett.92.076401.

[179] N. Manson and J. Harrison, "Photo-ionization of the nitrogen-vacancy center in diamond," *Diamond and Related Materials*, vol. 14, no. 10, pp. 1705–1710, 2005. doi:https://doi.org/10.1016/j.diamond.2005.06.027.

[180] F. Dolde, *et al.*, "Electric-field sensing using single diamond spins," *Nature Physics*, vol. 7, pp. 459–463, Jun 2011. doi:10.1038/nphys1969.

[181] B. Smeltzer, L. Childress, and A. Gali, "^{13}C hyperfine interactions in the nitrogen-vacancy centre in diamond," *New Journal Of Physics*, vol. 13, p. 025021, feb 2011. doi:10.1088/1367-2630/13/2/025021.

[182] S. Felton, A. M. Edmonds, M. E. Newton, P. M. Martineau, D. Fisher, and D. J. Twitchen, "Electron paramagnetic resonance studies of the neutral nitrogen vacancy in diamond," *Phys. Rev. B*, vol. 77, p. 081201, Feb 2008. doi:10.1103/PhysRevB.77.081201.

[183] V. Dobrovitski, G. Fuchs, A. Falk, C. Santori, and D. Awschalom, "Quantum control over single spins in diamond," *Annual Review of Condensed Matter Physics*, vol. 4, no. 1, pp. 23–50, 2013. doi:10.1146/annurev-conmatphys-030212-184238.

[184] L. Robledo, H. Bernien, T. v. d. Sar, and R. Hanson, "Spin dynamics in the optical cycle of single nitrogen-vacancy centres in diamond," *New Journal of Physics*, vol. 13, p. 025013, Feb 2011. doi:10.1088/1367-2630/13/2/025013.

[185] L. Childress, M. V. G. Dutt, J. M. Taylor, A. S. Zibrov, F. Jelezko, J. Wrachtrup, P. R. Hemmer, and M. D. Lukin, "Coherent dynamics of coupled electron and nuclear spin qubits in diamond," *Science*, vol. 314, no. 5797, pp. 281–285, 2006. doi:10.1126/science.1131871.

[186] H. Hirata and M. Ono, "Resonance frequency estimation of a bridged loop-gap resonator used for magnetic resonance measurements," *Review of Scientific Instruments*, vol. 67, no. 1, pp. 73–78, 1996. doi:10.1063/1.1146554.

[187] V. K. Sewani, H. H. Vallabhapurapu, Y. Yang, H. R. Firgau, C. Adambukulam, B. C. Johnson, J. J. Pla, and A. Laucht, "Coherent control of NV^- centers in diamond in a quantum teaching lab," *American Journal of Physics*, vol. 88, no. 12, pp. 1156–1169, 2020. doi:10.1119/10.0001905.

[188] F. Yan, S. Gustavsson, J. Bylander, X. Jin, F. Yoshihara, D. G. Cory, Y. Nakamura, T. P. Orlando, and W. D. Oliver, "Rotating-frame relaxation as a noise spectrum analyser of a superconducting qubit undergoing driven evolution," *Nature Communications*, vol. 4, p. 2337, Aug 2013. doi:10.1038/ncomms3337.

[189] T. Gaebel, *et al.*, "Room-temperature coherent coupling of single spins in diamond," *Nature Physics*, vol. 2, pp. 408–413, Jun 2006. doi:10.1038/nphys318.

[190] G. de Lange, T. van der Sar, M. Blok, Z.-H. Wang, V. Dobrovitski, and R. Hanson, "Controlling the quantum dynamics of a mesoscopic spin bath in diamond," *Scientific Reports*, vol. 2, p. 382, Apr 2012. doi:10.1038/srep00382.

[191] N. Aslam, *et al.*, "Single spin optically detected magnetic resonance with 60–90 GHz (E-band) microwave resonators," *Review of Scientific Instruments*, vol. 86, no. 6, p. 064704, 2015. doi:10.1063/1.4922664.

[192] W. Jia, Z. Shi, X. Qin, X. Rong, and J. Du, "Ultra-broadband coplanar waveguide for optically detected magnetic resonance of nitrogen-vacancy centers in diamond," *Review of Scientific Instruments*, vol. 89, no. 6, p. 064705, 2018. doi:10.1063/1.5028335.

[193] A. Morello, *et al.*, "Single-shot readout of an electron spin in silicon," *Nature*, vol. 467, pp. 687–691, Oct 2010. doi:10.1038/nature09392.

[194] P. Neumann, J. Beck, M. Steiner, F. Rempp, H. Fedder, P. R. Hemmer, J. Wrachtrup, and F. Jelezko, "Single-shot readout of a single nuclear spin," *Science*, vol. 329, no. 5991, pp. 542–544, 2010. doi:10.1126/science.1189075.

[195] Q. Zhang, *et al.*, "High-fidelity single-shot readout of single electron spin in diamond with spin-to-charge conversion," *Nature Communications*, vol. 12, p. 1529, Mar 2021. doi:10.1038/s41467-021-21781-5.

[196] R. Dassonneville, *et al.*, "Fast high-fidelity quantum nondemolition qubit readout via a nonperturbative cross-Kerr coupling," *Phys. Rev. X*, vol. 10, p. 011045, Feb 2020. doi:10.1103/PhysRevX.10.011045.

[197] L. Zhai, M. C. Löbl, G. N. Nguyen, J. Ritzmann, A. Javadi, C. Spinnler, A. D. Wieck, A. Ludwig, and R. J. Warburton, "Low-noise GaAs quantum dots for quantum photonics," *Nature Communications*, vol. 11, p. 4745, Sep 2020. doi:10.1038/s41467-020-18625-z.

[198] L. C. Camenzind, L. Yu, P. Stano, J. D. Zimmerman, A. C. Gossard, D. Loss, and D. M. Zumbühl, "Hyperfine-phonon spin relaxation in a single-electron GaAs quantum dot," *Nature Communications*, vol. 9, p. 3454, Aug 2018. doi:10.1038/s41467-018-05879-x.